THE IMPACT OF GRAIN-SCALE ELASTIC AND VISCOELASTIC CHANGES ON SEISMIC WAVE PROPAGATION

A DISSERTATION

SUBMITTED TO THE DEPARTMENT OF GEOPHYSICS

AND THE COMMITTEE ON GRADUATE STUDIES

OF STANFORD UNIVERSITY

IN PARTIAL FULFILLMENT OF THE REQUIREMENTS

FOR THE DEGREE OF

DOCTOR OF PHILOSOPHY

Nishank Saxena

July 2014

I certify that I have read this dissertation and that, in my opinion, it is fully adequate in scope and quality as a dissertation for the degree of Doctor of Philosophy.

(Gerald M. Mavko) Principal Adviser

I certify that I have read this dissertation and that, in my opinion, it is fully adequate in scope and quality as a dissertation for the degree of Doctor of Philosophy.

(Tapan Mukerji) Co-Adviser

I certify that I have read this dissertation and that, in my opinion, it is fully adequate in scope and quality as a dissertation for the degree of Doctor of Philosophy.

(Mark D. Zoback)

I certify that I have read this dissertation and that, in my opinion, it is fully adequate in scope and quality as a dissertation for the degree of Doctor of Philosophy.

(Jack P. Dvorkin)

Approved for the Stanford University Committee on Graduate Studies.

Abstract

"In general we look for a new law by the following process. First we guess it. Then we compute the consequences to see what would be implied if we guessed right. Then we compare the computation to nature, with experiment or experience. If it disagrees with the experiment, our guess is wrong. In that simple statement is the key to science" – Richard P. Feynman

Naturally occurring rocks are typically composed of various constituents with varied elastic properties, such as gases (CO_2, methane, vapor, etc.), low-viscosity liquids (water, oil, etc.), high-viscosity liquids (heavy-oil, magma, kerogen, etc.) and solids (quartz, feldspar, calcite, etc.).

The primary objective of this thesis is to identify the fundamental physical laws which govern the sensitivity of seismic velocities and effective rock stiffness to grain-scale changes in rock constituents. Developed analytical solutions of macroscopic physical laws are further probed, benchmarked, and analyzed with numerical simulations of already established grain-scale physics at complex pore boundaries using the finite element method (FEM). Also, we suggest approximations to the exact solutions since sometimes direct measurements of the required parameters may not be available.

For fluid and solid substitution, which is one of the most fundamental problems in rock physics, we find that the exact solution requires parameters that depend on pore geometry, thus substitution is *non-unique* if only pore-fill volume fraction is known. We also prove that the classical Gassmann's bulk modulus equation is *exact* for solid substitution if compression-induced mean stresses (pressure) in initial and final pore solids are homogeneous, and either the shear modulus of the substituted solid does not change or no shear stress is induced in pores. Using the new exact substitution equations, we interpret that predicting solid-filled rock stiffness from a dry rock stiffness measurement requires more information (i.e., assumptions about the pore shape) as compared to predicting the same from a fluid-saturated rock stiffness.

We also derive substitution relations for the P-wave modulus, assuming S-wave velocity or shear modulus is not known; this is a common practical problem. For the general case of solid substitution, exact P-wave modulus substitution equation depends on usually unknown parameters. However, for fluid substitution, fewer parameters are required and the *dependence* of exact substitution on these unknown parameters reduces with increase in Poisson's ratio of the mineral in rock frame. Thus we find that P-wave modulus fluid substitution, in the absence of shear velocity, can be performed with relatively higher confidence for rocks with calcite/dolomite frame (such as carbonates) as compared to those with quartz frame (such as sandstones).

Since information on pore geometry is seldom available, we present four embedded-bound constructions for fluid and solid substitution that are based on realizable materials. In the limiting case of pore fluids, for bulk modulus, two of these constructions reduce to the bounds of Gibiansky and Torquato, which illustrates that those bounds are optimum. The first two constructions correspond to a homogeneous pore stiffness and predict the smallest change in modulus. The third construction prediction corresponds to a pore space with heterogeneous stiffness, and predicts much larger change in modulus.

We also extend our *exact* substitution relations to substitute *one* or *more* phases in multimineralic isotropic rocks, these new solutions are also equivalent to relaxing the assumption of unchanging rock microstructure upon substitution – a core assumption in

the current models. Both pore-fill phase and rock microstructure can change due to digenesis, dissolution, precipitation, partial freezing or melting, etc., and these situations can be modeled using the new formulation. Approximate bounds for the change in effective rock stiffness upon change in pore geometry are also developed which are in good agreement with laboratory and numerical examples; these bounds depend only on initial effective stiffness, properties of constituents and volume fractions of constituents.

For high viscosity fluids (such as heavy-oil, magma, kerogen, etc.) Biot theory has consistently failed to reproduce laboratory measured dispersion. Over the years, grain-scale dispersion mechanisms such as squirt (local-flow) and shear-relaxation have been more successful in explaining the measured dispersion. We present a new method to quantify the combined high-frequency effects of squirt and shear-dispersion (solid-squirt) on the elastic properties of rocks saturated with viscous fluids. Viscous fluid at high-frequencies is idealized as an elastic solid of finite shear modulus, hydraulically locked in stiff and soft pores at high-frequencies. This method entails performing solid substitution in stiff pores of a dry rock frame which is unrelaxed due to solid-filled soft pores. The unrelaxed frame stiffness solutions require information on the pressure dependency of the rock stiffness and porosity. This method does not have any adjustable parameters and all required inputs can be directly measured. With various laboratory and numerical examples, we note that accounting for combined effects of squirt and shear-dispersion is necessary to explain laboratory measured velocities of rocks saturated with fluids of high viscosity. Predictions of the new method are in good agreement with laboratory data.

Finally, we present a simple approach to model effective creep and relaxation functions of organic-rich shales. We find that model curves corresponding to mixing mineral inclusions in kerogen background better fit both dynamic and static laboratory measurements when compared to those corresponding to mixing kerogen inclusions in mineral background. We find that the creep time exponents are anisotropic and depend on boundary conditions of rock deformation. Often it is not possible to directly measure all time exponents, thus we present a simple set of empirical relations which can yield crude estimates of unmeasured time exponents starting with those measured directly.

Acknowledgement

This work was supported by the Stanford Rock Physics and Borehole Geophysics Project. For my initial years I was supported by the Manus R. Foster Fellowship. I wish to thank my dissertation reading committee members – Gary M. Mavko, Tapan Mukerji, Mark D. Zoback and Jack P. Dvorkin. Thanks to Eric M. Dunham for serving on my defense committee, and David D. Pollard for serving as my PhD defense chair. I am grateful for their encouragement, advice and constructive comments.

I am deeply indebted to my friend and adviser Gary Mavko. Virtually every idea in this thesis originated while discussing with Gary. He selflessly gifted ideas, codes, books, and even his very own binder with hand written notes from graduate days, all with a pleasant smile. Through our daily interactions that went on for hours, Gary taught me the value of being open minded, unbiased and persistent while solving problems. We developed a synergy that instilled pure inspiration in me to work harder not to win accolades or awards but hoping it will make Gary happy, I hope I succeeded, I hope you are happy… First and foremost, I dedicate this thesis to you.

My wife and I are especially grateful to Barbara Mavko for her extraordinary kindness and incredible love. We really don't know how to thank you and Gary!

I am also indebted to my co-adviser Tapan Mukerji who has been the ultimate teacher and mentor. Tapan not only helped me lay the foundation of this thesis but also taught me the value of presenting theoretical work clearly and unapologetically. Everyone notices how smart Tapan is but a few get to see the amount of effort he puts into his students. I am humbled by Tapan's humility and willingness to embrace new ideas. Special thanks to Jan and Tapan for attending our wedding in India.

I am grateful to Jack Dvorkin for teaching me rock physics from his own unique perspective. Jack, along with Gary and Tapan, made rock physics accessible to students like me. Jack always made me feel smarter than I actually am. Thank you Jack!

I am grateful to Mark Zoback for advising me on my 2nd PhD project. I often wonder if Mark secretly owns a time machine, given that he is everywhere. Over the years, I learned a lot from Mark both scientifically and professionally. I would also like to thank Eric Dunham for helping me put research problems into a broader context and also for accommodating my last minute questions.

I also owe a lot of gratitude to Janos L. Urai (RWTH Aachen), Sankar Kumar Nath (IIT Kharagpur) and David W. Eaton (Univ. of Calgary) for inspiring me to pursue graduate school. Janos especially has played a major role in my career, without his guidance I wouldn't be here!

Thanks to Fuad Nijim, Tara Arenas, Nancy Massarweh, Susan Moskowitz, Jared Gregory and Diane Lau for making sure life at Stanford went smoothly.

My colleagues made the last five years at Stanford special. I acknowledge all members of the SRB family. Thanks to Tiziana, Adam (Allan), Jane, Yu, Kevin, Piyapa, Ramil, Dario, Amos, Richa, Stéphanie, Tanima, Chisato, Yuki, Ammar, Pinar, Abrar, Humberto, Abdulla, Amrita, Salma, Danica, Tony, Natt, and Iris. Over the years, I really enjoyed my discussions with Kenichi, Kaushik, Ezequiel, Fabian, Sabrina and Priyanka. I am especially grateful to Ratnanabha Sain for his mentorship in my first few years at Stanford, his thesis work inspired me. Special thanks to my office mates Adam Tew and Yu Xia. My friends Madhur, Suman and Indrajit made coffee/lunch breaks fun.

Thanks to Adrian Lew, David M. Barnett, Wei Cai, Ellen Kuhl, Eric Shaqfeh, Peter Pinsky and Parviz Moin for their wonderful classes, their teachings have had direct impact on this thesis.

The unflinching support of my family and friends helped me sail through the rough waters of graduate school. Special mention to my dear friends, Raj & Momo, Piyush, Khastgir, Madhur, Suman, Priyanka, Dibyendu, Ratna, Madhav, Sabrina, Dominik and Valentina. Without Raj & Momo I would have probably finished a year earlier…but then, as I think more about it, I doubt if I would have finished at all.

Apart from Gary, I dedicate this thesis to my family: my grandparents, my parents (Naresh Kumar Saxena & Beena Saxena), my parents-in-law (Col. Kishore Singh Shekhawat & Prem Shekhawat), my brother (Akshansh Saxena) and my brother-in-law (Mayur Dhwaj Singh Shekhawat), from the bottom of my heart for their love and encouragement. Special thanks to Benjo and Bullet for playing ball!

The love of my life, Mrinalini Shekhawat, is the glue that holds me together when the going gets tough; she tolerates my frustrations with a smile, listens patiently as if she has all the time in the world, encourages when I give up… Your love gives meaning to however little success I enjoy. With all my heart and soul, I share this thesis with you!

Contents

Abstract ..... **v**
Acknowledgements ..... **viii**
Contents ..... **xi**
List of Tables ..... **xvi**
List of Figures ..... **xvii**

Chapter 1 Introduction **1**
1.1 Motivation 1
1.1.1 The need for fundamental research on the problem of substitution 1
1.1.2 Estimate high-frequency grain-scale dispersion effects 2
1.1.3 Quantify the effects of change in pore shape on seismic velocity 3
1.1.4 Coupled physics grain-scale simulations: A tool to learn from 4
1.1.5 Modeling creep in organic-rich shale (2nd Project) 4
1.2 Chapter organization 4
1.3 References 6

Chapter 2 Exact equations for fluid and solid substitution **9**
2.1 Abstract 9
2.2 Introduction 10
2.3 Substitution Equations 13
2.3.1 Bulk Modulus 13
2.3.1.1 Derivation 13
2.3.1.2 Generalized Exactness Condition of Gassmann 18
2.3.1.3 Generalized Gassmann for Solid-filled Rocks 19
2.3.2 Shear Modulus 21
2.3.2.1 Derivation 21
2.3.2.2 Generalized Exactness of Gassmann and C&S 24
2.3.2.3 Generalized Gassmann for Solid-filled Rocks 24

2.4 Application 25
2.5 Approximate Substitution Relations 29
2.6 Chapter Summary 31
2.7 Acknowledgements 32
2.8 Appendix A 33
2.9 Appendix B 34
2.10 References 38

Chapter 3 Further insights into substitution from the method of volume averaging (VMA) 40
3.1 Abstract 40
3.2 Introduction 41
3.3 Solid substitution & main results 42
3.3.1 Composite compressibilities and inequalities 43
3.3.2 Limitations of Ciz and Shapiro's approximation 47
3.4 Theory of volume averaging & derivation of results 50
3.4.1 Quasi-static equations of motion: Pore-scale description 53
3.4.1.1 Continuity equations 53
3.4.1.2 Momentum conservation and stress equations 54
3.4.1.3 Boundary conditions 55
3.4.2 Quasi-static equations of motion: Macroscopic description 55
3.4.2.1 Macroscopic continuity equations 56
3.4.2.2 Macroscopic pressure equations 56
3.4.2.3 Spatial deviations about the averages 56
3.4.2.4 Macroscopic shear stress equations 57
3.4.2.5 Total macroscopic pressure and shear stress 57
3.4.2.6 Porosity and deviatoric strain equations 57
3.4.3 Effective compressibilities & constitutive parameters 58
3.4.3.1 Bulk modulus K_{bc} as a function of parameters δ^A & δ^B 58
3.4.3.2 Solid-filled effective bulk modulus 56
3.4.3.3 Relation between parameters δ^A & δ^B 56
3.5 Comparisons between equations from reciprocity and MVA 60
3.6 Chapter summary 61
3.7 Acknowledgements 62
3.8 Appendix A 62
3.9 Appendix B: Macroscopic description 65
3.10 Appendix C: Macroscopic description 69
3.11 References 70

Chapter 4 Predicting change in P-wave velocity upon substitution 73
4.1 Abstract 73
4.2 Introduction 74
4.3 Exact equations for substitution 75
4.4 Special case of fluid substitution 78
4.5 Estimating substitution parameters 81

4.6 Discussion 83
4.7 Substitution recipe 88
4.7.1 Fluid substitution in rocks with interconnected pores 88
4.7.2 Fluid or solid substitution in rocks with disconnected pores 89
4.8 Chapter summary 90
4.9 Acknowledgements 91
4.10 Appendix A: Derivation of the main result 91
4.11 Appendix B: Parameters for a single inclusion 94

4.12 References 95

Chapter 5 Fluid substitution in multimineralic rocks 98
5.1 Abstract 98
5.2 Introduction 99
5.3 Reformulation of Brown-Korringa & main results 102
5.3.1. Derivation 102
5.3.2. Approximations 105
5.4 Bounds on fluid substitution 108
5.4.1 Stiff initial and final fluids 109
5.4.2 Soft initial and final fluids 111
5.5 Examples and applications 112
5.6 Chapter summary 120
5.7 Acknowledgements 121
5.8 Appendix A: Derivation of Brown and Korringa 122
5.9 Appendix B: Hashin-Shtrkiman bounds 123
5.10 References 124

Chapter 6 Embedded bounds on fluid and solid substitution 127
6.1 Abstract 127
6.2 Introduction 128
6.3 Substitution on the bounds 129
6.4 Bounds on bulk modulus for fluid substitution 131
6.5 Solid substitution on the bounds 133
6.6 Solid substitution using embedded bounds 136
6.7 Properties of embedded bounds when pore-fills are fluid 141
6.7.1 Bulk modulus 141
6.7.2 Shear modulus 144
6.8 Marion's bound averaging method 145
6.9 Comparison with other methods 147
6.9.1 Ciz and Shapiro 147
6.9.2 Berrymann and Milton 147
6.10 FEM examples 148
6.11 Chapter summary 151
6.12 Acknowledgements 152
6.13 Appendix A: Numerical calculations of constructions 153

6.14 Appendix B: Closed form solutions 162
6.15 References 165

Chapter 7 Estimating effects of grain-scale mechanisms on seismic velocitiy dispersion (solid-squirt) 168
7.1 Abstract 168
7.2 Introduction 169
7.3 Saturated rock stiffness 172
7.4 Unrelaxed frame stiffness 177
7.4.1 Derivation of unrelaxed frame bulk modulus 179
7.4.2 Derivation of unrelaxed frame shear modulus 181
7.4.3 Analysis of the result for a weak pore-fill 184
7.4.4 Unrelaxed frame stiffnesses using other methods 186
7.5 High-frequency laboratory examples 186
7.5.1 Westerly granite 186
7.5.2 Glycerol-filled Fontainebleau sandstone 188
7.5.3 Uvalde heavy-oil rock 191
7.6 Chapter summary 192
7.7 Acknowledgements 193
7.8 Appendix A 193
7.9 References 197

Chapter 8 Estimating effects of change in rock microstructure on sesimic velocities 201
8.1 Abstract 201
8.2 Introduction 202
8.3 Main results 204
8.4 Substitution of two phases in a three phase composite 209
8.4.1 Exact solutions 209
8.4.2 Approximate bounds for weak contrast in substituted phases 210
8.4.3 FEM example of a heavy-oil rock 212
8.4.4 Laboratory example of permafrost 213
8.5 Modeling effects of dissolution or precipitation 214
8.5.1 Exact solutions 214
8.5.2 Approximate bounds for weak contrast in substituted phases 216
8.6 Chapter summary 220
8.7 Acknowledgements 221
8.8 Appendix A: Derivation of the main results 221
8.9 Appendix B: Hashin-Shtrikman bounds 224
8.10 References 225

Chapter 9 Modeling infinitesimal creep in organic-rich shale 228

9.1 Abstract 228
9.2 Introduction 229
9.3 Constitutive relations for VTI media 230
9.4 Effective field method for estimation of effective stiffness 233
9.5 Modeling dynamic properties 234
9.6. Modeling creep properties 240
9.7. Discussion 244
9.4.1 Which mixing scheme to use? 244
9.4.2 Can we predict creep exponent from sesimic 245
9.4.3 Predicting other creep exponents with n33? 246
9.8 Chapter summary 249
9.9 Acknowledgements 250
9.10 References 250

Chapter 10 Unsolved problems 253
10.1 Simulate physics at grain contacts 253
10.1.1 Overview 253
10.1.2 Introduction 254
10.1.3 Finite-element simulations of sphere contacts 257
10.1.4 Numerical results 258
10.1.4.1 Hertz contact 258
10.1.4.2 Convergence behavior of the non-linear solver 259
10.1.4.3 Stress distributions at sphere contacts 260
10.1.5 Future outlook 262
10.2 Range for substitution parameters 263
10.3 Anisotropic solid substitution relations 263
10.4 Strict bounds on substitution and coupled bounds 263
10.5 Numerically simulate poromechanical behavior of rocks saturated with high-viscosity fluid 264
10.5.1 Overview 264
10.5.2 Introduction 264
10.5.3 Microscopic description 265
10.5.3.1 Continuity equations 265
10.5.3.2 Momentum conservation and stress equations 265
10.5.3.3 Pore-scale fluid pressure equation 266
10.5.3.4 Boundary condition 267
10.5.4 Macroscopic description 267
10.5.4.1 Macroscopic continuity equations 268
10.5.4.2 Macroscopic equations of motion 269
10.5.4.3 Macroscopic stress equation 270
10.5.4.4 Macroscopic pressure equation 271
10.5.4.5 Interfacial body force equation 273
10.5.4.6 Porosity and deviatoric strain equation 274
10.5.5 Summary of macroscopic equations 275

10.5.6 Future outlook 277
10.6 Acknowledgements 277
10.7 References 277

List of Tables

Table 2.1: Calculated effective solid-filled bulk and shear moduli for the 3D composites shown in Figure 2.4. 26

Table 2.2: Calculated parameters $\alpha_{1,2}$ and $\beta_{1,2}$ for the 3D composites shown in Figure 2.4. 26

List of Figures

Figure 1.1: Global and grain-scale fluid flow induced by a passing pressure wave denoted by red arrows. Black dots represent the displacement in the porocontinuum shown in brown color. 3

Figure 2.1: Compressional tractions on an arbitrary pore shape composite. Case 1 (a): pores are filled with solid *A1*. Case 2 (b): pores are filled with solid *A2*. 14

Figure 2.2: (a) Embedded bound composite ($HS^{+}_{\min}$); Frame solid *B* is shown in gray color and pore solid *A1* is shown in black. (b) Substituted embedded bound composite. 20

Figure 2.3: Shear tractions on an arbitrary pore shape composite. Case 1 (a): pores are filled with solid *A1*. Case 2 (b): pores are filled with solid *A2*. 22

Figure 2.4: Case 1 (a) and case 2 (b): for both composites pore-filling solids (*A1* and *A2*) occupy black region and frame solid *B* occupies the white region. Note that in case 1 (a) pores are spherical in shape and in case 2 frame mineral occurs as spheres. 25

Figure 2.5: Digital Fontainebleau sandstone sample. Pores shown in black and rock frame mineral shown in white. Size of 200 x 200 x 200 and a voxel edge length is 7.5 μm. 27

Figure 2.6: Laboratory measurements of wax-filled moduli (circles) of Massillon light sandstone versus temperature, data taken from Wang (1988). The predictions of hot wax-filled sandstone bulk (Figure a) and shear moduli (Figure b) starting with cold wax-filled moduli (bulk and shear) are shown. These predictions are calculated from the temperature dependent elastic moduli of wax, also reported by Wang. The embedded bounds nearly contain the measurements and the lower embedded bound predictions improve on the Gassmann and C&S approximations. Predictions using Fontainebleau image calculated parameters $\alpha_{1,2}$ and $\beta_{1,2}$ are closer to the laboratory measurements. The best fit substitution curve, which is non-unique, is also shown for shear moduli with the corresponding values of β_1 and β_2. 28

Figure 3.1: Four pore geometries for FEM calculations shown in Figure 3.2. Quartz frame is transparent and dry pores are shown. a) porosity: 0.44, bulk: 3.24 GPa and shear: 4.33 GPa; b) porosity: 0.47, bulk: 1.92 GPa and shear: 2.66 GPa; c) porosity: 0.2, bulk: 19.6 GPa and shear: 21.9 GPa; d) porosity: 0.02, bulk: 34.2 GPa and shear: 42.1 GPa. 51

Figure 3.2: (a) Minimum required dry bulk modulus for C&S approx. predictions to be within Hashin-Shtrikman (HS) bounds for solid-filled bulk modulus with pore-filling A2: water (bulk 2.25 GPa, shear 0), kaolinite clay (bulk 1.5 GPa, shear 1.4 GPa), arbitrary solid (bulk 5 GPa, shear 5 GPa) and Han's clay (bulk 25 GPa, shear 9 GPa). For all cases frame solid has properties of Quartz (bulk 36 GPa, shear 45 GPa). FEM computed dry moduli (black filled circles) for geometries shown in Figure 3.1. (b) FEM computed effective solid-filled bulk moduli (gray filled circles) for the arbitrary solid (bulk 5 GPa, shear 5 GPa) compared with C&S approx. solid-filled moduli (circles). New approximation is shown in squares..... 52

Figure 3.3: A two-phase system with phases *A* and *B*. The method of volume averaging applied to volume *V* with the contact interface (shown with dash lines) between two phases *A* and *B*. The centroid of the averaging volume denoted by x_0 and y is the relative position vector for points within the volume..... 54

Figure 4.1: Calculated Ω^A using SC (self-consistent) and DEM (differential effective medium) approximations for a range of inclusion aspect ratios and elastic properties of pore-filling material (porosity = 0.3). Figures 1a and 1b show calculations for quartz and calcite as the frame solid, respectively.....84

Figure 4.2: Fontainebleau sandstone digital sample (Andrä et al., 2013). Pores shown in black and rock frame mineral shown in white, with as size of 200×200×200 and a voxel edge length of 7.5 μm.....85

Figure 4.3: (a) Change in dry sandstone (data by Han, 1986) P-wave modulus upon fluid (water) substitution (initial dry rock - water saturated rock) as predicted by full Gassmann (in black circles), and the two approximate methods. (b) plot for carbonates (Vanorio et al., 2008).....86

Figure 4.4: Hashin-Shtrkiman bounds for isotropic water-saturated sandstone of 20 % porosity. For all effective moduli combinations (P and S-wave), the increase in darkness indicates increasing difference in dry rock P-wave moduli (in GPa) as predicted by full Gassmann and the approximate P-wave modulus methods: (a) Ω^A for spheres (b) $\Omega^A = 1$ 87

Figure 5.1: Three-phase spherical composite.....112

Figure 5.2: Example of fluid substitution in the three-phase spherical composite shown in Figure 5.1: (a) soft clay (b) stiff clay. The true effective dry bulk modulus is shown in open black symbols. These plots show the predicted dry bulk moduli starting with the true fluid-saturated bulk moduli. The HS+ approximation provides exact predictions. The upper bound provides a rather unrestrictive range for the dry bulk modulus. The iso-stress and iso-strain approximations contain the true dry bulk modulus.....113

Figure 5.3: Digital Fontainebleau sandstone sample with fluid-saturated pores shown in black and quartz phase shown in gray. Digitally altered samples are shown in figures b, c and d; clay is shown in white. (b) clay occurs as a pore-lining phase (c) clay occurs as a dispersed

phase in the rock frame. Both cases (b and c) have the same volume fractions of pores, clay and quartz..... 115

Figure 5.4: Example of fluid substitution in the digitally altered Fontainebleau sandstone sample shown in Figures 3b and 3c, for soft clay. FEM computed effective dry and fluid-saturated bulk moduli are shown in open and filled black symbols, respectively. Plots show the predicted dry bulk moduli starting with FEM computed fluid-saturated bulk moduli. Plots (a) and (b) show calculations for pore-lining and dispersed clay, respectively..... 116

Figure 5.5: Fluid substitution in the digitally altered Fontainebleau sandstone sample: pore-lining soft clay (a) and dispersed soft clay (b). FEM computed effective dry and fluid-saturated bulk moduli are shown in open and filled black symbols, respectively. Plots show the predicted dry bulk moduli starting with FEM computed water-saturated bulk moduli, as a function of varying clay fraction in the mineral frame..... 117

Figure 5.6: Range of predicted fluid substitution in the digitally altered Fontainebleau sandstone sample: pore-lining soft clay (a) and dispersed soft clay (b). Range predicted by various model combinations is shown, each range plot is slightly shifted horizontally for clarity..... 117

Figure 5.7: Example of fluid substitution in the digitally altered Fontainebleau sandstone sample shown in Figures 3b and 3c, for stiff clay. FEM computed effective dry and fluid-saturated bulk moduli are shown in open and filled black symbols, respectively. Plots show the predicted dry bulk moduli starting with FEM computed fluid-saturated bulk moduli. Plots (a) and (b) show calculations for pore-lining and dispersed clay, respectively..... 119

Figure 5.8: Fluid substitution in the digitally altered Fontainebleau sandstone sample: pore-lining stiff clay (a) and dispersed stiff clay (b). FEM computed effective dry and fluid-saturated bulk moduli are shown in open and filled black symbols, respectively. Plots show the predicted dry bulk moduli starting with FEM computed water-saturated bulk moduli, as a function of varying clay fraction in the mineral frame..... 119

Figure 5.9: Range of predicted fluid substitution in the digitally altered Fontainebleau sandstone sample: pore-lining stiff clay (a) and dispersed stiff clay (b). Range predicted by various model combinations is shown, each range plot is slightly shifted horizontally for clarity 120

Figure 5.A-1: Three stress experiments applied to the same rock sample, for use in the Betti-Rayleigh reciprocity theorem 122

Figure 6.1: Hashin-Shtrikman bounds on bulk modulus. a) example for quartz mineral with pore filling moduli $K_2 = 3$ GPa and $G_2 = 2$ GPa. b) example for quartz mineral with pore filling moduli $K_2' = 2$ GPa and $G_2' = 1$ GPa. Materials that happen to fall on the bulk modulus bounds, points A and B, transform to points A' and B' 134

Figure 6.2: Hashin-Shtrikman bounds on bulk modulus. a) example for calcite mineral ($K_1 = 72$ GPa, $G_1 = 32$ GPa), with pore filling moduli $K_2 = 30$ GPa and $G_2 = 32$ GPa . b) same mineral with pore filling moduli $K_2' = 30$ GPa and $G_2' = 0$ GPa 135

Figure 6.3: Substitution of solid pore fill (K_2=1 GPa and G_2=0.5 GPa) with a different solid pore fill (K_2'=3 GPa, G_2'=2 GPa) using a modified upper *HS* bound construction. a) Dashed curves are absolute bounds for initial composition. Data point X falls between the bounds, but can be physically realized by a *HS*+ composite consisting of end members at P and Q. b) With new composition, absolute bounds shift. Points P and Q move to P' and Q'. The same realizable microgeometry used to fit X leads to the exact prediction X' at new composition 136

Figure 6.4: (a) and (b) similar to Figure 6.3 - Substitution of solid pore fill ($K_2 = 1$ GPa and $G_2 = 0.5$ GPa) with a different solid pore fill ($K_2' = 3$ GPa, $G_2' = 2$ GPa). Data point X can be physically realized by *an infinite number* of *HS* composites of end members at P_i and Q_i spanning along the upper and lower bounds, respectively. The range of realizable microgeometries used to fit X leads to a range of predicted X' at new composition. (c) and (d) same as (a) and (b) for shear modulus $G_X = 18$ GPa..... 138

Figure 6.5: Substitution of solid pore fill ($K_2 = 1$ GPa and $G_2 = 0.5$ GPa) with a different solid pore fill ($K_2' = 3$ GPa, $G_2' = 2$ GPa). a) data point X is realized by modified *HS*+ and *HS*- bounds passing from the mineral and pore-fill end members. b) substituting the pore fill from solid to liquid leads to a range of possible results. (c) and (d) same as (a) and (b) for shear modulus $G_X = 18$ GPa..... 139

Figure 6.6: Bulk modulus substitution of fluid pore fill ($K_2 = 1$ GPa and $G_2 = 0$) with a different fluid pore fill $K_2' = 10$ GPa and $G_2' = 0$. a) bulk modulus data point X is realized by modified *HS*+ and *HS*- bounds passing from the mineral point, as well as vertical *HS* bound. b) substituting the pore fluid leads to a range of possible results 141

Figure 6.7: Coated-sphere realizations of the constuctions in Figures 5 and 6. Black represents the pore-filling material. a) $HS^+_{\min}$ -- mix of mineral point and lower bound point *G*. b) HS^+_f --mix of fluid point and lower bound point *E*. c) HS^-_f -- mix of pore fill point and upper bound point *B* 141

Figure 6.8: Shear modulus substitution of fluid pore fill ($K_2 = 1$ GPa and $G_2 = 0.01$) with a different fluid pore fill $K_2' = 10$ GPa and $G_2' = 0.01$. a) shear modulus data point X is realized by modified *HS*+ and *HS*- bounds passing from the mineral point, as well as vertical *HS* bound 144

Figure 6.9: Comparison of *BAMHS* predictions with the modified *HS* constructions. Bulk and shear moduli substitution of solid pore fill ($K_2 = 1$ GPa, $G_2 = 0.5$ GPa) with a different fluid pore fill ($K_2' = 3$ GPa, $G_2' = 2$ GPa). Effective moduli measured with the initial composition are $K_X = 15$ GPa and $G_X = 18$ GPa..... 146

Figure 6.10: Comparison of the *C&S* approximation with the modified *HS* constructions. Substitution of solid pore fill ($K_2 = 1$ GPa, $G_2 = 0.5$ GPa) with a different solid pore fill ($K_2' = 3$ GPa, $G_2' = 2$ GPa).

Effective moduli measured with the initial composition are $K_X = 15$ GPa and $G_X = 18$ GPa. 147

Figure 6.11: Comparison of the Berryman and Milton predictions with the modified *HS* constructions. Bulk and shear moduli substitution of solid pore fill ($K_2 = 1$ GPa, $G_2 = 0.5$ GPa) with a different fluid pore fill ($K_2' = 3$ GPa, $G_2' = 2$ GPa). Effective moduli before substitution are $K_X = 15$ GPa and $G_X = 18$ GPa. 148

Figure 6.12: (a) Digitial rock bitumenous sand sample of size 1.6 mm and spatial resolution (x, y and z) of 0.004 mm. Quartz is shown in white and bitumen is shown in black. (b) Grossmont carbonate digital sample. Calcite grains shown in white and bitumen shown in black 149

Figure 6.13: Predictions of hot bitumen-filled rock moduli (shown in gray) starting with cold bitumen-filled sand rock moduli (shown in black), compared with FEM computed hot bitumen-filled sand rock moduli 150

Figure 6.14: Predictions of hot bitumen-filled rock moduli (shown in gray) starting with cold bitumen-filled carbonate rock moduli (shown in black), compared with FEM computed hot bitumen-filled carbonate rock moduli..... 150

Figure 7.1: Digital composites (a) only stiff pores and no soft pores (b) stiff and soft pores. Pores are shown in gray and the mineral is transparent 175

Figure 7.2: Dry and saturated elastic moduli of the composites shown in Figure 7.1, calculated using the FEM for a range of pore fill shear moduli (μ_f) and a fixed pore fill bulk modulus (K_f) of 2.25 GPa. (a) and (b) show bulk and shear moduli of the uncracked composite shown in Figure 7.1a, respectively; whereas (c) and (d) show bulk and shear moduli of the cracked composite shown in Figure 7.1b, respectively. Elastic moduli of the cracked composite deviate from the lower embedded bound predictions shown in dashed curves..... 176

Figure 7.3: A schematic of (a) dry rock with stiff and soft pores (b) high-pressure dry rock with all soft pores closed (c) unrelaxed frame with soft pores filled with a pore fill shown in black. Dry pores and mineral shown in white and gray, respectively 178

Figure 7.4: P and S-wave velocities for Westerley granite sample as a function of confining pressure. Laboratory measurements of dry and water-saturated rock velocities are shown in open and filled circles, respectively. Predictions for water-saturated velocities using the present method (calculated for $\mu_f = 0$; which are identical to the predictions using the Mavko-Jizba-Gurevich relations along with Gassmann) are shown in full black curves, whereas predictions for the viscous-fluid saturated rock ($\mu_f = 0.1$ GPa) are shown in dashed black curves 187

Figure 7.5: Dynamic ultrasonic shear modulus of glycerol for a range of temperatures 188

Figure 7.6: Dry Fontainebleau sandstone rock moduli measured at high confining pressures. Data from Han (1986) are shown in circles and data from Carmen (2009) are shown in diamonds. The modified upper HS bound describes the high pressure moduli quite well . 189

Figure 7.7: (a) P-wave and (b) S-wave velocities of dry (open circles) and glycerol saturated (filled circles) Fontainebleau sandstone sample as a function of temperature. Predictions of the present method are shown for a range of soft porosities (between 0.1 and 1 %) thus show a range shown in dark gray color, referred in plot as - Present method. Predictions using the Mavko-Jizba-Gurevich relations with Gassmann (identical to the present method with $\mu_f = 0$) are shown in light gray color, referred as - Mavko-Jizba-Gurevich. Embedded bound predictions are also shown in dashed black curves for comparison 190

Figure 7.8: Measured shear moduli of Uvalde heavy oil rock sample as a function of heavy-oil shear moduli. Measurements at various temperatures are shown with different symbols. Predictions of the present method are shown in the solid black curve, referred in plot as - Present method. Predictions using the Mavko-Jizba-Gurevich

relations along with Gassmann ($\mu_f = 0$) are shown in dashed gray curve. Embedded bound predictions are also shown in dashed black curves for comparison 192

Figure 8.1: (a) 2D slide of a digital 3D Fontainebleau sandstone sample (Andrä et al., 2013), composed of quartz grains (in gray) and brine saturated pores (in blue), dashed black lines show imaginary cuts. (b) Digitally altered sandstone sample with the region between pore boundaries and imaginary cuts (in Figure 8.1a) replaced with clay (in red) 207

Figure 8.2: (a) induced pressure upon compression in the original sandstone. (b) Induced pressure in clay sandstone. Color scale is normalized with the same maximum value for both (a) and (b) for direct comparison 208

Figure 8.3: Original bituminous sand sample digital cube of size 1.6 mm; sub-cube of size 0.8 mm is also shown 212

Figure 8.4: Predicted bulk (a) and shear (b) moduli of bituminous sand with cold bitumen, starting with the FEM computed moduli of bituminous sand with air and bitumen saturated pores. The range predicted by the Hashin-Shtrikman bounds are shown in gray region..... 212

Figure 8.5: Predicted P-wave (a) and S-wave (b) velocities of sand samples with partially ice-filled pores, starting with the measured velocities of a sand sample fully filled with ice..... 214

Figure 8.6: Conceptual diagram of before (a) and after dissolution (b). Frame solid is shown in gray and pore solid is shown in white. Solid curves represent pore boundaries whereas dashed curves represent imaginary cuts 215

Figure 8.7: Predictions of change in elastic moduli upon dissolution for dry carbonate samples from Vialle and Vanorio (2011). Open and filled symbols show measurements before and after dissolutions, respectively. Different symbols show different samples..... 218

Figure 8.8: Predictions of change in elastic moduli upon dissolution for water-saturated carbonate samples from Vialle and Vanorio (2011). Open and filled symbols show measurements before and after dissolutions, respectively. Different symbols show different samples.....219

Figure 9.1: Mixing schemes. Left: scheme 1, isotropic kerogen inclusions in elastic mineral background. Right: scheme 2, mineral inclusions in a kerogen background.....235

Figure 9.2: Effective stiffness coefficients for a range of kerogen volume fraction. The dashed green curves correspond to inclusions of elastic mineral in kerogen background; aspect ratios are also shown on the plots. The full red curves correspond to inclusions of kerogen in mineral background.....236

Figure 9.3: Thomsen's parameters for a range of kerogen volume fraction. The dashed green curves correspond to inclusions of elastic mineral in kerogen background; aspect ratios are also shown on the plots. The full red curves correspond to inclusions of kerogen in mineral background.....237

Figure 9.4: Effective compliance coefficients for a range of kerogen volume fraction. The dashed green curves correspond to inclusions of elastic mineral in kerogen background; aspect ratios are also shown on the plots. The full red curves correspond to inclusions of kerogen in mineral background.....239

Figure 9.5: Exponents m_{ij} for a range of kerogen volume fraction. The dashed green curves correspond to inclusions of elastic mineral in kerogen background; aspect ratios are also shown on the plots. The full red curves correspond to inclusions of kerogen in mineral background.....242

Figure 9.6: Exponents n_{ij} for a range of kerogen volume fraction. The dashed green curves correspond to inclusions of elastic mineral in kerogen background; aspect ratios are also shown on the plots. The full red curves correspond to inclusions of kerogen in mineral background.....243

Figure 9.7: Exponents n_{ij} for a range of kerogen volume fraction. The dashed green curves correspond to inclusions of elastic mineral in kerogen background; aspect ratios are also shown on the plots. The full red curves correspond to inclusions of kerogen in mineral background 245

Figure 9.8: Exponents m_{ij} versus n_{33}. The dashed green curves correspond to inclusions of elastic mineral in kerogen background; aspect ratios are also shown on the plots. The full red curves correspond to inclusions of kerogen in mineral background 247

Figure 9.9: Exponents n_{ij} versus n_{33}. The dashed green curves correspond to inclusions of elastic mineral in kerogen background; aspect ratios are also shown on the plots. The full red curves correspond to inclusions of kerogen in mineral background 248

Figure 10.1: Deformed Hertz contact between two equal spheres of radius R with definitions of contact radius a, displacement δ, overlap $\xi = 2\delta$ and virtual contact radius $b = \sqrt{2}a$. Red dashed lines represent two overlapping spheres with the radius R each 253

Figure 10.2: Geometries of contact simulations. In the undeformed configuration, two spheres share a contact point (a), while in the case of a cemented contact (b), a cement radius c is defined. We make use of the problem symmetry to minimize the computational domain Ω 254

Figure 10.3: Finite-element mesh before (left) and after adaptive mesh refinement (right) 256

Figure 10.4: Comparison of theoretical prediction and numerical simulation of a Hertz contact 257

Figure 10.5: Mean stress fields simulated for a sphere contact (left) and a contact with cement (right) 259

Figure 10.6: Simulated surface traction for the case of a Hertz contact and for a cemented contact. In both simulations, a normal displacement of $\delta/R = 1.6 \times 10^{-3}$ is imposed. The contact radius or the radius of the cemented contact, respectively, is in both cases $0.04R$.....259

Chapter 1
Introduction

1.1. Motivation

The objective of this thesis is to discover and understand the physical equations governing heterogeneous porous media saturated with a viscous material. Such a medium is a good approximation for heterogeneous rocks. We are specifically interested in excitation wavelengths which are much larger than the pore scale size, so that heterogeneous porous medium can be replaced by an *effective* homogeneous medium. This is the general macroscopic description we seek. The specific motivations for this thesis are:

1.1.1. The need for fundamental research on the problem of substitution

Gassmann's equations (1951) are commonly used to address one of the most fundamental problems in rock physics: predict the change in low-frequency seismic

velocities upon substitution (or replacement) of ideal fluids (for example, gas, water, light-oil, etc.) which fully saturate interconnected rock pores. Gassmann's results are inapplicable for rocks saturated with viscous *solid-like* materials such as bitumen, heavy oil, magma, glycerol, etc., since these viscous materials do not instantly flow and can also support shear tractions at the pore boundaries when loaded at finite rates. Ciz and Shapiro (2007) generalized Gassmann's equation for a solid pore-filling. However, their generalized equation requires specifying a heuristic rock compressibility which cannot be directly measured and is also poorly understood. To get around this problem, Ciz and Shapiro suggested an approximate equation by replacing their heuristic parameter by elastic properties of the pore-filling material. Recent findings by Makarynska et al. (2010) suggest that the accuracy of this approximation is very limited. Makarynska et al. (2010) also report that although the self-consistent approach (Berryman, 1992) improves the predictions, the results are not satisfactory.

Therefore, new exact solutions with clear mathematical description to the solid substitution problem are needed to develop accurate models which predict the change in seismic velocities upon substitution.

1.1.2. **Estimate high-frequency grain-scale dispersion effects**

Biot (1941; 1956a; 1956b; 1962) published a series of seminal papers and established the discipline of poromechanics. Biot theory describes wave propagation at seismic to ultrasonic frequencies in a fluid saturated porous medium by accounting for wave-induced relative motion between elastic solid and viscous pore fluid. This relative fluid motion (also sometimes referred as global flow) is caused by pressure gradients at the scale of the seismic wavelength (Figure 1.1).

Over the years, we have reached a fairly good understanding why Biot theory fails to predict laboratory measured dispersion in most fluid saturated rocks. This is so since Biot theory does not account for energy loss due to grain-scale (or squirt) fluid motion (Mavko and Nur, 1975; O'Connell and Budiansky, 1977; Chapman et al., 2002; Dvorkin et al.,

1995; also shown in Figure 1.1). Another significant problem with the very starting point of Biot's theory is the assumption of an elastic potential function to obtain stresses using the variational method (V. de la Cruz et al., 1993; V. de la Cruz et al., 1985; Sahay et al., 2001; Sahay, 2008). Such an elastic potential function will not be conserved for high viscosity fluids at high frequencies because of the strain-rate dependence or shear relaxation. Therefore, strictly speaking, Biot's theory cannot describe seismic wave propagation in rocks saturated with high viscosity fluids. Therefore, a new model is needed to quantify the combined high-frequency effects of global, squirt and shear-relaxation on seismic velocities.

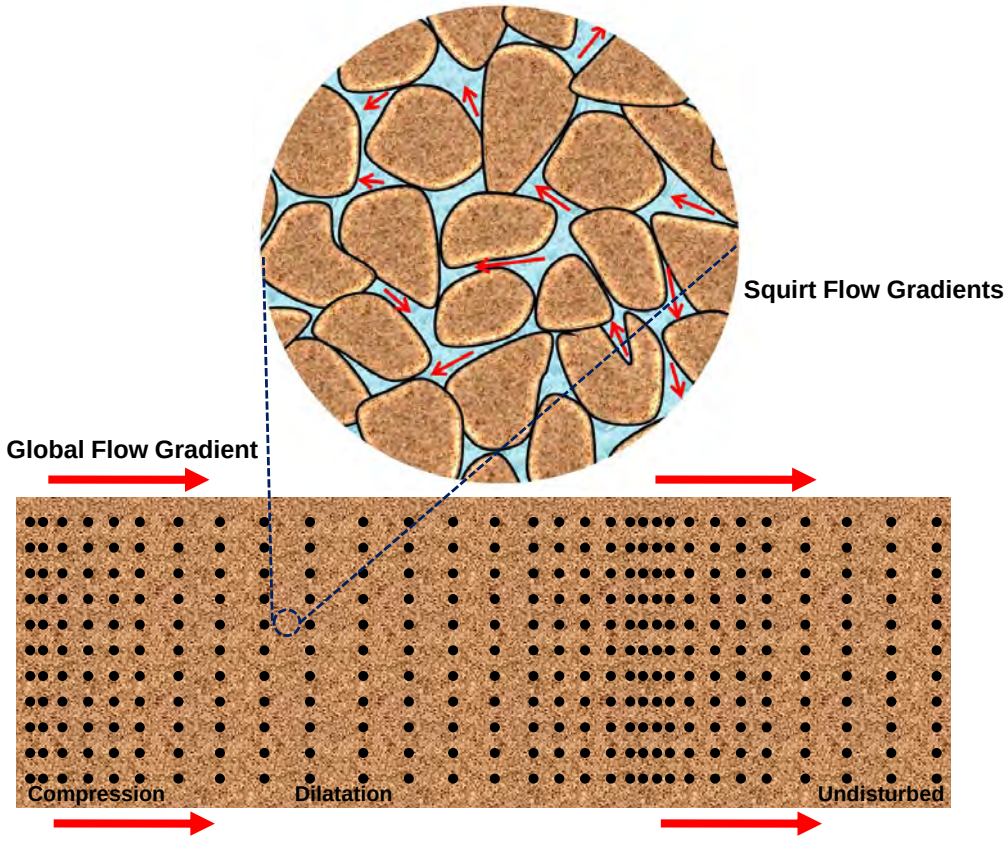

Figure 1.1: Global and grain-scale fluid flow induced by a passing pressure wave denoted by red arrows. Black dots represent the displacement in the porocontinuum shown in brown color.

1.1.3. **Quantify the effects of change in pore shape on seismic velocity**

Change in rock pore geometry can occur due to variety of geochemical processes such as dissolution, precipitation, adsorption, etc., these processes typically lead to partial replacement of existing and/or formation of new phases (Hoefiner and Fogler, 1988; Guen et al., 2007; Vanorio et al., 2011; Vialle and Vanorio, 2011). In such situations, since changes in elastic properties of rock constituents are also accompanied by changes in pore geometry, no exact solutions to such a substitution problem exist at this point. For example, such general substitution relations are required for modeling time-lapse seismic signatures of subsurface movement of chemically reactive CO_2 due to possible changes in the rock frame (Lumley, 2010).

1.1.4. **Coupled physics grain-scale simulations: A tool to learn from**

With the availability of superior computing power, we can now simulate coupled physics in complex rock pore-geometries to estimate properties. Similar approach has been successfully taken by various authors (Yeong and Torquato, 1998; Keehm, 2003; Sain, 2010). These pore-scale simulations are able to capture multi-physics, coupled boundary conditions and complex geometries. In this thesis, the physical insight gained from grain-scale simulations proved to be crucial.

1.1.5. **Modeling creep in organic-rich shale (2nd Project)**

Shale gas are vast energy reserves, but these complicated rocks are very difficult to characterize. Understanding the dependence of mechanical properties (static and dynamic) of shale on composition is critically important for various applications such as detection of organic rich shale from seismic, hydraulic fracturing to boost production, designing safe and cost effective drilling approach, etc. Laboratory measurements, although vital to our understanding of the fundamentals properties of shale, are typically limited to a few rock samples. The problem is further compounded due to experimental inaccessibility of certain mechanical properties. Therefore, theoretical modeling is required to compliment experiments as well as to further probe properties of shale rocks.

1.2. Chapter organization

In chapters 2 and 3, we derive new exact equations for fluid and solid substitution for two phase isotropic rocks. For this problem, we discover that load-induced pore stress heterogeneity plays a pivotal role, and suggest methods to account for it quantitatively. The required parameters for the exact solution depend on the details of microstructure. In chapter 4, we present exact substitution relations for P-wave modulus for situations where measurements of rock shear velocity or shear modulus is not available.

In chapter 5, we extend our two-phase solid substitution equations (in chapter 2) to multiphase rocks. These new solutions lead to approximate bounds for fluid and solid substitution. For fluid substitution, the mean of these approximate bounds improves on using Gassmann with Voigt-Ruess-Hill mineral average as a guess.

Since the exact solutions to the substitution problem depend on parameters that require information of pore geometry, in chapter 6 we introduce the embedded bound method which is based on recursive usage of Hashin-Shtrikman bounds. This method is rigorous and the only geometric input required is the pore volume fraction. The embedded bounds seemingly bound the possible change in rock stiffness upon fluid or solid substitution in two phase isotropic rocks.

In chapter 7, we present a phenomenological model to estimate the combined high-frequency dispersion effects of grain-scale fluid flow and shear-relaxation in rocks saturated with high viscosity fluids, such as, magma, bitumen, etc. All required inputs for the model can be directly measured. This "solid-squirt" model is an extension to the Mavko-Jizba squirt model.

In chapter 8, we present generalized exact substitution relations which relax the assumption of unchanging pore shape or grain geometry – which is a core assumption in the present theoretical models. These solutions can be used to estimate the change in seismic velocity upon change in microstructure due to dissolution, precipitation, and other geochemical processes that alter pore shape. In the absence of information on rock microstructure, we develop approximate bounds for such problem.

In chapter 9, we present a rock physics strategy for modeling creep and elastic properties of organic-rich shale rocks. The proposed modeling approach provides a simple recipe to investigate possible relations between elastic and creep properties of these very complicated source rocks. We find that for certain shale formations, modeling kerogen as the background phase yields better match with both static and dynamic laboratory measurements.

Finally, in chapter 10, we list the outstanding questions which require further investigation.

1.3. References

Biot, M.A., 1941, General theory of three dimensional consolidation, Journal of Applied Physics, 12, 155-164.

Biot, M.A., 1956, Theory of propagation of elastic waves in a fluid saturated porous solid. I Low frequency range, The Journal of the Acoustical Society of America, 28, 168-178.

Biot, M.A., 1956, Theory of propagation of elastic waves in a fluid saturated porous solid. II Higher frequency range. The Journal of the Acoustical Society of America, 28, 179-191.

Biot, M.A., 1962, Mechanics of deformation and acoustic propagation in porous media, Journal of Applied Physics, 33, 1482-1498

Berryman, J. G., 1992, Effective stress for transport properties of inhomogeneous porous rock: Journal of Geophysical Research, 97, 17409–17424.

Ciz, R., and S., A., Shapiro, 2007, Generalization of Gassmann equations for porous media saturated with a solid material, Geophysics, 72, A75–A79.

Chapman, M., S. V. Zatsepin, and S. Crampin, 2002, Derivation of a microstructural poroelastic model: Geophysical Journal International, 151, 427–451.

Dvorkin, J., G. Mavko, and A. Nur, 1995, Squirt flow in fully saturated rocks, Geophysics, 60, 97–107.

Gassmann, F., 1951, Über die Elastizität poröser Medien: Vierteljahrschrift der Naturforschenden Gessellschaft in Zürich, 96, 1-23.

Hoefiner, M. L., and H. S. Fogler, 1988, Pore evolution and channel formation during flow and reaction in porous media: AIChE Journal, **34**, 1, 45–54.

Keehm, Y., Computational Rock Physics: Transport Properties in Porous media and applications, PhD Thesis, Stanford University, California, 2003.

Le Guen, Y., F. Renard, R. Hellmann, E. Brosse, M. Collombet, D. Tisserand, and J.P. Gratier, 2007, Enhanced deformation of limestone and sandstone in the presence of high PCO2 fluids: Journal of Geophysical Research, 112, B05421.

Mavko, G., and D. Jizba, 1991, Estimating grain-scale fluid effects on velocity dispersion in rocks, Geophysics, 56, 1940–1949.

Mavko, G., and A. Nur, 1975, Melt squirt in the asthenosphere: Journal of Geophysical Research, 80, 1444–1448.

Makarynska, D., Gurevich, B., Behura J., and Batzle, M., 2010, Fluid substitution in rocks saturated with viscoelastic fluids, Geophysics, **75**, E115-E122.

O'Connell, R., and Budiansky, B., 1977, Viscoelastic properties of fluid-saturated cracked solids, Journal of Geophysical Research, 82, 36, 5719-5735.

Sain, R., 2010, Numerical simulation of pore-scale heterogeneity and its effects on elastic, electrical and transport properties: PhD thesis, Stanford University.

Sahay, P., 1996, Elastodynamics of deformable porous media, Proceedings of Royal Society London, 452, 1517-1529.

Sahay, P., Spanos, T., and V. de la Cruz, 2001, Seismic wave propagation in inhomogeneous and anisotropic porous media, Geophys. J. Int., 145, 209-222.

de la Cruz, Spanos, T., 1985, Seismic wave propagation in a porous medium, Geophysics, 50, 1556-1565.

de la Cruz, Sahay, P., Spanos, T., 1993, Thermodynamics of Porous Media, Mathematical and Physical Science, 443, 1917.

Vanorio, T., G. Mavko, S. Vialle, and K. Spratt, 2010, The rock physics basis for 4D seismic monitoring of CO_2 fate: Are we there yet?: The Leading Edge, 29, 156.

Vanorio, T., A. M. Nur, and Y. Ebert, 2011, Rock physics analysis and time-lapse rock imaging of geochemical effects due to the injection of CO2 into reservoir rocks: Geophysics, in review.

Vialle, S., and T. Vanorio, 2011, Laboratory measurements of elastic properties of carbonate rocks during injection of reactive CO2-saturated water: Geophysical Research Letters, **38**, L01302.

Yeong, C. L. Y. and Torquato, S., 1998, Reconstructing random media. II. Three-dimensional media from two-dimensional cuts, Physical Review E, 58, 224-233.

Chapter 2

Exact equations for fluid and solid substitution

2.1. Abstract

We derive exact equations, elastic bulk and shear, for fluid and solid substitution in monomineralic isotropic rocks of arbitrary pore shape, and suggest methods to obtain the required substitution parameters. We prove that the classical Gassmann's bulk modulus equation for fluid-to-fluid substitution is *exact* for solid-to-solid substitution if compression-induced mean stresses (pressure) or strains in initial and final pore solids are homogeneous, and either the shear modulus of the substituted solid does not change or no shear stress is induced in pores. Moreover, when compression-induced mean stresses in initial and final pore solids are homogeneous, we discuss exact generalizations of Gassmann's bulk modulus equation, which depend on usually known parameters. For

Published in GEOPHYSICS: Vol. 79 (3)

effective shear modulus, we discuss general exactness conditions of Gassmann and other approximations. Using the new exact substitution equations, we interpret that predicting solid-filled rock stiffness from a dry rock stiffness measurement requires more information (i.e., assumptions about the pore shape) as compared to predicting the same from a fluid-saturated rock stiffness.

2.2. Introduction

In geophysics, it is of considerable practical interest to predict how the effective elastic properties of a rock change when the properties of the pore-filling material change. Naturally occurring pore-filling materials include gases (e.g., methane, CO_2, helium, steam), liquids (e.g., brine, light-oil, heavy oil, magma), and solids (e.g., clay, bitumen, kerogen, salt, calcite, gas hydrates). For monomineralic isotropic rocks, Gassmann's (1951) equations relate the quasi-static *fluid-saturated* ("undrained" denoted by subscript "*ud*") rock bulk and shear moduli with the corresponding dry ("drained" denoted by subscript "*dry*") rock moduli – the operation commonly known as "fluid substitution". These relations for fluid-to-fluid substitution can be written as:

$$\frac{K_{ud}^{(i)}}{K^B - K_{ud}^{(i)}} - \frac{K^{Ai}}{\phi\left(K^B - K^{Ai}\right)} = \frac{K_{dry}}{K^B - K_{dry}} \tag{2.1}$$

and

$$\mu_{ud}^{(i)} = \mu_{dry} \quad . \tag{2.2}$$

where ϕ is the porosity (pore volume fraction); i = 1, 2, such that K^{A1} and K^{A2} are the bulk moduli of the initial (denoted by *A1*) and final (*A2*) pore fluids, respectively; K^B is the bulk modulus of the mineral in the rock frame; K_{dry} and μ_{dry} are the dry or drained effective bulk and shear moduli. Equations 2.1 and 2.2 relate the *known* or *measured* fluid-

saturated effective moduli (bulk: $K_{ud}^{(1)}$ and shear: $\mu_{ud}^{(1)}$) containing the fluid *A1* to the *unknown* fluid-saturated effective moduli (bulk: $K_{ud}^{(2)}$ and shear: $\mu_{ud}^{(2)}$) containing fluid *A2*. If the load-induced pore-pressure (mean stress in pores) is homogeneous, Gassmann's relations in equations 1 and 2 are exact for fluid-saturated rocks. This requirement is satisfied by any monomineralic isotropic fluid-saturated rock with interconnected pores, thus Gassmann's relations have considerable practical value.

Ciz and Shapiro (2007) made a significant contribution by generalizing Gassmann's relations to the case of *solid-filled* effective moduli. Their derivation is exact; however their expressions depend on additional (generally unknown) pore compliance parameters. Making heuristic approximations to the new parameters, Ciz and Shapiro proposed the following approximate *solid-to-solid* substitution equations:

$$\frac{K_{ud}^{(i)}}{K^B - K_{ud}^{(i)}} - \frac{K^{Ai}}{\phi\left(K^B - K^{Ai}\right)} \approx \frac{K_{dry}}{K^B - K_{dry}} \tag{2.3}$$

and

$$\frac{\mu_{ud}^{(i)}}{\mu^B - \mu_{ud}^{(i)}} - \frac{\mu^{Ai}}{\phi\left(\mu^B - \mu^{Ai}\right)} \approx \frac{\mu_{dry}}{\mu^B - \mu_{dry}} \quad , \tag{2.4}$$

where i = 1, 2; K^{A1} and μ^{A1} are the bulk and shear moduli of the initial pore-filling solid (*A1*), and K^{A2} and μ^{A2} are the bulk and shear moduli of the final pore-filling solid (*A2*); K^B and μ^B are the bulk and shear moduli of the mineral in the rock frame. Equations 2.3 and 2.4 relate the solid-filled effective moduli (bulk: $K_{ud}^{(1)}$ and shear: $\mu_{ud}^{(1)}$) containing the solid *A1* to the solid-filled effective moduli (bulk: $K_{ud}^{(2)}$ and shear: $\mu_{ud}^{(2)}$) containing solid *A2*. In this chapter, we refer to equations 2.3 and 2.4 as the *Ciz-Shaprio (C&S) approximations*.

The dependence of Ciz and Shapiro's new compliance parameters on pore geometry and material constants is not known, thus our understanding of the accuracy and validity of Ciz and Shapiro's approximations (equations 2.3 and 2.4) has been incomplete. Unlike Gassmann's relation for fluid-to-fluid substitution, we do not understand when and under

what conditions Ciz and Shapiro's approximations are *exact* for fluid-to-solid, solid-to-fluid or for the general problem of solid-to-solid substitutions. Therefore, this subject still requires further investigation and clarifications.

In this chapter, we derive exact solid-to-solid substitution equations (bulk and shear) for monomineralic isotropic rocks using an alternative approach: reciprocity. This approach provides significant physical insight into the problem of fluid and solid substitution. Our new exact equations differ from those obtained by Ciz and Shapiro (2007) although both sets of equations are exact. The motivation here is to identify *precise conditions* under which the original Gassmann's equations (2.1 and 2.2) and Ciz and Shapiro's equations (2.3 and 2.4) are *exact* for solid-to-solid substitution; and to derive new generalizations to these equations. One of the goals of this chapter is to express, whenever possible, the solid-filled effective stiffnesses in terms of other measurable quantities instead of heuristic compressibilities, and identify the precise general conditions under which solid-to-solid substitution is exact, like we currently understand these conditions for Gassmann's fluid-to-fluid substitution relations.

Using the recently proposed embedded bound method of Mavko and Saxena (2013; chapter 6), we obtain generalizations of Gassmann's bulk modulus relation (equation 2.1) for solid-to-solid substitution. These generalizations require the same assumption of compression-induced homogeneous pore-pressure - required by the original Gassmann's relation for bulk modulus. We also discuss the limitations associated with estimating solid-filled stiffnesses starting with fluid-saturated and/or dry rock measurements, and address if some effective stiffness measurements yield better estimates than others.

The sections are organized as follows. In the next section we derive exact fluid and solid substitution equations for bulk and shear, and present our main findings. Further clarifications on derivations are discussed in the Appendices. In the subsequent section we discuss how the new substitution parameters can be estimated and compare our theoretical predictions with numerical and laboratory data. Chapter ends with discussion and conclusions.

2.3. Substitution Equations

In this section, we derive substitution equation for effective bulk and shear moduli relating the *first* solid-filled effective moduli (bulk: $K_{ud}^{(1)}$ and shear: $\mu_{ud}^{(1)}$) of an isotropic monomineralic rock containing a linear elastic pore-filling solid *A1* (bulk: K^{A1} and shear: μ^{A1}) and linear elastic frame mineral solid *B* (bulk: K^{B} and shear: μ^{B}) to *second* solid-filled effective moduli (bulk: $K_{ud}^{(2)}$ and shear: $\mu_{ud}^{(2)}$) of the same rock but containing pore-filling solid *A2* (bulk: K^{A2} and shear: μ^{A2}). We use the term *porosity* as the volume fraction of pore-filling material even though we consider solid-filled pores.

2.3.1. Bulk Modulus

2.3.1.1. Derivation

Let the *outer surface* (denoted by Ω) of an isotropic composite sample, as shown in Figure 2.1a, be subjected to compressive surface tractions as

$$T_i^{\Omega} = -Pn_i \quad (i = 1, 2, 3) \text{ on } \Omega \ , \tag{2.5}$$

where T_i^{Ω} are traction components, n_i are the components of an outward-pointing surface normal vector to the surface Ω, and P is constant. The spatially-variable stresses induced at any point in frame-filling solid *B* are given by σ_{ij}^{B}. These stresses are similarly related to tractions within *B*, T_i^{B}, as

$$T_i^{B} = \sigma_{ij}^{B} n_j \quad (i = 1, 2, 3) \ . \tag{2.6}$$

Here we use standard summation over repeated indices. Stresses σ_{ij}^{B} can be decomposed as

$$\sigma_{ij}^{B} = -P^{B}\delta_{ij} + \tau_{ij}^{B} \ , \tag{2.7}$$

where P^B is the pressure (negative of mean stress, $-\sigma_{kk}^B/3$), and τ_{ij}^B are deviatoric stresses.

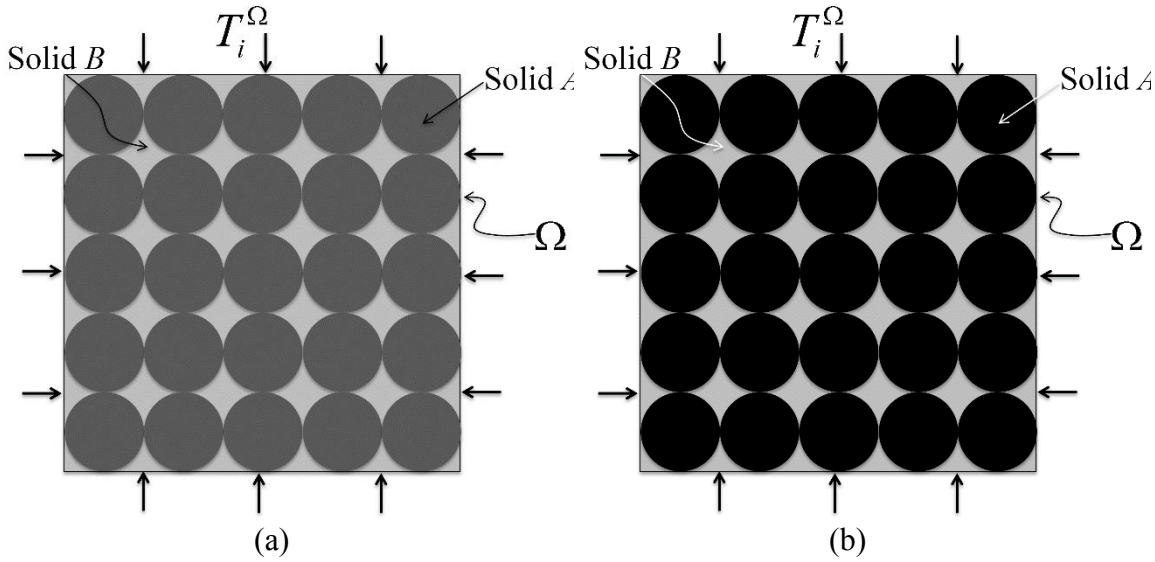

Figure 2.1: Compressional tractions on an arbitrary pore shape composite. Case 1 (a): pores are filled with solid *A1*. Case 2 (b): pores are filled with solid *A2*.

Let's suppose the pores are filled with solid *A1* (case 1) such that the compression-induced stresses within solid *A1* are given by σ_{ij}^{A1}. These stresses are related to tractions T_i^{A1} as

$$T_i^{A1} = \sigma_{ij}^{A1} n_j \quad (i = 1, 2, 3) \ . \tag{2.8}$$

Stresses in solid *A1* are related to strains ε_{ij}^{A1} by Hooke's law:

$$\sigma_{ij}^{A1} = K^{A1}\varepsilon_{kk}^{A1}\delta_{ij} + 2\mu^{A1}\left(\varepsilon_{ij}^{A1} - \frac{1}{3}\varepsilon_{kk}^{A1}\delta_{ij}\right) \ . \tag{2.9}$$

Stresses and strains in solid *A1* can be decomposed as

$$\sigma_{ij}^{A1} = -P^{A1}\delta_{ij} + \tau_{ij}^{A1} \tag{2.10}$$

and

$$\varepsilon_{ij}^{A1} = \frac{e^{A1}}{3}\delta_{ij} + \gamma_{ij}^{A1} \quad ,$$

where P^{A1} is the pressure, and τ_{ij}^{A1} are deviatoric stresses in the pore-solid *A1*; e^{A1} and γ_{ij}^{A1} are mean and deviatoric parts of strains in solid *A1*.

If instead of solid *A1*, the pores are filled by solid *A2* (Figure 2.1b; case 2) then the corresponding equations 2.8, 2.9 and 2.10 are

$$T_i^{A2} = \sigma_{ij}^{A2} n_j \quad (i = 1, 2, 3) \quad , \tag{2.11}$$

$$\sigma_{ij}^{A2} = K^{A2}\varepsilon_{kk}^{A2}\delta_{ij} + 2\mu^{A2}\left(\varepsilon_{ij}^{A2} - \frac{1}{3}\varepsilon_{kk}^{A2}\delta_{ij}\right) \quad , \tag{2.12}$$

$$\sigma_{ij}^{A2} = -P^{A2}\delta_{ij} + \tau_{ij}^{A2} \tag{2.13}$$

and

$$\varepsilon_{ij}^{A2} = \frac{e^{A2}}{3}\delta_{ij} + \gamma_{ij}^{A2} \quad .$$

If the composite is isotropic, using the Betti-Rayleigh reciprocity theorem (Walsh, 1965; Mavko and Jizba, 1991) we can write the difference ΔE_{12} in elastic energy stored in the two cases above as

$$\Delta E_{12} = \left(\frac{(P)^2}{2K_{ud}^{(1)}} - \frac{(P)^2}{2K_{ud}^{(2)}}\right)V = \frac{1}{2}\int_{S_\phi}\left(T_i^{A2}u_i^{A1} - T_i^{A1}u_i^{A2}\right)dS_\phi \quad , \tag{2.14}$$

where $u_i^{A1,A2}$ are displacements at the pore boundaries in the *i*th direction. The surface integral is over the surface S_ϕ of pore boundaries, and V is total composite volume. Detailed derivation of equation 2.14 is presented in Appendix A; a special case of equation 2.14 was discussed previously by Hashin (1962; equation 8 in his paper). Using equations 2.8 and 2.11, and Gauss' divergence theorem along with equilibrium conditions and Hooke's law, equation 2.14 can be rewritten in the following form

$$\Delta E_{12} = \left(\frac{(P)^2}{2K_{ud}^{(1)}} - \frac{(P)^2}{2K_{ud}^{(2)}} \right) V = \frac{1}{2} \int_{V_\phi} \left(\left(\frac{1}{K^{A1}} - \frac{1}{K^{A2}} \right) P^{A1} P^{A2} + \frac{1}{2} \left(\frac{1}{\mu^{A1}} - \frac{1}{\mu^{A2}} \right) \tau_{ij}^{A1} \tau_{ij}^{A2} \right) dV_\phi \quad . \tag{2.15}$$

The volume integral in equation 2.15 is over pore volume V_ϕ. Note that the second term containing $\tau_{ij}^{A1}\tau_{ij}^{A2}$ is summed over repeated indices. For convenience we adopt the following volume average notation:

$$\overline{\psi} = \frac{1}{V_\phi} \int_{V_\phi} \psi \, dV_\phi \quad , \tag{2.16}$$

where $\overline{\psi}$ is the pore volume average of any quantity ψ. Rewriting equation 2.15 in the volume average notation and taking out the constant terms from the right hand side, we get

$$\left(\frac{(P)^2}{K_{ud}^{(1)}} - \frac{(P)^2}{K_{ud}^{(2)}} \right) \frac{V}{V_\phi} = \left(\frac{1}{K^{A1}} - \frac{1}{K^{A2}} \right) \overline{P^{A1} P^{A2}} + \frac{1}{2} \left(\frac{1}{\mu^{A1}} - \frac{1}{\mu^{A2}} \right) \overline{\tau_{ij}^{A1} \tau_{ij}^{A2}} \quad , \tag{2.17}$$

where V_ϕ / V is porosity ϕ. Now if in equation 2.17 we put solid *B* in place of pore-filling solid *A2*, then the composite for the second case becomes homogeneous and $K_{ud}^{(2)} = K^B$.

$$\left(\frac{(P)^2}{K_{ud}^{(1)}} - \frac{(P)^2}{K^B} \right) \frac{1}{\phi} = \left(\frac{1}{K^{A1}} - \frac{1}{K^B} \right) \overline{P^B P^{A1}} + \frac{1}{2} \left(\frac{1}{\mu^{A1}} - \frac{1}{\mu^B} \right) \overline{\tau_{ij}^B \tau_{ij}^{A1}} \quad , \tag{2.18}$$

which also guarantees $P^B = P$ and $\tau_{ij}^B = 0$ everywhere in the composite. Hence, equation 2.18 reduces to

$$\frac{\left(\frac{1}{K_{ud}^{(1)}} - \frac{1}{K^B} \right)}{\phi \left(\frac{1}{K^{A1}} - \frac{1}{K^B} \right)} = \frac{\overline{P^{A1}}}{P} \quad . \tag{2.19}$$

Similarly, if we replace pore-filling solid *A1* with solid *B* we get

$$\frac{\left(\frac{1}{K_{ud}^{(2)}}-\frac{1}{K^{B}}\right)}{\phi\left(\frac{1}{K^{A2}}-\frac{1}{K^{B}}\right)}=\frac{\overline{P^{A2}}}{P} \quad . \tag{2.20}$$

Next, rearranging terms from equation 2.17 we get

$$(P)^2=\frac{\left(\frac{1}{K^{A1}}-\frac{1}{K^{A2}}\right)}{\left(\frac{1}{K_{ud}^{(1)}}-\frac{1}{K_{ud}^{(2)}}\right)\frac{1}{\phi}}\overline{P^{A1}P^{A2}}+\frac{1}{2}\frac{\left(\frac{1}{\mu^{A1}}-\frac{1}{\mu^{A2}}\right)}{\left(\frac{1}{K_{ud}^{(1)}}-\frac{1}{K_{ud}^{(2)}}\right)\frac{1}{\phi}}\overline{\tau_{ij}^{A1}\tau_{ij}^{A2}} \quad . \tag{2.21}$$

Multiplying equations 2.19 and 2.20 we get

$$(P)^2=\frac{\overline{P^{A1}}}{\frac{\left(\frac{1}{K_{ud}^{(1)}}-\frac{1}{K^{B}}\right)}{\phi\left(\frac{1}{K^{A1}}-\frac{1}{K^{B}}\right)}}\frac{\overline{P^{A2}}}{\frac{\left(\frac{1}{K_{ud}^{(2)}}-\frac{1}{K^{B}}\right)}{\phi\left(\frac{1}{K^{A2}}-\frac{1}{K^{B}}\right)}} \quad . \tag{2.22}$$

Equating equations 2.21 and 2.22 we get

$$\left(\frac{1}{K^{A1}}-\frac{1}{K^{A2}}\right)\alpha_1+\left(\frac{1}{\mu^{A1}}-\frac{1}{\mu^{A2}}\right)\alpha_2=\phi\frac{\left(\frac{1}{K^{A2}}-\frac{1}{K^{B}}\right)\left(\frac{1}{K^{A1}}-\frac{1}{K^{B}}\right)}{\left(\frac{1}{K_{ud}^{(1)}}-\frac{1}{K^{B}}\right)\left(\frac{1}{K_{ud}^{(2)}}-\frac{1}{K^{B}}\right)}\left(\frac{1}{K_{ud}^{(1)}}-\frac{1}{K_{ud}^{(2)}}\right) \quad , \tag{2.23}$$

where

$$\alpha_1=\frac{\overline{P^{A1}P^{A2}}}{\overline{P^{A1}}\,\overline{P^{A2}}}=\frac{\overline{e^{A1}e^{A2}}}{\overline{e^{A1}}\,\overline{e^{A2}}} \tag{2.24}$$

and

$$\alpha_2=\frac{1}{2}\frac{\overline{\tau_{ij}^{A1}\tau_{ij}^{A2}}}{\overline{P^{A1}}\,\overline{P^{A2}}}=2\frac{\overline{\gamma_{ij}^{A1}\gamma_{ij}^{A2}}}{\overline{e^{A1}}\,\overline{e^{A2}}}\frac{\mu^{A1}\mu^{A2}}{K^{A1}K^{A2}}=\alpha_2'\frac{\mu^{A1}\mu^{A2}}{K^{A1}K^{A2}} \quad . \tag{2.25}$$

Note that equation 2.23 is the exact solid-to-solid substitution equation for effective bulk modulus.

Parameter α_1 describes the heterogeneity of compression-induced mean stress (or pressure) in initial and final pore-filling materials; parameter α_2 describes the contribution of compression-induced shear stresses in initial and final pore-filling materials. Certain properties of parameters α_1 and α_2 are known: if $K^{A1} \le K^{A2}$ and $\mu^{A1} \le \mu^{A2}$, then $K_{ud}^{(1)} \le K_{ud}^{(2)}$ (Hill, 1963); hence, α_1, α_2 and α_2' must be non-negative. For fluid-saturated rocks, Gibiansky and Torquato (1998) have shown that Gassmann's bulk modulus equation is, in fact, a strict lower bound on the change in effective bulk modulus upon fluid-to-fluid substitution; this statement is identical to putting $\alpha_1 \ge 1$ and $\alpha_2 = 0$ in equation 2.23. For solid-to-solid substitution a general argument for $\alpha_1 \ge 1$ can be made but it is not rigorously proven here.

Interestingly, when effective modulus of a composite is described by an exact closed-form equation, we can estimate its load-induced stress heterogeneity from equation 2.23. For example, when shear modulus of the pore-solid and the frame mineral solid are equal, the exact expression for the effective bulk modulus is given by Hill's closed-form relation (Hill, 1963), from equation 2.23 we can check that for such composites compression-induced mean stress in pores (pore-pressure) is homogeneous or constant, i.e., $\alpha_1 = 1$.

2.3.1.2. General exactness condition of Gassmann

We recover an equation identical to the original Gassmann's fluid-to-fluid substitution equation (2.1) for effective bulk modulus, if for any composite, $\alpha_1 = 1$ (homogeneous mean stress in pores) and either $\mu^{A1} = \mu^{A2}$ or $\alpha_2 = 0$. This proves that Gassmann's effective bulk modulus equation is *exact* for solid-to-solid substitution in any arbitrary pore shape solid-filled composite for which compression-induced mean stress or strain in initial and final pores (pore-pressure) is homogeneous and shear modulus of the substituted pore-filling does not change, i.e., $\mu^{A1} = \mu^{A2} \ge 0$.

2.3.1.3. Generalized Gassmann for Solid-filled Rocks

In chapter 6 we will discuss the *embedded bound method* (Mavko and Saxena, 2013) for estimating the change in effective bulk modulus upon substitution (solid or fluid). The approach is based on recursive use of the Hashin-Shtrikman (HS) (1963) bounds for two-phase materials, which guarantees that the results are physically realizable. We note that exact solutions of the substitution parameters α_1 and α_2 can be obtained for composites which realize some of the infinitely many embedded bound constructions that are consistent with a given effective modulus $K_{ud}^{(1)}$. Since there are an infinite number of embedded constructions, the substituted bulk modulus and the parameters α_1 and α_2 have a range of possible values each corresponding to a different microstructure. Among these embedded constructions, two constructions – referred in chapter 6 as $HS_{\min}^{+}$ and $HS_{\min}^{-}$, seem to predict the smallest change in bulk modulus upon substitution; and two constructions – HS_f^{+} and HS_f^{-}, seem to predict the largest change. Further details on these constructions can be found in chapter 6. The corresponding closed form substitution equations can also be found in Appendix B.

For fluid-to-fluid substitution, these four constructions are strict bounds on the substituted effective bulk modulus since these reduce to the rigorous bounds obtained by Gibiansky and Torquato (1998).

Using equation 2.23 and equations B-3 to B-14, we obtain $\alpha_1 = 1$ (compression-induced homogeneous mean stress in pores) for composites that attain $HS_{\min}^{+}$ and $HS_{\min}^{-}$ constructions, whereas the parameter $\alpha_2 \neq 0$ differs for the two constructions. Realization of $HS_{\min}^{+}$ is shown in Figure 2.2. The recipe to obtain substitution parameter α_2 for these constructions is also discussed in the Appendix B. For both $HS_{\min}^{+}$ and $HS_{\min}^{-}$ composites, the solid-to-solid substitution equations can be exactly written as:

$$\frac{K_{ud}^{(i)}}{K^B - K_{ud}^{(i)}} - \frac{K^{Ai}}{\phi\left(K^B - K^{Ai}\right)} = \frac{K_{zb}^{(i)}}{K^B - K_{zb}^{(i)}} \quad , \tag{2.26}$$

where i = 1, 2; bulk modulus $K_{zb}^{(i)}$ is the solid-filled effective modulus of the embedded composite ($HS_{\min}^{+}$ or $HS_{\min}^{-}$) in the special case when pores are filled with a *hypothetical* solid of *zero* bulk modulus and *non-zero* shear modulus of μ^{Ai} .

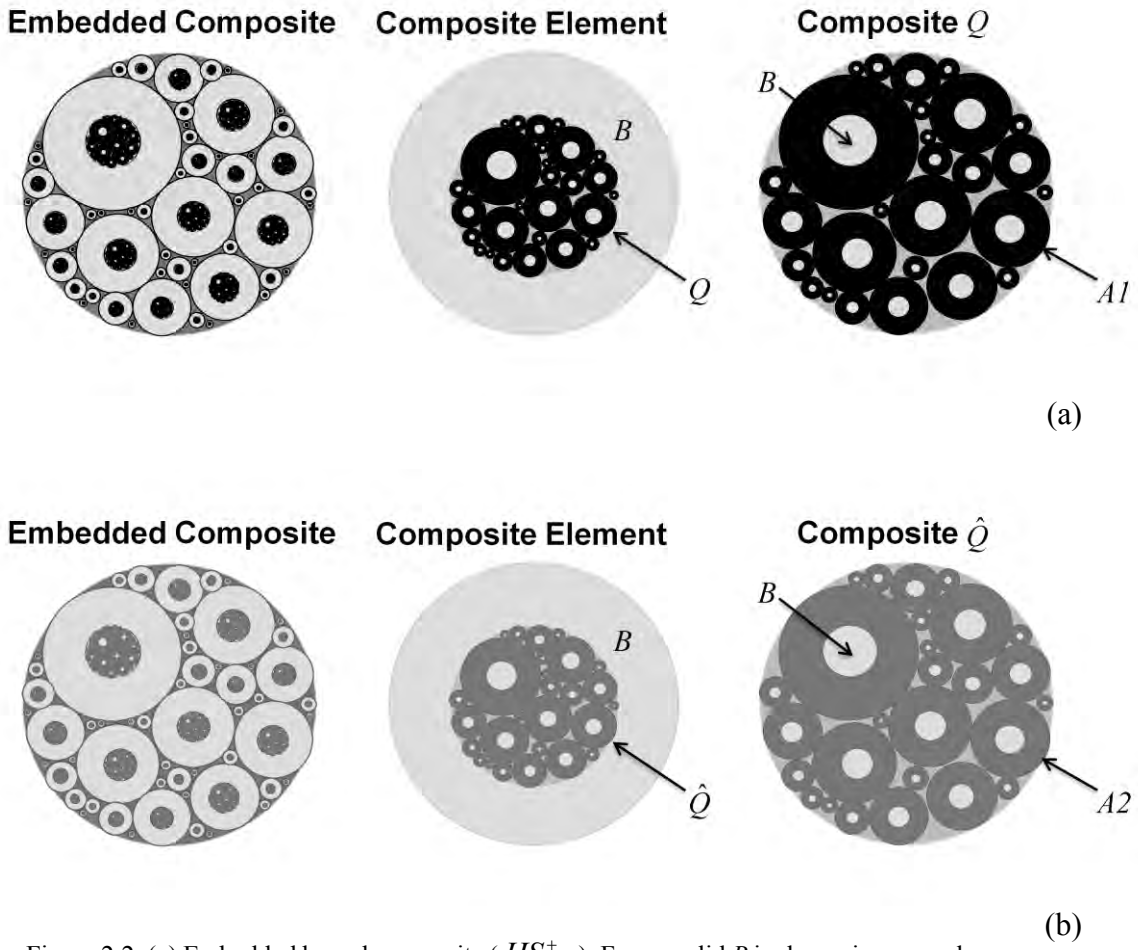

Figure 2.2: (a) Embedded bound composite ($HS_{\min}^{+}$); Frame solid *B* is shown in gray color and pore solid *A1* is shown in black. (b) Substituted embedded bound composite.

Generally for rocks of arbitrary pore shape, bulk modulus $K_{zb}^{(i)}$ is related to the solid-filled bulk modulus $K_{ud}^{(i)}$ by the inequality

$$\frac{K_{ud}^{(i)}}{K^{B}-K_{ud}^{(i)}}-\frac{K^{Ai}}{\phi\left(K^{B}-K^{Ai}\right)}\geq\frac{K_{zb}^{(i)}}{K^{B}-K_{zb}^{(i)}} \quad . \tag{2.27}$$

Further details of equation 2.27 are in chapter 3. For the $HS^{+}_{\min}$ or $HS^{-}_{\min}$ composites equation 2.26 *exactly and uniquely* relate $K^{(i)}_{zb}$ to $K^{(i)}_{ud}$. For the $HS^{+}_{\min}$ composite, bulk modulus $K^{(i)}_{zb}$ can be further related to the dry bulk modulus K_{dry} as

$$K^{(i)}_{zb} = \frac{(1-\phi)\left(\frac{1}{K^B} - \frac{1}{K_{dry}}\right) + \frac{3\phi}{4}\left(\frac{1}{\mu^B} - \frac{1}{\mu^{Ai}}\right)}{\frac{1}{K^B}\left(\frac{1}{K^B} - \frac{1}{K_{dry}}\right) + \frac{3\phi}{4}\left(\frac{1}{K^B\mu^B} - \frac{1}{\mu^{Ai}K_{dry}}\right)} \quad \text{and } i = 1, 2\,. \tag{2.28}$$

For the $HS^{-}_{\min}$ composite, the relation between the bulk modulus $K^{(i)}_{zb}$ and the dry bulk modulus K_{dry} is a bit complicated but can be estimated using equations B-9 to B-14.

Effective bulk modulus equations describing the composites that realize $HS^{+}_{\min}$ (equations 2.26 and 2.28) or $HS^{-}_{\min}$ constructions (equations B-9 to B-14) can be described as exact generalizations of the original Gassmann's equation (2.1) to the case of solid-filled rocks for which compression-induced mean stress (or pressure) in pores is homogeneous. For fluid-to-fluid substitution, these reduce to Gassmann's equation (2.1).

The HS^{+}_{f} and HS^{-}_{f} constructions, which seem to predict the largest change upon substitution, correspond to $\alpha_1 > 1$, i.e., heterogeneous compression-induced mean-stress; this can be shown using equation 2.23 and equations B-15 to B-24.

2.3.2. **Shear Modulus**

2.3.2.1. **Derivation**

Similar to the effective bulk modulus derivation we consider the following surface shear tractions (referred in this chapter as shear field) at the outer surface Ω (as shown in Figure 2.3a)

$$\begin{pmatrix} T_1^{\Omega} \\ T_2^{\Omega} \\ T_3^{\Omega} \end{pmatrix} = \begin{pmatrix} 0 & \tau & 0 \\ \tau & 0 & 0 \\ 0 & 0 & 0 \end{pmatrix} \begin{pmatrix} n_1 \\ n_2 \\ n_3 \end{pmatrix} \quad . \tag{2.29}$$

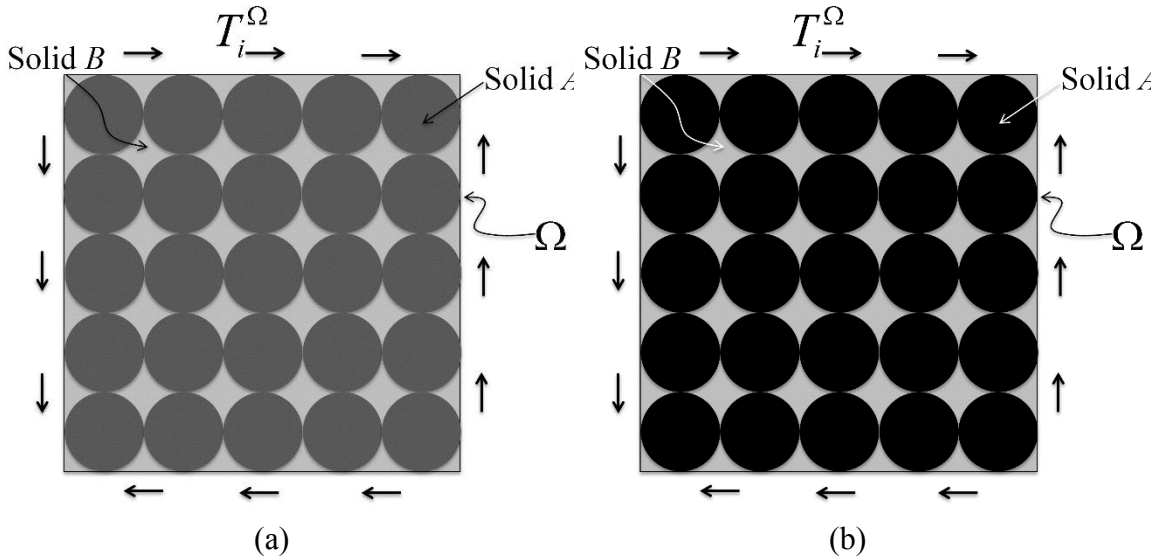

Figure 2.3: Shear tractions on an arbitrary pore shape composite. Case 1 (a): pores are filled with solid *A1*. Case 2 (b): pores are filled with solid *A2*.

For these tractions, the difference ΔE_{12} in elastic energy stored between the two cases: composite filled with solid *A1* and solid *A2* (Figures 3a and 3b), is given by

$$\Delta \mathrm{E}_{12} = \left(\frac{(\tau)^2}{2\mu_{ud}^{(1)}} - \frac{(\tau)^2}{2\mu_{ud}^{(2)}} \right) V = \frac{1}{2} \int_{V_\phi} \left(\left(\frac{1}{K^{A1}} - \frac{1}{K^{A2}} \right) P^{A1} P^{A2} + \frac{1}{2} \left(\frac{1}{\mu^{A1}} - \frac{1}{\mu^{A2}} \right) \tau_{ij}^{A1} \tau_{ij}^{A2} \right) dV_\phi \quad . \tag{2.30}$$

Rearranging terms and using the volume averaging notation we get

$$\left(\frac{(\tau)^2}{\mu_{ud}^{(1)}} - \frac{(\tau)^2}{\mu_{ud}^{(2)}} \right) \frac{1}{\phi} = \left(\frac{1}{K^{A1}} - \frac{1}{K^{A2}} \right) \overline{P^{A1} P^{A2}} + \frac{1}{2} \left(\frac{1}{\mu^{A1}} - \frac{1}{\mu^{A2}} \right) \overline{\tau_{ij}^{A1} \tau_{ij}^{A2}} \quad . \tag{2.31}$$

If instead of solid *A2,* the pores are filled with solid *B* then the composite becomes homogeneous and $\mu_{ud}^{(2)} = \mu^B$. In this case, equation 2.31 reduces to

$$\left(\frac{(\tau)^2}{\mu_{ud}^{(1)}}-\frac{(\tau)^2}{\mu^B}\right)\frac{1}{\phi}=\left(\frac{1}{K^{A1}}-\frac{1}{K^B}\right)\overline{P^B P^{A1}}+\frac{1}{2}\left(\frac{1}{\mu^{A1}}-\frac{1}{\mu^B}\right)\overline{\tau_{ij}^{A1}\tau_{ij}^B} \quad . \tag{2.32}$$

Also if pores are filled with solid B, then $P^B=0$, $\tau_{11}^B=\tau_{22}^B=\tau_{33}^B=\tau_{23}^B=\tau_{13}^B=0$ and $\tau_{12}^B=\tau_{21}^B=\tau$ everywhere, this results in

$$\left(\frac{\tau}{\mu_{ud}^{(1)}}-\frac{\tau}{\mu^B}\right)\frac{1}{\phi}=\left(\frac{1}{\mu^{A1}}-\frac{1}{\mu^B}\right)\overline{\tau_{12}^{A1}} \quad . \tag{2.33}$$

Similarly, if solid *A1* is replaced by solid *B*, equation 2.31 becomes

$$\left(\frac{\tau}{\mu_{ud}^{(2)}}-\frac{\tau}{\mu^B}\right)\frac{1}{\phi}=\left(\frac{1}{\mu^{A2}}-\frac{1}{\mu^B}\right)\overline{\tau_{12}^{A2}} \quad . \tag{2.34}$$

From equations 2.31, 2.33 and 2.34 we obtain

$$\left(\frac{1}{\mu^{A1}}-\frac{1}{\mu^{A2}}\right)\beta_1+\left(\frac{1}{K^{A1}}-\frac{1}{K^{A2}}\right)\beta_2=\phi\frac{\left(\frac{1}{\mu^{A2}}-\frac{1}{\mu^B}\right)\left(\frac{1}{\mu^{A1}}-\frac{1}{\mu^B}\right)}{\left(\frac{1}{\mu_{ud}^{(1)}}-\frac{1}{\mu^B}\right)\left(\frac{1}{\mu_{ud}^{(2)}}-\frac{1}{\mu^B}\right)}\left(\frac{1}{\mu_{ud}^{(1)}}-\frac{1}{\mu_{ud}^{(2)}}\right) \quad , \tag{2.35}$$

Parameters β_1 and β_2 are given by

$$\beta_1=\frac{1}{2}\frac{\overline{\tau_{ij}^{A1}\tau_{ij}^{A2}}}{\overline{\tau_{12}^{A1}}\;\overline{\tau_{12}^{A2}}}=\frac{1}{2}\frac{\overline{\gamma_{ij}^{A1}\gamma_{ij}^{A2}}}{\overline{\gamma_{12}^{A1}}\;\overline{\gamma_{12}^{A2}}} \quad , \tag{2.36}$$

and

$$\beta_2=\frac{\overline{P^{A1}P^{A2}}}{\overline{\tau_{12}^{A1}}\;\overline{\tau_{12}^{A2}}}=\frac{1}{4}\frac{\overline{e^{A1}e^{A2}}}{\overline{\gamma_{12}^{A1}}\;\overline{\gamma_{12}^{A2}}}\frac{K^{A1}K^{A2}}{\mu^{A1}\mu^{A2}}=\beta_2'\frac{K^{A1}K^{A2}}{\mu^{A1}\mu^{A2}} \quad . \tag{2.37}$$

For effective shear modulus, equation 2.35 is the *exact* solid-to-solid substitution equation. Parameter β_1 describes the heterogeneity of shear field-induced deviatoric stresses in initial and final pore-filling materials; parameter β_2 describes the contribution

of shear field-induced mean stresses (or pressure) in initial and final pore-filling materials. Since if $K^{A1} \le K^{A2}$ and $\mu^{A1} \le \mu^{A2}$, then, $\mu_{ud}^{(1)} \le \mu_{ud}^{(2)}$ (Hill, 1963), therefore parameters β_1, β_2 and β_2' must be non-negative.

2.3.2.2. General exactness of Gassmann and C&S

If $\beta_1 = 1$ (homogeneous deviatoric stresses or strains in pores), and either $K^{A1} = K^{A2}$ or $\beta_2 = 0$, then equation 2.35 is identical to equation 2.4 and under these conditions Ciz and Shapiro's approximation is *exact*. Clearly, the original Gassmann's equation (2.2) is a special case of equation 2.35.

2.3.2.3. Generalized Gassmann for Solid-filled Rocks

For the four limiting embedded bound constructions ($HS^{+}_{\min}$, $HS^{-}_{\min}$, HS^{+}_{f} and HS^{+}_{f}) we were not able to directly estimate shear substitution parameters β_1 and β_2; this is simply due to the fact that there are two unknowns (β_1 and β_2) for each construction equation, and also it is not trivial when $\beta_1 = 1$. However, the shear solid-to-solid substitution equation using the $HS^{+}_{\min}$ construction (which seem to predict the smallest change along with the $HS^{-}_{\min}$ construction) can be simplified as

$$\frac{\mu_{ud}^{(i)}}{\mu^{B} - \mu_{ud}^{(i)}} - \frac{\mu^{Ai}}{\phi\left(\mu^{B} - \mu^{Ai}\right)} = \frac{\mu_{bc}^{(i)}}{\mu^{B} - \mu_{bc}^{(i)}} \quad , \tag{2.38}$$

where,

$$\mu_{bc}^{(i)} = \frac{(1-\phi)\left(\frac{1}{\mu^{B}} - \frac{1}{\mu_{dry}}\right) + \phi\left(\frac{1}{\chi^{B}} - \frac{1}{\chi^{Ai}}\right)}{\frac{1}{\mu^{B}}\left(\frac{1}{\mu^{B}} - \frac{1}{\mu_{dry}}\right) + \phi\left(\frac{1}{\mu^{B}\chi^{B}} - \frac{1}{\chi^{Ai}\mu_{dry}}\right)} \quad \text{and } i = 1, 2 \, , \tag{2.39}$$

and

$$\chi = \frac{\mu}{6}\frac{(9K+8\mu)}{(K+2\mu)} \quad . \tag{2.40}$$

For fluid-to-fluid substitution equation 2.38 reduces to Gassmann's equation 2.2. Shear substitution equations for the remaining constructions: $HS^{-}_{\min}$, HS^{+}_{f} and HS^{+}_{f} can be obtained by using shear equations for the HS bounds in place of bulk equations; these are discussed in chapter 6.

2.4. Application

Substitution parameters $\alpha_{1,2}$ and $\beta_{1,2}$ have clear mathematical definitions and thus can be easily calculated if induced stresses (point-by-point) in the initial and final pores are known. As an example, in Tables 2.1 and 2.2 we summarize these parameters calculated using the Finite Element Method (FEM) for two composites: first with spherical pores (case 1) and second with concave shape pores (case 2; same as case 1 but flipped frame and pore); composites are shown in Figure 2.4.

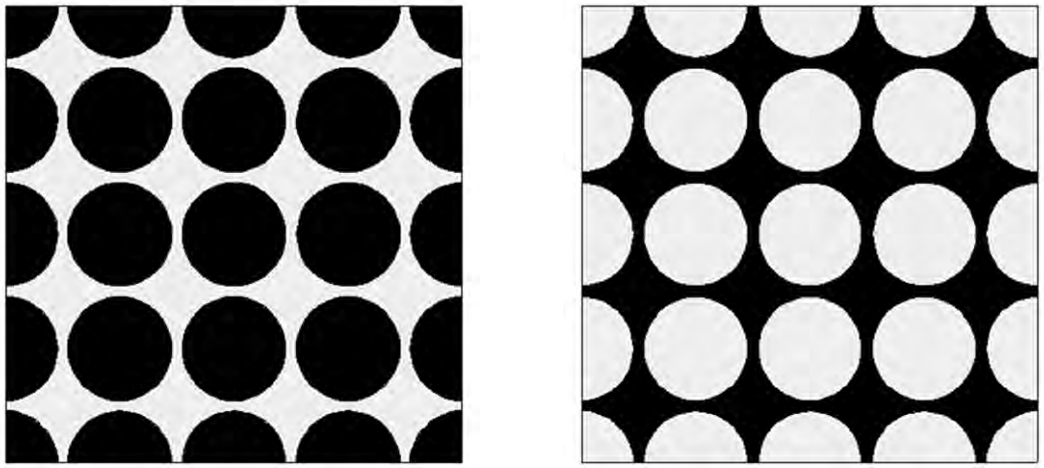

(a) (b)

Figure 2.4: Case 1 (a) and case 2 (b): for both composites pore-filling solids (*A1* and *A2*) occupy black region and frame solid *B* occupies the white region. Note that in case 1 (a) pores are spherical in shape and in case 2 frame mineral occurs as spheres.

The numerically calculated values of $\alpha_{1,2}$ and $\beta_{1,2}$ (in Tables 1 and 2) satisfy the derived exact equations 2.23 and 2.35. We note that these parameters are smaller for case

1 in which pores are of spherical shape when compared to case 2 in which pores are of concave shape. This example demonstrates that pore shape affects the substitution parameters; however the extent and degree of this dependence requires further investigation.

	Porosity ϕ	*Frame Solid* K^B, μ^B (GPa)	*Pore Solid* K^{A1}, μ^{A1} (GPa)	*Pore Solid* K^{A2}, μ^{A2} (GPa)	*Moduli* $\mu_{ud}^{(1)}, K_{ud}^{(1)}$ (GPa)	*Moduli* $\mu_{ud}^{(2)}, K_{ud}^{(2)}$ (GPa)
Case						
1	0.6	36, 45	4, 2	10, 7	4.03, 7.24	12.06, 15.54
2	0.4	36, 45	4, 2	10, 7	12.82, 14.9	21.12, 22.13

Table 2.1: Calculated effective solid-filled bulk and shear moduli for the 3D composites shown in Figure 2.4.

	Porosity ϕ	*Frame Solid* K^B, μ^B (GPa)	*Pore Solid* K^{A1}, μ^{A1} (GPa)	*Pore Solid* K^{A2}, μ^{A2} (GPa)	*Parameters* α_1, α_2	*Parameters* β_1, β_2
Case						
1	0.6	36, 45	4, 2	10, 7	1.01, 0.08	1.17, 0.03
2	0.4	36, 45	4, 2	10, 7	1.09, 0.11	1.35, 0.08

Table 2.2: Calculated parameters $\alpha_{1,2}$ and $\beta_{1,2}$ for the 3D composites shown in Figure 2.4.

We note that for substitution problems parameters $\alpha_{1,2}$ and $\beta_{1,2}$ can also be estimated using rock images as an alternative to assuming predefined values. As an example we consider the following substitution problem - predict effective stiffness measurements of wax-filled Massillon light sandstone (porosity 0.22) at high temperature starting with the stiffness measurements at low temperature, as reported by Wang (1988). Temperature

dependent wax (pore solid) bulk and shear moduli were also reported by Wang (1988). Since 3D image of a Massillon light sandstone sample is not available we use a pre-segmented 3D image of Fontainebleau sandstone (porosity 0.15; Andrä et al., 2013), shown in Figure 2.5. For the digital Fontainebleau sample, assuming Quartz as frame mineral (bulk: 36 GPa; shear: 45 GPa) and temperature dependent wax bulk and shear moduli we numerically calculate parameters $\alpha_{1,2}$ and $\beta_{1,2}$ using FEM. In Figure 2.6 we compare high temperature wax-filled laboratory measurements with those predicted by equations 2.23 and 2.35 with the FEM calculated parameters $\alpha_{1,2}$ and $\beta_{1,2}$ starting with the low temperature wax-filled sandstone laboratory measurements (although these parameters depend on initial and final pore-filling material properties, for this problem these are roughly: $\alpha_1 = 1.1$, $\alpha_2' = 0.7$, $\beta_1 = 1.9$ and $\beta_2' = 0.2$). We also compare predictions of Gassmann's equation, the *C&S* approximation and the embedded bounds.

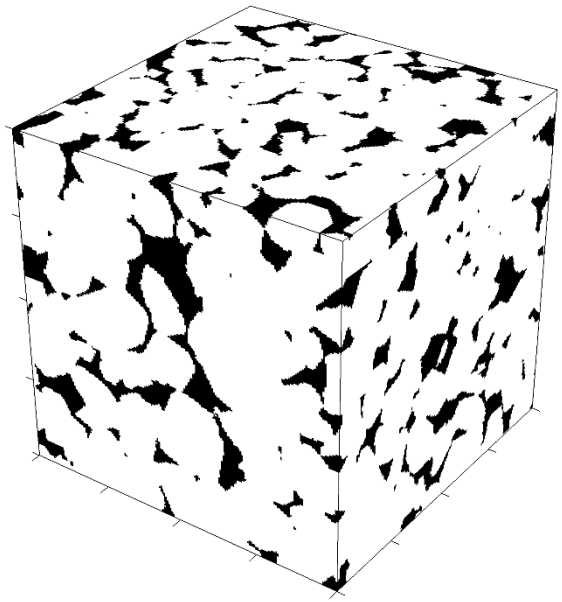

Figure 2.5: Digital Fontainebleau sandstone sample. Pores shown in black and rock frame mineral shown in white. Size of 200 x 200 x 200 and a voxel edge length is 7.5 μm.

The least change predicted by the embedded bounds is closer to the laboratory measurements when compared to that predicted by Gassmann and the *C&S* approximation. The embedded bounds contain the laboratory measurements. Predictions using the FEM calculated Fontainebleau sample parameters $\alpha_{1,2}$ and $\beta_{1,2}$ are closer to the laboratory measurements when compared to any of the above models. However, the laboratory measured change in effective shear modulus is much larger, which could be due to various plausible reasons, such as difference in pore shape between Massillon and Fontainebleau sandstones, dispersion effects and errors in laboratory measurement. In addition to these, it is possible that the rock images do not resolve thin compliant pores or cracks, which could impact the numerically calculated parameters $\alpha_{1,2}$ and $\beta_{1,2}$. It is expected that if cracks were included in this calculation, due to increase in pore compliance heterogeneity we will actually calculate larger values for the substitution parameters. For instance, if we heuristically choose $\beta_1 = 2.4$ and $\beta_2' = 0.6$, parameters larger than those calculated with the FEM, we can fit the measured effective shear moduli quite well, as shown in Figure 2.6b.

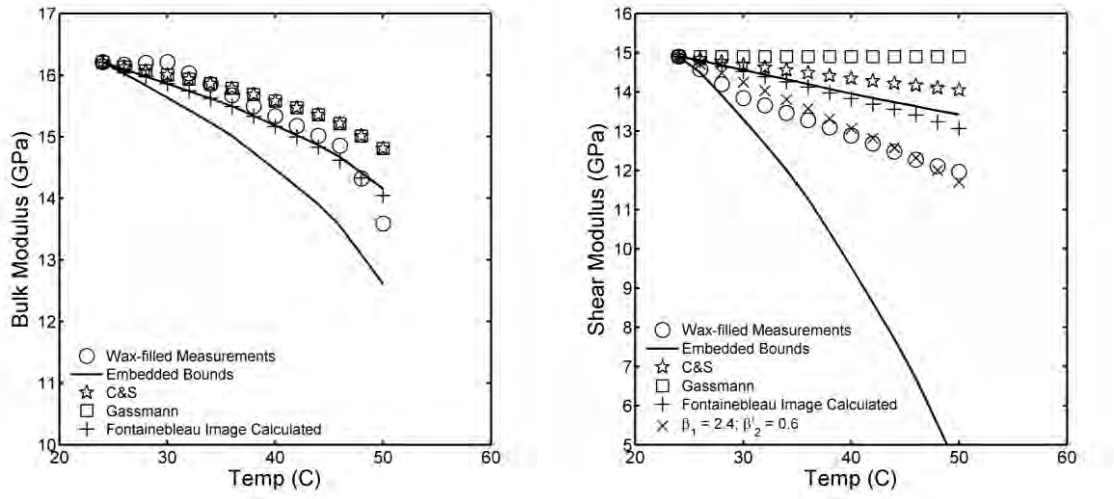

(a) (b)

Figure 2.6: Laboratory measurements of wax-filled moduli (circles) of Massillon light sandstone versus temperature, data taken from Wang (1988). The predictions of hot wax-filled sandstone bulk (Figure a) and shear moduli (Figure b) starting with cold wax-filled moduli (bulk and shear) are shown. These predictions are calculated from the temperature dependent elastic moduli of wax, also reported by Wang. The embedded bounds nearly contain the measurements and the lower embedded bound predictions improve on the Gassmann and C&S approximations. Predictions using

Fontainebleau image calculated parameters $\alpha_{1,2}$ and $\beta_{1,2}$ are closer to the laboratory measurements. The best fit substitution curve, which is non-unique, is also shown for shear moduli with the corresponding values of β_1 and β_2.

2.5. Approximate Substitution Relations

Here we discuss specific substitution problems: dry to solid, fluid to solid, dry to fluid, etc. Exact solid-to-solid substitution for effective bulk modulus, equation 2.23, leads to the following *exact* equations

$$\frac{K_{ud}}{K^B - K_{ud}} = \frac{K_{dry}}{K^B - K_{dry}} + \frac{\alpha_1 K^A + \alpha_2' \mu^A}{\phi\left(K^B - K^A\right)} \quad , \tag{2.41}$$

$$\frac{K_{ud}}{K^B - K_{ud}} = \frac{K_{zs}}{K^B - K_{zs}} + \frac{\alpha_2' \mu^A}{\phi\left(K^B - K^A\right)} \tag{2.42}$$

and

$$\frac{K_{ud}}{K^B - K_{ud}} = \frac{K_{zb}}{K^B - K_{zb}} + \frac{\alpha_1 K^A}{\phi\left(K^B - K^A\right)} \quad , \tag{2.43}$$

where K_{ud} is the solid-filled effective bulk modulus with pore-filling solid of bulk modulus K^A and shear modulus μ^A. Bulk modulus K_{zs} is the fluid-saturated effective modulus when pores are filled with a fluid of bulk modulus K^A (assuming elastic fluid of zero shear modulus). Bulk modulus K_{zb} is the solid-filled effective modulus when pores are filled with a *hypothetical* solid of *zero* bulk modulus and *non-zero* shear modulus of μ^A. Note that parameters α_1 and α_2' in equations 2.41, 2.42 and 2.43 may not be identical, since they depend on initial and final pore-filling materials.

If only α_2' is known then solid-filled bulk modulus K_{ud} can be predicted starting with fluid-saturated bulk modulus K_{zs} using equation 2.42. Similarly, if only α_1 is known (for example, $\alpha_1 = 1$), solid-filled bulk modulus K_{ud} can be predicted starting with bulk

modulus K_{zb} using equation 2.43. However, predicting solid-filled bulk modulus K_{ud} starting with the dry bulk modulus (in equation 2.41) requires knowledge of both parameters α_1 and α_2'. Clearly, predicting solid-filled bulk modulus from fluid-saturated bulk modulus measurement requires fewer assumptions as compared to predicting solid-filled shear modulus from dry bulk modulus measurement.

Using equations 2.41, 2.42 and 2.43 and replacing the usually unknown parameters α_1 and α_2', the effective bulk moduli can be *approximately* written as a function of various effective stiffnesses:

$$\frac{K_{ud}}{K^B - K_{ud}} \approx \frac{K_{zb}}{K^B - K_{zb}} + \frac{K_{zs}}{K^B - K_{zs}} - \frac{K_{dry}}{K^B - K_{dry}} \quad . \tag{2.44}$$

Bulk modulus K_{zb} in equation 2.44 can be further approximated as a function of K_{dry} using equation 2.28.

Similarly, equation 2.35 for effective shear modulus leads to the following exact equations

$$\frac{\mu_{ud}}{\mu^B - \mu_{ud}} = \frac{\mu_{dry}}{\mu^B - \mu_{dry}} + \frac{\beta_1 \mu^A + \beta_2' K^A}{\phi\left(\mu^B - \mu^A\right)} \quad , \tag{2.45}$$

$$\frac{\mu_{ud}}{\mu^B - \mu_{ud}} = \frac{\mu_{zs}}{\mu^B - \mu_{zs}} + \frac{\beta_1 \mu^A}{\phi\left(\mu^B - \mu^A\right)} \tag{2.46}$$

and

$$\frac{\mu_{ud}}{\mu^B - \mu_{ud}} = \frac{\mu_{zb}}{\mu^B - \mu_{zb}} + \frac{\beta_2' K^A}{\phi\left(\mu^B - \mu^A\right)} \quad , \tag{2.47}$$

where same subscripts (*ud*, *dry*, *zs* and *zb*) are used as in equations 2.41-2.43 to denote different effective shear moduli. Similar to the discussion on effective bulk modulus, from equations above, we note that predicting solid-filled shear modulus from fluid-saturated shear modulus measurement requires fewer assumptions as compared to predicting solid-

filled shear modulus from dry shear modulus measurement. Using equations 2.45, 2.46 and 2.47, the effective shear moduli can be related approximately as:

$$\frac{\mu_{ud}}{\mu^B - \mu_{ud}} \approx \frac{\mu_{zb}}{\mu^B - \mu_{zb}} + \frac{\mu_{zs}}{\mu^B - \mu_{zs}} - \frac{\mu_{dry}}{\mu^B - \mu_{dry}} \quad . \tag{2.48}$$

Shear modulus μ_{zb} in equation 2.48 can be approximated as a function of μ_{dry} using equations 2.38 and 2.39.

For fluid-saturated porous media with connected or disconnected pores the exact results in equations 2.41 and 2.45 reduce to

$$\frac{K_{ud}}{K^B - K_{ud}} = \frac{K_{dry}}{K^B - K_{dry}} + \frac{K^A}{\phi\left(K^B - K^A\right)} + \frac{\left(\alpha_1 - 1\right)K^A}{\phi\left(K^B - K^A\right)} \tag{2.49}$$

and

$$\frac{\mu_{ud}}{\mu^B - \mu_{ud}} = \frac{\mu_{dry}}{\mu^B - \mu_{dry}} + \frac{\beta_2' K^A}{\phi \mu^B} \quad , \tag{2.50}$$

where K^A is the bulk modulus of pore fluid. The last terms in equation 2.49 and 2.50 capture the contribution of load-induced heterogeneous pore-pressure.

2.6. Chapter Summary

For arbitrary pore shape isotropic monomineralic rocks we derive exact substitution equations for effective bulk and shear moduli using reciprocity (equations 2.23 and 2.35). General substitution equations depend on usually unknown parameters $\alpha_{1,2}$ and $\beta_{1,2}$ but these can be calculated computationally if information on rock microstructure is available. With the advent of fast computing and availability of digital rock images such as, CAT scans, SEM images, etc., substitution parameters can be calculated instead of making heuristic assumptions. However, digital images of rocks often do not sufficiently resolve thin compliant pores which may affect the calculated substitution parameters. If absolutely

no information on microstructure is known, *substitution is inherently non-unique* since parameters $\alpha_{1,2}$ and $\beta_{1,2}$ cannot be constrained; in this situation the possible range of change in effective moduli can be contained by the embedded bound method.

With the derived exact equations, we reproduce the known result that the classical Gassmann's effective bulk modulus equation for fluid-to-fluid substitution is *exact* if the compression-induced pore-pressure (or mean stress in pores) is homogeneous. Moreover, we prove that this equation is *also exact* for the general case of solid-to-solid substitution, if in addition to homogeneous mean stresses (pressure) in initial and final pores, the shear modulus of substituted pore solid does not change. Similarly, for effective shear modulus, Ciz and Shapiro's approximation is *exact* if shear field-induced deviatoric stresses (or strains) initial and final pore-filling solids are homogeneous, and either the bulk modulus of the substituted solid does not change upon substitution or no mean stresses are induced in pores.

We note that embedded bound method equations which predict the smallest change upon substitution are generalizations of Gassmann's bulk modulus equation to the case of solid-filled rocks. These *exact* equations require the same exactness condition as required by the original Gassmann's bulk modulus equation - compression-induced homogeneous mean stress (or pore-pressure). Solid-filled rocks with connected pores might not satisfy this requirement. These generalizations depend on known parameters and thus should be used to obtain a conservative guess on the change in effective stiffness upon substitution.

Predicting solid-filled rock stiffness (both bulk and shear) starting with a dry rock measurement requires relatively more information and assumptions when compared to predicting the same with a fluid-saturated measurement. Therefore, to predict or model solid-filled stiffness, whenever possible, we recommend selecting fluid-saturated measurements (low or ultrasonic frequency) instead of dry measurements. We provide approximate expressions for solid-filled effective stiffnesses in terms of other measurable effective stiffnesses.

2.7. Acknowledgements

This work was supported by the Stanford Rock Physics and Borehole Geophysics (SRB) Project, and U.S. Department of Energy award DE-FE0001159. The authors thank T. Mukerji for discussions.

2.8. Appendix A

Betti-Rayleigh theorem states that traction $T^{(1)}$ acting on the surface (S_B) of a linear elastic solid *B* associated with displacement field $u_i^{(1)}$ (i = 1,2,3), and traction $T^{(2)}$ acting on the same solid and associated with displacement field $u_i^{(2)}$ are related as

$$\int_{S_B} \left(T_i^{(1)} u_i^{(2)}\right) dS_B = \int_{S_B} \left(T_i^{(2)} u_i^{(1)}\right) dS_B \quad . \tag{A-1}$$

To derive equation 2.14 we now use equation A-1. For the two pore-fill cases discussed in the main body, let's consider tractions acting on the frame mineral solid *B* as follows: For the first case when pores are filled with solid *A1*, traction T_i^{Ω} acting on the outer surface Ω (associated with displacement field $u_i^{(1)}$) and traction T_i^{A1} on the pore boundaries (associated with displacement field u_i^{A1}). For the second case when pores are filled with solid *A2*, traction T_i^{Ω} acting on the outer surface (associated with displacement field $u_i^{(2)}$) and traction T_i^{A2} on the pore boundaries (associated with displacement field u_i^{A2}). Using equation A-1 we get

$$\int_{S_\Omega} T_i^{\Omega} u_i^{(1)}\, dS_\Omega + \int_{S_\phi} T_i^{A2} u_i^{A1}\, dS_\phi = \int_{S_\Omega} T_i^{\Omega} u_i^{(2)}\, dS_\Omega + \int_{S_\phi} T_i^{A1} u_i^{A2}\, dS_\phi \quad . \tag{A-2}$$

Multiplying equation A-2 by ½ on both sides and collecting terms we obtain

$$\frac{1}{2}\int_{S_\Omega} T_i^{\Omega} u_i^{(2)}\, dS_\Omega - \frac{1}{2}\int_{S_\Omega} T_i^{\Omega} u_i^{(1)}\, dS_\Omega = \frac{1}{2}\int_{S_\phi} T_i^{A2} u_i^{A1}\, dS_\phi - \frac{1}{2}\int_{S_\phi} T_i^{A1} u_i^{A2}\, dS_\phi \quad . \tag{A-3}$$

LHS of equation A-3 is the difference in elastic energy between the two cases, i.e., ΔE_{12}.

2.9. Appendix B

2.9.1. Parameters $\alpha_{1,2}$ for $HS^{+}_{\min}$ construction

To calculate the change in effective bulk modulus upon substitution as predicted by the $HS^{+}_{\min}$ construction, start by first calculating the parameters f_Q and ϕ_Q from the following equations

$$K_{ud}^{(1)} = K^B + \frac{f_Q}{\left(K_Q^{(1)} - K^B\right)^{-1} + \left(1 - f_Q\right)\left(K^B + \frac{4}{3}\mu^B\right)^{-1}} \quad , \tag{B-3}$$

where $\phi = f_Q \phi_Q$. Expression for $K_Q^{(1)}$ is given by

$$K_Q^{(1)} = K^{A1} + \frac{1 - \phi_Q}{\left(K^B - K^{A1}\right)^{-1} + \phi_Q\left(K^{A1} + \frac{4}{3}\mu^{A1}\right)^{-1}} \quad . \tag{B-4}$$

Next, from the calculated f_Q and ϕ_Q estimate the new modulus using the following equations

$$K_{ud}^{(2)} = K^B + \frac{f_Q}{\left(K_Q^{(2)} - K^B\right)^{-1} + \left(1 - f_Q\right)\left(K^B + \frac{4}{3}\mu^B\right)^{-1}} \quad , \tag{B-5}$$

where,

$$K_Q^{(2)} = K^{A2} + \frac{1 - \phi_Q}{\left(K^B - K^{A2}\right)^{-1} + \phi_Q\left(K^{A2} + \frac{4}{3}\mu^{A2}\right)^{-1}} \quad . \tag{B-6}$$

For the $HS^{+}_{\min}$ construction, from equations 2.23 and B-3 to B-6 we obtain the bulk modulus substitution parameters

$$\alpha_1 = 1 \tag{B-7}$$

and

$$\alpha_2 = \frac{12\mu^{A1}\mu^{A2}\left(1-\phi_Q\right)\left(K^B - K^{A1}\right)\left(K^B - K^{A2}\right)}{K^{A1}K^{A2}\left(4\mu^{A1} + 3K^B\right)\left(4\mu^{A2} + 3K^B\right)} \quad . \tag{B-8}$$

2.9.2. Parameters $\alpha_{1,2}$ for $HS^{-}_{\min}$ construction

The change in effective modulus as predicted by the $HS^{-}_{\min}$ construction can be calculated by equations B-9 to B-14. To estimate this change, start by calculating f_Q and ϕ_Q from the following equations:

$$K^{(1)}_{ud} = K^{(1)}_Q + \frac{1-f_Q}{\left(K^B - K^{(1)}_Q\right)^{-1} + f_Q\left(K^{(1)}_Q + \frac{4}{3}\mu^{(1)}_Q\right)^{-1}} \quad , \tag{B-9}$$

where $\phi = f_Q\phi_Q$. The expressions for $K^{(1)}_Q$ and $\mu^{(1)}_Q$ are given by

$$K^{(1)}_Q = K^B + \frac{\phi_Q}{\left(K^{A1} - K^B\right)^{-1} + \left(1-\phi_Q\right)\left(K^B + \frac{4}{3}\mu^B\right)^{-1}} \quad , \tag{B-10}$$

$$\mu^{(1)}_Q = \mu^B + \frac{\phi_Q}{\left(\mu^{A1} - \mu^B\right)^{-1} + \frac{2\left(1-\phi_Q\right)\left(K^B + 2\mu^B\right)}{5\mu^B\left(K^B + \frac{4}{3}\mu^B\right)}} \quad . \tag{B-11}$$

Next, calculate the new modulus using the following equations

$$K_{ud}^{(2)} = K_Q^{(2)} + \frac{1 - f_Q}{\left(K^B - K_Q^{(2)}\right)^{-1} + f_Q\left(K_Q^{(2)} + \frac{4}{3}\mu_Q^{(2)}\right)^{-1}} \quad , \tag{B-12}$$

where,

$$K_Q^{(2)} = K^B + \frac{\phi_Q}{\left(K^{A2} - K^B\right)^{-1} + \left(1 - \phi_Q\right)\left(K^B + \frac{4}{3}\mu^B\right)^{-1}} \quad , \tag{B-13}$$

$$\mu_Q^{(2)} = \mu^B + \frac{\phi_Q}{\left(\mu^{A2} - \mu^B\right)^{-1} + \frac{2\left(1 - \phi_Q\right)\left(K^B + 2\mu^B\right)}{5\mu^B\left(K^B + \frac{4}{3}\mu^B\right)}} \quad . \tag{B-14}$$

For the $HS_{\min}^{-}$ construction, substitution parameter $\alpha_1 = 1$ and the parameter α_2 can be calculated using equations 2.23 and calculated ϕ_Q.

2.9.3. **Parameters $\alpha_{1,2}$ for HS_f^+ construction**

The change predicted by the HS_f^+ construction can be calculated by solving equations B-15 to B-20. To estimate the substituted modulus start by calculating f_P and ϕ_P from the following equations:

$$K_{ud}^{(1)} = K_P^{(1)} + \frac{1 - f_P}{\left(K^{A1} - K_P^{(1)}\right)^{-1} + f_P\left(K_P^{(1)} + \frac{4}{3}\mu_P^{(1)}\right)^{-1}} \quad , \tag{B-15}$$

where $\phi = 1 - f_P + f_P\phi_P$. The expressions for $K_P^{(1)}$ and $\mu_P^{(1)}$ are given by

$$K_P^{(1)} = K^{A1} + \frac{1 - \phi_P}{\left(K^B - K^{A1}\right)^{-1} + \phi_P\left(K^{A1} + \frac{4}{3}\mu^{A1}\right)^{-1}} \quad , \tag{B-16}$$

$$\mu_P^{(1)} = \mu^{A1} + \frac{1-\phi_P}{\left(\mu^B - \mu^{A1}\right)^{-1} + \dfrac{2\phi_P\left(K^{A1} + 2\mu^{A1}\right)}{5\mu^{A1}\left(K^{A1} + \dfrac{4}{3}\mu^{A1}\right)}} \quad . \tag{B-17}$$

Next, calculate the new effective modulus using

$$K_{ud}^{(2)} = K_Q^{(2)} + \frac{1-f_Q}{\left(K^{A2} - K_Q^{(2)}\right)^{-1} + f_Q\left(K_Q^{(2)} + \dfrac{4}{3}\mu_Q^{(2)}\right)^{-1}} \quad , \tag{B-18}$$

where,

$$K_P^{(2)} = K^{A2} + \frac{1-\phi_P}{\left(K^B - K^{A2}\right)^{-1} + \phi_P\left(K^{A2} + \dfrac{4}{3}\mu^{A2}\right)^{-1}} \quad , \tag{B-19}$$

$$\mu_P^{(2)} = \mu^{A2} + \frac{1-\phi_P}{\left(\mu^B - \mu^{A2}\right)^{-1} + \dfrac{2\phi_P\left(K^{A2} + 2\mu^{A2}\right)}{5\mu^{A2}\left(K^{A2} + \dfrac{4}{3}\mu^{A2}\right)}} \quad . \tag{B-20}$$

2.9.4. **Parameters $\alpha_{1,2}$ for HS_f^- construction**

The change predicted by the HS_f^- construction can be estimated by solving equations B-21 to B-24. Start by estimating f_P and ϕ_P from the following equations:

$$K_{ud}^{(1)} = K^{A1} + \frac{f_P}{\left(K_P^{(1)} - K^{A1}\right)^{-1} + \left(1-f_P\right)\left(K^{A1} + \dfrac{4}{3}\mu^{A1}\right)^{-1}} \quad , \tag{B-21}$$

where $\phi = 1 - f_P + f_P\phi_P$. The expression for $K_P^{(1)}$ is

$$K_P^{(1)} = K^B + \frac{\phi_P}{\left(K^{A1} - K^B\right)^{-1} + \left(1-\phi_P\right)\left(K^B + \dfrac{4}{3}\mu^B\right)^{-1}} \quad , \tag{B-22}$$

Next, calculate the new effective modulus using

$$K_{ud}^{(2)} = K^{A2} + \frac{f_P}{\left(K_P^{(2)} - K^{A2}\right)^{-1} + \left(1 - f_P\right)\left(K^{A2} + \frac{4}{3}\mu^{A2}\right)^{-1}} \quad , \tag{B-23}$$

where,

$$K_P^{(2)} = K^B + \frac{\phi_P}{\left(K^{A2} - K^B\right)^{-1} + \left(1 - \phi_P\right)\left(K^B + \frac{4}{3}\mu^B\right)^{-1}} \quad , \tag{B-24}$$

For the HS_f^+ and HS_f^- constructions, $\alpha_1 > 1$ can be shown by solving equations 23 and B-15 to B-24 and assuming $\mu^{A1} = \mu^{A2}$.

2.10. References

Andrä, H., N. Combaret, J. Dvorkin, E. Glatt, J. Han, M. Kabel, Y. Keehm, F. Krzkilla, M. Lee, C. Madonna, M. Marsh, T. Mukerji, E. H. Saenger, R. Sain, N. Saxena, S. Ricker, A. Wiegmann and X. Zhan, 2013, Digital rock physics benchmarks - Part I: Imaging and segmentation: Computers & Geosciences, **50**, 25-32.

Ciz, R., and S. A. Shapiro, 2007, Generalization of Gassmann equations for porous media saturated with a solid material: Geophysics, **72**, A75–A79.

Gassmann, F., 1951, Über die Elastizität poröser Medien: Vierteljahrschrift der Naturforschenden Gessellschaft in Zürich, **96**, 1-23.

Gibiansky, L., and S. Torquato, 1998, Rigorous connection between physical properties of porous rock: Journal of Geophysical Research, **103**, 23911-23923.

Hashin, Z., 1962, The elastic moduli of heterogeneous materials, Journal of Applied Mechanics, **29**, 143-150.

Hashin, Z., and S. Shtrikman, 1963, A variational approach to the elastic behavior of multiphase materials: Journal of the Mechanics and Physics of Solids, **11**, 127–140.

Hill, R., 1963, Elastic properties of reinforced solids: some theoretical principles: Journal of the Mechanics and Physics of Solids, **11**, 357-372.

Mavko, G., and D. Jizba, 1991, Estimating grain-scale fluid effects on velocity dispersion in rocks: Geophysics, **56**, 1940–1949.

Mavko, G. and N. Saxena, 2013, Embedded-bound method for estimating the change in bulk modulus under either fluid or solid substitution: Geophysics, **78**, 5, L87-L99.

Saxena, N., G. Mavko and T. Mukerji, 2013, Change in effective bulk modulus upon fluid or solid substitution: Geophysics, **78**, 4, L45-L56.

Wang, Z., 1988, Wave velocities in hydrocarbons and hydrocarbon saturated rocks – with applications to EOR monitoring: PhD thesis, Stanford University.

Walsh, J., 1965, The effect of cracks on the compressibility of rock: Journal of Geophysical Research, **70**, 381-389.

Chapter 3

Further insights into substitution from the method of volume averaging (MVA)

3.1. Abstract

Using the method of volume averaging (MVA), we re-derive the exact solid substitution equation for isotropic effective bulk modulus for porous media with solid-filled pores. Similar to our previous result which was derived using the principle of reciprocity, the new result also requires an additional parameter which might not be directly measured or known. Both solutions are exact. However, unlike the previous exact solution which needed two additional dimensionless parameters, the parameter required in the new solution (using the MVA) is a heuristic effective rock stiffness. We establish rigorous inequalities between the required additional stiffness and other measurable effective stiffnesses.

Published in GEOPHYSICS: Vol 78 (4)

3.2. Introduction

Gassmann's equation (1951) is known as a fluid substitution equation, as it predicts the change in effective elastic moduli of a fluid-saturated porous medium when replacing one pore-fluid with another. The *only* inputs required are the initial effective fluid-saturated bulk modulus, porosity, elastic moduli of frame solid, and moduli of initial and final pore-fluids. It makes this prediction without detailed knowledge of pore geometry, except for the necessary condition of homogeneous pore-pressure (Grechka, 2009). If absolutely no information on rock geometry is available (except for porosity), Gibiansky and Torquato (1998) have shown that fluid substitution is non-unique: there exist an infinite number of rock microstructures of same porosity and initial fluid-filled effective bulk modulus but their fluid substituted effective bulk modulus may differ. Gibiansky and Torquato have also shown that Gassmann's effective bulk equation is, in fact, a strict lower bound on the change in bulk modulus upon fluid substitution which corresponds to cases where the pore-space is connected or the induced pore-pressure is homogeneous. Gibiansky and Torquato also obtained an upper bound on fluid substitution which corresponds to cases where the pore-space is disconnected or the induced pore-pressure is heterogeneous. This upper bound is generally tighter than the corresponding Hashin-Shtrikman (1963, referred here as *HS*) upper bound.

Fluid substitution using Gassmann's equation is frequently implemented in exploration geophysics, with applications ranging from time-lapse seismic analysis, fluid detection from seismic signatures, invasion compensation for sonic well logs, etc. However, when rock pores are filled with solids or viscoelastic materials such as cold heavy-oil, bitumen, clay, kerogen, gas-hydrates, pore-mineral precipitates, etc, traditional fluid-to-fluid substitution is not applicable. For such fluid-to-solid, solid-to-fluid or solid-to-solid substitution problems, Kantor and Bergman (1984), and Berryman and Milton (1988) have suggested rigorous bounds on the change in effective elastic properties upon solid substitution. Although these bounds are tighter than Hashin-Shtrikman bounds, they still provide a wide range of possible effective stiffness upon solid substitution.

In this chapter, we re-derive exact solid substitution equation for effective bulk modulus by relating different composite or solid-filled porous medium stiffnesses using rigorous volume averaging (Whitaker, 1999). We restrict this study to the case of isotropic and mono-mineralic frame, but we consider general pore structure including disconnected pores. The volume averaging approach used to derive the exact solution is distinct from using the approach of reciprocity discussed in Chapter 2. But both solutions are exact and comparable. The goal of this chapter is to provide further insights into the problem of substitution using the method of volume averaging, and also to relate the required additional substitution parameters with measurable parameters through inequalities.

As discussed in the previous chapter, Ciz and Shapiro (2007) also had previously generalized Gassmann's effective fluid-saturated bulk and shear equations for solid-filled porous media with a heuristic effective compressibility parameter. Approximating this parameter, Ciz and Shapiro proposed approximate solid substitution equations, one each for effective bulk and shear moduli. For effective bulk modulus, this approximate equation is identical to Gassmann's fluid-saturated substitution equation. Makarynska *et al*. (2010) have pointed out some deficiencies of Ciz and Shapiro's approximation, in their attempts to model laboratory measurements of heavy oil saturated rocks. In this chapter, we show in some detail, that Ciz and Shapiro's approximate solid substitution equation is limited to rocks with stiff identical ellipsoidal pores. We also show that Ciz and Shapiro's approximation may not always fall within Hashin-Shtrikman bounds, especially for low porosity compliant rocks.

The sections are organized as follows. In the next section all of the main results are first described without the derivations. Since the theoretical methodology and the associated algebra are quite involved, all derivations are kept in a separate section following the main results. Further details of the derivations are in the appendices.

3.3. Solid substitution & main results

We consider an isotropic porous medium composed of a pore-filling elastic solid (denoted by superscript A; bulk and shear moduli: K^A, μ^A) and frame elastic solid (denoted

by superscript *B*; bulk and shear moduli: K^B, μ^B). The volume fraction of pore solid *A* (or porosity) is denoted by ϕ and the volume fraction of frame solid *B* is $(1-\phi)$. In this section, we will summarize composite compressibilities, and present exact and approximate solid substitution equations. Derivations will be discussed in the next section.

3.3.1. **Composite compressibilities and inequalities**

Hickey *et al*. (1995) defined compressibilities for fluid-filled media with interconnected pores using macroscopic equations obtained by volume averaging. Similarly we consider five compressibilities of a composite with total initial volume V_0 and initial pore volume $V_0^A = \phi_0 V_0$. For the first compressibility C_{bc}, we apply pressure $\hat{P}$ (pressure averaged over total volume, referred in this chapter as total macroscopic pressure) with a constraint that pressure $\overline{P}^A$ (spatially varying pore-pressure P^A averaged over pore volume) is kept constant (equation 3.1); no constraint is placed on mass conservation of the pore-fill. For the second compressibility C_{ud}, we apply increments of total macroscopic pressure $\hat{P}$ while keeping the mass of both solids ($\mathcal{M}^{A,B}$) conserved (equation 3.2). The second compressibility is the effective solid-filled compressibility of the composite. Following the notation of Hickey *et al*. (1995) and Zimmerman (1991) we define the two effective compressibilities and bulk moduli as

$$C_{bc} = \frac{1}{K_{bc}} = -\frac{1}{V_0}\left(\frac{\partial V}{\partial \hat{P}}\right)_{\frac{1}{V^A}\int_V P^A dV \,=\, \overline{P}^A \,=\, Cons.} \tag{3.1}$$

and

$$C_{ud} = \frac{1}{K_{ud}} = -\frac{1}{V_0}\left(\frac{\partial V}{\partial \hat{P}}\right)_{\mathcal{M}^{A,B} \,=\, conserved} \quad . \tag{3.2}$$

Effective solid-filled bulk modulus K_{ud} can be expressed exactly as a function of the bulk modulus K_{bc} in the form

$$K_{ud} = \Omega\left(K_{bc}\right) \quad , \tag{3.3}$$

where

$$\Omega(x) = \frac{\phi_0\left(\frac{1}{K^B} - \frac{1}{K^A}\right) + \left(\frac{1}{K^B} - \frac{1}{x}\right)}{\frac{\phi_0}{x}\left(\frac{1}{K^B} - \frac{1}{K^A}\right) + \frac{1}{K^B}\left(\frac{1}{K^B} - \frac{1}{x}\right)} \quad .$$

Derivation of equation 3.3 is discussed in the later section on volume averaging. Using the traction-free condition at the pore boundaries, we define the effective dry rock compressibility as previously suggested by various authors (Shapiro and Kaselow, 2005; Ciz and Shapiro, 2007)

$$C_{dry} = \frac{1}{K_{dry}} = -\frac{1}{V_0}\left(\frac{\partial V}{\partial \hat{P}}\right)_{Pore \;\; boundary \;\; traction = \text{Const.}} \quad . \tag{3.4}$$

Next, with the aim of further expressing bulk modulus K_{bc} in terms of known quantities and/or pore-filling independent effective moduli, such as dry bulk modulus K_{dry}, we define two more composite compressibilites as

$$C_{zb} = \frac{1}{K_{zb}} = -\frac{1}{V_0}\left(\frac{\partial V}{\partial \hat{P}}\right)_{P^A = Cons.} \tag{3.5}$$

and

$$C_{sq} = \frac{1}{K_{sq}} = -\frac{1}{V_0}\left(\frac{\partial V}{\partial \hat{P}}\right)_{\sigma^A_{ij(i\neq j)}, \overline{P}^A = Cons.} \quad . \tag{3.6}$$

The central difference between moduli in equations 3.1 and 3.5 is that for bulk modulus K_{zb} point-by-point (in space) pore-pressure is kept constant, whereas, for bulk modulus K_{bc} pore volume averaged pore-pressure is kept constant. The motivation of selecting bulk

moduli K_{zb} and K_{sq} from a number of possible composite stiffnesses is since these are related to bulk modulus K_{bc} through the following inequalities:

$$K_{bc} \geq K_{sq} \geq K_{dry} \tag{3.7}$$

and

$$K_{bc} \geq K_{zb} \geq K_{dry} \quad . \tag{3.8}$$

Proof of inequalities in equations 3.7 and 3.8 is discussed in Appendix A. These inequalities and equation 3.3 yield strict *lower* bounds on K_{ud} in terms of stiffnesses K_{dry}, K_{zb} and K_{sq} expressed as

$$K_{ud} \geq \Omega\left(K_{zb}\right) \geq \Omega\left(K_{dry}\right) \quad , \tag{3.9}$$

$$K_{ud} \geq \Omega\left(K_{sq}\right) \geq \Omega\left(K_{dry}\right) \quad .$$

One way to achieve the required conditions for K_{zb} is by filling the pores with a *hypothetical* pore-filling solid of zero bulk modulus $\left(K^A = 0\right)$ and shear modulus μ^A, keeping the same solid frame and volume fractions. Obviously most real materials do not satisfy this condition (zero bulk and finite shear), but nevertheless this is a convenient mathematical quantity. Conditions for bulk modulus K_{sq} can be achieved by filling the pores with a fluid of finite bulk modulus K^A and zero shear modulus $\left(\mu^A = 0\right)$ with the additional constraint that the increment of average pore-pressure is kept at zero. In this study, we will use the above properties to approximate K_{bc} with K_{zb} and K_{sq}, and further express K_{zb} and K_{sq} in terms of known quantities.

So far no assumption about the pore geometry has been made, and throughout this Chapter we discuss the general case of connected or disconnected and heterogeneous geometry of pores.

Now we invoke as yet *unknown* function Φ which relates the bulk modulus K_{bc} to the dry bulk modulus K_{dry} as

$$K_{bc} = \Phi(K_{dry}) \quad . \tag{3.10}$$

If details of pore geometry are not known, the function Φ is non-unique since a number of microstructures can have the same dry stiffness but their fluid or solid-filled stiffness may differ. It is possible to express function Φ using parameters α_1 and α_2 discussed in the previous chapter.

Using equations 3.3 and 3.10 we can obtain a transform for substituting a linear elastic solid with another linear elastic solid in the pores of a porous medium. For convenience, we name the initial pore-solid as solid *A1* (bulk: K^{A1} and shear: μ^{A1}) and the final pore-solid as solid *A2* (bulk: K^{A2} and shear: μ^{A2}).

Solving equation (3.3) for $K_{bc}^{(1)}$ gives:

$$K_{bc}^{(1)} = \frac{K_{ud}^{(1)}\left(\frac{\phi_0 K^B}{K^{A1}} + 1 - \phi_0\right) - K^B}{\frac{\phi_0 K^B}{K^{A1}} + \frac{K_{ud}^{(1)}}{K^B} - 1 - \phi_0} \quad ,$$

Then relating the *known* or *measured* solid-filled bulk modulus $(K_{ud}^{(1)})$ with the pore-solid *A1* to the *unknown* solid-filled bulk modulus $(K_{ud}^{(2)})$ with pore-solid *A2* using equations 3.3 and 3.10, we get

$$K_{bc}^{(2)} = \Phi_2\left(\Phi_1^{-1}\left(K_{bc}^{(1)}\right)\right) \quad ,$$

$$K_{ud}^{(2)} = K_{bc}^{(2)} + \frac{\left(1 - \frac{K_{bc}^{(2)}}{K^B}\right)^2}{\frac{\phi_0}{K^{A2}} + \frac{1-\phi_0}{K^B} - \frac{K_{bc}^{(2)}}{\left(K^B\right)^2}} \quad , \tag{3.11}$$

where $K_{bc}^{(1)}$ and $K_{bc}^{(2)}$ are the effective bulk modulus K_{bc} associated with pore-solid *A1* and *A2*, respectively. Functions $\Phi_{1,2}$ relate the dry bulk modulus with bulk moduli $K_{bc}^{(1),(2)}$. Note that the above equation for bulk modulus $K_{ud}^{(2)}$, is algebraically equivalent to the form given in equation (3.3).

Equation 3.11 is the exact solid substitution equation (in an implicit form), which can be used to predict the unknown solid-filled bulk modulus $K_{ud}^{(2)}$, but requires the knowledge of functions Φ_1 and Φ_2 (or in general $K_{bc}^{(2)}$ as a function of $K_{bc}^{(1)}$), in addition to the known initial pore solid-filled bulk modulus $(K_{ud}^{(1)})$, porosity, bulk properties of the pore and frame solids (solids *A1*, *A2* and *B*). However, if for a particular pore geometry composite, $K_{bc}^{(1)} = K_{bc}^{(2)}$, equation 3.11 does not require functions Φ_1 and Φ_2 since $K_{bc}^{(1)}$ and $K_{bc}^{(2)}$ cancel out, which can be easily checked.

Detailed study of all possible composites for which function Φ is known is beyond the scope of this study, but some examples include the composites which realize Hashin-Shtrikman bounds (Hashin and Shtrkiman, 1963), for which analytical expressions for effective stiffness were obtained by Hashin (1962).

3.3.2. **Limitations of Ciz and Shapiro's approximation**

Ciz and Shapiro (2007) derived the following *exact* solid substitution equation for effective solid-filled bulk modulus by invoking a stiffness $K_{if}^{(i)}$

$$K_{ud}^{(i)} = \frac{\phi_0\left(\frac{1}{K^B} - \frac{1}{K_{if}^{(i)}}\right) + \left(\frac{1}{K^B} - \frac{1}{K_{dry}}\right)}{\frac{\phi_0}{K_{dry}}\left(\frac{1}{K^B} - \frac{1}{K_{if}^{(i)}}\right) + \frac{1}{K^B}\left(\frac{1}{K^B} - \frac{1}{K_{dry}}\right)}, \tag{3.12}$$

where $i = 1, 2$. Both equations 3.3 and 3.12 are exact but equation 3.3 instead features bulk modulus K_{bc}. Using equation 3.3 stiffness $K_{if}^{(i)}$ can be written as

$$K_{if}^{(i)} = K^{Ai} + \frac{\phi_0\left(K_{bc} - K_{dry}\right)\left(K^B - K^{Ai}\right)^2}{\left(K^B - K_{dry}\right)\left(K^B - K_{bc}\right) + \phi_0\left(K_{bc} - K_{dry}\right)\left(K^B - K^{Ai}\right)} \quad . \tag{3.13}$$

If details of pore geometry are not known, Ciz and Shapiro suggested approximating $K_{if}^{(i)} \approx K^{Ai}$ which is equivalent to $K_{bc}^{(i)} \approx K_{dry}$ resulting in

$$K_{ud}^{(i)} \approx K_{ud}^{CS(i)} = \frac{\phi_0\left(\frac{1}{K^B} - \frac{1}{K^{Ai}}\right) + \left(\frac{1}{K^B} - \frac{1}{K_{dry}}\right)}{\frac{\phi_0}{K_{dry}}\left(\frac{1}{K^B} - \frac{1}{K^{Ai}}\right) + \frac{1}{K^B}\left(\frac{1}{K^B} - \frac{1}{K_{dry}}\right)} \quad , \tag{3.14}$$

$$K_{bc}^{(i)} = \Phi(K_{dry}) \approx K_{dry} \quad ,$$

where $i = 1, 2$. Equation 3.14 is referred here as the C&S approximation.

Interpreting the constraints on $K_{bc}^{(i)}$ (equation 3.1) suggests that approximating $K_{if}^{(i)} \approx K^{Ai}$ or $K_{bc}^{(i)} \approx K_{dry}$ implies that for a bulk compression the induced pore-shear stress is negligible and the induced pore-pressure is homogeneous. This is in agreement with our findings on the C&S approximation for bulk modulus in the previous Chapter 2. Also, this is further substantiated by the fact that equation 3.14 is the exact equation for effective bulk modulus of a composite with a spherical inclusion (solid *A*) and a spherical shell frame (solid *B*). For this composite, upon bulk compression the induced pore-pressure is homogeneous and no shear stress is induced in the pores (Hashin, 1962), and the exact expression for $K_{ud}^{(i)}$ and K_{dry} are

$$K_{ud}^{(i)} = \frac{K^B}{1 + \frac{\phi_0\left(K^B - K^{Ai}\right)\left(4\mu^B + 3K^B\right)}{K^B\left(4\mu^B + 3K^{Ai}\right) - 4\mu^B\left(K^B - K^{Ai}\right)\phi_0}} \quad , \tag{3.15}$$

$$K_{dry} = \frac{K^B}{1 + \frac{\phi_0\left(4\mu^B + 3K^B\right)}{\left(1-\phi_0\right)4\mu^B}} \quad .$$

The C&S approximation (equation 3.14) can be obtained by expressing and equating μ^B as a function of $K_{ud}^{(i)}$ and K_{dry} in equation 3.15. Note that a different relation is obtained if we equate K^B instead of μ^B. A solid-to-solid substitution form of the C&S approximation is

$$K_{ud}^{(2)} \approx K_{ud}^{CS(2)} = \frac{K^B}{1 + \left(\frac{K_{ud}^{(1)}}{K^B - K_{ud}^{(1)}} - \frac{K^{A1}}{\phi_0\left(K^B - K^{A1}\right)} + \frac{K^{A2}}{\phi_0\left(K^B - K^{A2}\right)} \right)^{-1}} \quad . \tag{3.16}$$

Since a two phase spherical composite is a realization of Ciz and Shapiro's approximation we note that this approximation (equation 3.14) is inconsistent for composites for which bulk compression induced pore-shear stress is large, for example, any composite that realizes the lower Hashin-Shtrikman bound (if frame solid *B* is stiffer, both in bulk and shear, than pore solid *Ai)*. The solid-to-solid substitution form (equation 3.16) instead assumes that either the pore-shear modulus remains invariant upon substitution ($\mu^{A1} \approx \mu^{A2}$) or no shear stresses are induced in pores. Therefore, Ciz and Shapiro's approximate substitution equation (equation 3.16) for effective solid-filled bulk modulus is limited to cases where bulk compression induced pore-pressure is homogeneous and shear contrast between substituted pore solids is negligible, for example, rocks with stiff identical ellipsoidal pores.

In Appendix A, we show that if $\left(\mu^{A2} - \mu^{A1}\right)\left(K^{A2} - K^{A1}\right) \geq 0$, Ciz and Shapiro's approximation will under predict the change in magnitude of effective solid-filled bulk modulus upon substitution, or

$$\left|K_{ud}^{(2)} - K_{ud}^{(1)}\right| \geq \left|K_{ud}^{CS(2)} - K_{ud}^{(1)}\right| \quad . \tag{3.17}$$

As an example, we consider four solid-filled granular composites with known porosities, as shown in Figure 3.1. For each of these geometries, frame solid (*B*) has elastic properties of Quartz (bulk: 36 GPa, shear: 45 GPa) and its effective dry bulk modulus is computed using the finite element method (FEM). Next, we predict the approximate solid-filled bulk moduli using the C&S approximation starting with the FEM computed dry bulk moduli, porosity, elastic properties of frame solid (*B*) and elastic properties of final pore-filling solid *A2*. Note that for this case the initial pore-filling solid *A1* has zero bulk and shear stiffness (dry rock). These solid-filled bulk moduli predictions are compared with those numerically computed using FEM as shown in Figure 3.2. We note that Ciz and Shapiro's approximate substitution under predicts the FEM computed solid-filled bulk moduli. Also, since Ciz and Shapiro's approximate substitution equation ignores the induced pore-shear stress, for soft granular geometries its predictions are below the lower Hashin-Shtrikman bound (Figure 3.2, right). This can be easily predicted by comparing equation 3.14 with the expressions of Hashin-Shtrikman bounds (Mavko *et al*., 2009). In Figure 3.2 we also show the minimum initial dry bulk moduli for different final pore-filling solids (*A2*) for which the predictions by C&S approximate solid substitution equation will be within Hashin-Shtrikman bounds. We can see from these curves that for low porosity compliant composites, Ciz and Shapiro's approximate substitution equation provides unphysical predictions. This is regardless of pore geometry. The predictions of upper and lower embedded bounds contain the FEM computed moduli, and the lower embedded bound is a better approximation than the C&S approximation.

3.4. Theory of volume averaging & derivation of results

In this section, we derive equation 3.3 using the method of volume averaging. We begin with a brief review of the general method of volume averaging for two phase systems (Whitaker, 1999), with two phases denoted by *A* and *B*, respectively. The method of volume averaging is a *mathematically rigorous* approach to spatially average equations, valid within a particular phase, in order to obtain their macro-scale continuum description.

The method of volume averaging links the averages of derivatives to derivatives of averages with the following averaging theorem:

$$\frac{1}{V}\int_V \partial_i \Psi^A \, dV \quad = \quad \partial_i \frac{1}{V}\int_V \Psi^A \, dV \quad + \quad \frac{1}{V}\int_{S^{AB}} \Psi^A \hat{n}_i \, dS \quad . \tag{3.23}$$

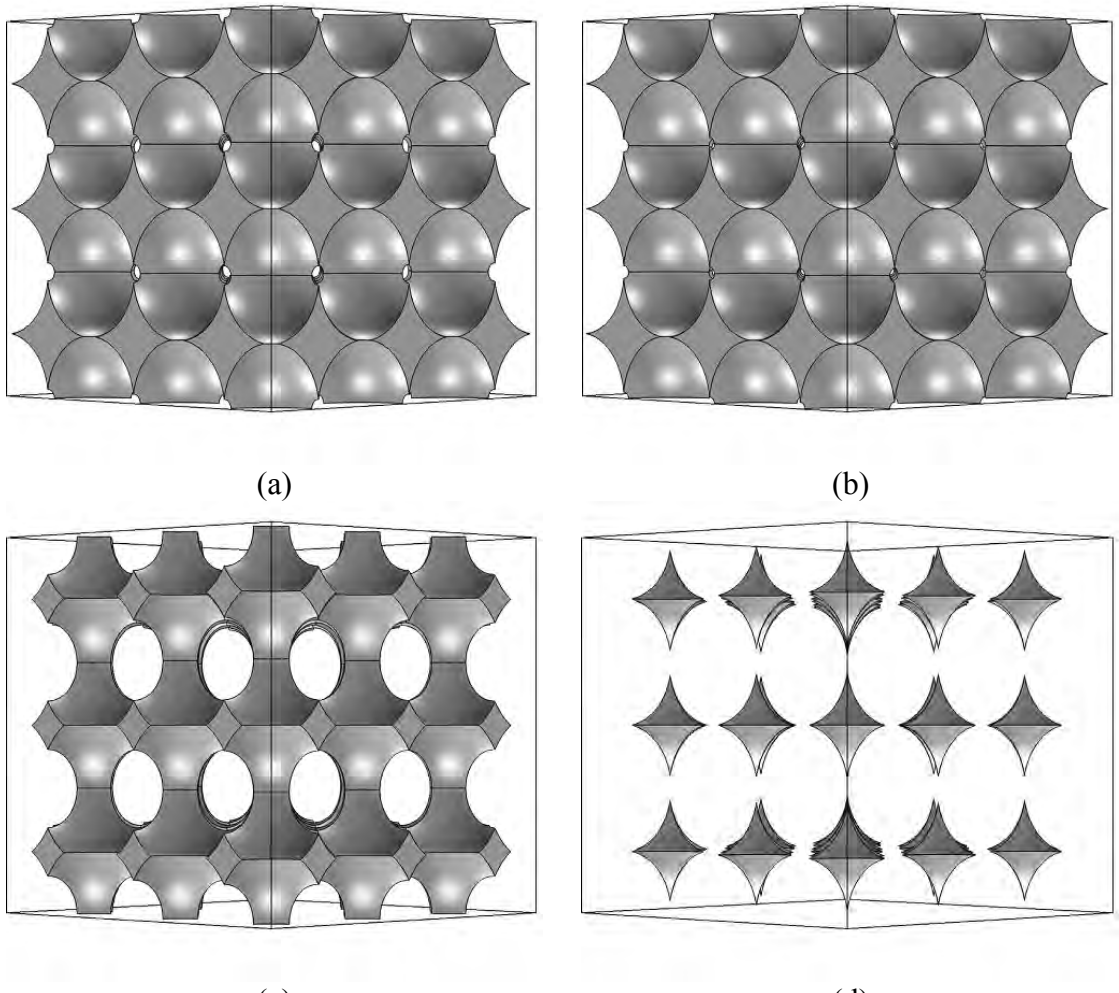

Figure 3.1: Four pore geometries for FEM calculations shown in Figure 3.2. Quartz frame is transparent and dry pores are shown. a) porosity: 0.44, bulk: 3.24 GPa and shear: 4.33 GPa; b) porosity: 0.47, bulk: 1.92 GPa and shear: 2.66 GPa; c) porosity: 0.2, bulk: 19.6 GPa and shear: 21.9 GPa; d) porosity: 0.02, bulk: 34.2 GPa and shear: 42.1 GPa.

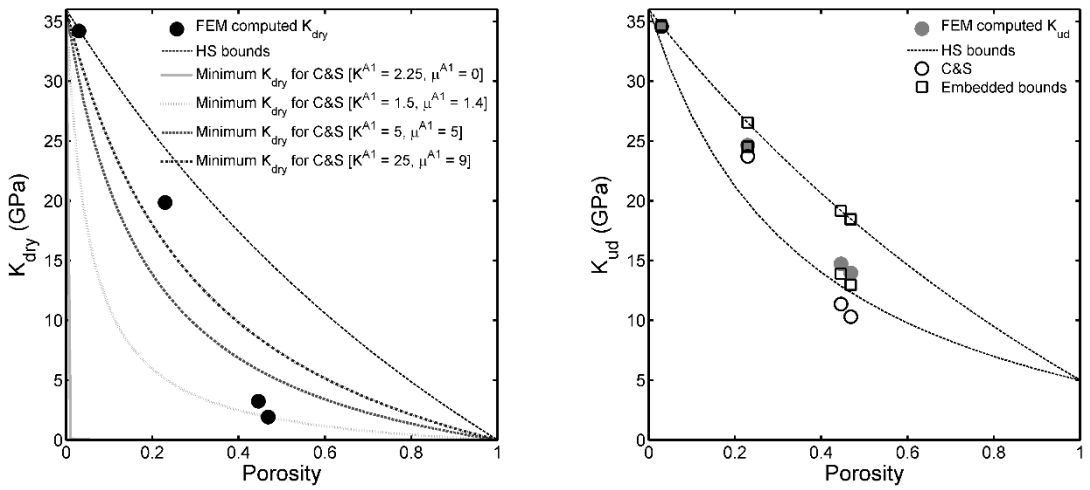

Figure 3.2: (a) Minimum required dry bulk modulus for C&S approx. predictions to be within Hashin-Shtrikman (HS) bounds for solid-filled bulk modulus with pore-filling A2: water (bulk 2.25 GPa, shear 0), kaolinite clay (bulk 1.5 GPa, shear 1.4 GPa), arbitrary solid (bulk 5 GPa, shear 5 GPa) and Han's clay (bulk 25 GPa, shear 9 GPa). For all cases frame solid has properties of Quartz (bulk 36 GPa, shear 45 GPa). FEM computed dry moduli (black filled circles) for geometries shown in Figure 3.1. (b) FEM computed effective solid-filled bulk moduli (gray filled circles) for the arbitrary solid (bulk 5 GPa, shear 5 GPa) compared with C&S approx. solid-filled moduli (circles). New approximation is shown in squares.

Here Ψ^A is any quantity associated with the phase A, and is defined to be zero everywhere outside phase A. Symbol ∂_i is the spatial derivative operator. The symbol S^{AB} refers to the interface between phases A and B within the averaging volume V and $\hat{n}_j$ is the unit normal pointing from phase A to B. To denote phasic average, we use an overbar $\left(\overline{\Psi}^A\right)$; we use a hat symbol $\left(\hat{\Psi}^A\right)$ for the average over volume V:

$$\overline{\Psi}^A = \frac{1}{V^A}\int_V \Psi^A \, dV \quad , \tag{3.24}$$

$$\hat{\Psi}^A = \frac{1}{V}\int_V \Psi^A \, dV \quad .$$

Both averages $\overline{\Psi}^A$ and $\hat{\Psi}^A$ are defined at centroid x_0 of the averaging volume V. To complete the averaging process, we define the point-by-point spatial deviation at position vector y within the averaging volume as

$$\tilde{\psi}^A = \psi^A - \overline{\psi}^A \quad , \tag{3.25}$$

where $\tilde{\psi}^A$ is the spatial deviation of the quantity Ψ^A about its phasic average $\overline{\psi}^A$. Using equation 3.24, we can write

$$\phi = \frac{\hat{\psi}^A}{\overline{\psi}^A} = \frac{V^A}{V} \quad . \tag{3.26}$$

Theorem 1 (equation 3.23) represents a three-dimensional version of the Leibniz rule for interchanging differentiation and integration. It has been derived by various authors (Marle, 1967; Slattery, 1967). Extensive discussion on this subject can be found in Whitaker (1999). A conceptual diagram of the volume averaging process is shown in Figure 3.3 for two phases A and B. In this chapter, phase A is the pore-filling elastic solid and phase B is the frame elastic solid.

3.4.1. Quasi-static equations of motion: Pore-scale description

The standard linearized quasi-static equations of motion, in Einstein's summation convention for repeated indices, at the pore-scale (point-by-point in space) for pore-filling (denoted by superscript A) and frame elastic solid (denoted by superscript B) are as follows:

3.4.1.1. Continuity equations

$$\frac{\rho^A - \rho_0^A}{\rho_0^A} = -\partial_j \left(u_j^A \right) \quad , \tag{3.27}$$

$$\frac{\rho^B - \rho_0^B}{\rho_0^B} = -\partial_j \left(u_j^B \right) \quad .$$

Here, $u_j^{A,B}$ are the point-by-point j^{th} displacement components and $\rho^{A,B}$ are the respective densities. The subscript *0* indicates the unperturbed value.

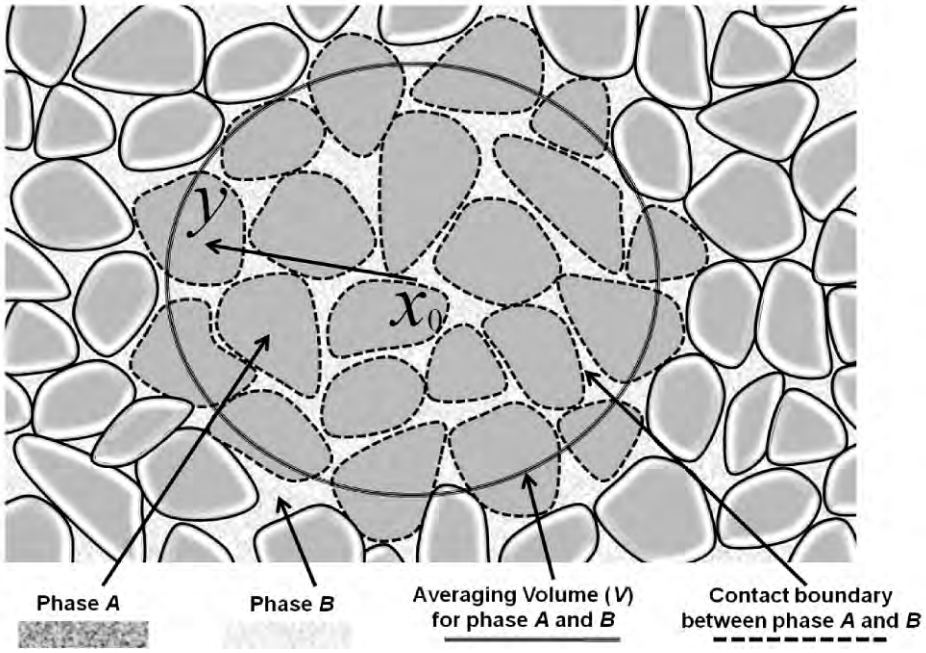

Figure 3.3: A two-phase system with phases *A* and *B*. The method of volume averaging applied to volume *V* with the contact interface (shown with dash lines) between two phases *A* and *B*. The centroid of the averaging volume denoted by x_0 and y is the relative position vector for points within the volume.

3.4.1.2. Momentum conservation and stress equations

$$\partial_j\left(\sigma_{ij}^A\right)=0 \quad , \tag{3.28}$$

$$\partial_j\left(\sigma_{ij}^B\right)=0 \quad ,$$

where σ_{ij}^A and σ_{ij}^B are the linear elastic stress tensors (point-by-point) for each phase, given by

$$\sigma_{ij}^A = C_{ijkl}^A u_{kl}^A \quad , \tag{3.29}$$

$$\sigma_{ij}^{B} = C_{ijkl}^{B} u_{kl}^{B} \quad .$$

Here, C_{ijkl}^{A} and C_{ijkl}^{B} are standard fourth rank linear elastic stiffness tensors, which for isotropic solids are expressed as:

$$C_{ijkl}^{A} = K^{A}\delta_{ij}\delta_{kl} + \mu^{A}\left(\delta_{ik}\delta_{jl} + \delta_{il}\delta_{jk} - \frac{2}{3}\delta_{ij}\delta_{kl}\right) \quad , \tag{3.30}$$

$$C_{ijkl}^{B} = K^{B}\delta_{ij}\delta_{kl} + \mu^{B}\left(\delta_{ik}\delta_{jl} + \delta_{il}\delta_{jk} - \frac{2}{3}\delta_{ij}\delta_{kl}\right) \quad ,$$

where $K^{A,B}$ and $\mu^{A,B}$ are the bulk and shear moduli of elastic solids, respectively. The strain tensors are

$$u_{kl}^{A} = \frac{1}{2}\left(\partial_{k}u_{l}^{A} + \partial_{l}u_{k}^{A}\right) \quad , \tag{3.31}$$

$$u_{kl}^{B} = \frac{1}{2}\left(\partial_{k}u_{l}^{B} + \partial_{l}u_{k}^{B}\right) \quad .$$

If $\mu^{A} = 0$ pore-filling phase *A* will be an *ideal* pore fluid.

3.4.1.3. Boundary conditions

At the phase-phase interface we impose no-slip condition and continuity of traction:

$$u_{j}^{A} = u_{j}^{B} \quad , \tag{3.32}$$

$$\sigma_{jk}^{A} n_{k} = \sigma_{jk}^{B} n_{k} \quad ,$$

where n_{k} is the normal vector to the phase-phase interface.

3.4.2. Quasi-static equations of motion: Macroscopic description

Using volume-averaging Theorem 1 (equation 3.23), we volume average the pore-scale physics equations to obtain the macroscopic descriptions and their corresponding point-by-point spatial deviation equations using equation 3.25. These equations are listed in equations 3.33-3.40 and their derivation is discussed in Appendix B.

3.4.2.1. Macroscopic continuity equations

$$\frac{\overline{\rho}^{A}-\rho_0^{A}}{\rho_0^{A}}+\partial_j\overline{u}_j^{A}-\frac{\phi_0-\phi}{\phi_0}=0 \quad , \tag{3.33}$$

$$\frac{\overline{\rho}^{B}-\rho_0^{B}}{\rho_0^{B}}+\partial_j\overline{u}_j^{B}-\frac{\phi-\phi_0}{1-\phi_0}=0 \quad .$$

3.4.2.2. Macroscopic pressure equations

Phasic averages are

$$\overline{P}^{A} = -\overline{\sigma}_{jj}^{A}/3=-K^{A}\left(\partial_j\overline{u}_j^{A}+\frac{\phi-\phi_0}{\phi_0}\right) \quad ,$$

$$\overline{P}^{B} = -\overline{\sigma}_{jj}^{B}/3=-K^{B}\left(\partial_j\overline{u}_j^{B}+\frac{\phi_0-\phi}{1-\phi_0}\right) \quad . \tag{3.34}$$

3.4.2.3. Spatial deviations about the averages

$$\widetilde{P}^{A} = -K^{A}\left\{\partial_l\widetilde{u}_l^{A}-\frac{1}{V^{A}}\int_{S^{AB}}\left(\widetilde{u}_l^{A}\hat{n}_l\right)dS\right\} \quad ,$$

$$\widetilde{P}^{B} = -K^{B}\left\{\partial_l\widetilde{u}_l^{B}-\frac{1}{V^{B}}\int_{S^{BA}}\left(\widetilde{u}_l^{B}\hat{n}_l\right)dS\right\} \quad . \tag{3.35}$$

3.4.2.4. Macroscopic shear stress equations

Phasic averages are

$$\overline{\sigma}_{ij}^{A} = \mu^{A}\left\{\partial_i \overline{u}_j^{A} + \partial_j \overline{u}_i^{A}\right\} - 2\frac{\mu^{A}}{\phi_0} D_{ij}$$

$$\overline{\sigma}_{ij}^{B} = \mu^{B}\left\{\partial_i \overline{u}_j^{B} + \partial_j \overline{u}_i^{B}\right\} + 2\frac{\mu^{B}}{1-\phi_0} D_{ij} \quad , \tag{3.36}$$

where D_{ij}, is defined in equation B-8, and $i \neq j$. Shear stresses $\overline{\sigma}_{12}^{A,B}$, $\overline{\sigma}_{13}^{A,B}$ and $\overline{\sigma}_{23}^{A,B}$ are the volume averaged shear stresses in *x*-*y*, *x*-*z* and *y*-*z* planes, respectively.

Spatial deviations about the averages are

$$\widetilde{\sigma}_{ij}^{A} = \mu^{A}\left\{\frac{1}{2}\left(\partial_i \widetilde{u}_j^{A} + \partial_j \widetilde{u}_i^{A}\right) - \frac{1}{V^{A}}\int_{S^{AB}} \frac{1}{2}\left(\widetilde{u}_i^{A}\hat{n}_j + \widetilde{u}_j^{A}\hat{n}_i\right) dS\right\} \quad ,$$

$$\widetilde{\sigma}_{ij}^{B} = \mu^{B}\left\{\frac{1}{2}\left(\partial_i \widetilde{u}_j^{B} + \partial_j \widetilde{u}_i^{B}\right) - \frac{1}{V^{B}}\int_{S^{BA}} \frac{1}{2}\left(\widetilde{u}_i^{B}\hat{n}_j + \widetilde{u}_j^{B}\hat{n}_i\right) dS\right\} \quad . \tag{3.37}$$

3.4.2.5. Total macroscopic pressure and shear stress

$$\hat{P} = \phi_0 \overline{P}^{A} + (1-\phi_0)\overline{P}^{B} \quad ,$$

$$\hat{\sigma}_{ij} = \phi_0 \overline{\sigma}_{ij}^{A} + (1-\phi_0)\overline{\sigma}_{ij}^{B} \quad , \tag{3.38}$$

where total macroscopic pressure and shear stress $(i \neq j)$ are denoted by $\hat{P}$ and $\hat{\sigma}_{jk}$, respectively.

3.4.2.6. Porosity and deviatoric strain equations

Following the thermodynamic study presented by de la Cruz *et al*. (1993) and later discussed by Sahay (1996) and Spanos (2009), we write the porosity perturbation equation as

$$\phi - \phi_0 = \delta^B \bar{u}^B_{l,l} - \delta^A \bar{u}^A_{l,l} \quad , \tag{3.39}$$

Deviatoric strain equation is

$$2D_{ij} = \chi^B \left\{ \partial_i \bar{u}^B_j + \partial_j \bar{u}^B_i - \frac{2}{3}\delta_{ij}\partial_p \bar{u}^B_p \right\} - \chi^A \left\{ \partial_i \bar{u}^A_j + \partial_j \bar{u}^A_i - \frac{2}{3}\delta_{ij}\partial_p \bar{u}^A_p \right\} \quad . \tag{3.40}$$

The parameters $\delta^{A,B}$ and $\chi^{A,B}$ are phenomenological constitutive parameters which depend on pore geometry and the elastic properties of the poro-continuum constituents. The rest of the symbols have their usual meaning, as listed in Appendix C. Next, using equations 3.33-3.40 we will derive expressions for effective bulk moduli K_{ud} and K_{bc} as defined in equations 3.1 and 3.2.

3.4.3. Effective compressibilities & constitutive parameters

3.4.3.1. Bulk modulus K_{bc} as a function of parameters δ^A and δ^B

To measure bulk modulus K_{bc} we keep the increment of average pore pressure at zero while the total macroscopic pressure is changed. The fractional change in total volume under these conditions is used to quantify the measured bulk modulus. For this stiffness, the mass of the frame solid *B* has to be conserved, which means

$$dM^B = d\left((1-\phi)\rho^B V\right) = 0 \quad , \tag{3.41}$$

$$\frac{dV}{V_0} = -\frac{d(1-\phi)\rho^B}{(1-\phi_0)\rho_0^B} \quad .$$

Using equation 3.41 we can redefine the bulk modulus K_{bc} in terms of mass density:

$$\frac{1}{K_{bc}} = \frac{1}{(1-\phi_0)\rho_0^B}\left(\frac{\partial(1-\phi)\rho^B}{\partial \bar{P}}\right)_{\bar{P}^A=0} \quad . \tag{3.42}$$

Using equations 3.33, 3.34, 3.38 and 3.39 we obtain

$$\frac{1}{K_{bc}} = \frac{1}{(1-\phi_0)K^B}\left[\frac{1-\delta^A/\phi_0}{1-\delta^B/(1-\phi_0)-\delta^A/\phi_0}\right] \quad . \tag{3.43}$$

3.4.3.2. Solid-filled effective bulk modulus K_{ud} as a function of parameters δ^A and δ^B

To measure bulk modulus K_{ud} we individually conserve masses of both elastic solids of the composite as

$$(1-\phi)\rho^B V = (1-\phi_0)\rho_0^B V_0 \quad , \tag{3.44}$$

$$\phi\rho^A V = \phi_0\rho_0^A V_0 \quad . \tag{3.45}$$

Hickey *et al*. (1995) suggested that the above equations result in a simple condition

$$\frac{(1-\phi)\rho^B}{\phi\rho^A} = \frac{(1-\phi_0)\rho_0^B}{\phi_0\rho_0^A} \quad . \tag{3.46}$$

Solving equation 3.2 with condition in equation 3.46 and equations 3.33, 3.34, 3.38 and 3.39 we get

$$K_{ud} = (1-\eta_0^A)K^B + \eta_0^A K^A + (\delta^A - \delta^B)(K^B - K^A) \quad . \tag{3.47}$$

Equation 3.47 can also be obtained by simply invoking

$$\bar{u}^A = \bar{u}^B \quad , \tag{3.48}$$

in equations 3.34 and 3.38, since for an effective solid-filled bulk modulus experiment the average displacement for pore solid *A* and frame solid *B* will be equal.

3.4.3.3. Relation between parameters δ^A and δ^B

The macroscopic parameters, δ^A and δ^B, in equation 3.39 relate the divergence in macroscopic displacements with the change in volume fraction of the two constituents. In a macroscopic sense, finite shear moduli must affect this process. Hence both δ^A and δ^B depend on the bulk and shear properties of the elastic constituents. A straightforward use of displacement continuity yields

$$\delta^A / K^A = \delta^B / K^B \quad . \tag{3.49}$$

The validity of equation 3.49 was also recently discussed by Spanos (2009). Using equation 3.49 along with the result from the solid-filled experiment presented in equation 3.47, we can obtain expressions for δ^A and δ^B:

$$\delta^A = \frac{K^A}{\left(K^A - K^B\right)^2}\left[\underbrace{\phi_0 K^A + (1-\phi_0)K^B}_{Voigt\ Average} - K_{ud}\right] \quad , \tag{3.50}$$

$$\delta^B = \frac{K^B}{\left(K^B - K^A\right)^2}\left[\underbrace{\phi_0 K^A + (1-\phi_0)K^B}_{Voigt\ Average} - K_{ud}\right] \quad .$$

Equation 3.50 suggest that both δ^A and δ^B are positive quantities (Spanos, 2009). This is because the Voigt average of the two bulk moduli will always be larger than the effective solid-filled bulk modulus (Mavko *et al*., 2009). Using equations 3.43, 3.47 and 3.49, K_{ud} can be related to K_{bc} which leads to equation 3.3.

3.5. Comparisons between equations from reciprocity and MVA

Exact result in equation 3.3 derived using the MVA can be written as

$$\frac{K_{ud}}{K^B - K_{ud}} - \frac{K^A}{\phi\left(K^B - K^A\right)} = \frac{K_{bc}}{K^B - K_{bc}} \tag{3.51}$$

If the induced pressure in the pore space is homogenous, then by definition we must have $K_{bc} = K_{zb}$. Using reciprocity we can also express K_{ud} in terms of K_{zb} (equation 2.43) to obtain:

$$\frac{K_{ud}}{K^B - K_{ud}} - \frac{\alpha_1 K^A}{\phi\left(K^B - K^A\right)} = \frac{K_{zb}}{K^B - K_{zb}} \quad , \tag{3.52}$$

If load-induced pore-pressure is homogenous, it is equivalent to substituting $\alpha_1 = 1$ in equation 3.52. Therefore, under this assumption both reciprocity and the MVA yield the same result. However, the result obtained using reciprocity is seemingly more intuitive than that obtained using the MVA.

3.6. Chapter summary

We derive an exact solid substitution equation for bulk modulus which generally requires an additional stiffness; we relate this additional stiffness to other measurable effective stiffnesses using rigorous inequalities. We show that a closer/better estimate of the *true* solid-filled rock bulk modulus can be obtained starting with bulk modulus measurement of the same rock but filled with a hypothetical pore-filling or a fluid-saturated bulk modulus, as compared to starting with the dry rock bulk modulus measurement.

We conclude that Ciz and Shapiro's approximation implies homogeneous pore-pressure and invariant pore-filling shear modulus upon substitution. Due to these assumptions, Ciz and Shapiro's approximation does not always fall within Hashin-Shtrikman bounds, especially for low porosity compliant rocks. Furthermore, depending on stiffness of the initial and final pore-filling solids, it underestimates the change in magnitude of effective solid-filled bulk modulus upon substitution. Although Ciz and

Shapiro's approximation seem to have limited practical utility due to the assumptions above, it can provide good estimates for rocks with stiff identical ellipsoidal pores. As discussed in the previous chapter, the lower embedded bound provides closer estimates to the true rock stiffness when compared to Ciz and Shapiro's approximation.

3.7. Acknowledgements

This work was supported by the Stanford Rock Physics and Borehole Geophysics (SRB) Project, and U.S. Department of Energy award DE-FE0001159.

3.8. Appendix A

3.8.1. Proofs of inequalities/statements in equations 3.7, 3.8 and 3.17

3.8.1.1. Proof $K_{bc} \geq K_{sq} \geq K_{dry}$

Gibiansky and Torquato (1998) have shown that fluid-filled effective bulk modulus (pores filled with a fluid of elastic properties: $K^A, \mu^A = 0$) as predicted by Gassmann's equation starting with measured dry bulk modulus K_{dry} is a lower bound on the *true* fluid-filled effective bulk modulus, hence the following inequality holds

$$K_{ud}^{fluid} = \Omega\left(K_{sq}\right) \geq \Omega\left(K_{dry}\right) \quad , \tag{A-1}$$

where K_{ud}^{fluid} is the *true* fluid-filled effective bulk modulus and function Ω is given in equation 3.3. Now if the shear stiffness of the pore-filling increases, i.e., $\mu^A > 0$, then the new effective bulk modulus K_{ud} must also increase from K_{ud}^{fluid}, i.e,

$$K_{ud} \geq K_{ud}^{fluid} \quad , \tag{A-2}$$

from equation 3.3, A-1 and A-2 we get

$$K_{bc} \geq K_{sq} \geq K_{dry} \quad . \tag{A-3}$$

3.8.1.2. Proof $K_{bc} \geq K_{zb} \geq K_{dry}$

Due to energy considerations, solid-filled effective bulk modulus K_{ud}, hypothetical pore-fill bulk modulus K_{zb} and bulk modulus K_{bc} (which can be expressed as a function of K_{ud} from equation 3.3) must monotonically increase with increment in shear stiffness μ^A of the pore-filling solid A if other elastic constants: K^A, K^B and μ^B, pore-shape and volume fractions remain unchanged. Also, for a given composite when $\mu^A = 0$ we know from Gibiansky and Torquato (1998)

$$K_{bc} = K_{sq} \geq K_{zb} = K_{dry} \quad , \tag{A-4}$$

and when $\mu^A = \mu^B$, from Hill (1963), and Hashin and Shtrikman (1963) it can be shown that

$$K_{bc} = K_{zb} \geq K_{dry} \quad , \tag{A-5}$$

note that equations A-4 and A-5 are true regardless of the value of K^A. Also if $K^A = 0$, then $K_{bc} = K_{zb}$ for $0 \leq \mu^A \leq \mu^B$, therefore when $K^A \geq 0$ and $0 \leq \mu^A \leq \mu^B$ we must have

$$K_{bc} \geq K_{zb} \geq K_{dry} \quad . \tag{A-6}$$

3.8.1.3. Proof that C&S approximation underestimates stiffness change upon substitution

Inequality in equation A-6 can also be written as

$$K_{bc} = K_{zb} + h \quad , \tag{A-7}$$

where *h* is an *unkown* non-negative quantity that depends on the elastic properties of the composite. Certain properties of *h* are known: when $\mu^A = 0$, from equation A-4 we have

$$h = K_{sq} - K_{dry} \geq 0 \quad . \tag{A-8}$$

When $\mu^A = \mu^B$, from equation A-5 we have

$$h = 0 \quad . \tag{A-9}$$

Now since when $K^A = 0$, $h = 0$ for $0 \leq \mu^A \leq \mu^B$, h must increase/decrease if both K^A, μ^A increase/decrease such that other elastic constants $\left(K^B, \mu^B\right)$, pore-shape and volume fractions remain unchanged.

Next, using these properties of quantity *h*, we will prove that Ciz and Shapiro's approximation will under predict the change in magnitude of effective solid-filled bulk modulus, when substituting pore solid *A1* with pore solid *A2* if $\left(\mu^{A1} - \mu^{A2}\right)\left(K^{A1} - K^{A2}\right) \geq 0$. Consider first if $\mu^{A2} \geq \mu^{A1}$, then we know

$$K_{zb}^{(2)} \geq K_{zb}^{(1)} \quad . \tag{A-10}$$

From equations 3.11 and A-7 we get

$$K_{zb}^{(2)} = \frac{K_{ud}^{(2)}\left(\frac{\phi_0 K^B}{K^{A2}} + 1 - \phi_0\right) - K^B}{\frac{\phi_0 K^B}{K^{A2}} + \frac{K_{ud}^{(2)}}{K^B} - 1 - \phi_0} - h^{(2)} \quad , \tag{A-11}$$

$$K_{zb}^{(1)} = \frac{K_{ud}^{(1)}\left(\frac{\phi_0 K^B}{K^{A1}} + 1 - \phi_0\right) - K^B}{\frac{\phi_0 K^B}{K^{A1}} + \frac{K_{ud}^{(1)}}{K^B} - 1 - \phi_0} - h^{(1)} \quad .$$

The C&S approximation predicted solid *A2* filled effective bulk modulus (referred here as $K_{ud}^{CS(2)}$) is given by

$$\frac{K_{ud}^{CS(2)}\left(\frac{\phi_0 K^B}{K^{A2}}+1-\phi_0\right)-K^B}{\frac{\phi_0 K^B}{K^{A2}}+\frac{K_{ud}^{(2)}}{K^B}-1-\phi_0}=\frac{K_{ud}^{(1)}\left(\frac{\phi_0 K^B}{K^{A1}}+1-\phi_0\right)-K^B}{\frac{\phi_0 K^B}{K^{A1}}+\frac{K_{ud}^{(1)}}{K^B}-1-\phi_0} \quad . \tag{A-12}$$

Now if in addition to $\mu^{A2} \geq \mu^{A1}$, $K^{A2} \geq K^{A1}$ then we know $h^{(2)} \geq h^{(1)}$; using this along with equations A-10, A-11 and A-12 we get

$$K_{ud}^{CS(2)} \leq K_{ud}^{(2)} \quad . \tag{A-13}$$

Similarly, if $\mu^{A2} \leq \mu^{A1}$ and $K^{A2} \leq K^{A1}$, we get

$$K_{ud}^{CS(2)} \geq K_{ud}^{(2)} \quad . \tag{A-14}$$

3.9. Appendix B: Macroscopic description

3.9.1. Macroscopic continuity equations

Volume-averaging the solid continuity equations we get

$$\frac{1}{V}\int_V \left[\frac{\rho^A-\rho_0^A}{\rho_0^A}+\partial_j\left(u_j^A\right)\right]dV=0 \quad , \tag{B-1}$$

simplifying equation B-1 for an elastic solid results in

$$\phi_0\,\frac{\overline{\rho}^A-\rho_0^A}{\rho_0^A}+\ \phi_0\ \partial_j\overline{u}_j^A+\frac{1}{V}\int_{S^{AB}} u_j^A\hat{n}_j dS=0 \quad . \tag{B-2}$$

The quantity $u_j^A\hat{n}_j dS$ is the volume swept out by the solid displacement u_j^A at the pore interfaces; hence its area integral in equation B-2 is actually the change in volume fraction of the pore-filling solid and is equal to $\phi-\phi_0$. This is valid regardless of the local fluctuations in solid displacement u_j^A. Therefore, equation B-2 reduces to

$$\frac{\bar{\rho}^{A}-\rho_0^{A}}{\rho_0^{A}}+\partial_j\bar{u}_j^{A}-\frac{\phi_0-\phi}{\phi_0}=0 \quad , \tag{B-3}$$

and similarly for phase B we obtain,

$$\frac{\bar{\rho}^{B}-\rho_0^{B}}{\rho_0^{B}}+\partial_j\bar{u}_j^{B}-\frac{\phi-\phi_0}{1-\phi_0}=0 \quad , \tag{B-4}$$

where ϕ_0 denotes the unperturbed volume fraction.

3.9.2. **Macroscopic stress equations**

Volume-averaging the pore-scale stress tensors and using boundary conditions, we get

$$\phi_0\bar{\sigma}_{ij}^{A} = C_{ijkl}^{A}\left[\frac{1}{2}\eta_0^{A}\left\{\partial_k\bar{u}_l^{A}+\partial_l\bar{u}_k^{A}\right\}+\xi_{kl}\right] \tag{B-4}$$

and

$$(1-\phi_0)\bar{\sigma}_{ij}^{B} = C_{ijkl}^{B}\left[\frac{1}{2}\eta_0^{B}\left\{\partial_k\bar{u}_l^{B}+\partial_l\bar{u}_k^{B}\right\}-\xi_{kl}\right] \quad , \tag{B-5}$$

where

$$\xi_{kl}=\frac{1}{V}\int_{S^{BA}}\frac{1}{2}\left(u_k^{B}\hat{n}_l+u_l^{B}\hat{n}_k\right)dS=-\frac{1}{V}\int_{S^{AB}}\frac{1}{2}\left(u_k^{A}\hat{n}_l+u_l^{A}\hat{n}_k\right)dS \quad . \tag{B-6}$$

We can separate the dilatational part of ξ_{kl} from its deviatoric part in the following way:

$$\xi_{kl}=-\frac{1}{3}\delta_{kl}(\phi-\phi_0)+\frac{1}{V}\int_{S^{BA}}\frac{1}{2}\left(u_k^{B}\hat{n}_l+u_l^{B}\hat{n}_k-\frac{2}{3}\delta_{kl}u_p^{B}\hat{n}_p\right)dS \quad . \tag{B-7}$$

It is convenient to refer to the area integral in equation B-7 as D_{kl}, i.e.

$$D_{kl} = \frac{1}{V}\int_{S^{BA}} \frac{1}{2}\left(u_k^B \hat{n}_l + u_l^B \hat{n}_k - \frac{2}{3}\delta_{kl} u_p^B \hat{n}_p \right) dS \quad . \tag{B-8}$$

For the isotropic stiffnesses, equations B-4 and B-5 reduce to the following:

$$\overline{\sigma}_{ij}^A = K^A \delta_{ij} \left\{ \partial_l \overline{u}_l^A - \frac{(\phi_0 - \phi)}{\phi_0} \right\} + \mu^A \left\{ \partial_i \overline{u}_j^A + \partial_j \overline{u}_i^A - \frac{2}{3}\delta_{ij}\partial_p \overline{u}_p^A \right\} - 2\frac{\mu^A}{\eta_0^A} D_{ij} \tag{B-9}$$

and

$$\overline{\sigma}_{ij}^B = K^B \delta_{ij} \left\{ \partial_l \overline{u}_l^B - \frac{(\phi - \phi_0)}{1 - \phi_0} \right\} + \mu^B \left\{ \partial_i \overline{u}_j^B + \partial_j \overline{u}_i^B - \frac{2}{3}\delta_{ij}\partial_p \overline{u}_p^B \right\} + 2\frac{\mu^B}{\eta_0^B} D_{ij} \quad . \tag{B-10}$$

Average pressure for the two phases are defined as

$$\overline{P}^A = -\frac{\overline{\sigma}_{ll}^A}{3} \tag{B-11}$$

and

$$\overline{P}^B = -\frac{\overline{\sigma}_{ll}^B}{3} \quad . \tag{B-12}$$

Equations B-9 to B-12 represents the volume averaged fields defined at the centroid x_0 of the averaging volume *V*, for an arbitrary pore-shape composite media. To obtain the corresponding spatial deviation we decompose the stress tensor and displacement field as

$$\sigma_{ij}^A(x_0, y) = \overline{\sigma}_{ij}^A(x_0) + \widetilde{\sigma}_{ij}^A(x_0, y) \quad , \tag{B-13}$$

$$u_j^A(x_0, y) = \overline{u}_j^A(x_0) + \widetilde{u}_j^A(x_0, y)$$

and

$$\sigma_{ij}^{B}(x_0, y) = \bar{\sigma}_{ij}^{B}(x_0) + \tilde{\sigma}_{ij}^{B}(x_0, y) \quad , \tag{B-14}$$

$$u_{j}^{B}(x_0, y) = \bar{u}_{j}^{B}(x_0) + \tilde{u}_{j}^{B}(x_0, y) \quad .$$

where $\tilde{\sigma}_{ij}^{A,B}$ and $\tilde{u}_{j}^{A,B}$ are the spatial deviation stress tensors and displacement fields, respectively. These are defined at the relative position vector y for points within the volume. Substituting equations B-13 and B-14 in the pore-scale stress tensor equations and subtracting the resulting equations from equations B-9 and B-10 we get the spatial deviation equations for solid pressures and shear stresses

$$\tilde{P}^{A} = -K^{A}\left\{\partial_l \tilde{u}_l^{A} - \frac{1}{V^{A}}\int_{S^{AB}}\left(\tilde{u}_l^{A}\hat{n}_l\right)dS\right\} \quad , \tag{B-15}$$

$$\tilde{\sigma}_{ij}^{A} = \mu^{A}\left\{\frac{1}{2}\left(\partial_i \tilde{u}_j^{A} + \partial_j \tilde{u}_i^{A}\right) - \frac{1}{V^{A}}\int_{S^{AB}}\frac{1}{2}\left(\tilde{u}_i^{A}\hat{n}_j + \tilde{u}_j^{A}\hat{n}_i\right)dS\right\}$$

and

$$\tilde{P}^{B} = -K^{B}\left\{\partial_l \tilde{u}_l^{B} - \frac{1}{V^{B}}\int_{S^{BA}}\left(\tilde{u}_l^{B}\hat{n}_l\right)dS\right\} \quad , \tag{B-16}$$

$$\tilde{\sigma}_{ij}^{B} = \mu^{B}\left\{\frac{1}{2}\left(\partial_i \tilde{u}_j^{B} + \partial_j \tilde{u}_i^{B}\right) - \frac{1}{V^{B}}\int_{S^{BA}}\frac{1}{2}\left(\tilde{u}_i^{B}\hat{n}_j + \tilde{u}_j^{B}\hat{n}_i\right)dS\right\} \quad ,$$

where for shear stress in equations B-15 and B-16, $i \neq j$.

3.9.3. **Porosity and Deviatoric Strain Equation**

To complete the set of macroscopic equations, we need to define two macroscopic constitutive relations that link pore-scale physics to the macroscopic description. For the first such relation, we relate change in volume fraction to macroscopic displacement gradients as

$$\phi - \phi_0 = \delta^B \bar{u}^B_{l,l} - \delta^A \bar{u}^A_{l,l} \quad . \tag{B-17}$$

Similarly, we relate the deviatoric area integral in equation B-8 to traceless displacement gradient as

$$2D_{kl} = \chi^B \left\{ \partial_k \bar{u}^B_l + \partial_l \bar{u}^B_k - \frac{2}{3}\delta_{kl}\partial_p \bar{u}^B_p \right\} - \chi^A \left\{ \partial_k \bar{u}^A_l + \partial_l \bar{u}^A_k - \frac{2}{3}\delta_{kl}\partial_p \bar{u}^A_p \right\} \quad . \tag{B-18}$$

Parameters $\delta^{A,B}$ and $\chi^{A,B}$ are phenomenological constitutive parameters and depend on pore geometry and the elastic properties of the poro-continuum constituents.

3.10. Appendix C

A, B : Superscript for solid A (pore-filling) and B (frame solid)

$A1, A2$: Superscript for initial pore-filling solid $A1$ and final pore-filling solid $A2$

V : Averaging or total volume

V^A, V^B : Volumes of solid A and B

S^{AB} : Surface integral over pore boundaries, normal pointing from solid A to B

$\overline{\psi}$: Phase volume average of any quantity ψ

$\hat{\psi}$: Bulk volume average of any quantity ψ

$\tilde{\psi}$: Spatial deviation of any quantity ψ

x_0 : Centroid of averaging volume

y : Relative position vector with respect to the centroid

ϕ : Volume fraction of solid A

0 : Denotes unperturbed value

$\hat{n}$: Surface normal

ρ^A, ρ^B : Densities of solid A and B

u^A, u^B : Displacement of solid *A* and *B*

M^B : Mass of solid *B*

$\sigma_{ij}^A, \sigma_{ij}^B$: Stress in solid *A* and *B*, shear stress tensors in solid *A* and *B,* if $i \neq j$

P^A, P^B : Pressure in solid *A* and *B*

C^A, C^B : Stiffness tensors

K^A, K^B : Bulk modulus of solid *A* and *B*

μ^A, μ^B : Shear modulus of solid *A* and *B*

δ^A, δ^B : Macroscopic volume fraction constitutive parameters

χ^A, χ^B : Macroscopic deviatoric strain constitutive parameters

K_{bc} : Effective bulk modulus as defined in equation 3.1

K_{ud} : Effective saturated or solid-filled bulk modulus

K_{zb} : Effective bulk modulus as defined in equation 3.5

K_{sq} : Effective bulk modulus as defined in equation 3.6

K_{dry} : Effective dry or drained bulk modulus as defined in equation 3.4

3.11. References

Berryman, J. G., and G. W. Milton, 1988, Microgeometry of random composites and porous media: Journal of Physics D: Applied Physics, **21**, 87-94.

Ciz, R., and S. A. Shapiro, 2007, Generalization of Gassmann equations for porous media saturated with a solid material: Geophysics, **72**, A75–A79.

de la Cruz, V., P. N. Sahay, T. J. T. Spanos, 1993, Thermodynamics of Porous Media: Mathematical and Physical Science, **443**, 247-255.

Gassmann, F., 1951, Über die Elastizität poröser Medien: Vierteljahrschrift der Naturforschenden Gessellschaft in Zürich, **96**, 1-23.

Gibiansky, L. V., and S. Torquato, 1998, Rigorous connection between physical properties of porous rock: Journal of Geophysical Research, **103**, 23911-23923.

Grechka, V., 2009, Fluid-solid substitution in rocks with disconnected and partially connected porosity: Geophysics, **74**, WB89–WB95.

Gurevich, B., D. Makarynska, and M. Pervukhina, 2009, Ultrasonic moduli for fluid-saturated rocks: Mavko-Jizba relations rederived and generalized: Geophysics, **74**, 25-30.

Hashin, Z., 1962, The elastic moduli of heterogeneous materials: Journal of Applied Mechanics, **29**, 143-150.

Hashin, Z., and S. Shtrikman, 1963, A variational approach to the elastic behavior of multiphase materials: Journal of the Mechanics and Physics of Solids, **11**, 127–140.

Hickey, C. J., T. J. T. Spanos, and V. de la Cruz, 1995, Deformation parameters of permeable media: Geophysical Journal International, **121**, 359–370.

Hill, R., 1963, Elastic properties of reinforced solids, Some theoretical principles: Journal of the Mechanics and Physics of Solids, **11**, 357–372.

Kantor, Y., and D. J. Bergman, 1984, Improved rigorous bounds on the effective elastic moduli of a composite material: Journal of the Mechanics and Physics of Solids, **32**, 41-62.

Makarynska, D., B. Gurevich, J. Behura, and M. Batzle, 2010, Fluid substitution in rocks saturated with viscoelastic fluids, Geophysics, **75**, E115–E122.

Marion, D., and A. Nur, 1991, Pore-filling material and its effect on velocity in rocks: Geophysics, **56** (2), 225–230.

Marle, C., 1967, Ecoulements monophasiques en milieu poreux: Revue de l'I.F.P. XXII, No. 10.

Mavko, G., T. Mukerji, and J. Dvorkin, 2009, The rock physics handbook: Cambridge University Press.

Mavko, G., and D. Jizba, 1991, Estimating grain-scale fluid effects on velocity dispersion in rocks: Geophysics, **56**, 1940–1949.

Sahay, P., 1996, Elastodynamics of deformable porous media: Proceedings of Royal Society London, **452**, 1517-1529.

Shapiro, S. A., and A. Kaselow, 2005, Porosity and elastic anisotropy of rocks under tectonic stress and pore-pressure changes: Geophysics, **70**, N27–N38.

Slattery, J. C., 1967, Flow of viscoelastic fluids through porous media: AIChEJ, **13**, 1066-1072.

Spanos, T., 2009, Seismic wave propagation in composite elastic media: Transport in Porous Media, **79**, 135-148.

Wang, Z., 1988, Wave velocities in hydrocarbons and hydrocarbon saturated rocks – with applications to EOR monitoring: PhD thesis, Stanford University.

Whitaker, S., 1999, The Method of Volume Averaging, Kluwer, Academic Publisher, Boston.

Zimmerman, R. W., 1991, Compressibility of Sandstones, in Development in Petroleum Science, vol **29**, Elsevier, Amsterdam.

Chapter 4

Predicting change in P-wave modulus upon substitution with missing S-wave modulus

4.1. Abstract

The problem of predicting change in seismic velocities (P and S-wave) upon change in pore-fill material is commonly known as *substitution*. For isotropic rocks, P and S-wave velocities are fundamentally linked to the effective P-wave and shear moduli. Change in S-wave velocity (or shear modulus) upon fluid substitution can be predicted with Gassmann starting with only the initial S-wave velocity, however, predicting the change in P-wave velocity (or P-wave modulus) using Gassmann requires knowledge of both initial P and S-wave velocities or moduli.

Published in GEOPHYSICS: Upcoming

In this study, we present a rigorous derivation of P-wave modulus fluid and solid substitution in monomineralic isotropic rocks, assuming S-wave velocity or shear modulus is not known. For the general case of solid substitution, exact P-wave modulus substitution equation depends on usually unknown parameters. However, for fluid substitution, fewer parameters are required and the *dependence* of exact substitution on these unknown parameters reduces with increase in Poisson's ratio of the mineral in rock frame. Thus we find that P-wave modulus fluid substitution, in the absence of shear velocity, can be performed with relatively higher confidence for rocks with calcite/dolomite frame as compared to those with quartz frame. In addition, we propose a new P-wave modulus fluid substitution recipe which in the absence of initial shear modulus improves on a previously suggested approximation, and thus is recommended for practice.

4.2. Introduction

The effective elastic moduli that govern P and S-wave velocities (V_P, V_S) in rocks are sensitive to change in properties of pore-filling materials. In nature, pore-filling materials occur as gaseous, liquid and solid phases. Quantifying the degree to which the effective elastic properties change with change in pore-filling material is commonly referred to as the substitution problem; fluid or solid substitution is one of the most fundamental problems in Rock Physics and has a range of practical applications, such as sonic log invasion correction, seismic reservoir monitoring, AVO modeling, etc.

For isotropic monomineralic fluid-saturated rocks, Gassmann (1951) provides relations that operate separately on initial effective bulk and shear moduli, which are typically estimated from the combination of P and S-wave velocities, and density. Using Gassmann's relations we can predict the change in V_S without the knowledge of V_P, but the reverse is not true, i.e., both V_P and V_S are needed to predict the change in V_P. These predictions are exact if load-induced pore-pressure is homogeneous under quasi-static deformation.

A common practical problem arises when V_P is measured but V_S is not measured or is unreliable; in such situations both initial bulk and shear moduli are not known individually and thus Gassmann's relations are not directly applicable. To tackle this practical problem, two broad approaches are commonly used in geophysics (Bachrach et al., 1998; Sengupta et al., 2003; Røgen et al., 2004; Han and Batzle, 2004; Dvorkin et al., 2007; Yan and Han, 2010). First approach is to guess the missing V_S using an empirical relation, and then use Gassmann's relations. The second approach is to employ the Gassmann-like approximation suggested by Mavko et al. (1995) which directly estimates the substituted change in P-wave modulus without the shear modulus. This approximation was motivated by a rigorous graphical interpretation of Gassmann's bulk modulus equation – extended heuristically to P-wave modulus. Since the precise implicit physical assumption in this approximate equation is not well understood, its range of applicability is not clear. Moreover, both of these approaches are not applicable to the general case of solid substitution - required when pore space is occupied with heavy-oil, solid hydrocarbon, clay, salt, mineral precipitate, etc.

In this paper, we present the first formal derivation of an exact expression that operates on P-wave modulus for either fluid or solid substitution. We restrict this study to monomineralic isotropic solid-filled rocks but consider arbitrary pore geometry.

The organization of this paper is as follows: We begin with presenting the exact fluid and solid substitution equations with further clarifications discussed in the Appendices. We discuss techniques to approximate substitution parameters required in the exact substitution equation, and compare the substitution predictions with numerical and laboratory examples. Finally, we present a recipe for practitioners to perform P-wave modulus substitution.

4.3. Exact equations for substitution

In chapter 2 we derived exact substitution equations for effective bulk and shear moduli (Saxena and Mavko, 2014) relating the *initial* solid-filled effective moduli (bulk: $K_{ud}^{(1)}$ and

shear: $\mu_{ud}^{(1)}$) of an isotropic monomineralic rock containing a pore-filling solid *A1* (bulk: K^{A1} and shear: μ^{A1}) and frame mineral solid *B* (bulk: K^{B} and shear: μ^{B}) to the *second* solid-filled effective moduli (bulk: $K_{ud}^{(2)}$ and shear: $\mu_{ud}^{(2)}$) of the same rock but containing pore-filling solid *A2* (bulk: K^{A2} and shear: μ^{A2}). The bulk modulus equation is:

$$\left(K^{A1}-K^{A2}\right)\alpha_1+\left(\mu^{A1}-\mu^{A2}\right)\alpha_2'=\phi\frac{\left(K^{B}-K^{A2}\right)\left(K^{B}-K^{A1}\right)}{\left(K^{B}-K_{ud}^{(1)}\right)\left(K^{B}-K_{ud}^{(2)}\right)}\left(K_{ud}^{(1)}-K_{ud}^{(2)}\right)\ , \tag{4.1}$$

where

$$\alpha_1=\frac{\overline{e^{A1}e^{A2}}}{\overline{e^{A1}}\ \overline{e^{A2}}}=\frac{\overline{P^{A1}P^{A2}}}{\overline{P^{A1}}\ \overline{P^{A2}}}\quad , \tag{4.2}$$

and

$$\alpha_2'=\frac{K^{A1}K^{A2}}{\mu^{A1}\mu^{A2}}\alpha_2=\frac{K^{A1}K^{A2}}{\mu^{A1}\mu^{A2}}\left(\frac{1}{2}\frac{\overline{\tau_{ij}^{A1}\tau_{ij}^{A2}}}{\overline{P^{A1}}\ \overline{P^{A2}}}\right)=2\frac{\overline{\gamma_{ij}^{A1}\gamma_{ij}^{A2}}}{\overline{e^{A1}}\ \overline{e^{A2}}}\quad . \tag{4.3}$$

In equation 4.1, ϕ is the volume fraction of pore-filling solid (i.e., porosity); P^{A} and τ_{ij}^{A} are bulk-compression induced pressure (negative of mean stress) and deviatoric stresses within the pore-filling phase; e^{A} and γ_{ij}^{A} are the corresponding compression-induced volumetric and deviatoric strains within pore-filling solid A (A ≡ *A1* or *A2*). These are formally related to stress σ_{ij}^{A} and strain $\varepsilon_{ij}^{\mathrm{A}}$ as

$$\sigma_{ij}^{\mathrm{A}}=-P^{\mathrm{A}}\delta_{ij}+\tau_{ij}^{\mathrm{A}}\quad , \tag{4.4}$$

$$\varepsilon_{ij}^{\mathrm{A}}=\frac{e^{\mathrm{A}}}{3}\delta_{ij}+\gamma_{ij}^{\mathrm{A}}\quad . \tag{4.5}$$

The stress and strains in equations 4.4 and 4.5 are related by Hooke's law. The overbar operator, $\overline{\Phi}$ represents pore volume average of any quantity Φ. Here we use standard summation over repeated indices. Further details are in chapter 2. Parameter $\alpha_1 \geq 1$

describes the heterogeneity of compression-induced mean stress (or pressure) in initial and final pore-filling materials; with $\alpha_1 = 1$ occurring in the special case of perfectly uniform stress/strains in the pores. The parameter $\alpha_2 \geq 0$ describes the relative contributions of compression-induced to average shear stresses in the initial and final pore-filling materials. The corresponding exact substitution equation for effective shear modulus is:

$$\left(\mu^{A1} - \mu^{A2}\right)\beta_1 + \left(K^{A1} - K^{A2}\right)\beta_2' = \phi \frac{\left(\mu^B - \mu^{A2}\right)\left(\mu^B - \mu^{A1}\right)}{\left(\mu^B - \mu_{ud}^{(1)}\right)\left(\mu^B - \mu_{ud}^{(2)}\right)}\left(\mu_{ud}^{(1)} - \mu_{ud}^{(2)}\right) \ , \tag{4.6}$$

where

$$\beta_1 = \frac{1}{2}\frac{\overline{\tau_{ij}^{A1}\tau_{ij}^{A2}}}{\overline{\tau_{12}^{A1}}\,\overline{\tau_{12}^{A2}}} = \frac{1}{2}\frac{\overline{\gamma_{ij}^{A1}\gamma_{ij}^{A2}}}{\overline{\gamma_{12}^{A1}}\,\overline{\gamma_{12}^{A2}}} \ , \tag{4.7}$$

and

$$\beta_2' = \frac{\mu^{A1}\mu^{A2}}{K^{A1}K^{A2}}\beta_2 = \frac{\mu^{A1}\mu^{A2}}{K^{A1}K^{A2}}\left(\frac{\overline{P^{A1}P^{A2}}}{\overline{\tau_{12}^{A1}}\,\overline{\tau_{12}^{A2}}}\right) = \frac{1}{4}\frac{\overline{e^{A1}e^{A2}}}{\overline{\gamma_{12}^{A1}}\,\overline{\gamma_{12}^{A2}}} \ . \tag{4.8}$$

Parameter $\beta_1 \geq 1$ describes the heterogeneity of shear field-induced deviatoric stresses in initial and final pore-filling materials; parameter $\beta_2 \geq 0$ describes the contribution of shear field-induced mean stresses (or pressure) in initial and final pore-filling materials. Note that substitution parameters α_1, α_2, β_1 and β_2 depend on induced stresses/strains in pores of both initial and final rocks.

The new result in this paper, is the exact relation between the *initial* solid-filled effective P-wave modulus ($M_{ud}^{(1)}$) containing pore-filling solid *A1* and frame solid *B* to *second* solid-filled P-wave effective modulus ($M_{ud}^{(2)}$) of the same rock but containing pore-filling solid *A2*:

$$\frac{\left(M_{ud}^{(2)}-M^{B}\right)\left(M_{ud}^{(1)}-M^{B}\right)}{\left(M_{ud}^{(2)}-M_{ud}^{(1)}\right)}=\frac{\phi\left(K^{B}-K^{A2}+\left(\mu^{B}-\mu^{A2}\right)\frac{4}{3}\Omega^{A2}\right)\left(K^{B}-K^{A1}+\left(\mu^{B}-\mu^{A1}\right)\frac{4}{3}\Omega^{A1}\right)}{\left(K^{A2}-K^{A1}\right)\delta_1+\left(\mu^{A2}-\mu^{A1}\right)\delta_2'} \tag{4.9}$$

where

$$\delta_1=\frac{\overline{e^{A1}e^{A2}}}{\overline{e^{A1}}\;\overline{e^{A2}}}=\frac{\overline{P^{A1}P^{A2}}}{\overline{P^{A1}}\;\overline{P^{A2}}}\quad;\delta_2'=\frac{K^{A1}K^{A2}}{\mu^{A1}\mu^{A2}}\quad;\delta_2=\frac{K^{A1}K^{A2}}{\mu^{A1}\mu^{A2}}\left(\frac{1}{2}\frac{\overline{\tau_{ij}^{A1}\tau_{ij}^{A2}}}{\overline{P^{A1}}\;\overline{P^{A2}}}\right)=2\frac{\overline{\gamma_{ij}^{A1}\gamma_{ij}^{A2}}}{\overline{e^{A1}}\;\overline{e^{A2}}}\quad, \tag{4.10}$$

and

$$\Omega^{\mathrm{A}}=\frac{3\overline{\varepsilon_{11}^{\mathrm{A}}}}{2\overline{e^{\mathrm{A}}}}-\frac{1}{2}\quad. \tag{4.11}$$

Derivation of equation 4.9 is discussed in Appendix A. The substitution parameters δ_1 and δ_2' depend on induced stress/strains (in pores of both initial and final rocks) upon *uniaxial* strain deformation (as per equation A-1). Parameter Ω^{A} describes the ratio of pore-filling solid strain component (for uniaxial strain applied in direction 1) and volumetric strain. If $\mu^{A1}=\mu^{A2}=\mu$, then equation 4.9 becomes independent of parameter δ_2' and reduces to

$$\frac{\left(M_{ud}^{(2)}-M^{B}\right)\left(M_{ud}^{(1)}-M^{B}\right)}{\left(M_{ud}^{(2)}-M_{ud}^{(1)}\right)}=\frac{\phi\left(\left(K^{B}-K^{A2}\right)+\left(\mu^{B}-\mu\right)\frac{4}{3}\Omega^{A2}\right)\left(\left(K^{B}-K^{A1}\right)+\left(\mu^{B}-\mu\right)\frac{4}{3}\Omega^{A1}\right)}{\left(K^{A2}-K^{A1}\right)\delta_1} \tag{12}$$

4.4. Special case of fluid substitution

Assuming ideal elastic pore fluids i.e., $\mu^{A1} = \mu^{A2} = 0$, equations 4.1, 4.6 and 4.9 reduce to the following exact fluid substitution relations

$$\left(K^{A1} - K^{A2}\right)\alpha_1 = \phi \frac{\left(K^B - K^{A2}\right)\left(K^B - K^{A1}\right)}{\left(K^B - K_{ud}^{(1)}\right)\left(K^B - K_{ud}^{(2)}\right)}\left(K_{ud}^{(1)} - K_{ud}^{(2)}\right) \quad , \tag{4.13}$$

$$\left(K^{A1} - K^{A2}\right)\beta_2' = \frac{\phi\left(\mu^B\right)\left(\mu^B\right)}{\left(\mu^B - \mu_{ud}^{(1)}\right)\left(\mu^B - \mu_{ud}^{(2)}\right)}\left(\mu_{ud}^{(1)} - \mu_{ud}^{(2)}\right) \quad , \tag{4.14}$$

and

$$\frac{\left(K^{A1} - K^{A2}\right)\delta_1}{\left(K^B - K^{A2} + \frac{4}{3}\Omega^{A2}\mu^B\right)\left(K^B - K^{A1} + \frac{4}{3}\Omega^{A1}\mu^B\right)} = \frac{\phi\left(M_{ud}^{(1)} - M_{ud}^{(2)}\right)}{\left(M^B - M_{ud}^{(2)}\right)\left(M^B - M_{ud}^{(1)}\right)} \quad . \tag{4.15}$$

Equations 4.13, 4.14 and 4.15 depend on parameters α_1, β_2', δ_1, Ω^{A1} and Ω^{A2} which in turn depend on the details of rock microstructure. For rocks with inter-connected pores such that induced fluid pore-pressure can equilibrate at very low frequencies, we must have $\alpha_1 = \delta_1 = 1$ and $\beta_2' = 0$ (Berryman, 1999), under these special conditions, equations 4.13, 4.14 and 4.15 further reduce to

$$\left(K^{A1} - K^{A2}\right) = \phi \frac{\left(K^B - K^{A2}\right)\left(K^B - K^{A1}\right)}{\left(K^B - K_{ud}^{(1)}\right)\left(K^B - K_{ud}^{(2)}\right)}\left(K_{ud}^{(1)} - K_{ud}^{(2)}\right) \quad , \tag{4.16}$$

$$\mu_{ud}^{(1)} = \mu_{ud}^{(2)} \quad , \tag{4.17}$$

and

$$\frac{\left(K^{A1} - K^{A2}\right)}{\left(K^B - K^{A2} + \frac{4}{3}\Omega^{A2}\mu^B\right)\left(K^B - K^{A1} + \frac{4}{3}\Omega^{A1}\mu^B\right)} = \frac{\phi\left(M_{ud}^{(1)} - M_{ud}^{(2)}\right)}{\left(M^B - M_{ud}^{(2)}\right)\left(M^B - M_{ud}^{(1)}\right)} \quad . \tag{4.18}$$

In the special case of inter-connected fluid saturated pores, substitution equations 4.16 (for bulk) and 4.17 (for shear) are *independent of further details of pore geometry* and are identical to Gassmann's equations, where as the P-wave modulus substitution equation still requires knowledge of parameters Ω^{A1} and Ω^{A2}. If both initial bulk ($K_{ud}^{(1)}$) and shear ($\mu_{ud}^{(1)}$) moduli are known, then fluid substituted bulk and shear moduli $K_{ud}^{(2)}$ and $\mu_{ud}^{(2)}$ can be obtained by solving equations 4.16 and 4.17; also the substituted P-wave modulus ($M_{ud}^{(2)}$) can be obtained by the simple relation: $M_{ud}^{(2)} = K_{ud}^{(2)} + 4\mu_{ud}^{(2)}/3$. However, if only the initial P-wave modulus $M_{ud}^{(1)}$ is known and no initial measurements of $K_{ud}^{(1)}$ and $\mu_{ud}^{(1)}$ are available, then parameters Ω^{A1} and Ω^{A2} are needed to estimate the fluid substituted P-wave modulus $M_{ud}^{(2)}$. To understand the dependence of equation 4.18 on parameters Ω^{A1} and Ω^{A2} we rewrite this equation in the following way

$$\frac{\left(K^{A1} - K^{A2}\right)}{\left(1 - \frac{K^{A2}}{K^{B}} + \Omega^{A2}\Delta^{B}\right)\left(1 - \frac{K^{A1}}{K^{B}} + \Omega^{A1}\Delta^{B}\right)} = \frac{\phi\left(M_{ud}^{(1)} - M_{ud}^{(2)}\right)}{\left(1 + \Delta^{B} - \frac{M_{ud}^{(2)}}{K^{B}}\right)\left(1 + \Delta^{B} - \frac{M_{ud}^{(1)}}{K^{B}}\right)}, \qquad (4.19)$$

where

$$\Delta^{B} = \frac{2\left(1 - 2\nu^{B}\right)}{1 + \nu^{B}}. \qquad (4.20)$$

In equation 4.20, ν^{B} is the Poisson's ratio of frame solid *B*. Note that as ν^{B} increases Δ^{B} decreases, and the dependence of P-wave modulus substitution equation (4.19) on Ω^{A} ($A \equiv A1, A2$) subsequently diminishes. This has clear practical implications. For instance, compared to quartz which has a Poisson's ratio of $\nu^{B} = 0.08$ (i.e., $\Delta^{B} \approx 1.7$) and P-wave modulus of $M^{B} = 119$ GPa (Mavko et al., 2009), calcite has a relatively large Poisson's ratio $\nu^{B} = 0.32$ (i.e., $\Delta^{B} \approx 0.55$) but similar P-wave modulus as quartz ($M^{B} = 96$ GPa). Therefore, when parameter Ω^{A} is not well constrained, P-wave modulus fluid substitution in rocks with calcite as the frame solid can be performed with less uncertainty than in rocks composed of quartz. In the next section, with the aid of effective media models, we will

show that parameter Ω^{A} also generally reduces with increase in frame solid Poisson's ratio; this reinforces the above argument.

Now we will discuss some properties of parameter Ω^{A} defined in equation 4.11 (and A-13). If the rock is uniaxially deformed (as per equation A-1) the ratio $\overline{\varepsilon_{11}^{A}} / \overline{e^{A}}$ (and Ω^{A}) will increase as the pore fluid becomes more resistive. For example, if in equation 4.11, we put $K^{A} \to \infty$ i.e., make the pore-filling material incompressible then we must have $\overline{e^{A}} \to 0$ and $\Omega^{A} \to \infty$. Similarly, parameter Ω^{A} will assume large values for rocks with fluid-filled crack like pores (of near zero volume). Clearly, Ω^{A} depends on both properties of rock constituents and details of the microstructure.

Comparing exact result in equation 4.19 with the approximation suggested by Mavko et al. (1995) we note that their approximation implicitly assumes $\Omega^{A} = 1$ (when deformed as per equation A-1). The physical assumption of this approximation is that all of the pore volume change comes about due to strain in the uniaxial strain direction, i.e., $\overline{\varepsilon_{11}^{A}} = \overline{e^{A}}$. Hence, this approximation is not strictly valid for situations when $\Omega^{A} \neq 1$ or $\overline{\varepsilon_{11}^{A}} \neq \overline{e^{A}}$, for example, when pore fluid is incompressible or pores are crack like.

In the next section, we discuss exact solutions to Ω^{A} for a single ellipsoidal inclusion embedded in an infinite elastic medium. Subsequently, we approximate the effects of inclusion interactions on Ω^{A} and other substitution parameters using established effective media models.

4.5. Estimating substitution parameters

For a single ellipsoidal inclusion (pore) embedded in an infinite elastic medium (frame), *exact* analytic solutions to substitution parameters α_1, α_2', β_1, β_2', δ_1, δ_2', Ω^{A1} and Ω^{A2} can be obtained. These solutions are as follows:

$$\alpha_1 = \beta_1 = \delta_1 = 1 \quad , \tag{4.21}$$

$$\alpha_2' = \beta_2' = 0 \quad , \tag{4.22}$$

$$\delta_2' = \frac{4}{3}\frac{\Lambda^{BA1}}{\Sigma^{BA1}}\frac{\Lambda^{BA2}}{\Sigma^{BA2}} \quad , \tag{4.23}$$

$$\Omega^{A1} = \frac{\Lambda^{BA1}}{\Sigma^{BA1}} \quad , \tag{4.24}$$

$$\Omega^{A2} = \frac{\Lambda^{BA2}}{\Sigma^{BA2}} \quad . \tag{4.25}$$

where Λ^{BA} and Σ^{BA} ($\mathrm{A} \equiv A1, A2$) are shape coefficients (Eshelby, 1957; Wu, 1966; Berryman, 1980; Torquato, 2001). For a spherical inclusion these are given as

$$\Sigma^{BA} = \frac{K^B + (4/3)\mu^B}{K^A + (4/3)\mu^B} \quad , \tag{4.26}$$

$$\Lambda^{BA} = \frac{\mu^B + H^B}{\mu^A + H^B} \quad , \tag{4.27}$$

$$H^B = \left(\mu^B / 6\right)\left(9K^B + 8\mu^B\right)/\left(K^B + 2\mu^B\right) \quad , \tag{4.28}$$

Details of the derivation of equations 4.21 to 4.25 are discussed in the Appendix B. Note that parameters: δ_2', Ω^{A1} and Ω^{A2} do not depend on the absolute values of Σ^{BA} and Λ^{BA} but instead depend on their ratio: Λ^{BA}/Σ^{BA}.

Parameters in equations 4.21 to 4.25 do not include effects of inclusion interaction in a composite with multiple inclusions. Such effects might be substantial. For instance, since the strain field within a single ellipsoidal inclusion is homogeneous we obtain $\alpha_1 = 1$, however a second nearby inclusion can make the strain field heterogeneous, resulting in $\alpha_1 \geq 1$.

Various effective medium models such as the self-consistent scheme (Wu, 1966; O' Connell and Budiansky, 1974; Berryman, 1980), differential effective medium (Cleary et al., 1980; Norris, 1985), Kuster-Toksöz approximation (Kuster and Toksöz, 1974), etc., can be used to approximate the effects of inclusion interactions. For example, using the

self-consistent scheme, for two-phase composite of solids *B* and *A1* (or *A2*), we can approximate the shape coefficients $\Sigma^{BA} \approx P^{*A}$ and $\Lambda^{BA} \approx Q^{*A}$ (A ≡ *A1* or *A2*), which can be iteratively solved using the two equations:

$$(1-\phi)\left(K^B - K^*\right)P^{*B} + \phi\left(K^A - K^*\right)P^{*A} = 0 \quad , \tag{4.29}$$

$$(1-\phi)\left(\mu^B - \mu^*\right)Q^{*B} + \phi\left(\mu^A - \mu^*\right)Q^{*A} = 0 \quad . \tag{4.30}$$

Expressions for P^{*i} and Q^{*i} ($i \equiv$ *A1*, *A2* and *B*) for various ellipsoidal shapes (assuming randomly oriented so that every orientation is equally probable) can be found in Mavko et al. (2009). For ellipsoidal shape pores, equations 4.29 and 4.30 can be solved iteratively using expressions in equations 4.26 and 4.27 for P^{*i} and Q^{*i} (instead of Σ^{BA} and Λ^{BA}). Using effective media approach, we approximate the parameters δ_2', Ω^{A1} and Ω^{A2} as

$$\delta_2' \approx \frac{4}{3}\frac{Q^{*A1}}{P^{*A1}}\frac{Q^{*A2}}{P^{*A2}} \quad , \tag{4.31}$$

$$\Omega^{A1} \approx \frac{Q^{*A1}}{P^{*A1}} \quad , \tag{4.32}$$

$$\Omega^{A2} \approx \frac{Q^{*A2}}{P^{*A2}} \quad . \tag{4.33}$$

4.6. Discussion

Figure 4.1a shows calculated Ω^A (A ≡ *A1* or *A2*) when $\phi = 0.3$ as a function of various inclusion aspect ratios and elastic properties of inclusion material embedded in a quartz frame ($K^B = 36$ GPa; $\mu^B = 45$ GPa; $\nu^B = 0.08$). We note that for aspect ratio > 0.2, the calculated value of Ω^A from both the self-consistent (SC) and the differential effective medium (DEM) approximations is nearly idependent on inclusion elastic properties and is approximately constant ~ 1.2. For aspect ratio < 0.2, the calculated Ω^A becomes

increasingly sensitive to inclusion elastic properties and assumes larger values than 1.2. Similarly, Figure 4.1b shows the same example but for calcite frame ($K^B = 77$ GPa; $\mu^B = 32$ GPa; $\nu^B = 0.32$); for this case the calculated value of Ω^A for aspect ratio > 0.2 is nearly idependent on inclusion elastic properties with an approximate value of ~ 0.9. Therefore, from Figures 1a, b we note that when aspect ratio > 0.2 the calculated Ω^A is nearly a constant value.

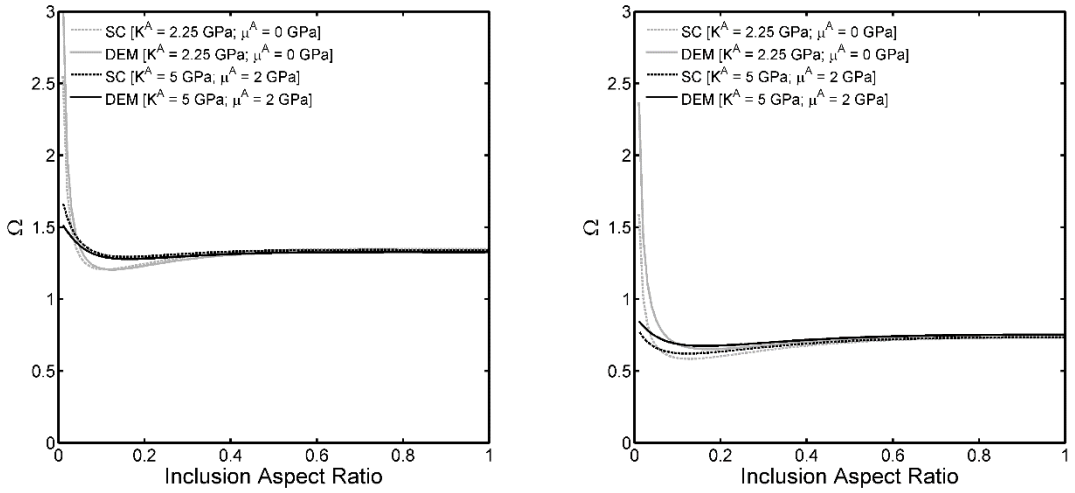

Figure 4.1: Calculated Ω^A using SC (self-consistent) and DEM (differential effective medium) approximations for a range of inclusion aspect ratios and elastic properties of pore-filling material (porosity = 0.3). Figures 1a and 1b show calculations for quartz and calcite as the frame solid, respectively.

After some algebra, for aspect ratio > 0.2, Ω^A as obtained using SC can be approximated as

$$\Omega^A \approx \frac{\left(\mu^B + H^B\right)\left(K^A + (4/3)\mu^B\right)}{\left(\mu^A + H^B\right)\left(K^B + (4/3)\mu^B\right)}\left(1 - \phi/3\right) \quad . \tag{4.34}$$

Also, if $K^A, \mu^A << K^B, \mu^B$ then Ω^A can be further approximated as

$$\Omega^A \approx \frac{4\left(\nu^B - 0.5\right)}{\left(\nu^B - 1.4\right)}\left(1 - \phi/3\right) \quad . \tag{4.35}$$

Using Ω^{A} in equation 4.35, the term $\Omega^{\mathrm{A}}\Delta^{B}$ in the denominator (on the LHS) of the exact fluid substitution equation 4.19 can be simplified as

$$\Omega^{\mathrm{A}}\Delta^{B} \approx \frac{4\left(1-2\nu^{B}\right)^{2}}{\left(1.4-\nu^{B}\right)\left(1+\nu^{B}\right)}\left(1-\phi/3\right) \quad . \tag{4.36}$$

If $\phi = 0.3$, for quartz frame rock we obtain $\Omega^{\mathrm{A}}\Delta^{B} \approx 1.8$, whereas for calcite frame rock we get $\Omega^{\mathrm{A}}\Delta^{B} \approx 0.32$. Hence, we note for calcite frame rocks with pores aspect ratio > 0.2, $\Omega^{\mathrm{A}}\Delta^{B} << 1$ thus estimating Ω^{A} for calcite rocks is relatively less important as compared to quartz frame rocks for which $\Omega^{\mathrm{A}}\Delta^{B} >> 1$.

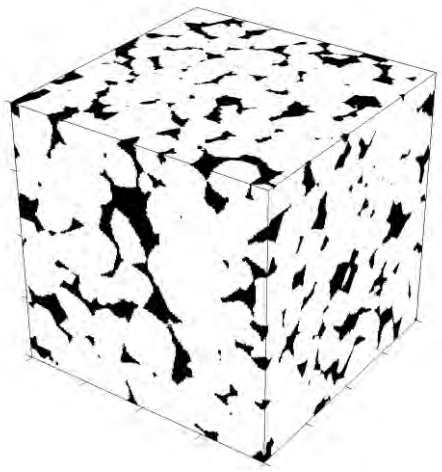

Figure 4.2: Fontainebleau sandstone digital sample (Andrä et al., 2013). Pores shown in black and rock frame mineral shown in white, with as size of 200×200×200 and a voxel edge length of 7.5 μm.

To illustrate this let's consider an example of a digital Fontainebleau sandstone sample (porosity 0.15; Andrä et al., 2013; shown in Figure 4.2). Assuming quartz frame, using the FEM, we numerically compute the following dry rock effective stiffnesses: $K_{ud}^{(1)} = 23.5$ GPa, $\mu_{ud}^{(1)} = 27$ GPa and $M_{ud}^{(1)} = 59.4$ GPa. We simulate dry pores by assuming zero stiffness of pore-filling material (i.e., K^{A1} = 0 GPa; μ^{A1} = 0 GPa). Next, using full Gassmann (equations 4.16 and 4.17), we can estimate the effective P-wave modulus

corresponding to brine-filled pores ($K^{A2} = 3$ GPa; $\mu^{A2} = 0$ GPa), which comes out to be $M_{ud}^{(2)} = 61.7$ GPa. Here we assume full Gassmann provides exact estimates. Similarly, we obtain predictions for $M_{ud}^{(2)}$ assuming $\Omega^{A} = 1$ (Mavko et al., 1995) and Ω^{A} for spherical inclusions in equation 4.19; these predictions are 62.3 GPa and 61.5 GPa, respectively. The disagreement between predictions of the change in P-wave modulus ($M_{ud}^{(2)} - M_{ud}^{(1)}$) between the full Gassmann and the two approximate methods is ~ 26 % ($\Omega^{A} = 1$) and 7 % (Ω^{A} for spherical inclusions). Next, we consider the *same* digital rock sample but digitally replace quartz with calcite as the frame solid and re-compute the dry rock effective stiffnesses to obtain $K_{ud}^{(1)} = 37.4$ GPa, $\mu_{ud}^{(1)} = 20.6$ GPa and $M_{ud}^{(1)} = 64.9$ GPa. For this case, the full Gassmann predicted brine-saturated P-wave modulus is $M_{ud}^{(2)} = 69.8$ GPa. Equation 4.19 with $\Omega^{A} = 1$ predicts $M_{ud}^{(2)} = 68.9$ GPa whereas equation 4.19 with Ω^{A} for spherical inclusions predicts $M_{ud}^{(2)} = 69.6$ GPa. The new error in predicting the change in P-wave modulus upon substitution by the two methods is 17 % and 3 %, respectively, which is significantly lower when compared to the error calculated for quartz frame case.

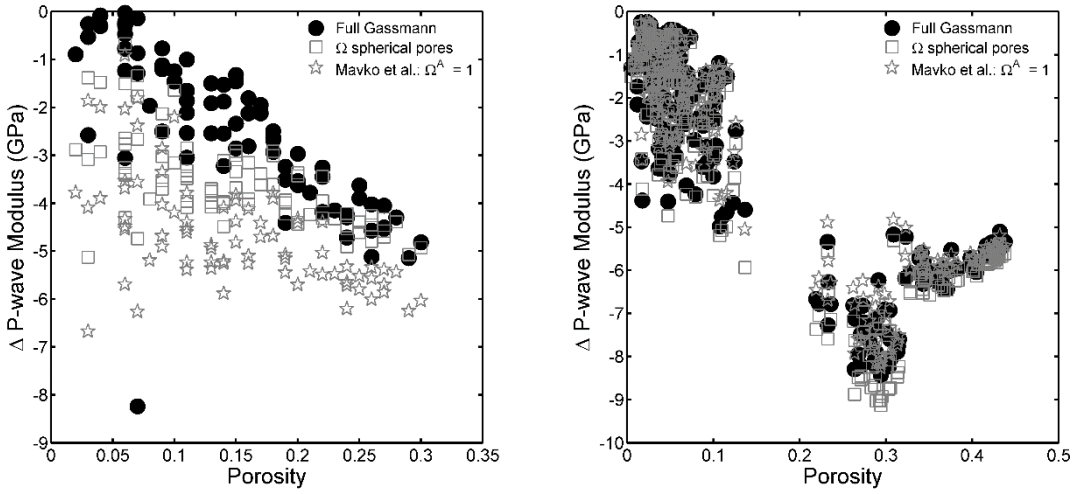

Figure 4.3: (a) Change in dry sandstone (data by Han, 1986) P-wave modulus upon fluid (water) substitution (initial dry rock - water saturated rock) as predicted by full Gassmann (in black circles), and the two approximate methods. (b) plot for carbonates (Vanorio et al., 2008).

Similar to numerical examples above, Figures 3a,b show P-wave modulus fluid substitution starting with laboratory measured dry sandstone (Han, 1986) and dry carbonate (Vanorio et al., 2008) data. In these plots, we compare the change in P-wave modulus upon substitution (dry rock P-wave modulus - brine-saturated rock P-wave modulus) as predicted by full Gassmann, equation 4.19 with $\Omega^A = 1$, and using equation 4.19 with approximate Ω^A for spherical inclusions. Both approximate methods work quite well for carbonates when compared to sandstones. For sandstones, predictions using equation 4.19 with Ω^A for spherical inclusions are much closer to full Gassmann when compared to predictions using Mavko et al. approximation (i.e., equation 4.19 with $\Omega^A = 1$). These examples again demonstrate that the approximate methods work better for rocks with higher Poisson's ratio frame mineral.

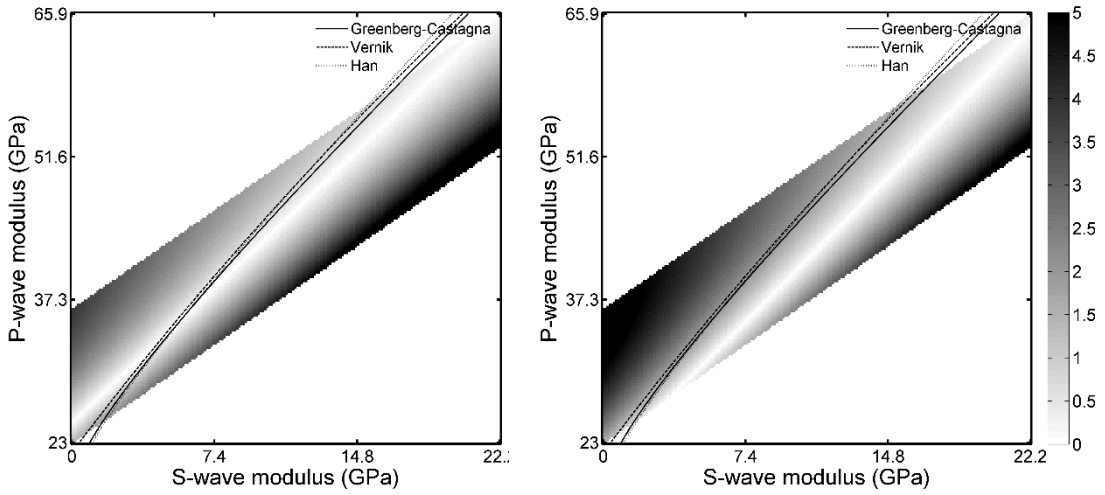

Figure 4.4: Hashin-Shtrkiman bounds for isotropic water-saturated sandstone of 20 % porosity. For all effective moduli combinations (P and S-wave), the increase in darkness indicates increasing difference in dry rock P-wave moduli (in GPa) as predicted by full Gassmann and the approximate P-wave modulus methods: (a) Ω^A for spheres (b) $\Omega^A = 1$.

The above numerical and laboratory examples sample limited P-wave and shear moduli combinations. For a general test of the approximate methods, in Figures 4a,b we show Hashin-Shtrkiman bounds (Hashin and Shtrikman, 1963) for water-saturated sandstones of

20% porosity ($\phi = 0.2$; $K^B = 36$ GPa; $\mu^B = 45$ GPa; $K^{A1} = 2.25$ GPa). These plots display all combinations of effective P-wave and shear moduli of water-saturated sandstones. Starting with these effective water-saturated moduli combinations we predict dry P-wave moduli, using full Gaassmann (using both effective P-wave and shear moduli) and approximate methods (using only effective P-wave modulus). The difference between predictions of full Gassmann and the approximate methods are shown in color on these plots (absolute values). We note that predictions using equation 4.19 with approximate Ω^A for spherical inclusions (shown in Figure 4.4a) generally are in better agreement with full Gassmann predictions as compared to assuming $\Omega^A = 1$ (Figure 4.4b). Also, the former method performs best for moduli combination consistent with known $V_P - V_S$ empirical curves for water-saturated sandstones (Castagna et al., 1993; Greenberg and Castagna, 1992; Vernik et al., 2002; Han, 1986; Mavko et al., 2009). Therefore, substitution using equation 4.19 with approximate Ω^A for spherical inclusions will be quite close to substitution predictions using full Gassmann with measured V_P and *predicted* V_S from the known empirical $V_P - V_S$ relations for sandstones.

4.7. Substitution recipe

4.7.1. Fluid substitution in rocks with interconnected pores

Start by estimating the initial P-wave modulus using the measured P-wave velocity $V_P^{(1)}$ and bulk density $\rho^{(1)}$

$$M_{ud}^{(1)} = \rho^{(1)}\left(V_P^{(1)}\right)^2 \quad . \tag{4.37}$$

Bulk density is related to rock mineral density ρ^B and intial pore-fluid density ρ^{A1} as

$$\rho^{(1)} = (1-\phi)\rho^B + \phi\rho^{A1} \quad . \tag{4.38}$$

Next, approximate the parameter Ω^{A} ($\mathrm{A} \equiv$ *A1* or *A2*) using the preferred effective media method by solving equations 4.32 and 4.33. This will typically require information on the inclusion aspect ratio. For stiff pores (i.e., aspect ratio > 0.2) saturated with relatively soft fluids (i.e., $K^{\mathrm{A}} << K^{B}$), instead of solving equations 4.32 and 4.33 with effective media models, we can simply approximate Ω^{A} as

$$\Omega^{\mathrm{A}} \approx \frac{4\left(\nu^{B}-0.5\right)}{\left(\nu^{B}-1.4\right)}\left(1-\phi/3\right) \quad . \tag{4.39}$$

Now estimate the fluid substituted effective P-wave modulus using

$$M_{ud}^{(2)} = M^{B} - \left(\frac{1}{M^{B}-M_{ud}^{(1)}} - \frac{K^{A1}-K^{A2}}{\phi\left(K^{B}-K^{A2}+\frac{4}{3}\Omega^{A2}\mu^{B}\right)\left(K^{B}-K^{A1}+\frac{4}{3}\Omega^{A1}\mu^{B}\right)} \right)^{-1} \quad . \tag{4.40}$$

Finally, obtain the new P-wave velocity as

$$V_{P}^{(1)} = \sqrt{\frac{M_{ud}^{(2)}}{\rho^{(2)}}} \quad , \tag{4.41}$$

where $\rho^{(2)}$ is the final bulk density related to final pore-fluid density ρ^{A2} as

$$\rho^{(2)} = \rho^{(1)} + \phi\left(\rho^{A2}-\rho^{A1}\right) \quad . \tag{4.42}$$

4.7.2. **Fluid or solid substitution in rocks with disconnected pores**

Follow the steps above except in place of equation 4.40 use equation 4.9 to obtain the substituted effective P-wave modulus. This substitution exercise will require knowledge of parameters δ_1 and δ_2' in addition to parameters Ω^{A1} and Ω^{A2}. The latter three parameters can be approximated using equations 4.31 to 4.33. If pore space compliance is heterogeneous, the parameters δ_1 will typically assume a value larger than 1.

4.8. Chapter summary

For arbitrary pore shape isotropic monomineralic rocks we derive fluid and solid substitution equations for effective P-wave modulus using reciprocity (equation 4.9). In its most general form this equation depend on usually unknown parameters, however these have a clear physical interpretation and mathematical description. Exact solution to these substitution parameters can be obtained for a single ellipsoidal inclusion embedded in an infinite matrix. In this paper, we explored the possibility of including the effects of inclusion interaction on these substitution parameters by using effective media approximations such as the self-consistent, differential effective medium, etc.

In the special case of fluid substitution in rocks with interconnected pores, only substitution parameters Ω^{A1} and Ω^{A2} are needed. The contribution of these parameters to the substitution equation is weighted by the Poisson's ratio of the frame solid (or mineral), such that a higher frame solid Poisson's ratio leads to substitution predictions which are less sensitive to obtaining accurate approximations to parameters Ω^{A1} and Ω^{A2}. This implies that P-wave modulus substitution (without initial shear modulus or velocity) can be performed with higher confidence for carbonates or limestones when compared to sandstones.

We find that if pore aspect ratio > 0.2, effective media model approximated parameters, Ω^{A1} and Ω^{A2}, are nearly constant and this value depends on elastic properties of rock constituents and porosity. In contrast, previously suggested heuristic approximation implicitly assumed $\Omega^{\mathrm{A}} = 1$ ($\mathrm{A} \equiv A1, A2$) for all cases. Also, we find that substitution predictions using approximate Ω^{A} for spherical pores provide better match with full Gassmann solution when compared to assuming $\Omega^{\mathrm{A}} = 1$; and also are consistent with substitution using full Gassmann with predicted V_S from known empirical $V_P - V_S$ relations. Therefore, we recommend the new fluid substitution recipe to predict the change in V_P when V_S is missing or is unreliable.

4.9. Acknowledgements

This work was supported by the Stanford Rock Physics and Borehole Geophysics (SRB) Project, and U.S. Department of Energy award DE-FE0001159. We thank T. Mukerji and J.P. Dvorkin for stimulating discussions.

4.10. Appendix A: Derivation of the main result

In this section, we will derive the exact P-wave modulus substitution equation relating the *initial* solid-filled effective P-wave modulus $M_{ud}^{(1)}$, of an isotropic monomineralic rock containing a pore-filling solid *A1* (bulk: K^{A1} and shear: μ^{A1}) and frame mineral solid *B* (bulk: K^B and shear: μ^B) to the *second* solid-filled P-wave modulus $M_{ud}^{(2)}$, of the same rock but containing pore-filling solid *A2* (bulk: K^{A2} and shear: μ^{A2}). Consider the following uniaxial displacement $\vec{u} = \left(u_1 , u_2 , u_3 \right)$ on the *outer surface* (denoted by Γ) of an isotropic composite sample

$$u_1^\Gamma = \xi x_1 \qquad \text{(A-1)}$$

$$u_2^\Gamma = u_3^\Gamma = 0 \quad \text{on} \quad \Gamma ,$$

where x_i are Cartesian coordinates (i = 1, 2, 3), u_i^Γ is displacement in the i^{th} direction, and ξ is constant. The spatially-variable stresses within solid *B* are given by σ_{ij}^B which are related to tractions T_i^B, as

$$T_i^B = \sigma_{ij}^B n_j \quad (i = 1, 2, 3) \quad , \qquad \text{(A-2)}$$

where n_j is the outward unit normal to any surface within *B*. Stresses σ_{ij}^B are related to strains ε_{ij}^B by Hooke's law:

$$\sigma_{ij}^{B} = K^{B}\varepsilon_{kk}^{B}\delta_{ij} + 2\mu^{B}\left(\varepsilon_{ij}^{B} - \frac{1}{3}\varepsilon_{kk}^{B}\delta_{ij}\right) \quad . \tag{A-3}$$

Strains ε_{ij}^{B} can be decomposed as

$$\varepsilon_{ij}^{B} = \frac{e^{B}}{3}\delta_{ij} + \gamma_{ij}^{B} \quad . \tag{A-4}$$

Let's suppose that the pores are filled with solid *A1* such that the induced stresses σ_{ij}^{A1} within solid *A1* are related to tractions T_i^{A1} as

$$T_i^{A1} = \sigma_{ij}^{A1} n_j \quad (i = 1, 2, 3) \quad . \tag{A-5}$$

Stresses in solid *A1* are related to strains ε_{ij}^{A1} by Hooke's law:

$$\sigma_{ij}^{A1} = K^{A1}\varepsilon_{kk}^{A1}\delta_{ij} + 2\mu^{A1}\left(\varepsilon_{ij}^{A1} - \frac{1}{3}\varepsilon_{kk}^{A1}\delta_{ij}\right) \quad . \tag{A-6}$$

If instead of solid *A1*, the pores are filled by solid *A2* then the corresponding equations A-5 and A-6 are

$$T_i^{A2} = \sigma_{ij}^{A2} n_j \quad (i = 1, 2, 3) \quad , \tag{A-7}$$

$$\sigma_{ij}^{A2} = K^{A2}\varepsilon_{kk}^{A2}\delta_{ij} + 2\mu^{A2}\left(\varepsilon_{ij}^{A2} - \frac{1}{3}\varepsilon_{kk}^{A2}\delta_{ij}\right) \quad . \tag{A-8}$$

As discussed in Saxena and Mavko (2014), we can write the difference ΔE_{12} in elastic energy stored in the two cases above as

$$\Delta E_{21} = \frac{1}{2}\left(M_{ud}^{(2)} - M_{ud}^{(1)}\right)\xi^2 V = \frac{1}{2}\int_{S_\phi}\left(T_i^{A2}u_i^{A1} - T_i^{A1}u_i^{A2}\right)dS_\phi \quad , \tag{A-9}$$

where $u_i^{A1,A2}$ are displacements at the pore boundaries in the *i*th direction. The surface integral is over the surface S_ϕ of pore boundaries, and *V* is total composite volume. Using

Gauss' divergence theorem and adopting volume average notation, equation A-9 can be rewritten in the following form

$$\left(M_{ud}^{(2)} - M_{ud}^{(1)}\right)\xi^2 \frac{1}{\phi} = \left(K^{A2} - K^{A1}\right)\overline{e^{A1}e^{A2}} + 2\left(\mu^{A2} - \mu^{A1}\right)\overline{\gamma_{ij}^{A1}\gamma_{ij}^{A2}} \quad , \tag{A-10}$$

where $\overline{\psi}$ is the pore volume average of any quantity ψ . Now if in equation A-10 we put solid *B* in place of pore-filling solid *A2*, then the composite for the second case becomes homogeneous and $M_{ud}^{(2)} = K^B + (4/3)\mu^B = M^B$.

$$\left(M^B - M_{ud}^{(1)}\right)\xi^2 \frac{1}{\phi} = \left(K^B - K^{A1}\right)\overline{e^{A1}e^B} + 2\left(\mu^B - \mu^{A1}\right)\overline{\gamma_{ij}^{A1}\gamma_{ij}^B} \quad , \tag{A-11}$$

which also guarantees $e^B = \xi$, $\gamma_{11}^B = 2\xi/3$ and $\gamma_{22}^B = \gamma_{33}^B = -\xi/3$ everywhere in the composite. Hence, equation A-11 reduces to

$$\left(M^B - M_{ud}^{(1)}\right)\xi \frac{1}{\phi} = \left(K^B - K^{A1}\right)\overline{e^{A1}} + \frac{2}{3}\left(\mu^B - \mu^{A1}\right)\left(\overline{2\gamma_{11}^{A1}} - \overline{\gamma_{22}^{A1}} - \overline{\gamma_{33}^{A1}}\right) \ . \tag{A-12}$$

For convenience we now define,

$$\Omega^{A1} = \frac{\gamma_{11}^{A1} - \frac{1}{2}\left(\overline{\gamma_{22}^{A1}} + \overline{\gamma_{33}^{A1}}\right)}{\overline{e^{A1}}} = \frac{3\overline{\varepsilon_{11}^{A1}}}{2\overline{e^{A1}}} - \frac{1}{2} \ . \tag{A-13}$$

Hence equation A-12 can be rewritten as

$$\left(M^B - M_{ud}^{(1)}\right)\xi \frac{1}{\phi} = \left(K^B - K^{A1}\right)\overline{e^{A1}} + \left(\mu^B - \mu^{A1}\right)\frac{4}{3}\Omega^{A1}\overline{e^{A1}} \ . \tag{A-14}$$

Similarly, if we replace pore-filling solid *A1* with solid *B* in equation 4.18 we get

$$\left(M^B - M_{ud}^{(2)}\right)\xi \frac{1}{\phi} = \left(K^B - K^{A2}\right)\overline{e^{A2}} + \left(\mu^B - \mu^{A2}\right)\frac{4}{3}\Omega^{A2}\overline{e^{A2}} \ . \tag{A-15}$$

Next, rearranging terms from equation A-10 we get

$$\xi^2 = \phi \frac{\left(K^{A2} - K^{A1}\right)\overline{e^{A1}e^{A2}} + 2\left(\mu^{A2} - \mu^{A1}\right)\overline{\gamma_{ij}^{A1}\gamma_{ij}^{A2}}}{\left(M_{ud}^{(2)} - M_{ud}^{(1)}\right)} \quad . \tag{A-16}$$

Multiplying equations A-14 and A-15 we get

$$\xi^2 = \frac{\phi\phi\left(\left(K^B - K^{A2}\right)\overline{e^{A2}} + \left(\mu^B - \mu^{A2}\right)\frac{4}{3}\Omega^{A2}\right)\left(\left(K^B - K^{A1}\right)\overline{e^{A1}} + \left(\mu^B - \mu^{A1}\right)\frac{4}{3}\Omega^{A1}\right)}{\left(M_{ud}^{(2)} - M^B\right)\left(M_{ud}^{(1)} - M^B\right)} \quad . \tag{A-17}$$

Equating equations A-16 and A-17 we obtain equation 4.9.

4.11. Appendix B: Parameters for a single inclusion

Eshelby (1957) showed that the strain ($\varepsilon_{ij}^{A1}, \varepsilon_{ij}^{A2}$) induced within a single ellipsoidal inclusion in an infinite isotropic matrix is homogeneous and is linearly related to constant strain ε_{ij}^0 applied at infinity as

$$\varepsilon_{ij}^{A1} = T_{ijkl}^{A1}\varepsilon_{kl}^0 \quad , \tag{B-1}$$

$$\varepsilon_{ij}^{A2} = T_{ijkl}^{A2}\varepsilon_{kl}^0 \quad ,$$

where tensor T^{A} (A ≡ *A1*, *A2*) is given by

$$T_{ijkl}^{\mathrm{A}} = \Sigma^{BA}\frac{\delta_{ij}\delta_{kl}}{3} + \Lambda^{BA}\left[\frac{1}{2}\left(\delta_{ik}\delta_{jl} + \delta_{il}\delta_{jk}\right) - \frac{\delta_{ij}\delta_{kl}}{3}\right] \quad . \tag{B-2}$$

When rock is deformed as per equation A-1, we have $\varepsilon_{11}^0 = \xi$ and $\varepsilon_{22}^0 = \varepsilon_{33}^0 = \varepsilon_{12}^0 = \varepsilon_{13}^0 = \varepsilon_{23}^0 = 0$, therefore equation B-1 reduces to

$$\varepsilon_{ij}^{A1} = T_{ij11}^{A1}\varepsilon_{11}^0 \quad , \tag{B-3}$$

$\varepsilon_{ij}^{A2} = T_{ij11}^{A2}\varepsilon_{11}^{0}$.

Moreover, since the induced strains within the inclusion are homogeneous, we readily obtain $\delta_1 = 1$. Solution of parameter δ_2' in equation 4.23 can be obtained by expanding and solving

$$\delta_2' = 2\frac{\overline{\gamma_{ij}^{A1}\gamma_{ij}^{A2}}}{\overline{e^{A1}}\,\overline{e^{A2}}} = 2\frac{\overline{\left(\varepsilon_{11}^{A1} - e^{A1}/3\right)\left(\varepsilon_{11}^{A2} - e^{A2}/3\right)}}{\overline{e^{A1}}\,\overline{e^{A2}}} + 2\frac{\overline{\left(\varepsilon_{22}^{A1} - e^{A1}/3\right)\left(\varepsilon_{22}^{A2} - e^{A2}/3\right)}}{\overline{e^{A1}}\,\overline{e^{A2}}} \ldots \qquad \text{(B-4)}$$

$$\ldots \quad 2\frac{\overline{\left(\varepsilon_{33}^{A1} - e^{A1}/3\right)\left(\varepsilon_{33}^{A2} - e^{A2}/3\right)}}{\overline{e^{A1}}\,\overline{e^{A2}}} + 4\frac{\overline{\varepsilon_{12}^{A1}\varepsilon_{12}^{A2}}}{\overline{e^{A1}}\,\overline{e^{A2}}} + 4\frac{\overline{\varepsilon_{31}^{A1}\varepsilon_{31}^{A2}}}{\overline{e^{A1}}\,\overline{e^{A2}}} + 4\frac{\overline{\varepsilon_{32}^{A1}\varepsilon_{32}^{A2}}}{\overline{e^{A1}}\,\overline{e^{A2}}} \quad .$$

Following the same procedure we obtain expressions for parameters Ω^{A1} and Ω^{A2} given in equations 4.24 and 4.25, respectively. Similarly, we can solve for parameters $\alpha_1, \alpha_2', \beta_1$ and β_2' (as defined in equations 4.2, 4.3, 4.7 and 4.8, respectively) using equations B-1 and B-2 under compressional and shear strains.

4.12. References

Andrä, H., N. Combaret, J. Dvorkin, E. Glatt, J. Han, M. Kabel, Y. Keehm, F. Krzikalla, M. Lee, C. Madonna, M. Marsh, T. Mukerji, E. H. Saenger, R. Sain, N. Saxena, S. Ricker, A. Wiegmann and X. Zhan, 2013, Digital rock physics benchmarks - Part I: Imaging and segmentation: Computers & Geosciences, **50**, 25-32.

Bachrach, R., J. Dvorkin, A. Nur., 1998, High-resolution shallow-seismic experiments in sand, Part II: Velocities in shallow unconsolidated sand: Geophysics, **63** (4), 1234-1240.

Berryman, J. G., 1980, Long-wavelength propagation in composite elastic media: Journal of the Acoustical Society of America, **68**, 1809–1831.

Berryman, J. G. , 1999, Origin of Gassmann's equations: Geophysics, **64**, 1627–1629.

Castagna, J. P., M. L. Batzle, and T. K. Kan, 1993, Rock physics: the link between rock properties and AVO response: in J. P. Castagna and M. M. Backus, Eds., Offset -

Dependent Reflectivity - Theory and Practice of AVO Analysis, Society of Exploration Geophysicists.

Cleary, M. P., I. W. Chen and S. M. Lee, 1980, Self-consistent techniques for heterogeneous media: ASCE Journal of Engineering Mechanics, **106**, 861-887.

Dvorkin, J., G. Mavko, and B. Gurevich, 2007, Fluid substitution in shaley sediment using effective porosity: Geophysics, 72 (3), O1-O8.

Eshelby, J. D., 1957, The determination of the elastic field of an ellipsoidal inclusion, and related problems: Proceedings of Royal Society London, A, 241, 376-396.

Gassmann, F., 1951, Über die Elastizität poröser Medien: Vierteljahrschrift der Naturforschenden Gessellschaft in Zürich, **96**, 1-23.

Greenberg, M.L., and J. P. Castagna, 1992, Shear-wave velocity estimtaion in porous rocks: theoretical formulation, preliminary verification and applications: Geophysical Prospecting, **40**, 195-209.

Han, G, 1986, Effects of porosity and clay content on acoustic properties of sandstones and unconsolidated sediments, PhD dissertation, Stanford University.

Han, G., and M. Batzle, 2004, Gassmann's equation and fluid-saturation effects on seismic velocities: Geophysics, **69**, 2, 398-405.

Kuster, G. T., and M. N. Toksöz, 1974, Velocity and attenuation of seismic waves in two phase media: Part I. theoretical formulations: Geophysics, **39**, 587-606.

Sengupta, M., G. Mavko, and T. Mukerji, 2003, Quantifying subresolution saturation scales from time-lapse seismic data: A reservoir monitoring case study: Geophysics, **68**:3, 803-814.

Mavko, G., C. Chan, and T. Mukerji, 1995, Fluid substitution: Estimating changes in Vp without knowing Vs: Geophysics, **60**, 1750–1755.

Mavko, G., T. Mukerji and J. Dvorkin, 2009, The Rock Physics Handbook: Cambridge University Press.

Norris, A. N., 1985, A differential scheme for the effective moduli of composites: Mechanics of Materials, **4**, 1-16.

O'Connell, R. J., B. Budiansky, 1974, Seismic velocities in dry and saturated cracked solids: Journal of Geophysical Research, **79**, 5412–5426.

Røgen, B., L. Gommesen, L. Fabricius, 2004, Methods of velocity prediction tested for North Sea chalk: a review of fluid substitution and Vs estimates: Journal of Petroleum Science and Engineering, **45**:1-2, 129-139.

Saxena, N., and G. Mavko, 2014, Exact equations for fluid and solid substitution: Geophysics, **79**, 3, L21-L32.

Torquato, S., 2001, Random heterogeneous materials: Microstructure and macroscopic properties: Springer.

Yan, F., and D. Han, 2010, Some consideration about fluid substitution without shear wave velocity: SEG Technical Program Expanded Abstracts, 2741-2745.

Vanorio, T., C. Scotallero, and G. Mavko, 2008, The effect of chemical and physical processes on the acoustic properties of carbonate rocks: The Leading Edge, **27**, 1040–1048.

Vernik, L., D. Fisher and S. Bahret, 2002, Estimation of net-to-gross from P and S impedance in deepwater turbidities: The Leading Edge, **21**, 380-387.

Wu, T. T., 1966, The effect of inclusion shape on the elastic moduli of a two-phase material: International Journal of Solids and Structures, **2**, 1-8.

Chapter 5

Fluid substitution in multimineralic rocks

5.1. Abstract

Brown and Korringa extended Gassmann's fluid substitution for bulk modulus to multimineralic rocks with interconnected pores; their strikingly simple yet general result requires two additional bulk stiffnesses - which despite mathematical elegance are less intuitive than those required for Gassmann. This creates a practical problem, so much so that even though virtually all rocks are multimineralic, in practice, Brown and Korringa's result is seldom used. Using reciprocity we revisit this substitution problem and obtain exact fluid substitution relation for bulk modulus, which much like Brown and Korringa, requires two additional bulk stiffnesses. Although, fundamentally identical to Brown and Korringa, our exact solution algebraically differs from Brown and Korringa's result, and

features two different additional bulk stiffnesses. This reformulation of Brown and Korringa's result leads to strict constraints/bounds on change in rock stiffness upon substitution; and a fluid substitution recipe which *significantly* improves on using Gassmann as a guess with Voigt-Ruess-Hill or Hashin-Shtrikman bound average of minerals in the rock frame.

5.2. Introduction

Gassmann's (1951) fluid substitution relations predict the change in effective rock stiffness upon change in saturating pore-fluid; these relations are frequently used to address a variety of problems in Geophysics, examples include fluid detection from seismic, fluid invasion correction for well log data, interpreting time-lapse seismic attributes, etc. Gassmann's equations are exact if rock frame is monomineralic (single mineral), initial and final pores are fully saturated with ideal elastic fluids, and load-induced pore-pressure under quasi-static deformation is homogeneous – a requirement satisfied by rocks with interconnected pores. Gassmann's equations can be written as

$$\frac{\left(\frac{1}{K_{ud}^{(1)}}-\frac{1}{K_{ud}^{(2)}}\right)}{\left(\frac{1}{K_{ud}^{(1)}}-\frac{1}{K^{B}}\right)\left(\frac{1}{K_{ud}^{(2)}}-\frac{1}{K^{B}}\right)}=\frac{\left(\frac{1}{K^{f1}}-\frac{1}{K^{f2}}\right)}{\phi_f\left(\frac{1}{K^{f1}}-\frac{1}{K^{B}}\right)\left(\frac{1}{K^{f2}}-\frac{1}{K^{B}}\right)}\quad , \tag{5.1}$$

and

$$\mu_{ud}^{(1)}=\mu_{ud}^{(2)}\quad , \tag{5.2}$$

where $K_{ud}^{(1)}$ and $K_{ud}^{(2)}$ are the initial and final (fluid substituted) undrained (saturated) bulk moduli, respectively; $\mu_{ud}^{(1)}$ and $\mu_{ud}^{(2)}$ are the initial and final (fluid substituted) effective shear moduli, respectively; K^{f1} and K^{f2} are bulk modulus of initial and final pore-fluid, respectively. K^{B} is the bulk modulus of the mineral in rock frame and ϕ_f is the volume fraction of interconnected pores (porosity). An important reason behind the popularity of

Gassmann's equations (5.1 and 5.2), is because all required inputs are usually known or measured.

Brown and Korringa (1975) extended Gassmann's bulk modulus equation to the case of multimineralic rock frame (of mixed mineralogy), thus generalizing equation 5.1 to obtain

$$\frac{\left(\frac{1}{K_{ud}^{(1)}}-\frac{1}{K_{ud}^{(2)}}\right)}{\left(\frac{1}{K_{ud}^{(1)}}-\frac{1}{K^{S}}\right)\left(\frac{1}{K_{ud}^{(2)}}-\frac{1}{K^{S}}\right)}=\frac{\left(\frac{1}{K^{f1}}-\frac{1}{K^{f2}}\right)}{\phi_m\left(\frac{1}{K^{f1}}-\frac{1}{K^{\phi S}}\right)\left(\frac{1}{K^{f2}}-\frac{1}{K^{\phi S}}\right)}\quad , \tag{5.3}$$

which contains two additional fluid-independent bulk moduli K^{S} and $K^{\phi S}$, defined as

$$\frac{1}{K^{S}}=-\frac{1}{V}\frac{\partial V}{\partial P_C}\bigg|_{P_D}\quad , \tag{5.4}$$

$$\frac{1}{K^{\phi S}}=-\frac{1}{V_f}\frac{\partial V_f}{\partial P_C}\bigg|_{P_D}\quad . \tag{5.5}$$

where V is the rock volume, V_f is the fluid-saturated pore volume (of fluids $f1$ or $f2$), P_C is the confining pressure, $P_D = P_C - P^f$ is the differential pressure and P^f is the pore pressure (fluid pressure in $f1$ or $f2$). Symbol $.\big|_P$ denotes that pressure P is held constant. Moduli K^{S} and $K^{\phi S}$ are related as (Mavko et al., 2009)

$$\frac{1}{K^{\phi S}}=\frac{1}{\phi_f K^{S}}-\frac{1-\phi_f}{\phi_f K^{mix}}\quad . \tag{5.6}$$

In equation 5.6, modulus K^{mix} is the *true* bulk modulus for the mineral mix and must satisfy Hashin-Shtrikman bounds (HS) (Hashin and Shtrikman, 1963). For monomineralic rocks, it is trivial to obtain $K^{S}=K^{\phi S}=K^{mix}=K^{B}$, thus we recover Gassmann's result in equation 5.1. For shear modulus, Brown and Korringa obtained the same result as Gassmann (equation 5.2), i.e., no change upon fluid substitution. More recently, Gassmann and Brown

and Korringa's relations have been generalized to rocks with solid filled rocks (Ciz and Shapiro, 2007; Chapter 2). But in this chapter, we focus only on the problem of fluid substitution in isotropic rocks with interconnected pores.

Brown and Korringa's exact solution is remarkably simple, especially for a theory that tackles mixed mineralogy of arbitrary mineral distribution, however, this result is difficult to use in practice since the required moduli K^S and $K^{\phi S}$ are (generally) neither trivially known nor easy to measure (Hart and Wang, 2010). In addition, approximations to these moduli are also not obvious. This is so since these capture an effective mechanical response of multiple minerals composing the rock frame. Moreover, in practice, information on mineral distribution is quite uncertain.

Therefore, a common alternative is to instead use Gassmann's equation as a guess with Voigt-Ruess-Hill (VRH) average or Hashin-Shtrikman bound average (HSA of the mineral mix (Mavko et al., 2009) as the modulus of an effective mineral in the rock frame, i.e., approximate $K^S \approx K^{\phi S} \approx K^B$. Several authors (Knackstedt et al., 2005; Ciz et al., 2008; Makarynska et al., 2007) have shown that such approximations although valid for spatially dispersed distribution of minerals, can induce large errors if either mineral distribution deviates from dispersed or the contrast between mineral phases becomes significant - for example, when soft clay occurs as a pore-lining phase in a sandstone. Mavko and Mukerji (2013) using effective media models along with analytical solutions for ideal shapes, discussed the applicability range of using Gassmann with VRH mineral average.

Quantifying the effects of combined uncertainty associated with both mineral distribution and their relative contrast on fluid substitution has clear practical implications. Therefore, in this chapter, we reformate Brown and Korringa's result, which leads to rigorous constraints on fluid substitution in multimineralic rocks. Exploring limiting solutions to the required parameters, we obtain three new approximations which describe the above discussed uncertainty. Also, when combined, these approximations lead to an approximation which provides significantly better predictions than using Gassmann's equation with VRH or HSA mineral average as a guess. In the limiting case of

monomineralic rock frame, all approximations discussed in this chapter, reduce to Gassmann's result in equation 5.1.

5.3. Reformulation of Brown-Korringa & main results

5.3.1. Derivation

Let the *outer surface* of an isotropic composite sample with N elastic phases be subjected to compressive surface tractions as

$$T = -Pn \ , \tag{5.7}$$

where n is the outward-pointing normal vector to the outer surface, and P is constant (confining pressure). Let the spatially variable stress induced in any phase q ($q = 1$ to N; of volume fraction ϕ_q) be given by σ_{ij}^q, which can be decomposed into isotropic and deviatoric parts as

$$\sigma_{ij}^q = -P^q \delta_{ij} + \tau_{ij}^q \ , \tag{5.8}$$

where P^q is the pressure (negative of mean stress, $-\sigma_{kk}^q / 3$), and τ_{ij}^q are deviatoric stresses. Here we use standard summation convention over repeated indices. Each phase q has bulk and shear moduli given by K^q and μ^q, respectively. Upon substitution, moduli of all but one of these phases change to K^{q2} and μ^{q2}; for convenience, we name the un-changing phase as B ($B \in q$). Now using Betti-Rayleigh reciprocity theorem (Hashin, 1962; Chapter 2), we can write the change in elastic energy (ΔE_{12}) upon substitution as

$$\Delta E_{12} = \left(\frac{1}{K_{ud}^{(1)}} - \frac{1}{K_{ud}^{(2)}} \right) (P)^2 = \sum_{\substack{q=1 \\ q \neq B}}^{N} \phi_q \left(\left(\frac{1}{K^{q1}} - \frac{1}{K^{q2}} \right) \overline{P^{q1} P^{q2}} + \frac{1}{2} \left(\frac{1}{\mu^{q1}} - \frac{1}{\mu^{q2}} \right) \overline{\tau_{ij}^{q1} \tau_{ij}^{q2}} \right) \ , \tag{5.9}$$

where $K_{ud}^{(1)}$ and $K_{ud}^{(2)}$ are initial and substituted effective bulk moduli, respectively; $\overline{\psi^q}$ is the volume average of any quantity ψ^q (over the volume of phase q). Now if in equation

5.9 we choose $K^{q2} = K^B$ and $\mu^{q2} = \mu^B$, then the composite upon substitution becomes homogeneous, i.e., $K_{ud}^{(2)} = K^B$ and

$$\left(\frac{1}{K_{ud}^{(1)}} - \frac{1}{K^B}\right)(P)^2 = \sum_{\substack{q=1 \\ q\neq B}}^{N} \phi_q \left(\left(\frac{1}{K^{q1}} - \frac{1}{K^B}\right)\overline{P^{q1}P^B} + \frac{1}{2}\left(\frac{1}{\mu^{q1}} - \frac{1}{\mu^B}\right)\overline{\tau_{ij}^{q1}\tau_{ij}^B} \right) \quad , \tag{5.10}$$

this also guarantees $P^B = P$ and $\tau_{ij}^B = 0$ everywhere in the second composite. Hence, equation 5.10 further reduces to

$$\left(\frac{1}{K_{ud}^{(1)}} - \frac{1}{K^B}\right)P = \sum_{\substack{q=1 \\ q\neq B}}^{N} \phi_q \left(\frac{1}{K^{q1}} - \frac{1}{K^B}\right)\overline{P^{q1}} \quad . \tag{5.11}$$

Similarly, if we choose $K^{q1} = K^B$ and $\mu^{q1} = \mu^B$ we get

$$\left(\frac{1}{K_{ud}^{(2)}} - \frac{1}{K^B}\right)P = \sum_{\substack{q=1 \\ q\neq B}}^{N} \phi_q \left(\frac{1}{K^{q2}} - \frac{1}{K^B}\right)\overline{P^{q2}} \quad . \tag{5.12}$$

Next, rearranging terms from equation 5.10 we get

$$(P)^2 = \sum_{\substack{q=1 \\ q\neq B}}^{N} \phi_q \left(\frac{\left(\frac{1}{K^{q1}} - \frac{1}{K^{q2}}\right)}{\left(\frac{1}{K_{ud}^{(1)}} - \frac{1}{K_{ud}^{(2)}}\right)}\overline{P^{q1}P^{q2}} + \frac{1}{2}\frac{\left(\frac{1}{\mu^{q1}} - \frac{1}{\mu^{q2}}\right)}{\left(\frac{1}{K_{ud}^{(1)}} - \frac{1}{K_{ud}^{(2)}}\right)}\overline{\tau_{ij}^{q1}\tau_{ij}^{q2}} \right) \quad . \tag{5.13}$$

Multiplying equations 5.11 and 5.12 we get

$$(P)^2 = \left(\sum_{\substack{q=1 \\ q\neq B}}^{N} \phi_q \frac{\left(\frac{1}{K^{q1}} - \frac{1}{K^B}\right)}{\left(\frac{1}{K_{ud}^{(1)}} - \frac{1}{K^B}\right)}\overline{P^{q1}} \right) \left(\sum_{\substack{q=1 \\ q\neq B}}^{N} \phi_q \frac{\left(\frac{1}{K^{q2}} - \frac{1}{K^B}\right)}{\left(\frac{1}{K_{ud}^{(2)}} - \frac{1}{K^B}\right)}\overline{P^{q2}} \right) \quad . \tag{5.14}$$

From equations 5.13 and 5.14, we obtain

$$\frac{\left(\frac{1}{K_{ud}^{(1)}}-\frac{1}{K_{ud}^{(2)}}\right)}{\left(\frac{1}{K_{ud}^{(1)}}-\frac{1}{K^{B}}\right)\left(\frac{1}{K_{ud}^{(2)}}-\frac{1}{K^{B}}\right)}=\frac{\sum_{\substack{q=1\\q\neq B}}^{N}\phi_q\left(\frac{1}{K^{q1}}-\frac{1}{K^{q2}}\right)\overline{P^{q1}P^{q2}}+\frac{1}{2}\sum_{\substack{q=1\\q\neq B}}^{N}\phi_q\left(\frac{1}{\mu^{q1}}-\frac{1}{\mu^{q2}}\right)\overline{\tau_{ij}^{q1}\tau_{ij}^{q2}}}{\left(\sum_{\substack{q=1\\q\neq B}}^{N}\phi_q\left(\frac{1}{K^{q1}}-\frac{1}{K^{B}}\right)\overline{P^{q1}}\right)\left(\sum_{\substack{q=1\\q\neq B}}^{N}\phi_q\left(\frac{1}{K^{q2}}-\frac{1}{K^{B}}\right)\overline{P^{q2}}\right)}. \tag{5.15}$$

Equation 5.15 is the *exact* substitution equation for effective bulk modulus for substitution of N-1 phases in a N phase composite. More details on equation 5.15 will be discussed elsewhere. In the special case of multimineralic isotropic rocks (composed of N phases) with fluid-saturated interconnected pores (denoted by phase $f1$), bulk modulus substitution equation 5.15, for substitution of *only* the fluid phase $f1$ with fluid phase $f2$, reduces to

$$\frac{\left(\frac{1}{K_{ud}^{(1)}}-\frac{1}{K_{ud}^{(2)}}\right)}{\left(\frac{1}{K_{ud}^{(1)}}-\frac{1}{K^{B}}\right)\left(\frac{1}{K_{ud}^{(2)}}-\frac{1}{K^{B}}\right)}=\frac{\left(\frac{1}{K^{f1}}-\frac{1}{K^{f2}}\right)}{\phi_f\left(\frac{1}{K^{f1}}-\frac{1}{K^{B}}+\frac{1}{K^{\Delta 1}}\right)\left(\frac{1}{K^{f2}}-\frac{1}{K^{B}}+\frac{1}{K^{\Delta 2}}\right)}, \tag{5.16}$$

where

$$\frac{1}{K^{\Delta 1}}=\sum_{\substack{q=1\\q\neq B,f}}^{N}\frac{\phi_q\overline{P^{q1}}}{\phi_f P^{f1}}\left(\frac{1}{K^{q}}-\frac{1}{K^{B}}\right)\quad,\frac{1}{K^{\Delta 2}}=\sum_{\substack{q=1\\q\neq B,f}}^{N}\frac{\phi_q\overline{P^{q2}}}{\phi_f P^{f2}}\left(\frac{1}{K^{q}}-\frac{1}{K^{B}}\right)\quad, \tag{5.17}$$

to obtain this result we used $\overline{P^{f1}P^{f2}}=\overline{P^{f1}}\;\overline{P^{f2}}$, since compression induced pore-pressure will be homogeneous under quasi-static conditions due to pore connectivity. Also we have dropped the volume averaging sign for pressure in fluid phases $f1$ and $f2$. Equations 5.15, 5.16 and 5.17 are the central results of this chapter. Equation 5.16 is fundamentally identical to Brown and Korringa's equation 5.3 which is also derived in Appendix A using the same principle of reciprocity (G. Mavko, personal communication).

Interestingly, if the mineral phases only vary in their shear moduli and the bulk moduli of all solid minerals are the same, i.e., rock frame is homogeneous in bulk modulus (say bulk modulus $K^q = K^B$), then, equation 5.16 further reduces to the original Gassmann (1951) bulk modulus relation in equation 5.1, and Brown and Korringa's moduli simply reduce to $K^S = K^{\phi S} = K^B$. This is true even if all minerals in the rock frame have different shear moduli; some can be *fluids* of bulk modulus K^B. Therefore, for this case, the original Gassmann's bulk modulus equation 5.1 is exact. This trivial case is not apparent from Brown and Korringa's result in equation 5.3.

5.3.2. **Approximations**

The only sets of unknowns in our exact result in equation 5.16 are parameters $\overline{P^q} / P^f$. In the absence of information on mineral distribution, these parameters must be approximated. Therefore, we will now analyze limiting values which should contain the true solution. The easiest solutions are to either invoke the iso-stress (i.e., $P^f = \overline{P^q}$) or the iso-strain (i.e., $P^f / K^f = \overline{P^q} / K^q$) condition in the exact result in equation 5.16. The iso-stress condition is satisfied when phase q is suspended in fluid phase f; for such cases the exact substitution equation is:

$$\frac{\left(\frac{1}{K_{ud}^{(1)}} - \frac{1}{K_{ud}^{(2)}}\right)}{\left(\frac{1}{K_{ud}^{(1)}} - \frac{1}{K^B}\right)\left(\frac{1}{K_{ud}^{(2)}} - \frac{1}{K^B}\right)} \approx$$

$$\frac{\left(\frac{1}{K^{f1}} - \frac{1}{K^{f2}}\right)}{\phi_f\left(\frac{1}{K^{f1}} - \frac{1}{K^B} + \sum_{\substack{q=1 \\ q\neq B,f}}^{N} \frac{\phi_q}{\phi_f}\left(\frac{1}{K^q} - \frac{1}{K^B}\right)\right)\left(\frac{1}{K^{f2}} - \frac{1}{K^B} + \sum_{\substack{q=1 \\ q\neq B,f}}^{N} \frac{\phi_q}{\phi_f}\left(\frac{1}{K^q} - \frac{1}{K^B}\right)\right)} . \qquad (5.18)$$

Similarly, if we invoke the iso-strain condition, the exact substitution equation reduces to

$$\frac{\left(\frac{1}{K_{ud}^{(1)}}-\frac{1}{K_{ud}^{(2)}}\right)}{\left(\frac{1}{K_{ud}^{(1)}}-\frac{1}{K^{B}}\right)\left(\frac{1}{K_{ud}^{(2)}}-\frac{1}{K^{B}}\right)} \approx$$

$$\frac{\left(\frac{1}{K^{f1}}-\frac{1}{K^{f2}}\right)}{\phi_f\left(\frac{1}{K^{f1}}-\frac{1}{K^{B}}+\sum_{\substack{q=1\\q\neq B,f}}^{N}\frac{\phi_q K^{q}}{\phi_f K^{f1}}\left(\frac{1}{K^{q}}-\frac{1}{K^{B}}\right)\right)\left(\frac{1}{K^{f2}}-\frac{1}{K^{B}}+\sum_{\substack{q=1\\q\neq B,m}}^{N}\frac{\phi_q K^{q}}{\phi_f K^{f2}}\left(\frac{1}{K^{q}}-\frac{1}{K^{B}}\right)\right)}. \tag{5.19}$$

Generally, since information of mineral distribution is unknown, exact results in equations 5.18 and 5.19 can be regarded as approximations if iso-stress and iso-strain conditions are not strictly satisfied. Thus, we refer to equations 5.18 and 5.19 as the *iso-stress* and *iso-strain* approximations, respectively; these are actually ***strict*** bounds on fluid substitution ***but only if*** initial and final pore-fluids (both) are either very soft or very stiff - which will be shown in the next section.

To obtain a more restrictive range of parameters $\overline{P^q}/P^f$ we now use Hashin-Shtrikman bounds (Hashin and Shtrikman, 1963). Assuming an isotropic mix of the fluid phase f and mineral phase q, such that this mix can be represented by a two-phase composite, using Hashin-Shtrikman bounds and equation 5.11 (for a two phase composite) we obtain the following inequalities

$$\frac{K^{q}\left(K_{fq-mix}^{HS+}-K^{f}\right)}{K^{f}\left(K^{q}-K_{fq-mix}^{HS+}\right)} \geq \frac{\phi_q\overline{P^q}}{\phi_f P^f} \geq \frac{K^{q}\left(K_{fq-mix}^{HS-}-K^{f}\right)}{K^{f}\left(K^{q}-K_{fq-mix}^{HS-}\right)}\ , \tag{5.20}$$

where, K_{fq-mix}^{HS+} and K_{fq-mix}^{HS-} are upper and lower Hashin-Shtrikman (HS) bounds on bulk modulus for a mix of phases q and f, respectively (HS bounds expressions are presented in Appendix B). Using this result for the lower HS bound, we obtain the following approximation

$$\frac{\left(\frac{1}{K_{ud}^{(1)}}-\frac{1}{K_{ud}^{(2)}}\right)}{\left(\frac{1}{K_{ud}^{(1)}}-\frac{1}{K^{B}}\right)\left(\frac{1}{K_{ud}^{(2)}}-\frac{1}{K^{B}}\right)}\approx$$

$$\frac{\left(\frac{1}{K^{f1}}-\frac{1}{K^{f2}}\right)}{\phi_f\left(\frac{1}{K^{f1}}-\frac{1}{K^{B}}+\sum_{\substack{q=1\\q\neq B,f}}^{N}\frac{\phi_q}{\phi_f}\left(\frac{1}{K^{q}}-\frac{1}{K^{B}}\right)\right)\left(\frac{1}{K^{f2}}-\frac{1}{K^{B}}+\sum_{\substack{q=1\\q\neq B,f}}^{N}\frac{\phi_q}{\phi_f}\left(\frac{1}{K^{q}}-\frac{1}{K^{B}}\right)\right)}\,, \qquad (5.21)$$

and using the upper HS bound we obtain

$$\frac{\left(\frac{1}{K_{ud}^{(1)}}-\frac{1}{K_{ud}^{(2)}}\right)}{\left(\frac{1}{K_{ud}^{(1)}}-\frac{1}{K^{B}}\right)\left(\frac{1}{K_{ud}^{(2)}}-\frac{1}{K^{B}}\right)}\approx\frac{\left(\frac{1}{K^{f1}}-\frac{1}{K^{f2}}\right)}{\phi_f\left(\frac{1}{K^{f1}}-\frac{1}{K^{B}}+\Pi^{(1)}\right)\left(\frac{1}{K^{f2}}-\frac{1}{K^{B}}+\Pi^{(2)}\right)}\,, \qquad (5.22)$$

where

$$\Pi^{(1)}=\sum_{\substack{q=1\\q\neq B,f}}^{N}\frac{\phi_q\left(K^{B}-K^{q}\right)\left(4\mu^{q}+3K^{f1}\right)}{\phi_f K^{f1}K^{B}\left(4\mu^{q}+3K^{q}\right)};\quad \Pi^{(2)}=\sum_{\substack{q=1\\q\neq B,f}}^{N}\frac{\phi_q\left(K^{B}-K^{q}\right)\left(4\mu^{q}+3K^{f1}\right)}{\phi_f K^{f2}K^{B}\left(4\mu^{q}+3K^{q}\right)}\,.$$

Note that the result in equation 5.21 is actually identical to the *iso-stress* approximation, which is no surprise since both cases assume phase *q* as a suspension in fluid phase *f*. For a three phase spherical shell composite, if phase *q* is the inner shell and fluid phase *f* is the inner sphere, then equation 5.22 is the exact substitution equation; we refer to it as the *HS+* approximation.

The range predicted by the *iso-stress* and *iso-strain* approximations describes the uncertainty associated with fluid substitution in multimineralic isotropic rocks when

mineral distribution within the rock frame is unknown. This range will be narrower if we instead choose to describe the range with *iso-stress* and *HS*+ approximations.

For rocks saturated with soft fluids, the *iso-stress* approximation will overestimate the true change upon fluid substitution, whereas the *iso-strain* and *HS*+ approximations will underestimate the true change; this will be justified in the next section. In the limiting case of monomineralic rocks, all of these approximations converge to Gassmann's equation.

As an example of the substitution range predicted by these approximations, consider a sandstone of 25 % porosity and dry rock bulk modulus of 15 GPa, say the mineral frame of this sandstone is composed of 50 % quartz (bulk modulus: 36 GPa; shear modulus: 45 GPa) and 50% clay (bulk modulus: 12 GPa; shear modulus: 10 GPa); such that the clay distribution within the rock frame is unknown. Using the *iso-stress* and *iso-strain* approximations, we predict brine (bulk modulus: 3 GPa) saturated bulk modulus of 18 GPa (assuming iso-stress) and 16 GPa (assuming iso-strain), respectively. Similarly, using the *iso-stress* and *HS*+ approximations, we predict a slightly tighter range of 16.6 - 18 GPa. Using Gassmann with the Voigt-Ruess-Hill mineral average, we obtain brine-saturated bulk modulus of 15.9 GPa, which is **outside** the range predicted by either set of approximations. Similarly, using Gassmann with the Hashin-Shtrikman bound mineral average, we obtain brine-saturated bulk modulus of 16 GPa, which is also **outside** our predicted range. Using Gassmann with the mineral modulus obtained from the upper HS bound of the mineral mix and again with the lower HS bound of the mix yields a range of 15.8 - 16.2 GPa, this range **is not contained** by the range predicted by the *iso-stress* and *HS*+ approximations.

5.4. Bounds on fluid substitution

Rigorous constraints on stiffnesses $K^{\Delta 1}$ and $K^{\Delta 2}$ (defined in equation 5.17) will lead to bounds on fluid substitution. For this analysis, from this point onwards, we assume that phase B is the ***stiffest*** phase in the composite which may or may not be the predominant phase, unless specified otherwise.

Hill's theorem states that the overall effective rock stiffness increases with increase in stiffness of any rock phase (Page 370 in Hill, 1963). A consequence of this theorem is that the confining pressure and volume averaged pressure in each phase must have the same sign. Therefore, stiffnesses $K^{\Delta 1}$ and $K^{\Delta 2}$ must be positive (negative) if phase B is the stiffest (softest) in the rock; which leads to a *strict upper* (lower) bound on the change in effective bulk modulus upon substitution in multimineralic rocks

$$\frac{\left|\frac{1}{K_{ud}^{(1)}}-\frac{1}{K_{ud}^{(2)}}\right|}{\left(\frac{1}{K_{ud}^{(1)}}-\frac{1}{K^{B}}\right)\left(\frac{1}{K_{ud}^{(2)}}-\frac{1}{K^{B}}\right)} \leq \frac{\left|\frac{1}{K^{f1}}-\frac{1}{K^{f2}}\right|}{\phi_f\left(\frac{1}{K^{f1}}-\frac{1}{K^{B}}\right)\left(\frac{1}{K^{f2}}-\frac{1}{K^{B}}\right)} \quad . \tag{5.23}$$

Equation 5.23 is identical to Gassmann's equation (if inequality sign is replaced with equality). This result proves that if mixed mineralogy is ignored and we use Gassmann's equation assuming the stiffest solid as the predominant frame mineral phase, i.e., idealize rock frame as monomineralic, then the predicted change in effective bulk modulus upon fluid substitution will *always overestimate* the *true* change. Result in equation 5.23 may seem sharp but baring cases where the rock frame is more or less homogeneous in bulk modulus; this strict bound is not very restrictive, which will be shown with examples later. Also note that if equation 5.23 is used as equality it can yield implausible predictions of effective bulk modulus for large contrast in initial and final pore fluids stiffness; this is so, since there may not be any physically realizable effective bulk modulus that can satisfy the forced equality.

5.4.1. **Stiff initial and final fluids**

In equation 5.11 (or 5.12), choosing iso-stress conditions, i.e., $\overline{P^q} = P^f = P$ we recover Reuss average for the effective bulk modulus. Hill (1963) proved that this choice of iso-stress condition results in the softest possible effective bulk modulus, therefore whatever the rock microstructure, the following inequality holds

$$\frac{P^f}{P}\left(\frac{1}{K^f}-\frac{1}{K^B}+\frac{1}{K^\Delta}\right)\le\frac{1}{K^f}-\frac{1}{K^B}+\sum_{\substack{q=1\\q\neq B,f}}^{N}\frac{\phi_q}{\phi_f}\left(\frac{1}{K^q}-\frac{1}{K^B}\right)\quad . \tag{5.24}$$

Similarly, if we invoke the iso-strain condition, i.e., $e=P/K_{ud}=e^f=P^f/K^f=\overline{P^q}/K^q=\overline{P^B}/K^B$, which yields the stiffest possible effective bulk modulus (Hill, 1963), we obtain the inequality

$$\frac{e^f}{e}\left(\frac{1}{K^f}-\frac{1}{K^B}+\frac{1}{K^\Delta}\right)\ge\frac{1}{K^f}-\frac{1}{K^B}+\sum_{\substack{q=1\\q\neq B,m}}^{N}\frac{\phi_q K^q}{\phi_f K^f}\left(\frac{1}{K^q}-\frac{1}{K^B}\right)\quad , \tag{5.25}$$

where, e is the volumetric strain in the composite and e^f is the volumetric strain in fluid phase *f*. Inequalities in equation 5.24 (or 5.25) feature unknown parameter P^f/P (or e^f/e). The parameter P^f/P is simply the Skempton's coefficient (Mavko et al., 2009); for isotropic multimineralic rocks with interconnected pores, Green and Wang (1986) obtained the following relation in terms of Brown and Korringa's moduli

$$\frac{P^f}{P}=\left(1+\phi_f\left(\frac{1}{K^f}-\frac{1}{K^{\phi S}}\right)\left(\frac{1}{K_{dry}}-\frac{1}{K^S}\right)^{-1}\right)^{-1}\quad , \tag{5.26}$$

where K_{dry} is the dry effective bulk modulus. Also equation 5.26 can be rewritten in terms of strains as

$$\frac{e^f}{e}=\frac{K_{ud}}{K^f}\left(1+\phi_f\left(\frac{1}{K^f}-\frac{1}{K^{\phi S}}\right)\left(\frac{1}{K_{dry}}-\frac{1}{K^S}\right)^{-1}\right)^{-1}\quad . \tag{5.27}$$

If $P^f/P\ge 1$, then from equation 5.27 we obtain

$$\frac{1}{K^\Delta}\le\sum_{\substack{q=1\\q\neq B,f}}^{N}\frac{\phi_q}{\phi_f}\left(\frac{1}{K^q}-\frac{1}{K^B}\right)\ . \tag{5.28}$$

Thus equations 5.16 and 5.28 describe a lower bound on the change in bulk modulus upon substitution (the *iso-stress* approximation in equation 5.18), valid if $P^f / P \geq 1$ (for rock with both initial and final pore-fluids). This condition can be achieved if both initial and final fluid phases are very stiff, i.e., $K^f > K^{\phi S}$. Clearly, this condition will be difficult to achieve for naturally occurring rocks since usually the fluid phase is much softer than mineral phases. However, it is known that $K^{\phi S}$ can take quite small values for rocks with compliant pore-lining clay, and sometimes even negative (Berge and Berryman, 1995). Similarly, if $e^f / e \leq 1$, then equation 5.25 leads to the following inequality

$$\frac{1}{K^{\Delta}} \geq \sum_{\substack{q=1 \\ q \neq B,f}}^{N} \frac{\phi_q K^q}{\phi_f K^f} \left(\frac{1}{K^q} - \frac{1}{K^B} \right) \quad . \tag{5.29}$$

Equations 5.16 and 5.29 describe an upper bound on the change in bulk modulus (the *iso-strain* approximation in equation 5.19), if $e^f / e \leq 1$; this condition can be achieved if both initial and fluid phases are quite stiff, i.e., $K^f > K_{ud} / \left(1 + \left(K_{ud}^{-1} - K_S^{-1}\right) / \left(K_{dry}^{-1} - K_{ud}^{-1}\right)\right)$.

5.4.2. **Soft initial and final fluids**

If both initial and final pore-fluids are very soft, i.e., $K^f \to 0^+$ then regardless of mineral distribution, $P^f << \overline{P^q}$ and $e^f >> \overline{e^q}$, which leads to the following inequalities

$$\frac{1}{K^{\Delta}} = \sum_{\substack{q=1 \\ q \neq B,f}}^{N} \frac{\phi_q \overline{P^q}}{\phi_f P^f} \left(\frac{1}{K^q} - \frac{1}{K^B} \right) \geq \sum_{\substack{q=1 \\ q \neq B,f}}^{N} \frac{\phi_q}{\phi_f} \left(\frac{1}{K^q} - \frac{1}{K^B} \right) \quad , \tag{5.30}$$

and

$$\frac{1}{K^{\Delta}} = \sum_{\substack{q=1 \\ q \neq B,f}}^{N} \frac{\phi_q \overline{P^q}}{\phi_f P^f} \left(\frac{1}{K^q} - \frac{1}{K^B} \right) \leq \sum_{\substack{q=1 \\ q \neq B,f}}^{N} \frac{\phi_q K^q}{\phi_f K^f} \left(\frac{1}{K^q} - \frac{1}{K^B} \right) \quad . \tag{5.31}$$

Therefore, the *iso-stress* and *iso-strain* approximations, for rocks with very soft initial and final fluids (i.e., $K^f \rightarrow 0^+$) will overestimate and underestimate the true change upon fluid substitution, respectively.

5.5. Examples and applications

In this section, using various theoretical and numerical examples, we will demonstrate the practical utility of the *iso-stress* approximation in equation 5.18, the *iso-strain* approximation in equation 5.19, the *HS+* approximation in equation 5.22, and the strict upper/lower bound on change in bulk modulus upon fluid substitution in equation 5.23.

As the first example, we discuss fluid substitution in a three phase spherical composite (shown in Figure 5.1). Exact closed form solutions to the effective bulk modulus of the three phase spherical composite are known, these are not repeated here since already published in Christensen (1991) or Mavko and Mukerji (2013).

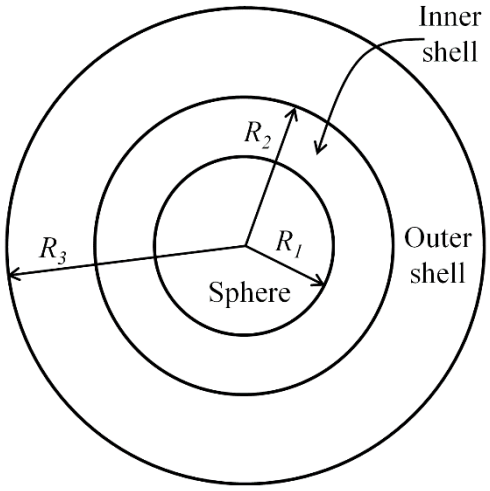

Figure 5.1: Three-phase spherical composite.

We consider the following geometric and elastic details: outer quartz shell of radius *R1* = 2.5 (elastic properties $K^B = 36$ GPa; $\mu^B = 45$ GPa), soft clay inner shell of radius *R2* =

2.3 (elastic properties $K^q = 5$ GPa; $\mu^q = 3$ GPa) and an empty inner sphere of radius *R3* = 1.8; this yields $\phi_f = 0.37$ and $\phi_q = 0.4$. For this case, we calculate $K_{dry} = 6.9$ GPa, and the following Brown and Korringa's moduli: $K^S = 16.1$ GPa and $K^{\phi S} = 91.4$ GPa.

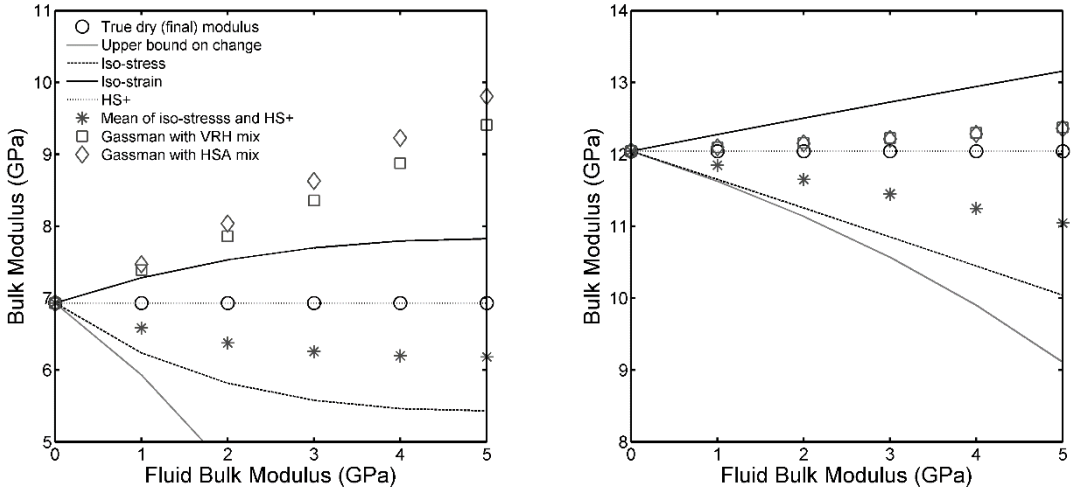

(a) (b)

Figure 5.2: Example of fluid substitution in the three-phase spherical composite shown in Figure 5.1: (a) soft clay (b) stiff clay. The true effective dry bulk modulus is shown in open black symbols. These plots show the predicted dry bulk moduli starting with the true fluid-saturated bulk moduli. The HS+ approximation provides exact predictions. The upper bound provides a rather unrestrictive range for the dry bulk modulus. The iso-stress and iso-strain approximations contain the true dry bulk modulus.

Using the *iso-stress*, *iso-strain* and *HS+* approximations, along with the upper bound in equation 5.23, we predict the dry bulk modulus (with empty inner sphere) starting with the *true* fluid-saturated bulk moduli calculated for a range of fluids filling the inner sphere (true, since calculated from the closed form solution), K^{f1} between 0 and 5 GPa. We compare these predictions with the analytically computed dry bulk modulus. These results are shown in Figure 5.2a. For such this composite, the *HS+* approximation is the exact equation for fluid substitution. Predictions of the *iso-stress* and *iso-strain* approximations contain the dry bulk modulus; these approximations overestimate and underestimate the true change in bulk modulus upon substitution, respectively. The range predicted by the *iso-stress* and *HS+* is much narrower, since for this case the *HS+* approximation is the

exact solution. We also compare the predictions using Gassmann's equation (equation 5.1) with Voigt-Ruess-Hill (VRH) mineral average of phases *B* and *q* - referred as "*Gassmann with VRH mix*"; these predictions fall outside the range predicted by the above approximations. Also compared are the predictions of Gassmann's equation with HS bound mineral average of phases *B* and *q* - referred as "*Gassmann with HSA mix*", these predictions are quite close to the predictions of *Gassmann with VRH mix*. Figure 5.2b shows the same example in Figure 5.2a but for stiff clay of $K^q = 21$ GPa and $\mu^q = 15$ GPa. For both cases, predictions of using the mean of the *iso-stress* and *HS+* approximations - referred as "*Mean of iso-stress and HS+*" improve on the prediction of *Gassmann with VRH mix* or *Gassmann with HSA mix*.

In the next few examples, we will compare model predictions with the finite element method (FEM) computed elastic moduli of digital sandstone rocks. The FEM computed moduli are assumed to be "exact" since the associated numerical error is found to be smaller than the symbols used for plotting.

Figure 5.3a shows a segmented 3D image of Fontainebleau sandstone sample (porosity $\phi_f = 0.15$; Andrä et al., 2013). The FEM was first carefully benchmarked with the monomineralic digital rock (in Figure 5.3a) by matching the fluid substitution computations with Gassmann's predictions. Next, the monomineralic rock frame which was mainly composed of quartz is digitally altered to replace some quartz parts with clay. We consider two cases: in the first case (shown in Figure 5.3b) we digitally replace a part of quartz with a pore-lining clay phase, and in the second case (Figure 5.3c) we randomly replace some quartz with clay to obtain a dispersed distribution of clay in the rock frame.

Using the FEM we calculate the dry and fluid-saturated effective bulk modulus for a range of fluid bulk moduli, between 0 and 5 GPa, such that the clay volume fraction is 0.27. We assume quartz bulk and shear moduli of 36 GPa and 45 GPa, respectively; and soft clay with bulk and shear moduli of 5 GPa and 3 GPa, respectively. Next, starting with the FEM calculated fluid-saturated bulk modulus we predict the dry rock effective bulk modulus using the methods discussed above. These calculations are shown in Figure 5.4.

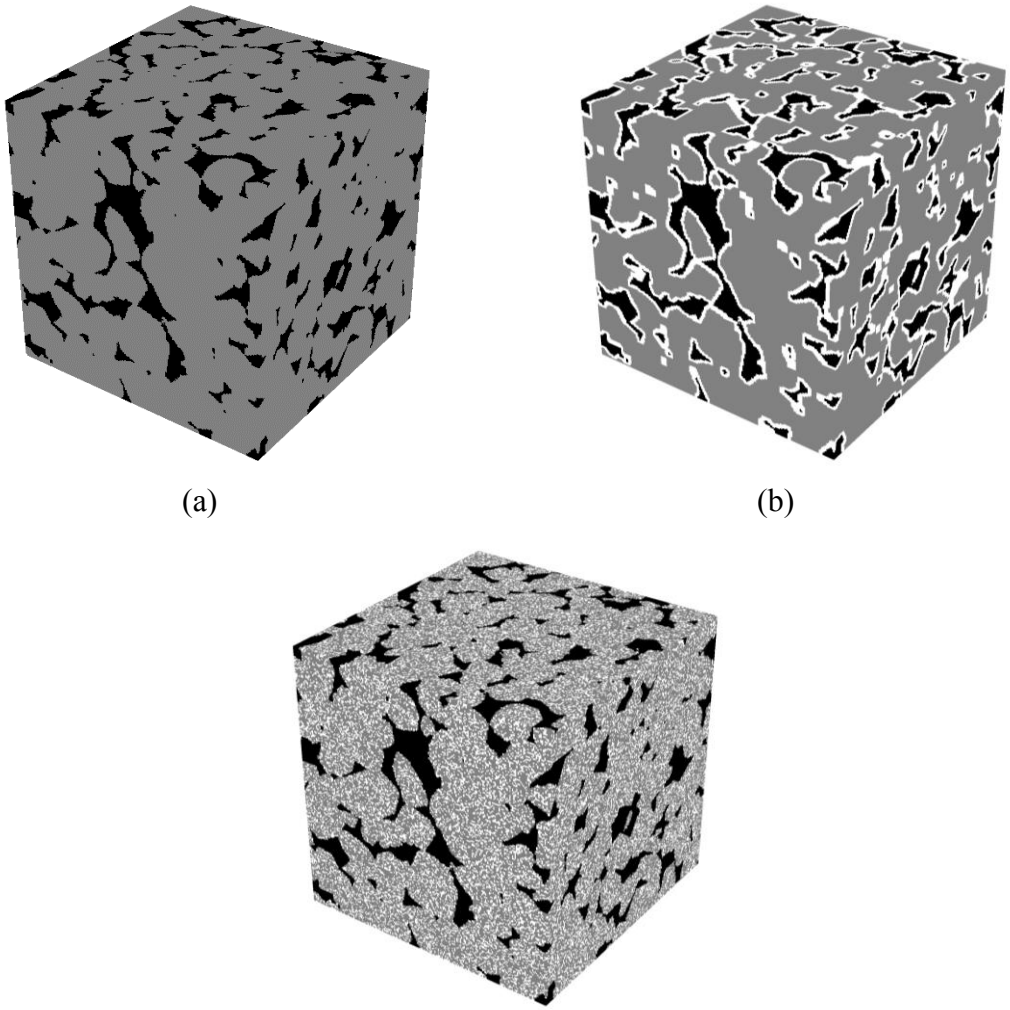

Figure 5.3: Digital Fontainebleau sandstone sample with fluid-saturated pores shown in black and quartz phase shown in gray. Digitally altered samples are shown in figures b, c and d; clay is shown in white. (b) clay occurs as a pore-lining phase (c) clay occurs as a dispersed phase in the rock frame. Both cases (b and c) have the same volume fractions of pores, clay and quartz.

In Figure 5.5, we perform the same modeling exercise as in Figure 5.4, but instead vary the soft clay mineral fraction keeping the initial fluid modulus fixed (water, of bulk modulus: 2.25 GPa). We note that the *iso-stress* and *iso-strain* approximations contain the FEM computed dry rock bulk modulus, but the range predicted by the *iso-stress* and *HS+* approximations is relatively narrower. Regardless of the mineral distribution, the predictions of *Gassmann with VRH mix* as well as *Gassmann with HSA mix* are quite off,

whereas predictions of *Mean of iso-stress and HS+* are significantly closer to the FEM calculated dry bulk modulus. Similarly, Figure 5.6 shows the same modeling exercise as in Figure 5.5, but in this plot we instead present the range of substituted moduli as predicted by various model combinations: the *iso-stress* and *HS+* approximations, the *iso-stress* and *iso-strain* approximations, using Gassmann once with Voigt bound on the mineral mix and again with Ruess bound on the mineral mix, and similarly using Gassmann with the HS lower and upper bound on the mineral mix. The range predicted by all model combinations contains the FEM computations. We note that the predicted range using Gassmann with either Voigt-Ruess or HS bounds is quite wide when compared to the range predicted using the *iso-stress* and *iso-strain* approximations; the *iso-stress* and *HS+* approximations further improve on this range.

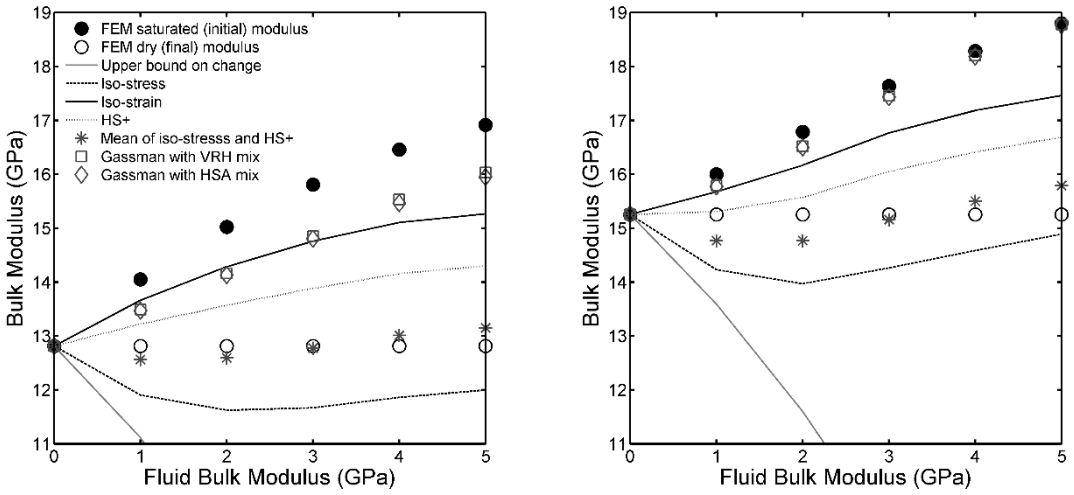

Figure 5.4: Example of fluid substitution in the digitally altered Fontainebleau sandstone sample shown in Figures 3b and 3c, for soft clay. FEM computed effective dry and fluid-saturated bulk moduli are shown in open and filled black symbols, respectively. Plots show the predicted dry bulk moduli starting with FEM computed fluid-saturated bulk moduli. Plots (a) and (b) show calculations for pore-lining and dispersed clay, respectively.

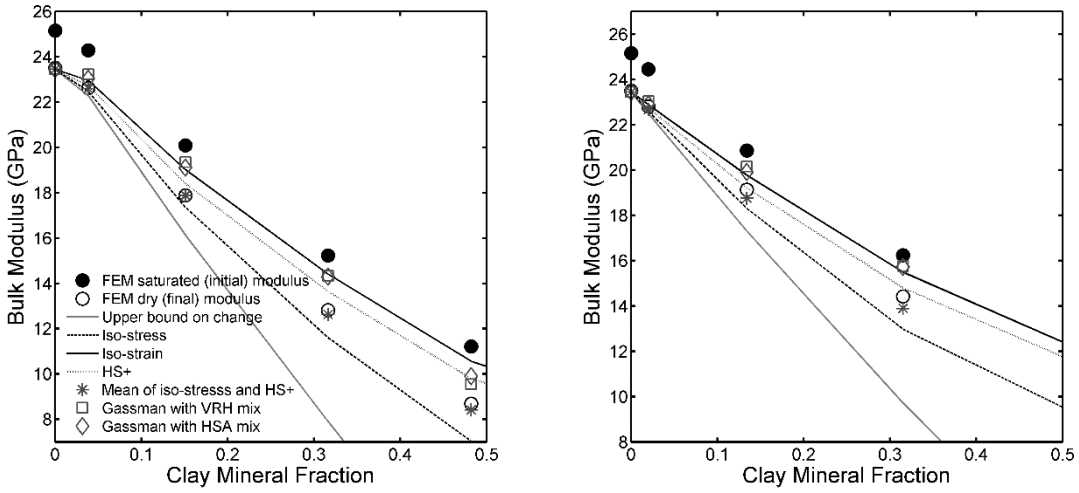

Figure 5.5: Fluid substitution in the digitally altered Fontainebleau sandstone sample: pore-lining soft clay (a) and dispersed soft clay (b). FEM computed effective dry and fluid-saturated bulk moduli are shown in open and filled black symbols, respectively. Plots show the predicted dry bulk moduli starting with FEM computed water-saturated bulk moduli, as a function of varying clay fraction in the mineral frame.

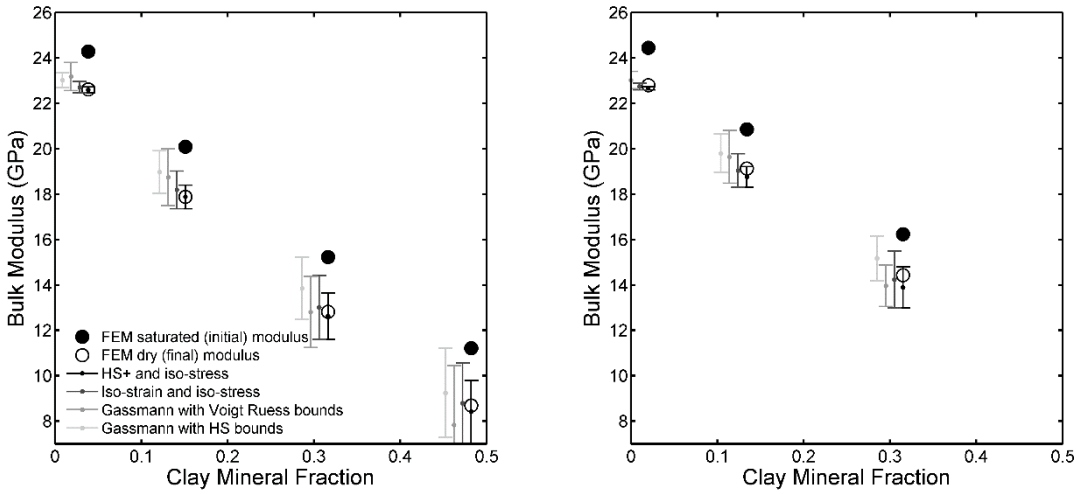

Figure 5.6: Range of predicted fluid substitution in the digitally altered Fontainebleau sandstone sample: pore-lining soft clay (a) and dispersed soft clay (b). Range predicted by various model combinations is shown, each range plot is slightly shifted horizontally for clarity.

Figures 5.7, 5.8 and 5.9 show the same calculations as in Figures 5.4, 5.5 and 5.6, respectively, but for a stiff clay of 21 GPa bulk modulus and 15 GPa shear modulus. For stiff clay the range predicted using any above method is relatively narrower than the

previous case of soft clay. Interestingly, the range predicted using Gassmann with either Voigt-Ruess or HS bounds is very narrow, but does ***not*** contain the FEM computations. The range predicted by the *iso-stress* and *iso-strain* approximations and the *iso-stress* and *HS+* approximations contains the FEM computations.

For all examples discussed above (stiff or soft clay) we note that the predictions of *Mean of iso-stress and HS+* generally fairs better than any other approximation.

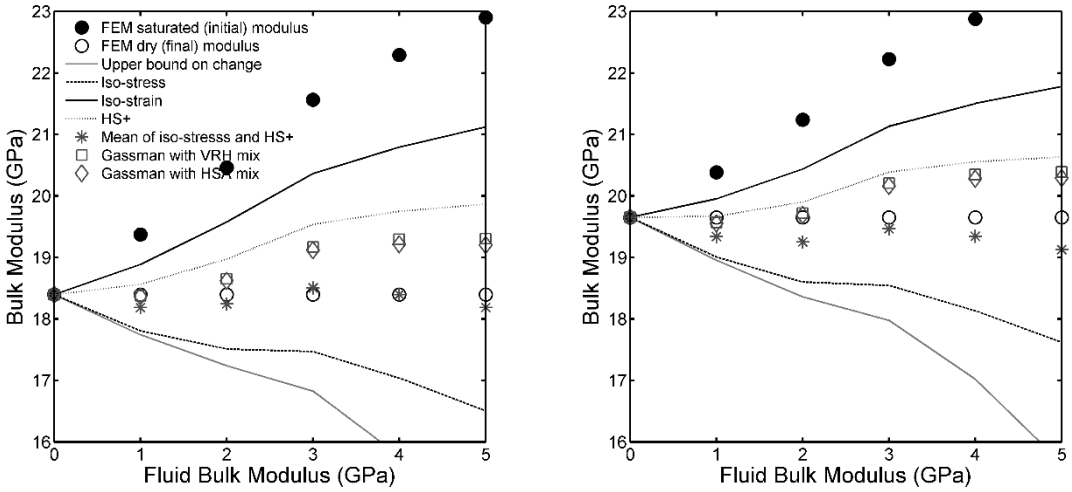

(a) (b)

Figure 5.7: Example of fluid substitution in the digitally altered Fontainebleau sandstone sample shown in Figures 3b and 3c, for stiff clay. FEM computed effective dry and fluid-saturated bulk moduli are shown in open and filled black symbols, respectively. Plots show the predicted dry bulk moduli starting with FEM computed fluid-saturated bulk moduli. Plots (a) and (b) show calculations for pore-lining and dispersed clay, respectively.

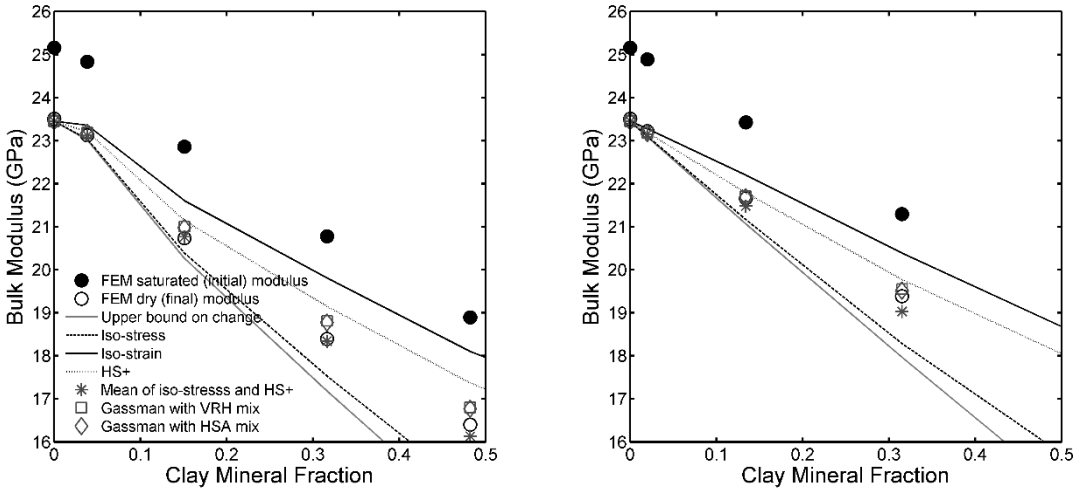

Figure 5.8: Fluid substitution in the digitally altered Fontainebleau sandstone sample: pore-lining stiff clay (a) and dispersed stiff clay (b). FEM computed effective dry and fluid-saturated bulk moduli are shown in open and filled black symbols, respectively. Plots show the predicted dry bulk moduli starting with FEM computed water-saturated bulk moduli, as a function of varying clay fraction in the mineral frame.

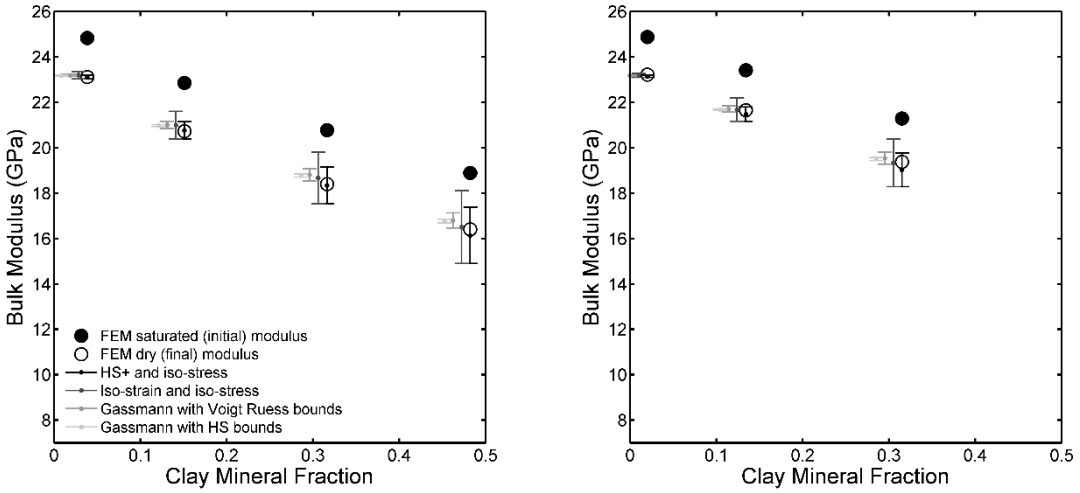

Figure 5.9: Range of predicted fluid substitution in the digitally altered Fontainebleau sandstone sample: pore-lining stiff clay (a) and dispersed stiff clay (b). Range predicted by various model combinations is shown, each range plot is slightly shifted horizontally for clarity.

5.6. Chapter summary

Equation 5.16 is the exact fluid substitution equation for bulk modulus in multimineralic isotropic rocks with interconnected pores. This equation is algebraically different yet fundamentally identical to Brown and Korringa's result. As in Brown and Korringa's bulk modulus equation, this new equation requires two additional moduli. However, unlike Brown and Korringa, the additional moduli in the new result explicitly depend on the ratio of bulk compression induced mean stresses (or pressure) in various rock phases, weighted by the respective phase volume fraction and the contrast in stiffness. This result proves that Gassmann's bulk modulus equation for fluid substitution is still *exact* for those multimineralic rocks for which the mineral phases only vary in their shear moduli and the bulk moduli of all minerals are the same, i.e., rock frame is homogeneous in bulk modulus. Similarly, the strict upper (lower) bound in equation 5.23 proves that if actual heterogeneous mixed mineralogy is ignored and Gassmann's equation is used assuming the stiffest (softest) solid as the predominant frame mineral phase, i.e., idealize rock frame as monomineralic, then the predicted change in effective bulk modulus upon fluid substitution will always overestimate (underestimate) the true change. This is regardless of mineral distribution.

We conclude that the new exact solution is easier to approximate (if needed) when compared to Brown and Korringa's result. For instance, the result in equation 5.16 leads to three new approximations in equations 5.18 (*iso-stress*), 5.19 (*iso-strain*) and 5.22 (*HS+*). The *iso-stress* and *iso-strain* approximations are proved to be strict bounds when initial and final pore-fluids are either very stiff or very soft. If the initial and final pore-fluids are very soft, then the predictions of *iso-stress* and *iso-strain* overestimate and underestimate the true change. The *HS+* approximation in equation 5.22 is exact for a three phase spherical composite; this approximation along with the *iso-stress* approximation provides a narrower range on bulk modulus upon fluid substitution when compared to that predicted by the *iso-stress* and *iso-strain* approximations. These approximations describe the uncertainty associated with not knowing the mineral distribution in the rock frame.

With the aid of several theoretical and numerical examples, we have shown that the mean of *iso-stress* and *HS+* approximations yields useful predictions (i.e., close to the true solution) for predicting the change in rock bulk modulus upon fluid substitution. For the examples studied in the chapter, this method provides significantly better predictions when compared to the predictions of using Gassmann with Voigt-Ruess-Hill or Hashin-Shtrikman bound average of minerals in the rock frame. Therefore, we propose using this approximation when information on mineral distribution in the rock frame is not available. However, if information on mineral distribution is available, geometry specific approximations may still yield better predictions.

5.7. Acknowledgements

We are grateful to Prof. Boris Gurevich for his comments and suggestions. This work was supported by the Stanford Rock Physics and Borehole Geophysics (SRB) Project, and U.S. Department of Energy award DE-FE0001159.

5.8. Appendix A: Derivation of Brown and Korringa

Consider experiments *A*, *B*, and *C* applied to a rock with total volume V and pore volume $V_f = \phi_f V$ as shown in Figure 5.A-1. Increments of confining pressure P_C and pore pressure P_f are applied in various combinations. For convince, we define an additional constant $K^{\phi\phi}$ which describes the dry rock pore space bulk modulus as

$$\frac{1}{K^{\phi\phi}} = -\frac{1}{V_f}\frac{\partial V_f}{\partial P_C}\bigg|_{P^f} \quad . \tag{A-1}$$

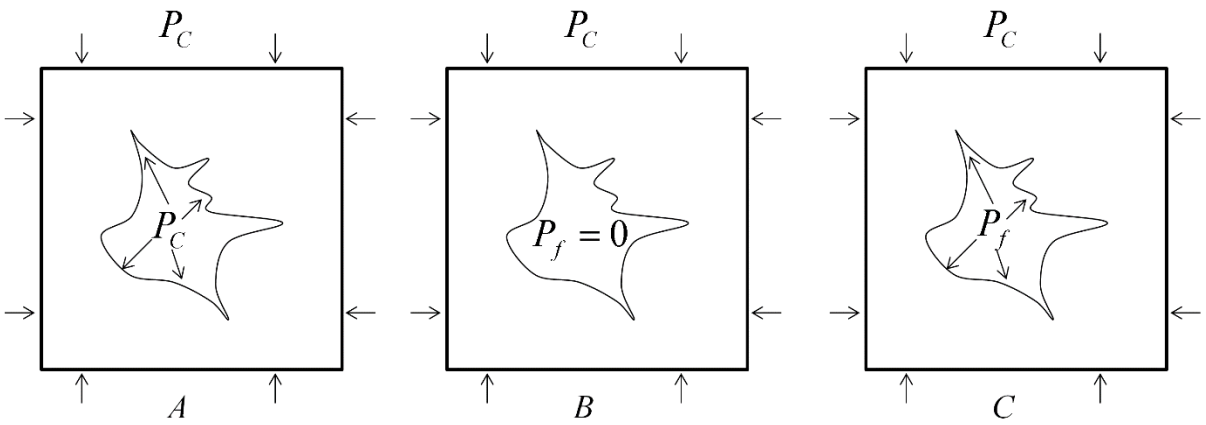

Figure 5.A-1: Three stress experiments applied to the same rock sample, for use in the Betti-Rayleigh reciprocity theorem.

Experiment *A* (Figure 5.A-1) has uniform confining pressure $P_C = P$ applied to all surfaces inside and outside the rock. In this case the overall volume of the rock sample shrinks as the minerals become elastically compressed by the applied pressure. Experiment *B* has the same confining pressure $P_C = P$ applied only to the outside surfaces of the rock. The pore surfaces are stress free. In this case the outside surfaces of the sample deform according to the effective *dry rock* bulk modulus, K_{dry}. Experiment *C* has the confining pressure $P_C = P$ applied to the outside surfaces of the sample, while the induced pore pressure increment P^f of the saturated rock is applied internally to the pore surfaces. In this case the outside surfaces deform according to the effective *saturated* or *un-drained* rock bulk modulus K_{ud}. Applying the reciprocity theorem to experiments *A* and *B* (Figure 5.A-1), we can write

$$-P\Delta V_{dry} + P\Delta V_{f-dry} = -P\Delta V_S \quad , \tag{A-2}$$

we can rewrite equation A-2 as

$$PPV / K_{dry} - PPV_f / K^{\phi\phi} = PPV / K^S \quad , \tag{A-3}$$

dividing through by $P^2 V$ gives

$$\frac{1}{K_{dry}} - \frac{\phi_f}{K^{\phi\phi}} = \frac{1}{K^S} \quad . \tag{A-4}$$

Similarly, applying the reciprocity theorem to experiments *B* and *C*, we can write

$$\frac{1}{K_{dry}} - \frac{\phi_f}{K^{\phi\phi}} \frac{P^f}{P} = \frac{1}{K_{ud}} \quad , \tag{A-5}$$

where P^f / P is the ratio of pore pressure induced in the pore space to the applied external confining pressure. The saturated pore volume change can be related to the pore pressure increment using the fluid bulk modulus:

$$\frac{\Delta V_{f-sat}}{V_f} = -\frac{P^f}{K^f} \quad . \tag{A-6}$$

Similarly, applying reciprocity theorem to experiments *A* and *C*, we can write

$$\frac{1}{K_{ud}} - \frac{1}{K^S} = \frac{\phi P^f}{P} \left(\frac{1}{K^f} - \frac{1}{K^{\phi S}} \right) \quad . \tag{A-7}$$

Combining equations A-4, A-5 and A-7 gives

$$\left(\frac{1}{K_{dry}} - \frac{1}{K_{ud}} \right) \left(\left(\frac{1}{K_{ud}} - \frac{1}{K^S} \right) \left(\frac{1}{K_{dry}} - \frac{1}{K^S} \right) \right)^{-1} = \left(\phi_f \left(\frac{1}{K^f} - \frac{1}{K^{\phi S}} \right) \right)^{-1} \quad , \tag{A-8}$$

replacing the dry modulus in equation A-8 we obtain Brown and Korringa's fluid substitution equation 5.3.

5.9. Appendix B: Hashin-Shtrikman bounds

The expressions for HS bounds on elastic bulk and shear moduli of an isotropic two-phase composite are given by

$$K^{HS+/-} = K^{(1)} + \frac{f_2}{\left(K^{(2)} - K^{(1)}\right)^{-1} + f_1\left(K^{(1)} + \frac{4}{3}\mu^{(1)}\right)^{-1}} \quad , \tag{B-1}$$

$$\mu^{HS+/-} = \mu^{(1)} + \frac{f_2}{\left(\mu^{(2)} - \mu^{(1)}\right)^{-1} + f_1\left(\mu^{(1)} + \frac{\mu^{(1)}}{6}\frac{9K^{(1)} + 8\mu^{(1)}}{K^{(1)} + 2\mu^{(1)}}\right)^{-1}} \quad , \tag{B-2}$$

where the superscripts (1) and (2) refer to the properties of the two phases. Equations B-1 and B-2 yield the upper bound when $K^{(1)}$ and $\mu^{(1)}$ are the *maximum* bulk and shear moduli of the individual phases, and the lower bounds when $K^{(1)}$ and $\mu^{(1)}$ are the *minimum* bulk and shear moduli of the phases.

5.10. References

Andrä, H., N. Combaret, J. Dvorkin, E. Glatt, J. Han, M. Kabel, Y. Keehm, F. Krzkilla, M. Lee, C. Madonna, M. Marsh, T. Mukerji, E. H. Saenger, R. Sain, N. Saxena, S. Ricker, A. Wiegmann and X. Zhan, 2013, Digital rock physics benchmarks - Part I: Imaging and segmentation: Computers & Geosciences, 50, 25-32.

Berge, P. A., and J. G. Berryman, 1995, Realizability of negative pore compressibility in poroelastic composites: Journal of Applied Mechanics and Technical Physics, 62, 1053–1062.

Brown, R., and J. Korringa, 1975, On the dependence of the elastic properties of a porous rock on the compressibility of the pore fluid: Geophysics, 40, 608–616.

Christensen, R. M., 1991, Mechanics of composite materials: Robert E. Krieger Publication Co.

Ciz, R., A. F. Siggins, B. Gurevich, and J. Dvorkin, 2008, Influence of microheterogeneity on effective stress properties of rocks: Geophysics, 73, no. 1, E7–E14.

Ciz, R., and S. A. Shapiro, 2007, Generalization of Gassmann equations for porous media saturated with a solid material: Geophysics, 72, A75–A79.

Gassmann, F., 1951, Über die Elastizität poröser Medien: Vierteljahrschrift der Naturforschenden Gessellschaft in Zürich, 96, 1-23.

Green, D. H., and H. F. Wang, 1986, Fluid pressure response to undrained compression in saturated sedimentary rocks: Geophysics, 51, 948–956.

Hashin, Z., 1962, The elastic moduli of heterogeneous materials, Journal of Applied Mechanics, 29, 143-150.

Hashin, Z., and S. Shtrikman, 1963, A variational approach to the elastic behavior of multiphase materials: Journal of the Mechanics and Physics of Solids, 11, 127–140.

Hart, D. J., and H. F. Wang, 2010, Variation of unjacketed pore compressibility using Gassmann's equation and an overdetermined set of volumetric poroelastic measurements: Geophysics, 75, no. 1, N9–N18.

Hill, R., 1963, Elastic properties of reinforced solids: some theoretical principles: Journal of the Mechanics and Physics of Solids, 11, 357-372.

Knackstedt, M. A., C. H. Arns, and W. Val Pinczewski, 2005, Velocity-porosity relationships: Predictive velocity model for cemented sands composed of multiple mineral phases: Geophysical Prospecting, 53, 349–372.

Makarynska, D., G. Gurevich, and R. Ciz, 2007, Finite element modeling of Gassmann fluid substitution of heterogeneous rocks: 69th Annual International Conference and Exhibition, EAGE, Extended Abstracts, 2152.

Mavko, G., T. Mukerji, and J. Dvorkin, 2009, The Rock physics handbook: Cambridge University Press.

Mavko, G., and T. Mukerji, 2013, Estimating Brown-Korringa constants for fluid substitution in multimineralic rocks: Geophysics, 78, no. 3, L27-L35.

Chapter 6

Embedded bounds on fluid and solid substitution

6.1. Abstract

Fluid and solid substitution of bulk and shear moduli are exact and unique for materials whose elastic bulk and/or shear moduli fall on the Hashin-Shtrikman bounds. For materials whose moduli lie between the bounds, solid and fluid substitution of bulk moduli can be computed *exactly*, but not *uniquely*. Every initial bulk modulus can be realized with an infinite number of microstructures and therefore transforms to an infinite number of moduli upon substitution of the pore fill. This non-uniqueness arises when detailed information on the material pore geometry is not available. We present four embedded-bound constructions for fluid and solid substitution that are based on realizable materials. In the limiting case of pore fluids, for bulk modulus, two of these constructions reduce to the

Published in GEOPHYSICS: Vol 78 (5)

bounds of Gibiansky and Torquato, which illustrates that those bounds are optimum. For solids, the first two constructions correspond to a homogeneous pore stiffness and predict the smallest change in modulus. The third construction prediction corresponds to a pore space with heterogeneous stiffness, and predicts much larger change in modulus.

6.2. Introduction

Predicting the change of rock elastic properties upon substitution of the pore-filling material is one of the most fundamental problems in rock physics. Gassmann (1951) derived expressions for the change in rock effective elastic moduli when the pore-filling materials are *ideal fluids*. His results are stunningly simple and general under the assumptions that the empty frame of the rock is linear elastic, the solid phase (mineral) is homogeneous, the pore-filling material has the same load-induced pressure everywhere, and the shear stress within the fluid is everywhere zero.

Although Gassmann's results apply to arbitrary anisotropy, we limit the discussion in this paper to the isotropic case, where the bulk modulus, K, and shear modulus, G, completely describe the rock's elasticity. In this case, Gassmann predicts

$$\frac{K_{sat}}{K_{min}-K_{sat}} = \frac{K_{dry}}{K_{min}-K_{dry}} + \frac{K_f}{\phi\left(K_{min}-K_f\right)} \quad , \tag{6.1}$$

$$G_{sat} = G_{dry} \quad , \tag{6.2}$$

where K_{dry} is the dry ("drained") rock effective bulk modulus, K_{sat} is the bulk modulus of the rock when fully saturated ("jacketed") with an ideal fluid, K_{min} is the elastic bulk modulus of the mineral, K_f is the bulk modulus of the pore fluid, and ϕ is the porosity. In equation 6.2, G_{sat} and G_{dry} are the effective shear moduli of the saturated and dry rock, which are predicted to remain unchanged with substitution of the pore fluid. (Brown and Korringa, 1975, extended Gassmann's derivation to the case of heterogeneous, though still linear elastic, mineralogy.)

The utility and simplicity of Gassmann's result comes from its dependence on only a single average stiffness parameter of the dry pore space, K_ϕ, defined as

$$\frac{1}{K_\phi} = \frac{1}{\bar{v}_\phi} \frac{\partial \bar{v}_\phi}{\partial P_c}\bigg|_{P_p} \quad , \tag{6.3}$$

where $\bar{v}_\phi$ is the total pore space volume, P_c is the confining pressure, and P_p is the pore pressure. The pore stiffness, K_ϕ, can be determined, for example, from dry rock measurements:

$$\frac{1}{K_\phi} = \frac{1}{\phi}\left(\frac{1}{K_{dry}} - \frac{1}{K_{\min}}\right). \tag{6.4}$$

In terms of K_ϕ, one can rewrite equation 6.1 as

$$\frac{1}{K_{sat}} = \frac{1}{K_{min}} + \frac{\phi}{K_\phi + F} \quad ; \quad F = \frac{K_f K_{min}}{K_{min} - K_f} \approx K_f \quad . \tag{6.5}$$

An infinite number of connected pore microstructures exist that share the same K_{min}, K_{dry}, K_ϕ, and ϕ. Each will have exactly the same Gassmann-predicted response to pore-fluid change. The same *cannot* be said if the pores become filled with solids or viscoelastic materials, or if the pore space becomes disconnected.

Solid substitution, rather than fluid substitution, applies, for example, when predicting how elastic moduli of heavy oil reservoirs change with saturation or upon heating or steam injection. Solid substitution is also necessary to model plugging of pore space with cement or salt or removal of minerals during the formation of secondary porosity. Solid substitution takes place during alteration of feldspar to clay, or when comparing clean pore space with clay-filled pores. Equations for solid substitution also allow predictions of changes in viscoelastic pore-filling materials, by virtue of the viscoelastic correspondence principle.

In this paper, we present techniques for computing the change in effective bulk modulus of a rock upon substituting solids, liquids, or viscoelastic materials in the pore

space. The approach is based upon recursive use of the Hashin-Shtrikman (1963) bounds for two-phase materials, which guarantees that the results are physically realizable. We reproduce the known result (Kanter and Bergman, 1984; Berryman and Milton, 1988) that the rock response to changes in (solid or fluid) pore fill is non-unique. The "embedded-bound" method reduces to the upper and lower bounds for fluid substitution developed by Gibianski and Torquato (2000), illustrating that those bounds are optimum. Changes in the effective bulk modulus are smallest when the pore space is stiff and homogeneous, and largest when the pore space is heterogeneous, including cracks.

In this paper, we generalize the term "porosity" to mean the volume fraction of rock that is being substituted. When substituting one pore fluid for another, porosity has its usual meaning; when the pore space is completely filled with a mineral, we still refer to that volume fraction as porosity.

We present here results only for the effective bulk modulus. Results for shear modulus will be presented in the future.

6.3. Substitution on the bounds

Hashin and Shtrikman (1963) and Walpole (1966) found expressions for bounds on the elastic bulk and shear moduli of an isotropic two-phase composite:

$$K^{HS+/-} = K_1 + \frac{f_2}{(K_2 - K_1)^{-1} + f_1\left(K_1 + \frac{4}{3}G_m\right)^{-1}} \quad , \tag{6.8}$$

$$G^{HS+/-} = G_1 + \frac{f_2}{(G_2 - G_1)^{-1} + f_1\left(G_1 + \frac{G_m}{6}\frac{9K_m + 8G_m}{K_m + 2G_m}\right)^{-1}} \quad , \tag{6.9}$$

where the subscripts 1 and 2 refer to the properties of the two phases. Equations 6.8 and 6.9 yield the upper bound when K_m and G_m are the *maximum* bulk and shear moduli of the individual phases, and the lower bounds when K_m and G_m are the *minimum* bulk and shear

moduli of the phases. We will refer to equations 6.8 and 6.9 as the *HS bounds*. Superscripts *HS*+ and *HS*- designate upper and lower bounds, respectively.

It has been known for some time that the HS bounds on the elastic moduli of two-phase porous media are Gassmann-consistent. That is, if the bulk modulus of a two-phase material, in which one of the phases is a fluid, falls on one of the HS bounds, then if the fluid is replaced by a second fluid, the modulus of the resulting composite remains on the bound. This was implied by the original derivation of Hashin and Shtrikman, (1963) in which their trial stress and strain fields in the pore phase were constant (Gibiansky and Torquato, 2000); in the case of fluids, this means uniform pressure and zero shear stress in the pore space, which are equivalent to Gassmann's assumptions. The uniformity of the inclusion stress for microstructures attaining the bound has also been pointed out, for example, by Gibiansky and Sigmund (2000). Yan and Han (2011) also discuss the consistency of the HS bounds with Gassmann's model. It is interesting that fluid-saturated two-phase media whose moduli fall on the bounds will be consistent with Gassmann fluid substitution, even if the pores are not connected.

6.4. Bounds on bulk modulus for fluid substitution

When two-phase materials do not fall on the bounds, then fluid substitution may not be Gassmann-consistent. In the geophysics literature, deviation from Gassmann's predictions has been extensively discussed in the context of unequilibrated pore pressure as occurs in disconnected pores or during unrelaxed "squirt flow" (Biot, 1962; Mavko and Nur, 1975; Budiansky and O'Connell, 1977; Stoll and Bryan, 1970; Mavko and Jizba, 1991; Chapman, et al., 2002; Gurevich, et al., 2009; Saxena and Mavko, 2014). Fluid substitution with unequilibrated pore fluids yields larger changes in bulk modulus than those predicted by Gassmann.

Gibiansky and Torquato (2000) discuss the non-uniqueness of fluid substitution and present rigorous bounds on the change in bulk modulus that can occur upon fluid substitution in a two-phase composite. If the initial bulk modulus is $K_{sat}^{(1)}$ when the rock is

saturated with fluid of bulk modulus $K_f^{(1)}$, then upon substituting a new fluid with bulk modulus $K_f^{(2)}$, the saturated bulk modulus $K_{sat}^{(2)}$ must lie in the interval

$$F_1 \le K_{sat}^{(2)} \le F_2 \quad \text{if} \quad K_f^{(2)} > K_f^{(1)} \quad , \tag{6.10}$$

$$F_1 \ge K_{sat}^{(2)} \ge F_2 \quad \text{if} \quad K_f^{(2)} < K_f^{(1)} \quad ,$$

where

$$F_1 = \frac{\alpha_1 K_{1*}^{(2)} A + K_h^{(2)} B}{\alpha_1 A + B} \quad ; \qquad F_2 = \frac{\alpha_2 K_{1*}^{(2)} A + K_h^{(2)} B}{\alpha_2 A + B} \quad ;$$

$$A = \left(K_h^{(1)} - K_{sat}^{(1)}\right)\left(K_{1*}^{(1)} - K_h^{(1)}\right) ; \quad B = \left(K_{1*}^{(1)} - K_{sat}^{(1)}\right)\left(K_h^{(2)} - K_{1*}^{(2)}\right) ;$$

$$\alpha_1 = \frac{\left(K_{min} - K_f^{(2)}\right)^2 \left((1-\phi)K_f^{(1)} - \phi K_{min}\right)^2}{\left(K_{min} - K_f^{(1)}\right)^2 \left((1-\phi)K_f^{(2)} - \phi K_{min}\right)^2} ; \alpha_2 = \alpha_1 \frac{K_f^{(2)}\left(3K_f^{(1)} + 4G_{min}\right)}{K_f^{(1)}\left(3K_f^{(2)} + 4G_{min}\right)} \quad ;$$

$$K_h^{(1)} = \left[\frac{1-\phi}{K_{min}} + \frac{\phi}{K_f^{(1)}}\right]^{-1} ; \qquad K_h^{(2)} = \left[\frac{1-\phi}{K_{min}} + \frac{\phi}{K_f^{(2)}}\right]^{-1} \quad ;$$

$$K_{1*}^{(1)} = (1-\phi)K_{min} + \phi K_f^{(1)} - \frac{\phi(1-\phi)\left(K_{min} - K_f^{(1)}\right)^2}{\phi K_{min} + (1-\phi)K_f^{(1)} + 4G_{\min}/3} \quad ;$$

$$K_{1*}^{(2)} = (1-\phi)K_{min} + \phi K_f^{(2)} - \frac{\phi(1-\phi)\left(K_{min} - K_f^{(2)}\right)}{\phi K_{min} + (1-\phi)K_f^{(1)} + 4G_{\min}/3} \quad .$$

Some properties of equation 6.10 are as follows.

- The modulus F_1 is equivalent to Gassmann's prediction of saturated bulk modulus. F_1 corresponds to the *smallest* possible change in bulk modulus upon fluid substitution, which occurs when the rock pore space is well connected and the pore pressure can equilibrate under bulk compression.
- The modulus F_2 corresponds to the *largest* possible change in bulk modulus upon fluid substitution. This occurs when the pore pressure is not uniform throughout the pore

space under bulk compression—for example, when the rock pore space is disconnected or tight and has very heterogeneous pore stiffness (i.e., unrelaxed squirt flow).

- If $K_f^{(1)}>0$ and $K_{sat}^{(1)}$ is on either the *HS*+ or *HS*- bound, then upon fluid substitution to $K_f^{(2)}>0$, $K_{sat}^{(2)}=F_1=F_2$, is on the same corresponding bound for the new fluid; hence, fluid substitution for an initially saturated rock whose bulk modulus falls on a bound is unique.
- If the initial case is dry ($K_f^{(1)}=0$), and if $K_{sat}^{(1)}$ is on *HS*+ or *HS*- bound, then upon fluid substitution, F_1 is still Gassmann's prediction of the saturated rock bulk modulus and will lie on the same corresponding *HS*+ or *HS*- bound computed with the new fluid. If the dry $K_{sat}^{(1)}$ is on the *HS*- bound, then F_2 will be on the *HS*+ bound, and if the dry $K_{sat}^{(1)}$ is on the *HS*+ bound, then F_2 will stay on the *HS*+ bound.
- If the initial case is dry ($K_f^{(1)}=0$), and if $K_{sat}^{(1)}$ lies anywhere between (but not on) the *HS*- and *HS*+ bounds, then F_2 is the *HS*+ bound computed with the new fluid. If the initial rock is saturated, the prediction for dry modulus F_2 lies on *HS*-.

Next, we introduce physical realizations of the Gibiansky and Torquato bounds.

6.5. Solid substitution on the bounds

For two-phase composites, the *HS* bounds, equations 6.8 and 6.9 are physically attainable by a multitude of microstructures (Hashin and Shtrikman, 1963; Norris, 1985; Milton, 1984; Gibiansky and Sigmund, 2000). For example, the *HS* bound on the bulk modulus, but not the shear modulus, can be realized by a multi-scale, space-filling pack of coated spheres. Milton (1984) found that both the bulk and shear bounds can be realized simultaneously by certain multi-rank laminate geometries. The differential effective medium approach was shown by Norris (1985) to achieve the bounds on both bulk and shear moduli simultaneously when the inclusions are disk-shaped. Bucher (1976) and Norris (1985) pointed out that the non-symmetric self-consistent scheme of Wu (1966) for disk-shaped geometries attain both bounds when $(K_1 - K_2)(G_1 - G_2) \geq 0$.

While two-phase microgeometries exist that can attain the bounds on bulk modulus, but not the shear modulus, Berryman and Milton (1988) have shown that any two-phase microgeometry that attains the bounds on shear modulus must necessarily attain the bound on bulk modulus. Reviews on the subject of realizability of the bounds can be found in Gibiansky and Sigmund (2000), Norris (1985), Milton (2002), and Liu (2011).

The significance of realizability for this paper is the following. Since the bounds are realizable, there exist multiple two-phase microstructures for which equations 6.8 and/or 6.9 are the exact equations for the effective moduli of those materials. If either bulk or shear modulus of the initial composite, composed of solid or fluid phases with moduli (K_1, G_1) and (K_2, G_2), falls on the upper or lower bound, then when phase (K_2, G_2) is replaced by another solid or fluid phase (K_2', G_2'), the corresponding moduli of the new composite are again on the respective bounds, as long as $(K_1 - K_2)(G_1 - G_2) \geq 0$ and $(K_1 - K_2')(G_1 - G_2') \geq 0$. That is, microstructures who's corresponding moduli fall exactly on a bound represent a class of materials for which we can perform both liquid and solid substitution, exactly and uniquely.

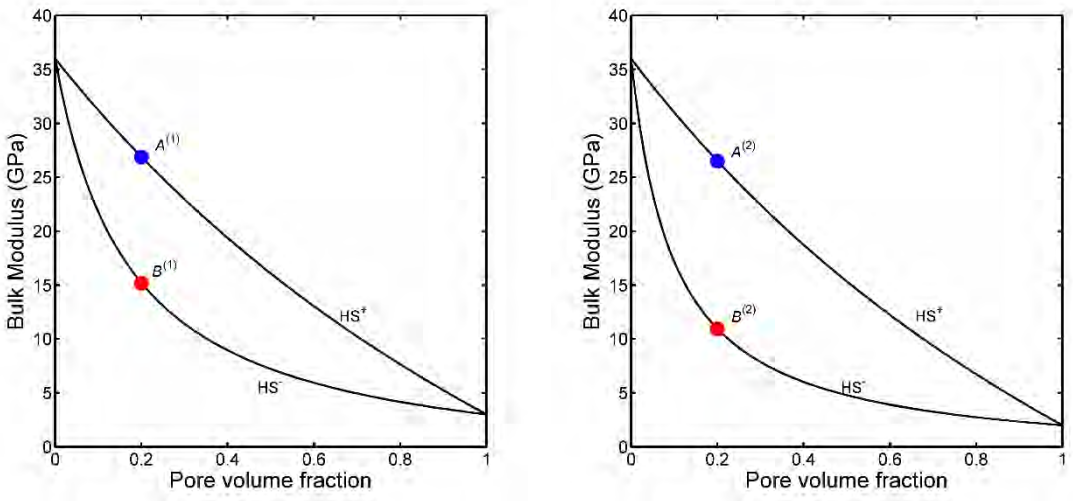

Figure 6.1: Hashin-Shtrikman bounds on bulk modulus. a) example for quartz mineral with pore filling moduli $K_2 = 3$ GPa and $G_2 = 2$ GPa. b) example for quartz mineral with pore filling moduli $K_2' = 2$ GPa and $G_2' = 1$ GPa. Materials that happen to fall on the bulk modulus bounds, points A and B, transform to points A' and B'.

Examples of the solid substitution on the bounds are shown in Figure 6.1. Figure 6.1a corresponds to a two-phase rock with quartz mineralogy (K_1 = 36 GPa, G_1 = 45 GPa) and solid pore fill with moduli K_2 = 3 GPa and G_2 = 2 GPa. Points A and B correspond to two realizable composites whose bulk moduli fall along the upper and lower bounds, respectively. Figure 6.1b corresponds to the same quartz mineralogy but a different pore filling material with moduli K_2' = 2 GPa and G_2' = 1 GPa. The substitution of the pore fill causes the composites at A and B to move with the bounds and transform to A' and B', respectively. As mentioned earlier, in this paper, we use the terms "porosity" and "pore volume fraction" to mean the volume fraction of the pore-filling material, even if it is a solid.

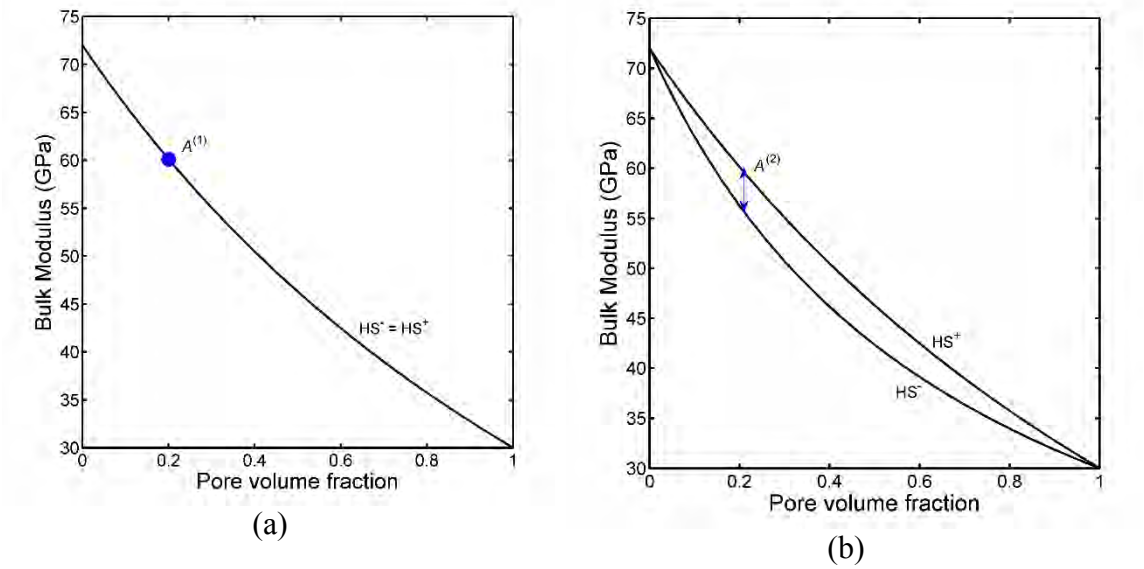

Figure 6.2. Hashin-Shtrikman bounds on bulk modulus. a) example for calcite mineral ($K_1 = 72$ GPa, $G_1 = 32$ GPa), with pore filling moduli $K_2 = 30$ GPa and $G_2 = 32$ GPa . b) same mineral with pore filling moduli $K_2' = 30$ GPa and $G_2' = 0$ GPa.

An exception to the uniqueness of the substitution on the bounds occurs when the shear moduli of all initial phases are equal, causing the initial upper and lower bounds to coincide, as in Figure 6.2. In this case, the point A (Figure 6.2a) corresponds to a composite with calcite mineralogy ($K_1 = 72$ GPa, $G_1 = 32$ GPa) and solid pore fill with moduli $K_2 = 30$ GPa and $G_2 = 32$ GPa. Upon substitution with a pore fill with moduli $K_2' = 30$ GPa and $G_2' = 0$ GPa, the upper and lower bounds separate (Figure 6.2b). The new

composite modulus A' could fall on or anywhere between the bounds, depending on the pore geometry. Another exception is the degenerate case when the initial pore-filling material is identical to the grain material.

6.6. Solid substitution using embedded bounds

Since equations 6.8 and 6.9 are physically realizable, we can embed the realizations recursively to represent additional pore space geometries, and to calculate exactly, but not uniquely, the change in effective modulus upon either solid or fluid substitution in the pore space.

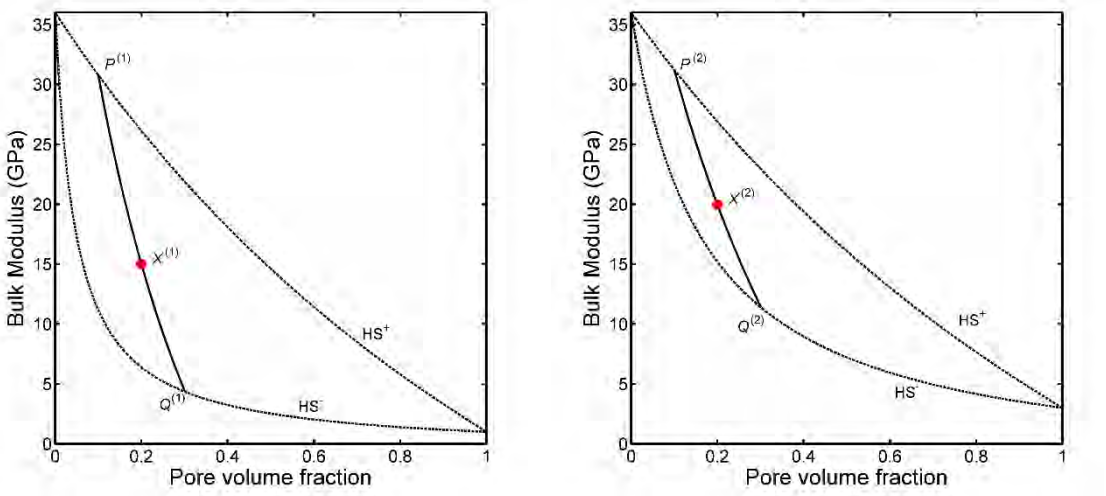

(a) (b)

Figure 6.3. Substitution of solid pore fill (K_2=1 GPa and G_2=0.5 GPa) with a different solid pore fill (K_2'=3 GPa, G_2'=2 GPa) using a modified upper *HS* bound construction. a) Dashed curves are absolute bounds for initial composition. Data point X falls between the bounds, but can be physically realized by a *HS+* composite consisting of end members at P and Q. b) With new composition, absolute bounds shift. Points P and Q move to P' and Q'. The same realizable microgeometry used to fit X leads to the exact prediction X' at new composition.

The *HS* bounds plotted in Figure 6.3a show the range of possible bulk moduli for rocks composed of quartz mineralogy ($K_1 = 36$ GPa, $G_1 = 45$ GPa) and solid pore fill ($K_2 = 1$ GPa and $G_2 = 0.5$ GPa) . Point X represents one rock with porosity ϕ_X=0.2 and bulk modulus K_X=15 GPa. Points P (ϕ_P=0.1; K_P=30.89 GPa) and Q (ϕ_Q=0.3; K_Q=4.32 GPa)

fall on the upper and lower and bounds, respectively (both bulk and shear moduli are on the respective bounds). We choose porosities ϕ_P and ϕ_Q so that a *HS*+ bound constructed from the materials P and Q passes through point X:

$$K_X = K_P + \frac{f_Q}{\left(K_Q - K_P\right)^{-1} + f_P\left(K_P + \frac{4}{3}G_P\right)^{-1}}, \tag{6.11}$$

where f_P is the volume fraction of material P and $f_Q = \left(1 - f_P\right)$ is the volume fraction of material Q, such that that $\phi_X = f_P\phi_P + f_Q\phi_Q$. With this construction, K_X is the modulus of a realizable composite of materials P and Q, which in turn, are realizable composites of the mineral and pore-fill materials. Therefore, equation 6.11 is the exact expression for multiple microgeometries that have modulus K_X.

Figure 6.3b shows the corresponding plot of bulk moduli when the solid pore fill (K_2=1 GPa, $G_2 = 0.5$ GPa) is replaced by a different solid pore fill (K_2'=3 GPa, G_2'=2 GPa). Upon solid substitution, the original points P and Q are transformed to points P' and Q', respectively, lying on the new bounds at porosities ϕ_P and ϕ_Q; the upper bound between points P and Q is transformed, as well. The bulk modulus K_X' at point X' corresponds to the original rock with the solid pore-fill replaced by the new solid. Hence, K_X' is an exact (though non-unique) prediction of the bulk modulus after substituting one solid pore fill with another solid pore fill:

$$K_X' = K_P' + \frac{f_Q}{\left(K_Q' - K_P'\right)^{-1} + f_P\left(K_P' + \frac{4}{3}G_P'\right)^{-1}}. \tag{6.12}$$

Although all of the constructions of the type discussed in Figure 6.3 are based on the same Hashin-Shtrikman equations, in this paper we refer to the *absolute HS bounds* to indicate mixtures of the mineral and pore-fill end members, and *modified HS bounds* to indicate embedded mixtures, such as that between materials at points P and Q.

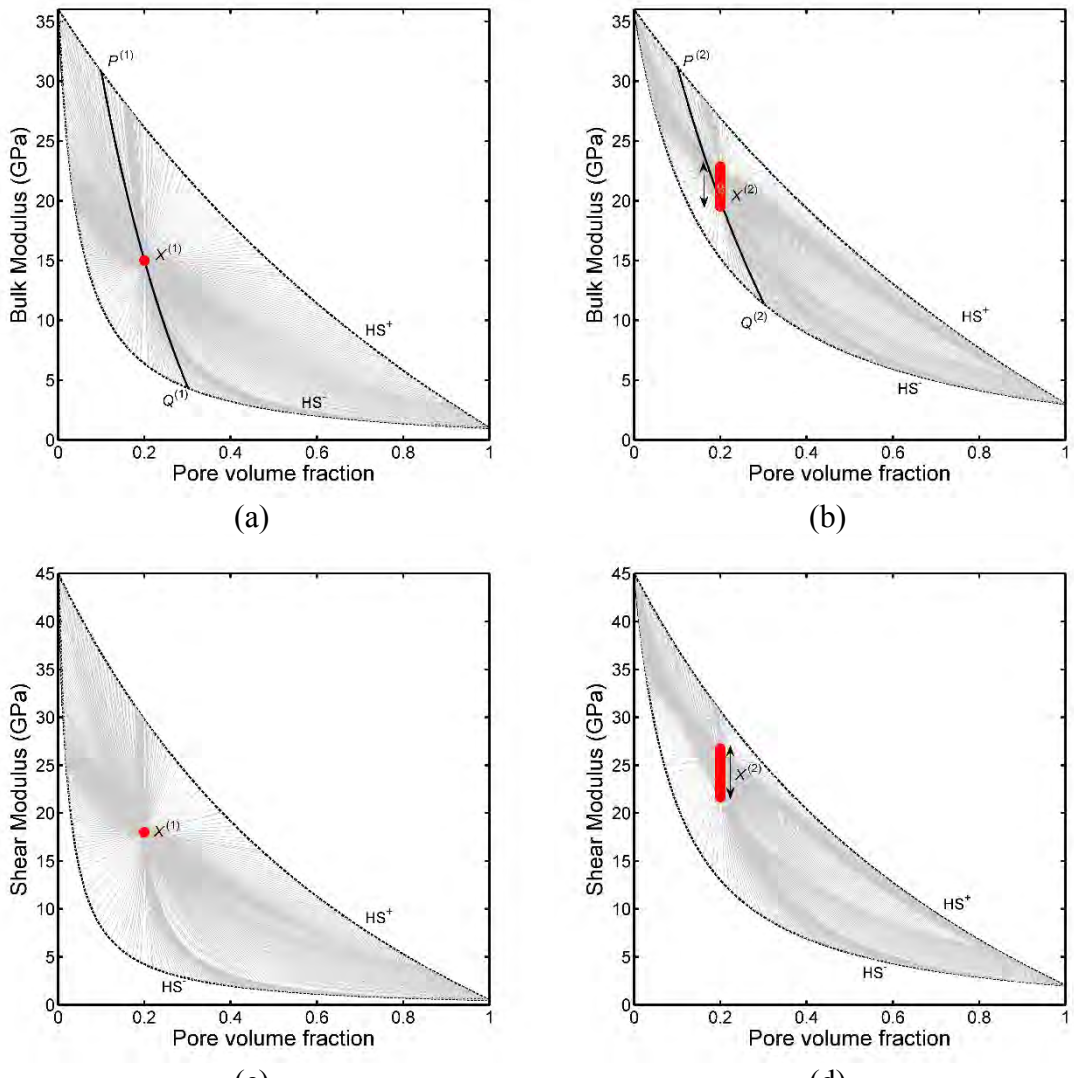

Figure 6.4. (a) and (b) similar to Figure 6.3 - Substitution of solid pore fill ($K_2 = 1$ GPa and $G_2 = 0.5$ GPa) with a different solid pore fill ($K'_2 = 3$ GPa, $G'_2 = 2$ GPa). Data point X can be physically realized by *an infinite number* of *HS* composites of end members at P_i and Q_i spanning along the upper and lower bounds, respectively. The range of realizable microgeometries used to fit X leads to a range of predicted X' at new composition. (c) and (d) same as (a) and (b) for shear modulus $G_X = 18$ GPa.

The intrinsic non-uniqueness of the solid substitution is illustrated in Figure 6.4. Figure 6.4a describes the same composition as in Figure 6.3a. The gray lines show some of the *infinite number* of modified upper *HS* realizations of point X constructed from pairs P'_i and Q'_i. The corresponding predictions of the composite bulk modulus when the solid pore

fill is replaced by the new solid pore fill are shown in Figure 6.4b. Each construction of the original point X transforms to a slightly different K'_X upon substitution of the pore material. *That is, upon solid substitution, the bulk modulus can take on a range of possible values, which depend on the (usually unknown) underlying microstructure.*

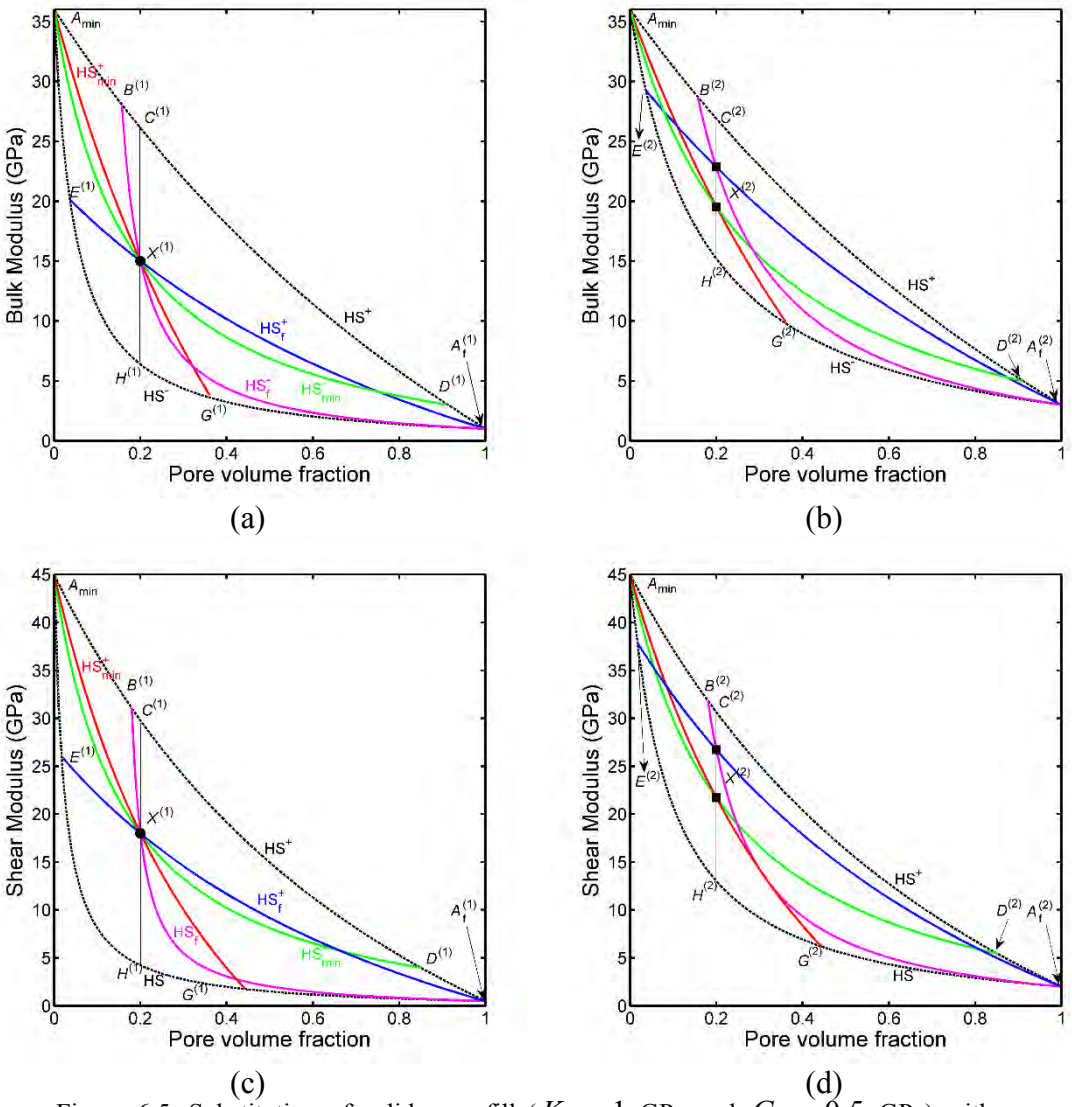

Figure 6.5. Substitution of solid pore fill ($K_2 = 1$ GPa and $G_2 = 0.5$ GPa) with a different solid pore fill ($K'_2 = 3$ GPa, $G'_2 = 2$ GPa). a) data point X is realized by modified *HS*+ and *HS*- bounds passing from the mineral and pore-fill end members. b) substituting the pore fill from solid to liquid leads to a range of possible results. (c) and (d) same as (a) and (b) for shear modulus $G_X = 18$ GPa.

Figures 6.4c and 6.4d show the same plots as in Figures 6.4a and 6.4b, but for shear modulus $G_X = 18$ GPa.

Figures 6.5a and 6.5b shows limiting cases of the constructions described in Figures 6.4a and 6.4b, respectively. In Figures 6.5a and 6.5b, curve ($A_{\min} - G$) and curve ($A_{\min} - D$) are modified upper and lower *HS* bound constructions from the mineral point, $A_{\min}$, passing through the point X. We refer to these as the $HS^{+}_{\min}$ and $HS^{-}_{\min}$ constructions, respectively. Curve ($A_f - E$) and curve ($A_f - B$) are *HS*+ and *HS*- constructions from the pore-fill point, A_f, passing through the point X. We refer to these as the HS^{+}_{f} and HS^{-}_{f} constructions, respectively. Curve (*C*–*H*) shows *HS*+ and *HS*- constructions from the upper and lower bounds at the data porosity 0.2. Figures 6.5c and 6.5d shows the same constructions after replacing the solid pore filling material with the second solid pore-fill material.

From numerical examples, we conjecture that the four embedded *HS* constructions ($HS^{+}_{\min}$, $HS^{-}_{\min}$, HS^{+}_{f}, HS^{-}_{f}) illustrated in Figure 6.5 bound the range of substituted moduli, K'_X and G'_X, that can be achieved with this class of embedded *HS* realizations. We have not found a rigorous proof that this is always so. However, we discuss in the next section that the $HS^{+}_{\min}$ and HS^{-}_{f} predictions of K'_X reduce to the Gibiansky and Torquato bounds when the pore-fills are fluids. Note that the points *G*, *D*, *E* and *B* for bulk and shear *HS* constructions may not be the same.

Closed-form expressions for the solid-to-solid substitution using $HS^{+}_{\min}$ and HS^{-}_{f} are given in the Appendix A. Strategies for numerical construction of the $HS^{-}_{\min}$ and HS^{+}_{f} are given in Appendix B.

6.7. Properties of embedded bounds when pore-fills are fluids

6.7.1. Bulk modulus

We now return to the problem of fluid substitution. We show that the $HS^{+}_{\min}$ and HS^{-}_{f} predictions reduce to the Gibiansky and Turquato bounds for bulk modulus, illustrating that those bounds are optimum.

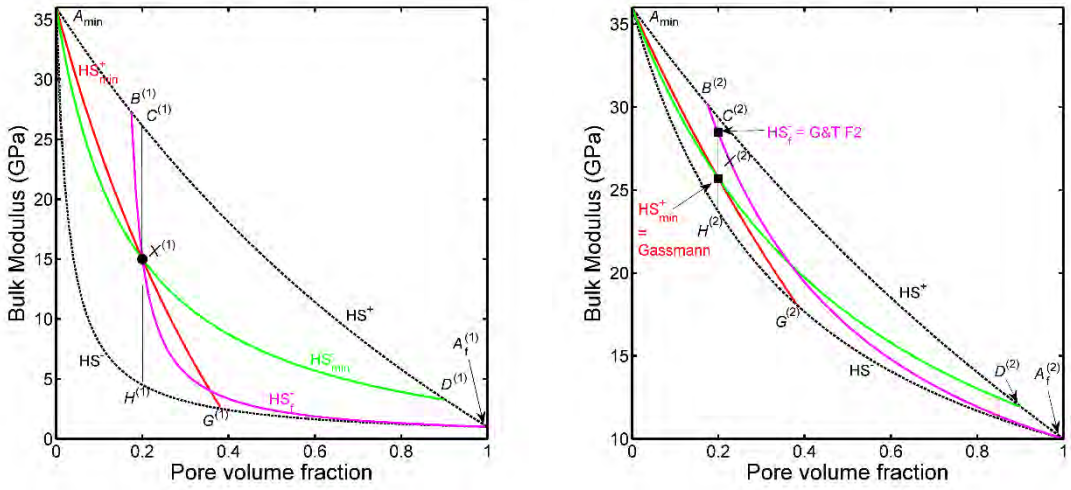

Figure 6.6. Bulk modulus substitution of fluid pore fill ($K_2 = 1$ GPa and $G_2 = 0$) with a different fluid pore fill $K'_2 = 10$ GPa and $G'_2 = 0$. a) bulk modulus data point X is realized by modified *HS*+ and *HS*- bounds passing from the mineral point, as well as vertical *HS* bound. b) substituting the pore fluid leads to a range of possible results.

Figure 6.6 shows the bulk modulus for rocks of quartz mineralogy and pore space filled with fluids. In Figure 6.6a, the pore fluid has moduli $K_2 = 1$ GPa and $G_2 = 0$. The embedded bound constructions in Figure 6.6 are the same as described earlier: the $HS^{+}_{\min}$ curve is the modified HS+ mix of the mineral point $A_{\min}$ and the absolute lower bound point G. Similarly, the $HS^{-}_{\min}$ curve is the modified HS- mix of the mineral point $A_{\min}$ and the absolute upper bound point D. When the pore fill is a fluid (or dry), the $HS^{+}_{\min}$-constructed substitutions of K_X to K'_X can be shown, with some algebra, to be exactly the same as Gassmann's prediction – or as Gibiansky and Torquato show, the smallest possible

change in bulk modulus. (The $HS^{-}_{\min}$ fluid substitution is also exactly equal to Gassmann's prediction, if the shear modulus at point *D* is also on the upper HS bound.) A coated-sphere realization of the $HS^{+}_{\min}$ constructions is illustrated in Figure 6.7. We see that for this choice of microstructure, the fluid phase always occurs in inclusions of the same shape (shells in 7a). We emphasize that there are numerous microgeometries, other than spheres, that also correspond to the embedded HS constructions.

When the pore-filling material is a fluid (zero shear modulus), the construction of the HS^{-}_{f} from the pore-fluid point A_f through point X is identical to the Gibiansky and Torquato second bound, F_2. This can also be proved algebraically. A coated-sphere realization of this construction is shown in Figure 6.7c.

When the pore-filling material is a fluid (zero shear modulus), the HS^{+}_{f} construction from the pore-fluid point A_f to any point on the lower bound stays on the lower bound. The point X cannot be realized in this way, unless it is on the lower bound. A coated-sphere example realization of this construction is shown in Figure 6.7b.

In summary, the embedded bound constructions represent physical realizations of the Gibiansky and Torquato bounds when the pore-filling materials are fluids. This illustrates that the Gibiansky and Torquato bounds are optimum.

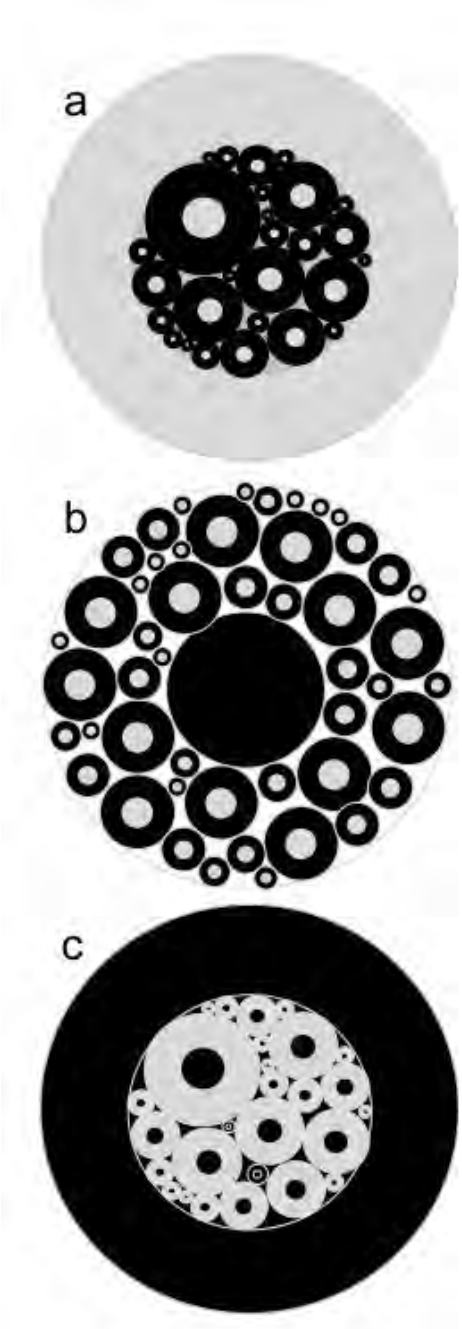

Figure 6.7. Coated-sphere realizations of the constuctions in Figures 5 and 6. Black represents the pore-filling material. a) HS^{+}_{min} -- mix of mineral point and lower bound point *G*. b) HS^{+}_{f} --mix of fluid point and lower bound point *E*. c) HS^{-}_{f} -- mix of pore fill point and upper bound point *B*.

6.7.2. **Shear modulus**

Figure 6.8a shows shear modulus of quartz mineralogy and pore space filled with solid of $K_2 = 1$ GPa and $G_2 = 0.0001$ GPa. The embedded bound constructions shown in Figure 6.8a are as follows: the $HS^+_{\min}$ curve is the modified HS+ mix of the mineral point $A_{\min}$ and the absolute lower bound point G. Similarly, the $HS^-_{\min}$ curve is the modified HS- mix of the mineral point $A_{\min}$ and the absolute upper bound point D. The HS^-_f curve is the modified HS- mix of the pore fill point A_f and the absolute upper bound point B. As the value of pore fill shear modulus approaches zero, i.e., $\bar{G}_2 \to 0$, the HS^-_f curve becomes increasingly indeterminant numerically. Figure 6.8b shows the substituted shear modulus corresponding to pore fill solid of $K'_2 = 10$ GPa and $G'_2 = 0.01$. Numerically, the substitution predictions of HS^-_f curve approaches the absolute HS+ mix of the mineral and pore fill.

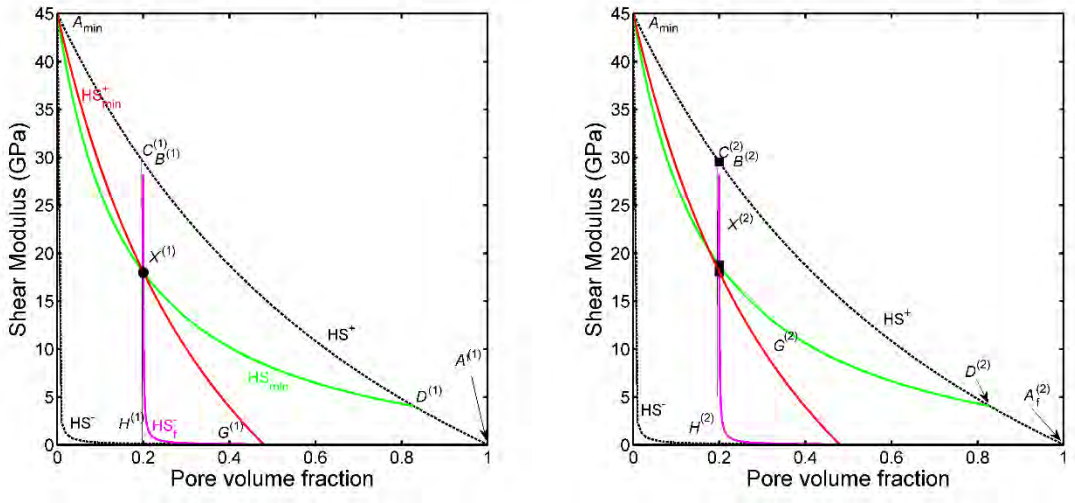

(a) (b)

Figure 6.8. Shear modulus substitution of fluid pore fill ($K_2 = 1$ GPa and $G_2 = 0.01$) with a different fluid pore fill $K'_2 = 10$ GPa and $G'_2 = 0.01$. a) shear modulus data point X is realized by modified *HS*+ and *HS*- bounds passing from the mineral point, as well as vertical *HS* bound.

6.8. Marion's bound average method

The vertical black lines in Figures 6.5-6.8 represent constructions of data point X from composites of point C on the absolute upper bound and point H on the absolute lower bound; both C and H lie at the same porosity ϕ_X as the data point X. Using equation 6.8, K_X can be constructed as a modified HS+ mix of the materials at point C (K^{HS+}, G^{HS+}) and point H (K^{HS-}, G^{HS-}), such that the fraction of material C is f^+ and the fraction of material H is $\left(1-f^+\right)$. Alternatively the data point K_X can be constructed as an HS- mix of the materials at point C (K^{HS+}, G^{HS+}) and point H (K^{HS-}, G^{HS-}), such that the fraction of material C is f^- and the fraction of material H is $\left(1-f^-\right)$. The fractions are given by

$$f^+ = \frac{\dfrac{1}{K_X + (4/3)G^{HS+}} - \dfrac{1}{K^{HS+} + (4/3)G^{HS+}}}{\dfrac{1}{K^{HS-} + (4/3)G^{HS+}} - \dfrac{1}{K^{HS+} + (4/3)G^{HS+}}}, \tag{6.13}$$

$$f^- = \frac{\dfrac{1}{K_X + (4/3)G^{HS-}} - \dfrac{1}{K^{HS+} + (4/3)G^{HS-}}}{\dfrac{1}{K^{HS-} + (4/3)G^{HS-}} - \dfrac{1}{K^{HS+} + (4/3)G^{HS-}}}. \tag{6.14}$$

After substituting the pore-filling material (fluid or solid), the absolute bounds are recomputed to yield the materials at points C' and H'. Finally, the substituted modulus is computed by once again constructing the HS+ and HS- mixes using fractions f^+ and f^-, respectively.

These modified HS constructions at constant porosity resemble the Bound Average Method (BAM) introduced by Marion and Nur (1991). In that work, Marion and Nur constructed the starting data point K_X as an arithmetic average (Voigt bound) of moduli on the upper and lower bounds. They predicted the change in elastic moduli upon solid or

liquid substitution in the pore space by taking the same arithmetic average after recomputing the upper and lower bounds for the new composition. Yan and Han (2011) further discussed the linear BAM approximation. We refer to the present constructions as the BAMHS+ and BAMHS- method of substitution.

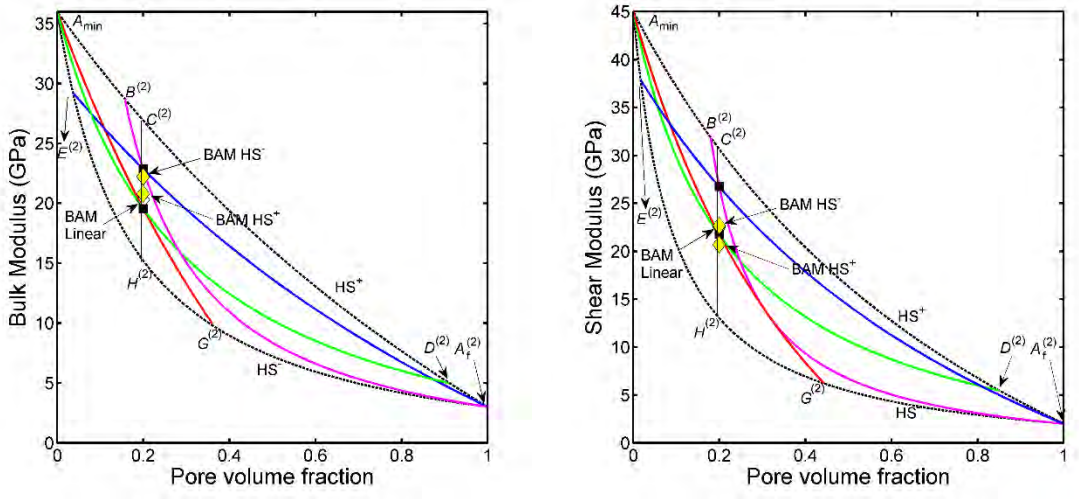

Figure 6.9. Comparison of *BAMHS* predictions with the modified *HS* constructions. Bulk and shear moduli substitution of solid pore fill ($K_2 = 1$ GPa, $G_2 = 0.5$ GPa) with a different fluid pore fill ($K_2' = 3$ GPa, $G_2' = 2$ GPa). Effective moduli measured with the initial composition are $K_X = 15$ GPa and $G_X = 18$ GPa.

Figure 6.9a illustrates our BAMHS solid-to-solid substitution (same parameters as in Figure 6.5); Figure 6.9b illustrates the corresponding prediction for shear modulus using fraction f obtained from equations 6.13 and 6.14. The BAMHS predictions are shown by yellow diamonds; the $HS^+_{\min}$, $HS^-_{\min}$, HS^+_f, and HS^-_f predictions are marked with squares. The HS-BAM predictions again illustrate the nonuniqueness of the substituted modulus, though they do not span the entire range of predicted K'_X or G'_X as the $HS^+_{\min}$, $HS^-_{\min}$, HS^+_f, and HS^-_f constructions. The linear BAM prediction is shown by open diamonds. For these examples the linear BAM prediction lies close to the $HS^+_{\min}$ prediction, which represents the smallest change in modulus upon substitution. The equations for predicting the solid substitution using the BAMHS method are much simpler than for the other constructions (see the Appendix A).

6.9. Comparison with other methods

6.9.1. Ciz and Shapiro

Figure 6.10 compares the modified bound solid-substitution predictions with those of Ciz and Shapiro (Eqns. 6 and 7), again using the same material parameters as in Figure 6.5. From numerical examples, we find that the *C&S* approximation tends to predict the minimum change in the modulus upon substitution. This is consistent with our findings in Chapter 3. In the case of Figure 6.10, the *C&S* prediction lies outside of the range defined by the modified bound constructions.

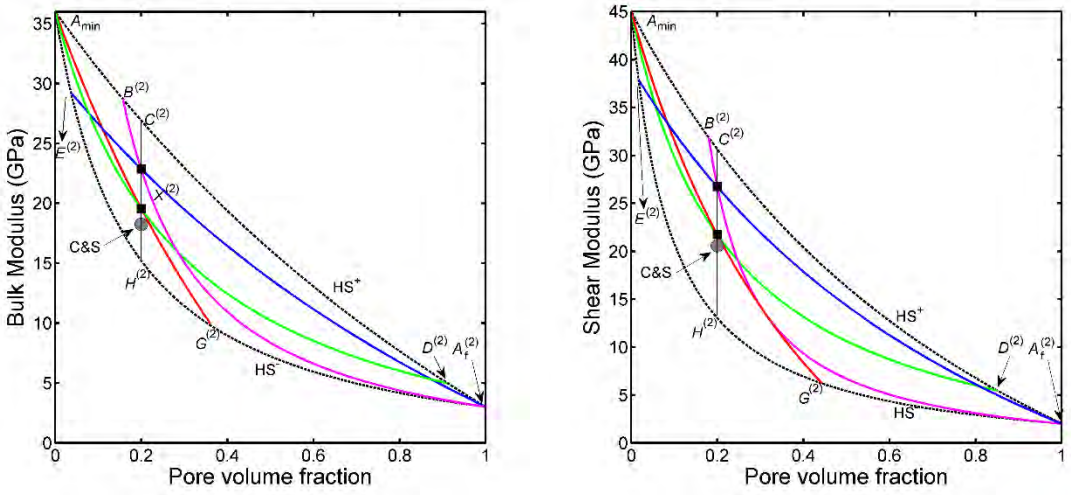

(a) (b)

Figure 6.10. Comparison of the *C&S* approximation with the modified *HS* constructions. Substitution of solid pore fill ($K_2 = 1$ GPa, $G_2 = 0.5$ GPa) with a different solid pore fill ($K_2' = 3$ GPa, $G_2' = 2$ GPa). Effective moduli measured with the initial composition are $K_X = 15$ GPa and $G_X = 18$ GPa.

6.9.2. Berryman and Milton

Berryman and Milton (1988) discussed bounds (B&M) on elastic bulk and shear moduli that incorporate information about the three-point correlations of the pore space geometry. The geometric information makes the *B&M* bounds more restrictive than the HS bounds, and at least as tight as the bounds of Beran and Molyneux (1966). Using the

B&M results, measured elastic moduli can be inverted for bounds on two parameters, which depend only on geometry. These parameters can, in turn, be used to put bounds on the elastic moduli if the pore-filling material is changed. Figure 6.11 compares solid-to-solid substitution using the B&M bounds with the HS_f^- and $HS_{\min}^+$ constructions, for the same material parameters presented in Figure 6.5. The *B&M* predictions are tighter than the *HS* bounds, but broader than the range spanned by the HS_f^- and $HS_{\min}^+$ constructions.

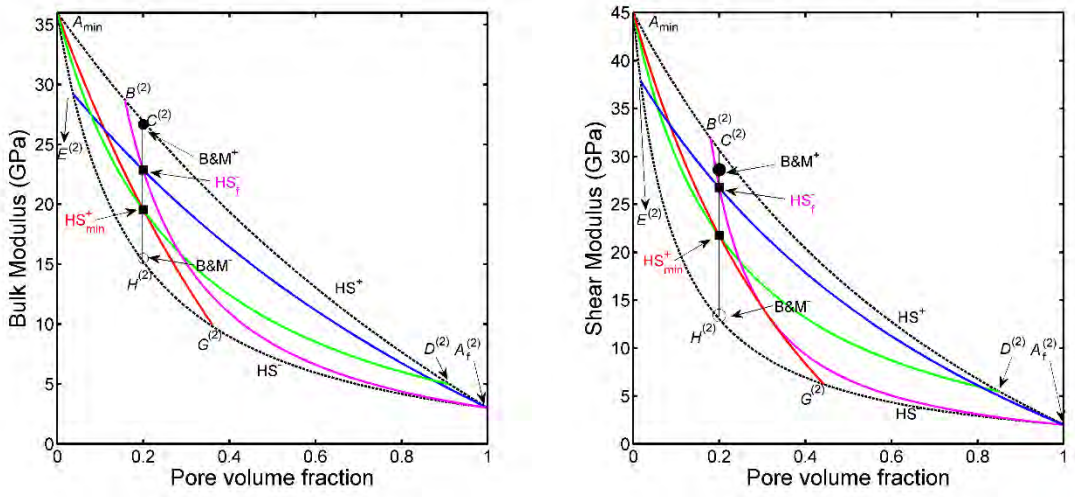

(a) (b)

Figure 6.11. Comparison of the Berryman and Milton predictions with the modified *HS* constructions. Bulk and shear moduli substitution of solid pore fill ($K_2 = 1$ GPa, $G_2 = 0.5$ GPa) with a different fluid pore fill ($K_2' = 3$ GPa, $G_2' = 2$ GPa). Effective moduli before substitution are $K_X = 15$ GPa and $G_X = 18$ GPa.

6.10. FEM examples

We next consider a digital bituminous-sand rock sample. This sample was imaged, processed and later segmented using a commercially available software. This digital sample is shown in Figure 6.12a. Imaging revealed that the sample has quartz grains (size roughly between 0.1 mm- 0.25 mm; volume fraction 0.56), bitumen-filled pores (volume fraction 0.37) and air-filled pores (volume fraction 0.07). The spatial resolution of this

segmented digital rock is 0.004 mm and the cube length is 1.6 mm. To avoid partial saturation we digitally replace all air-filled pores with quartz.

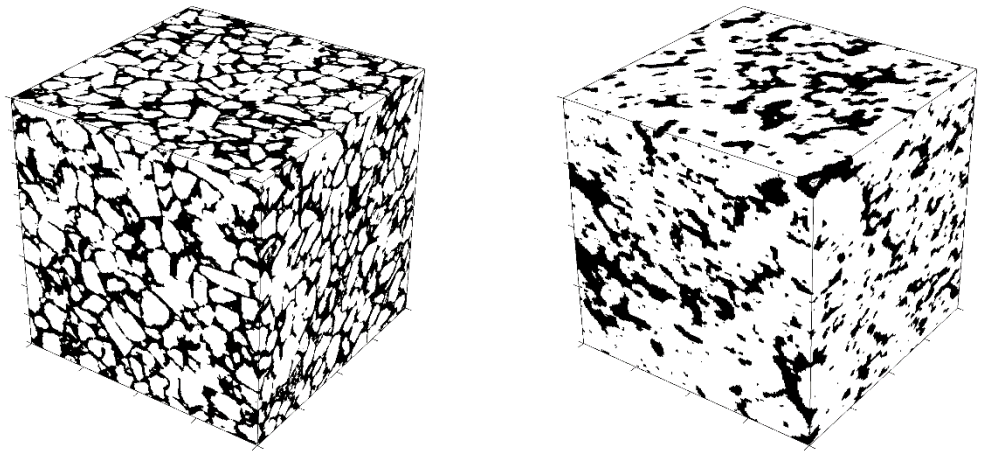

(a) (b)

Figure 6.12: (a) Digitial rock bitumenous sand sample of size 1.6 mm and spatial resolution (x, y and z) of 0.004 mm. Quartz is shown in white and bitumen is shown in black. (b) Grossmont carbonate digital sample. Calcite grains shown in white and bitumen shown in black.

Next, we assume that when bitumen is cold it behaves like an elastic solid of bulk modulus 4 GPa and shear modulus 0.7 GPa, and when bitumen is heated it still behaves like an ideal elastic solid, but with reduced bulk modulus of 3 GPa and reduced shear modulus varying between 0.7 GPa and 0.0001 GPa. We model quartz, which is the mineral in the rock frame, as a linear elastic isotropic solid of bulk modulus 36 GPa and shear modulus of 45 GPa. Next, we compute effective elastic moduli of the digital rock samples using the Finite Element Method (Garboczi and Berryman, 2001; Arns et al., 2002). In Figures 13a and 13b, we present the results for predicting hot bitumen-filled rock moduli starting with the FEM computed cold bitumen-filled rock moduli using above listed substitution models. These predictions are then compared with the numerically computed hot-bitumen moduli. The choice of this substitution case is motivated by the expected final pore saturation conditions as a result of heating a heavy oil reservoir - which reduces the shear and bulk moduli of heavy oil thus increasing mobility which leads to enhanced oil production. Similar to this example, Figure 6.14 shows the same modeling exercise as in

Figure 6.13 but for a digital Grossmont carbonate rock sample of porosity 0.28 (reported in Andrä et al., 2013).

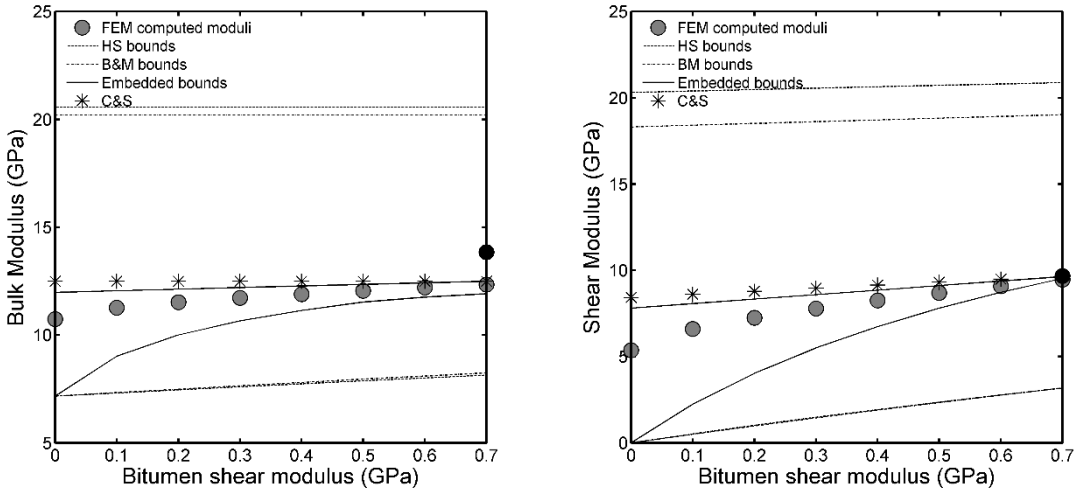

Figure 6.13: Predictions of hot bitumen-filled rock moduli (shown in gray) starting with cold bitumen-filled sand rock moduli (shown in black), compared with FEM computed hot bitumen-filled sand rock moduli.

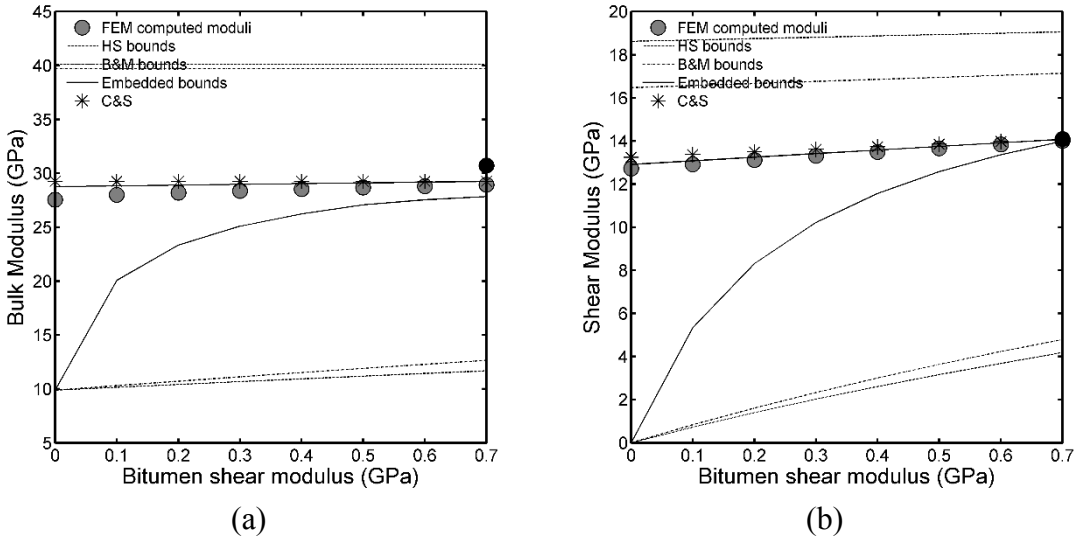

Figure 6.14: Predictions of hot bitumen-filled rock moduli (shown in gray) starting with cold bitumen-filled carbonate rock moduli (shown in black), compared with FEM computed hot bitumen-filled carbonate rock moduli.

6.11. Chapter summary

For materials whose bulk and/or shear moduli fall on the Hashin-Shtrikman bounds, fluid or solid substitution is exact and unique. For composites that fall between the bounds, fluid substitution of the bulk modulus is not unique: Gassmann's prediction yields the smallest possible change, while the largest possible change is predicted by the Gibiansky and Turquato bounds. Changes in modulus larger than predicted by Gassmann can be caused by disconnected pores or unrelaxed pore pressure gradients that can be associated with large fluid viscosities and/or high measurement frequencies.

Solid substitution of bulk moduli can be computed exactly, but not uniquely for points between the bounds. The embedded bound constructions shown in this paper yield exact answers, because they are the proper equations for bulk modulus, based on realizable materials. However, every initial bulk modulus can be realized with an infinite number of microstructures and therefore transforms to an infinite number of moduli upon substitution of the pore fill.

Our four limiting embedded bound constructions numerically appear to span the range of possible transformed bulk moduli. In the limiting case of pore fluids, two of these constructions reduce to the bounds of Gibiansky and Torquato, which illustrates that the G&T bounds are optimum. We also derive the Hashin-Shtrikman equivalent of Marion's Bounding Average Method, HS-BAM. HS-BAM predictions also reveal the nonuniqueness of solid and fluid substitution, are easy to implement, but do not span the entire range of nonuniqueness revealed by the other methods.

This work illustrates that fluid substitution and solid substitution cannot be performed uniquely without information about the pore space. If the pore space is well connected such that wave-induced pore fluid pressures are equilibrated, then Gassmann's equations are appropriate and are equal to Gibiansky and Torquato's lower bound, as well as the modified bound, $HS^{+}_{\min}$, prediction.

Disconnected pores, or unequilibrated fluid pressures cause larger changes in modulus upon fluid substitution, which are bounded by the HS^{-}_{f}, prediction as well as Gibiansky &

Torquato's upper bound. As has been shown in previous work (O'Connell and Budiansky, 1977; Mavko and Jizba, 1991; and Gurevich et al., 2009), the unequilibrated pore pressure has a much larger effect on modulus than unequilibrated viscous shear stress.

Solid substitution is inherently non-unique without detailed knowledge of the pore space geometry. The Ciz and Shapiro approximation assumes that the pore space is stiff and homogeneous, and tends to underpredict the change in bulk modulus upon solid substitution. The $HS^{+}_{\min}$, prediction in this paper also corresponds to relatively homogeneous pore stiffness. The presence of cracks and soft-grain contacts leads to larger changes in bulk modulus upon solid substitution.

Many effective medium models used in rock physics are geometry-specific. These include sphere-pack models for unconsolidated sediments, ellipsoidal-inclusion models for consolidated sediments, contact cement models for early diagenesis, and crack models for fractured rocks. Such models yield useful quantitative predictions that often fit observations.

Geometry-specific models yield unique predictions of modulus change with fluid or solid substitution. However, these predictions can be misleading, since geometry-specific models are almost always gross idealizations of actual pore microstructure. We have shown in this paper that a measurement of elastic modulus and porosity can be fit with an infinite number of geometric models; each will yield a different prediction of solid (and possibly fluid) substitution. Uncertainty in these predictions can only be improved when supported with additional information about the real pore space geometry.

6.12. Acknowledgements

This work was supported by the Stanford Rock Physics and Borehole Geophysics (SRB) Project, and U.S. Department of Energy award DE-FE0001159.

6.13. Appendix A: Numerical calculations of constructions

6.13.1. Equations for substitution of bulk modulus

Let the bulk and shear moduli of the initial pore-fill solid (or fluid) are given by: bulk $K_f^{(1)}$ and shear $G_f^{(1)}$, and the properties of the final pore-fill solid are given by: bulk $K_f^{(2)}$ and shear $G_f^{(2)}$. Also, let the elastic properties of the mineral in rock frame are: bulk K_{min} and shear G_{min}, and the rock porosity is given by ϕ.

6.13.1.1. $HS^{+}_{\min}$ construction

To calculate the change in effective bulk modulus upon substitution as predicted by the $HS^{+}_{\min}$ construction, start by first calculating the parameters f_Q and ϕ_Q from the following equations

$$K_{sat}^{(1)} = K_{min} + \frac{f_Q}{\left(K_Q^{(1)} - K_{min}\right)^{-1} + \left(1 - f_Q\right)\left(K_{min} + \frac{4}{3}G_{min}\right)^{-1}} \quad , \tag{A-1}$$

where $\phi = f_Q \phi_Q$. Expression for $K_Q^{(1)}$ is given by

$$K_Q^{(1)} = K_f^{(1)} + \frac{1 - \phi_Q}{\left(K_{min} - K_f^{(1)}\right)^{-1} + \phi_Q\left(K_f^{(1)} + \frac{4}{3}G_f^{(1)}\right)^{-1}} \quad . \tag{A-2}$$

Next, from the calculated f_Q and ϕ_Q estimate the new modulus using the following equations

$$K_{sat}^{(2)} = K_{min} + \frac{f_Q}{\left(K_Q^{(2)} - K_{min}\right)^{-1} + \left(1 - f_Q\right)\left(K_{min} + \frac{4}{3}G_{min}\right)^{-1}} \quad , \tag{A-3}$$

where,

$$K_Q^{(2)} = K_f^{(2)} + \frac{1-\phi_Q}{\left(K_{min} - K_f^{(2)}\right)^{-1} + \phi_Q\left(K_f^{(2)} + \frac{4}{3}G_f^{(2)}\right)^{-1}} \quad . \tag{A-4}$$

6.13.1.2. $HS_{\min}^{-}$ construction

The change in effective modulus as predicted by the $HS_{\min}^{-}$ construction can be calculated by equations A-5 to A-10. To estimate this change, start by calculating f_Q and ϕ_Q from the following equations:

$$K_{sat}^{(1)} = K_Q^{(1)} + \frac{1-f_Q}{\left(K_{min} - K_Q^{(1)}\right)^{-1} + f_Q\left(K_Q^{(1)} + \frac{4}{3}G_Q^{(1)}\right)^{-1}} \quad , \tag{A-5}$$

where $\phi = f_Q\phi_Q$. The expressions for $K_Q^{(1)}$ and $G_Q^{(1)}$ are given by

$$K_Q^{(1)} = K_{min} + \frac{\phi_Q}{\left(K_f^{(1)} - K_{min}\right)^{-1} + \left(1-\phi_Q\right)\left(K_{min} + \frac{4}{3}G_{min}\right)^{-1}} \quad , \tag{A-6}$$

$$G_Q^{(1)} = G_{min} + \frac{\phi_Q}{\left(G_f^{(1)} - G_{min}\right)^{-1} + \frac{2\left(1-\phi_Q\right)\left(K_{min} + 2G_{min}\right)}{5G_{min}\left(K_{min} + \frac{4}{3}G_{min}\right)}} \quad . \tag{A-7}$$

Next, calculate the new modulus using the following equations

$$K_{sat}^{(2)} = K_Q^{(2)} + \frac{1-f_Q}{\left(K_{min} - K_Q^{(2)}\right)^{-1} + f_Q\left(K_Q^{(2)} + \frac{4}{3}G_Q^{(2)}\right)^{-1}} \quad , \tag{A-8}$$

where,

$$K_Q^{(2)} = K_{min} + \frac{\phi_Q}{\left(K_f^{(2)} - K_{min}\right)^{-1} + \left(1-\phi_Q\right)\left(K_{min} + \frac{4}{3}G_{min}\right)^{-1}} \quad , \tag{A-9}$$

$$G_Q^{(2)} = G_{min} + \frac{\phi_Q}{\left(G_f^{(2)} - G_{min}\right)^{-1} + \frac{2\left(1-\phi_Q\right)\left(K_{min} + 2G_{min}\right)}{5G_{min}\left(K_{min} + \frac{4}{3}G_{min}\right)}} \quad . \tag{A-10}$$

6.13.1.3. HS_f^+ construction

The change predicted by the HS_f^+ construction can be calculated by solving equations A-11 to A-16. To estimate the substituted modulus start by calculating f_P and ϕ_P from the following equations:

$$K_{sat}^{(1)} = K_P^{(1)} + \frac{1-f_P}{\left(K_f^{(1)} - K_P^{(1)}\right)^{-1} + f_P\left(K_P^{(1)} + \frac{4}{3}G_P^{(1)}\right)^{-1}} \quad , \tag{A-11}$$

where $\phi = 1 - f_P + f_P\phi_P$. The expressions for $K_P^{(1)}$ and $G_P^{(1)}$ are given by

$$K_P^{(1)} = K_f^{(1)} + \frac{1-\phi_P}{\left(K_{min} - K_f^{(1)}\right)^{-1} + \phi_P\left(K_f^{(1)} + \frac{4}{3}G_f^{(1)}\right)^{-1}} \quad , \tag{A-12}$$

$$G_P^{(1)} = G_f^{(1)} + \frac{1-\phi_P}{\left(G_{min} - G_f^{(1)}\right)^{-1} + \frac{2\phi_P\left(K_f^{(1)} + 2G_f^{(1)}\right)}{5G_f^{(1)}\left(K_f^{(1)} + \frac{4}{3}G_f^{(1)}\right)}} \quad . \tag{A-13}$$

Next, calculate the new effective modulus using

$$K_{sat}^{(2)} = K_Q^{(2)} + \frac{1 - f_Q}{\left(K_f^{(2)} - K_Q^{(2)}\right)^{-1} + f_Q\left(K_Q^{(2)} + \frac{4}{3}G_Q^{(2)}\right)^{-1}} \quad , \tag{A-14}$$

where,

$$K_P^{(2)} = K_f^{(2)} + \frac{1 - \phi_P}{\left(K_{min} - K_f^{(2)}\right)^{-1} + \phi_P\left(K_f^{(2)} + \frac{4}{3}G_f^{(2)}\right)^{-1}} \quad , \tag{A-15}$$

$$G_P^{(2)} = G_f^{(2)} + \frac{1 - \phi_P}{\left(G_{min} - G_f^{(2)}\right)^{-1} + \frac{2\phi_P\left(K_f^{(2)} + 2G_f^{(2)}\right)}{5G_f^{(2)}\left(K_f^{(2)} + \frac{4}{3}G_f^{(2)}\right)}} \quad . \tag{A-16}$$

6.13.1.4. HS_f^- construction

The change predicted by the HS_f^- construction can be estimated by solving equations A-17 to A-20. Start by estimating f_P and ϕ_P from the following equations:

$$K_{sat}^{(1)} = K_f^{(1)} + \frac{f_P}{\left(K_P^{(1)} - K_f^{(1)}\right)^{-1} + \left(1 - f_P\right)\left(K_f^{(1)} + \frac{4}{3}G_f^{(1)}\right)^{-1}} \quad , \tag{A-17}$$

where $\phi = 1 - f_P + f_P\phi_P$. The expression for $K_P^{(1)}$ is

$$K_P^{(1)} = K_{min} + \frac{\phi_P}{\left(K_f^{(1)} - K_{min}\right)^{-1} + \left(1 - \phi_P\right)\left(K_{min} + \frac{4}{3}G_{min}\right)^{-1}} \quad , \tag{A-18}$$

Next, calculate the new effective modulus using

$$K_{sat}^{(2)} = K_f^{(2)} + \frac{f_P}{\left(K_P^{(2)} - K_f^{(2)}\right)^{-1} + \left(1 - f_P\right)\left(K_f^{(2)} + \frac{4}{3}G_f^{(2)}\right)^{-1}} \quad , \tag{A-19}$$

where,

$$K_P^{(2)} = K_{min} + \frac{\phi_P}{\left(K_f^{(2)} - K_{min}\right)^{-1} + \left(1 - \phi_P\right)\left(K_{min} + \frac{4}{3}G_{min}\right)^{-1}} \quad , \tag{A-20}$$

6.13.2. Equations for substitution of shear modulus

6.13.2.1. $HS_{\min}^{+}$ construction

To calculate the change in effective shear modulus $G_{sat}^{(1)}$ upon substitution as predicted by the $HS_{\min}^{+}$ construction, start by first calculating the parameters f_P and ϕ_Q from the following equations:

$$G_{sat}^{(1)} = G_{\min} + \frac{f_Q}{\left(G_Q^{(1)} - G_{\min}\right)^{-1} + \frac{2f_P\left(K_{\min} + 2\mu_{\min}\right)}{5G_{\min}\left(K_{\min} + \frac{4}{3}\mu_{\min}\right)}} \quad , \tag{A-21}$$

where f_P is the volume fraction of material $P^{(1)}$ (mineral point) and $f_Q = \left(1 - f_P\right)$ is the volume fraction of material $Q^{(1)}$, such that $\phi = f_Q\phi_Q$. Since material $Q^{(1)}$ is on *HS* bounds, the exact expressions for $K_Q^{(1)}$ and $G_Q^{(1)}$ are given by

$$G_Q^{(1)} = G_f^{(1)} + \frac{1 - \phi_Q}{\left(G_{min} - G_f^{(1)}\right)^{-1} + \frac{2\phi_Q\left(K_f^{(1)} + 2G_f^{(1)}\right)}{5G_f^{(1)}\left(K_f^{(1)} + \frac{4}{3}G_f^{(1)}\right)}} \quad . \tag{A-22}$$

Next, using the calculated parameters f_P and ϕ_Q estimate the new moduli using the equations

$$G_{sat}^{(2)} = G_{min} + \frac{f_Q}{\left(G_Q^{(2)} - G_{min}\right)^{-1} + \frac{2f_P\left(K_{min} + 2G_{min}\right)}{5G_{min}\left(K_{min} + \frac{4}{3}G_{min}\right)}} \quad , \tag{A-23}$$

where,

$$G_Q^{(2)} = G_f^{(2)} + \frac{1-\phi_Q}{\left(G_{min} - G_f^{(2)}\right)^{-1} + \frac{2\phi_Q\left(K_f^{(2)} + 2G_f^{(2)}\right)}{5G_f^{(2)}\left(K_f^{(2)} + \frac{4}{3}G_f^{(2)}\right)}} \quad . \tag{A-24}$$

6.13.2.2. $HS_{\min}^{-}$ construction

The predicted change in effective shear modulus using the $HS_{\min}^{-}$ construction can be calculated by equations A-25 to A-30. To estimate this change, start by calculating f_P and ϕ_Q from the following equations:

$$G_{sat}^{(1)} = G_Q^{(1)} + \frac{f_P}{\left(G_{\min} - G_Q^{(1)}\right)^{-1} + \frac{2f_Q\left(K_Q^{(1)} + 2G_Q^{(1)}\right)}{5G_Q^{(1)}\left(K_Q^{(1)} + \frac{4}{3}G_Q^{(1)}\right)}} \quad , \tag{A-25}$$

where f_P is the volume fraction of material $P^{(1)}$ (mineral point) and $f_Q = \left(1 - f_P\right)$ is the volume fraction of material $Q^{(1)}$, such that $\phi = f_Q\phi_Q$. The expressions for $K_Q^{(1)}$ and $G_Q^{(1)}$ are given by

$$K_Q^{(1)} = K_{min} + \frac{\phi_Q}{\left(K_f^{(1)} - K_{min}\right)^{-1} + \left(1-\phi_Q\right)\left(K_{min} + \frac{4}{3}G_{min}\right)^{-1}} \quad , \tag{A-26}$$

$$G_Q^{(1)} = G_{min} + \frac{\phi_Q}{\left(G_f^{(1)} - G_{min}\right)^{-1} + \frac{2\left(1-\phi_Q\right)\left(K_{\min} + 2G_{min}\right)}{5G_{min}\left(K_{min} + \frac{4}{3}G_{min}\right)}} \quad . \tag{A-27}$$

Next, calculate the new moduli using the following equations

$$G_{sat}^{(2)} = G_Q^{(2)} + \frac{f_P}{\left(G_{min} - G_Q^{(2)}\right)^{-1} + \frac{2f_Q\left(K_Q^{(2)} + 2G_Q^{(2)}\right)}{5G_Q^{(2)}\left(K_Q^{(2)} + \frac{4}{3}G_Q^{(2)}\right)}} \quad , \tag{A-28}$$

where,

$$K_Q^{(2)} = K_{min} + \frac{\phi_Q}{\left(K_f^{(2)} - K_{min}\right)^{-1} + \left(1-\phi_Q\right)\left(K_{min} + \frac{4}{3}G_{min}\right)^{-1}} \quad , \tag{A-29}$$

$$G_Q^{(2)} = G_{min} + \frac{\phi_Q}{\left(G_f^{(2)} - G_{min}\right)^{-1} + \frac{2\left(1-\phi_Q\right)\left(K_{min} + 2G_{min}\right)}{5G_{min}\left(K_{min} + \frac{4}{3}G_{min}\right)}} \quad . \tag{A-30}$$

6.13.2.3. HS_f^+ construction

The change predicted by the HS_f^+ construction can be calculated by equations A-31 to A-36. To estimate the substituted moduli start by calculating f_P and ϕ_Q from the following equations:

$$G_{sat}^{(1)} = G_Q^{(1)} + \frac{f_P}{\left(G_f^{(1)} - G_Q^{(1)}\right)^{-1} + \dfrac{2f_Q\left(K_Q^{(1)} + 2G_Q^{(1)}\right)}{5G_Q^{(1)}\left(K_Q^{(1)} + \dfrac{4}{3}G_Q^{(1)}\right)}} \quad , \tag{A-31}$$

where f_P is the volume fraction of material $P^{(1)}$ (pore material) and $f_Q = \left(1 - f_P\right)$ is the volume fraction of material $Q^{(1)}$, such that $\phi = \left(1 - f_Q\right) + f_Q\phi_Q$. The expressions for $K_Q^{(1)}$ and $G_Q^{(1)}$ are given by

$$K_Q^{(1)} = K_f^{(1)} + \frac{1-\phi_Q}{\left(K_{min} - K_f^{(1)}\right)^{-1} + \phi_Q\left(K_f^{(1)} + \dfrac{4}{3}G_f^{(1)}\right)^{-1}} \quad , \tag{A-32}$$

$$G_Q^{(1)} = G_f^{(1)} + \frac{1-\phi_Q}{\left(G_{min} - G_f^{(1)}\right)^{-1} + \dfrac{2\phi_Q\left(K_f^{(1)} + 2G_f^{(1)}\right)}{5G_f^{(1)}\left(K_f^{(1)} + \dfrac{4}{3}G_f^{(1)}\right)}} \quad . \tag{A-33}$$

Next, calculate the new effective moduli using

$$G_{sat}^{(2)} = G_Q^{(2)} + \frac{f_P}{\left(G_f^{(2)} - G_Q^{(2)}\right)^{-1} + \dfrac{2f_Q\left(K_Q^{(2)} + 2G_Q^{(2)}\right)}{5G_Q^{(2)}\left(K_Q^{(2)} + \dfrac{4}{3}G_Q^{(2)}\right)}} \quad , \tag{A-34}$$

where,

$$K_Q^{(2)} = K_f^{(2)} + \frac{1-\phi_Q}{\left(K_{min} - K_f^{(2)}\right)^{-1} + \phi_Q\left(K_f^{(2)} + \dfrac{4}{3}G_f^{(2)}\right)^{-1}} \quad , \tag{A-35}$$

$$G_Q^{(2)} = G_f^{(2)} + \frac{1-\phi_Q}{\left(G_{min} - G_f^{(2)}\right)^{-1} + \frac{2\phi_Q\left(K_f^{(2)} + 2G_f^{(2)}\right)}{5G_f^{(2)}\left(K_f^{(2)} + \frac{4}{3}G_f^{(2)}\right)}} \quad . \tag{A-36}$$

6.13.2.4. HS_f^- construction

The change predicted by the HS_f^- construction can be estimated by solving equations A-37 to A-40. Start by estimating f_Q and ϕ_P from the following equations:

$$G_{sat}^{(1)} = G_f^{(1)} + \frac{f_P}{\left(G_P^{(1)} - G_f^{(1)}\right)^{-1} + \frac{2f_f\left(K_f^{(1)} + 2G_f^{(1)}\right)}{5G_f^{(1)}\left(K_f^{(1)} + \frac{4}{3}G_f^{(1)}\right)}} \quad , \tag{A-37}$$

where $f_Q = \left(1 - f_P\right)$ and $\phi = \left(1 - f_Q\right) + f_Q\phi_Q$. The expressions for $K_P^{(1)}$ and $G_P^{(1)}$ are given by

$$G_P^{(1)} = G_{min} + \frac{\phi_P}{\left(G_f^{(1)} - G_{min}\right)^{-1} + \frac{2\left(1-\phi_P\right)\left(K_{min} + 2G_{min}\right)}{5G_{min}\left(K_{min} + \frac{4}{3}G_{min}\right)}} \quad . \tag{A-38}$$

Next, calculate the new effective moduli using

$$G_{sat}^{(2)} = G_f^{(2)} + \frac{f_P}{\left(G_P^{(2)} - G_f^{(2)}\right)^{-1} + \frac{2f_f\left(K_f^{(2)} + 2G_f^{(2)}\right)}{5G_f^{(2)}\left(K_f^{(2)} + \frac{4}{3}G_f^{(2)}\right)}} \quad , \tag{A-39}$$

where,

$$G_P^{(2)} = G_{min} + \frac{\phi_P}{\left(G_f^{(2)} - G_{min}\right)^{-1} + \frac{2\left(1-\phi_P\right)\left(K_{min} + 2G_{min}\right)}{5G_{min}\left(K_{min} + \frac{4}{3}G_{min}\right)}} \quad . \tag{A-40}$$

6.14. Appendix B: Closed form solutions

6.14.1. Bulk modulus

Starting with a solid or fluid saturated rock of original effective bulk modulus $K_{sat}^{(1)}$ (mineral moduli = K_{min}, G_{min}; original pore filling moduli = $K_f^{(1)}$, $G_f^{(1)}$), the two embedded bounds on the effective bulk modulus upon substitution with a new pore solid or fluid (moduli = $K_f^{(2)}$, $G_f^{(2)}$) can be calculated as

$$\frac{K_{sat}^{(2)HS_{\min}^{+}}}{K_{min} - K_{sat}^{(2)HS_{\min}^{+}}} = \frac{K_f^{(2)}}{\phi\left(K_{min} - K_f^{(2)}\right)} + \frac{4G_{min}\left(G_f^{(2)} - G_f^{(1)}\right) + \Delta}{\left(G_{min} - G_f^{(1)}\right)\left(4G_f^{(2)} + 3K_{min}\right)} \quad , \tag{B-1}$$

where

$$\Delta = \frac{4G_{min}K_{min}\left(G_f^{(1)} - G_f^{(2)}\right) + 3K_{min}K_{bc}^{(1)}\left(G_{min} - G_f^{(2)}\right) + 4G_f^{(2)}K_{bc}^{(1)}\left(G_{min} - G_f^{(1)}\right)}{\left(K_{min} - K_{bc}^{(1)}\right)} \quad , \tag{B-2}$$

and

$$K_{bc}^{(1)} = \frac{K_{sat}^{(1)}\left(\frac{\phi K_{\min}}{K_f^{(1)}} + 1 - \phi\right) - K_{\min}}{\frac{\phi K_{\min}}{K_f^{(1)}} + \frac{K_{sat}^{(1)}}{K_{\min}} - 1 - \phi} \quad . \tag{B-3}$$

$K_{sat}^{(2)HS_{\min}^{+}}$ is identical to Gassmann or C&S prediction if $G_f^{(2)} = G_f^{(1)}$. Explicit expression

for $K_{sat}^{(2)HS_f^-}$ is not presented here due to its complicated functional form, readers should calculate $K_{sat}^{(2)HS_f^-}$ using equations A-8 to A-10. Note that the difference between the two embedded bounds, $K_{sat}^{(2)HS_f^+}$ and $K_{sat}^{(2)HS_f^-}$, depends on the original effective bulk modulus.

If one instead starts with a dry or drained rock (effective dry bulk modulus K_{dry}) then the two embedded bounds on the effective bulk modulus upon substitution with a new pore solid or fluid (moduli = K_f, G_f) are

$$K_{sat}^{HS^+_{\min}} = \frac{\phi\left(\frac{1}{K_{\min}} - \frac{1}{K_f}\right) + \left(\frac{1}{K_{\min}} - \frac{1}{K_{bc}}\right)}{\frac{\phi}{K_{bc}}\left(\frac{1}{K_{\min}} - \frac{1}{K_f}\right) + \frac{1}{K_{\min}}\left(\frac{1}{K_{\min}} - \frac{1}{K_{bc}}\right)} \quad , \tag{B-4}$$

where K_{bc} is

$$K_{bc} = \frac{(1-\phi)\left(\frac{1}{K_{\min}} - \frac{1}{K_{dry}}\right) + \left(\frac{3\phi}{4}\right)\left(\frac{1}{G_{\min}} - \frac{1}{G_f}\right)}{\left(\frac{3\phi}{4}\right)\left(\frac{1}{K_{\min}G_{\min}} - \frac{1}{K_{dry}G_f}\right) + \frac{1}{K_{\min}}\left(\frac{1}{K_{\min}} - \frac{1}{K_{dry}}\right)} \quad , \tag{B-5}$$

and

$$K_{sat}^{HS_f^-} = \left[\frac{\phi}{K_f + (4/3)G_{\min}} + \frac{1-\phi}{K_{\min} + (4/3)G_{\min}}\right]^{-1} - (4/3)G_{\min} \quad . \tag{B-6}$$

Starting with a solid or fluid saturated rock (effective bulk modulus K_{sat}) the two embedded bounds on the dry or drained bulk modulus are

$$K_{dry}^{HS^+_{\min}} = \frac{K_{bc}\left(\frac{1}{K_{\min}} + \frac{3\phi}{4G_f}\right) + \phi - 1}{\frac{K_{bc}}{K_{\min}}\left(\frac{1}{K_{\min}} + \frac{3\phi}{4G_{\min}}\right) - \frac{(1-\phi)}{K_{\min}} + \frac{3\phi}{4}\left(\frac{1}{G_f} - \frac{1}{G_{\min}}\right)} \quad , \tag{B-7}$$

where K_{bc} in terms of K_{sat} is

$$K_{bc} = \frac{K_{sat}\left(\frac{\phi K_{\min}}{K_f} + 1 - \phi\right) - K_{\min}}{\frac{\phi K_{\min}}{K_f} + \frac{K_{sat}}{K_{\min}} - 1 - \phi} \quad , \tag{B-8}$$

and

$$K_{dry}^{HS^-_f} = 0 \quad . \tag{B-9}$$

6.14.2. **Shear modulus**

The shear solid-to-solid substitution equation using the $HS^+_{\min}$ construction (which seem to predict the smallest change along with the $HS^-_{\min}$ construction) can be simplified as

$$G_{sat}^{HS^+_{\min}} = \frac{\phi\left(\frac{1}{G_{\min}} - \frac{1}{G_f}\right) + \left(\frac{1}{G_{\min}} - \frac{1}{G_{bc}}\right)}{\frac{\phi}{G_{bc}}\left(\frac{1}{G_{\min}} - \frac{1}{G_f}\right) + \frac{1}{G_{\min}}\left(\frac{1}{G_{\min}} - \frac{1}{G_{bc}}\right)} \quad , \tag{B-10}$$

where,

$$G_{bc} = \frac{(1-\phi)\left(\frac{1}{G_{min}} - \frac{1}{G_{dry}}\right) + \phi\left(\frac{1}{z_{min}} - \frac{1}{z_f}\right)}{\frac{1}{G_{min}}\left(\frac{1}{G_{min}} - \frac{1}{G_{dry}}\right) + \phi\left(\frac{1}{G_{min}z_{min}} - \frac{1}{z_f G_{dry}}\right)} \quad , \tag{B-11}$$

and

$$z = \frac{G}{6}\frac{(9K+8G)}{(K+2G)} \quad . \tag{B-12}$$

6.15. References

Andra, H., N. Combaret, J. Dvorkin, E. Glatt, J. Han, M. Kabel, Y. Keehm, F. Krzkilla, M. Lee, C. Madonna, M. Marsh, T. Mukerji, E. H. Saenger, R. Sain, N. Saxena, D. Ricker, A. Wiegmann, X. Zhan, Digital rock physics benchmarks - Part II: Computing effective properties: Computers & Geosciences, **50**, 25-32.

Arns, C. H., M. A. Knackstedt, W. V. Pinczewski, E. J. Garboczi, 2002, Computation of linear elastic properties from microtomographic images: methodology and agreement between theory and experiment: Geophysics, **67** (5), P1395–P1405

Beran, M.J. and Molyneux, J., 1966, Use of classical variational principles to determine bounds for the effective bulk modulus in heterogeneous media, Quarterly of Applied Mathematics, 24, 107-118.

Berryman, J.G., 1980. Long-wavelength propagation in composite elastic media. *J. Acoust. Soc. Am.*, 68, 1809–1831.

Berryman, J.G. and Milton, G.W., 1988, Microgeometry of random composites and porous media, Journal of Physics D: Applied Physics, 21, 87-94.

Biot, M.A., 1962, Mechanics of deformation and acoustic propagation in porous media, J. Applied Physics, 33, 1482-1498.

Brown, R., and Korringa, J., 1975. On the dependence of the elastic properties of a porous rock on the compressibility of the pore fluid. *Geophys.*, 40, 608–616.

Boucher, S., 1974, On the effective moduli of isotropic two-phase elastic composites, Journal of Composite Materials, 8, 82

Chapman, M., Zatsepin, S. V., and Crampin, S., 2002. Derivation of a microstructural poroelasticity model. *Geophys. J. Int.*, 151, 427-451.

Ciz, R., and Shapiro, S., 2007. Generalization of Gassmann equations for porous media saturated with a solid material. *Geophysics*, 72, A75-A79.

Garboczi, E., and J. G. Berryman, 2001, Elastic moduli of a material containing composite inclusions: effective medium theory and finite element computations: Mechanics of Materials, **33**, 455–470.

Gassmann, F., 1951. Über die Elastizität poröser Medien. *Vier. der Natur. Gesellschaft in Zürich*, 96, 1–23.

Gibiansky, L.V., and Sigmund, O., 2000, Multiphase composites with extremal bulk modulus, Journal of the Mechanics and Physics of Solids, 48, 461-498.

Gibiansky, L, and Torquato, S., 2000, Rigorous connection between physical properties of porous rocks, Journal of Geophysical Research, 103, 23911-23923.

Gurevich, B., Makarynska, D., and Pervukhina, M., 2009, Ultrasonic moduli for fluid-saturated rocks: Mavko-Jizba relations rederived and generalized, Geophysics, 74, N25-N30.

Hashin, Z., and Shtrikman, S., 1963. A variational approach to the elastic behavior of multiphase materials. *J. Mech. Phys. Solids*, 11, 127–140.

Kanter, Y., and Bergman, D.J., 1984, Journal of the Mechanics and Physics of Solids, 32, 41-62.

Liu, L., 2011, New optimal microstructures and restrictions on the attainable Hashin-Shtrikman bounds for multiphase composite materials, Philosophical Magazine Letters.

Marion, D. and Nur, A., 1991, Pore-filling material and its effect on velocity in rocks, Geophysics, 56, 225-230.

Mavko, G., and Nur, A., 1975. Melt squirt in the asthenosphere. *J. Geophys. Res.*, 80, 1444–1448.

Mavko, G., and Jizba, D., 1991. Estimating grain-scale fluid effects on velocity dispersion in rocks. *Geophys*., 56, 1940–1949.

Milton, G.W., 1984a, Microgeometries corresponding exactly with effective medium theories, in: D.L. Johnson and P.N. Sen eds, Physics and Chemistry of Porous Media, AIP Conf. Proc. 107, American Institute of Physics, 66.

Milton, G.W., 1984b, Modeling the properties of composites by laminates, talk presented at the Workshop on Homogenization and Effective Moduli of Materials and Media, Institute for Mathematics and its Applications, Minneapolis.

Milton, G.W., 2002, The Theory of Composites, Cambridge University Press.

Norris, A.N., 1985. A differential scheme for the effective moduli of composites. *Mechanics of Materials*, 4, 1–16.

O'Connell, R., and B. Budiansky, 1977,Viscoelastic properties of fluid-saturated cracked solids: Journal of Geophysical Research, 82, 5719–5735.

Saxena, N. and G. Mavko, 2014, Exact equations for fluid and solid substitution: Geophysics, 79, 3, L21–L32.

Stoll, R.D., and Bryan, G.M., 1970. Wave attenuation in saturated sediments. *J. Acoust. Soc. Am.*, 47, 1440–1447.

Walpole, L., 1966. On bounds for the overall elastic moduli of inhomogeneous systems Journal of the Mechanics and Physics of Solids 14, 151-162.

Wu, T.T., 1966. The effect of inclusion shape on the elastic moduli of a two-phase material. *Int. J. Solids Structures*, 2, 1–8.

Yan, F. and Han, D.-H., 2011, Theoretical validation of fluid substitution by Hashin-Shtrikman bounds, 2011 SEG Annual Meeting, San Antonio.

Zou, W., He, Q., Huang, J., and Zheng, Q., 2010, Eshelby's problem of non-elliptical inclusions, Journal of the Mechanics and Physics of Solids, 58, 346-372.

Chapter 7

Estimating effects of grain-scale mechanisms on seismic velocity dispersion (solid-squirt)

7.1. Abstract

Laboratory measurements of rocks saturated with high viscosity fluids (such as heavy-oil, magma, kerogen, etc.) often exhibit considerable dispersion, which is usually under estimated by the Biot theory. Over the years, grain-scale dispersion mechanisms such as squirt (local-flow) and shear-relaxation have been more successful in explaining the measured dispersion. We present a new method to quantify the combined high-frequency effects of squirt and shear-dispersion (solid-squirt) on the elastic properties of rocks saturated with viscous fluids. Viscous fluid at high-frequencies is idealized as an elastic

solid of finite shear modulus, hydraulically locked in stiff and soft pores at high-frequencies. This method entails performing solid substitution in stiff pores of a dry rock frame which is unrelaxed due to solid-filled soft pores. The unrelaxed frame stiffness solutions require information on the pressure dependency of the rock stiffness and porosity. This method does not have any adjustable parameters and all required inputs can be directly measured. With various laboratory and numerical examples, we note that accounting for combined effects of squirt and shear-dispersion is necessary to explain laboratory measured velocities of rocks saturated with fluids of high viscosity. Predictions of the new method are in good agreement with laboratory data.

7.2. Introduction

Measured seismic wave velocities in fluid-saturated rocks are often much higher than those predicted by the Biot theory (Biot, 1956), which accounts for rock stiffening or increase in velocity due to viscous-fluid motion induced by the gradient of the passing wave (global flow). To explain this apparent inadequacy of the Biot-dispersion mechanism, over the years, various other fluid motion related dispersion mechanisms have been proposed and investigated. Mavko and Nur (1975) and O'Connell and Budiansky (1977) were the first to study the grain-scale local flow or squirt-flow mechanism - referred as the "squirt-dispersion". This mechanism accounts for the rock stiffening due to oscillatory movement of viscous-fluid in-and-out of compliant (soft) pores. This grain-scale fluid motion was neglected in Biot's larger scale global flow formulation. In the high-frequency limit, the fluid in the soft pores becomes hydraulically disconnected from the stiff pore space; thus in this limit rock stiffening due to unrelaxed squirt flow (squirt-dispersion) can be modeled as an elastic problem of fluid substitution in a rock with disconnected soft pores, for which a rigorous upper bound is given by Gibiansky and Torquato (2000). Biot (1962a,b) had also hinted towards inclusion of a similar grain-scale flow mechanism into his equations by the invoking the correspondence principle. Over the years, combined effects of Biot and squirt-dispersion have been studied; just a few of considerably many studies on this topic are: Stoll and Bryan (1970), Mavko and Jizba (1991), Dvorkin and

Nur (1993), Dvorkin et al. (1995), Hudson et al. (1996), Endres and Knight (1997), Chapman et al. (2002), Gurevich et al., (2009), Jakobsen and Chapman (2009).

Another dispersion mechanism related to wave-induced fluid motion is the so-called "patchy-saturation" mechanism which, much like squirt flow, accounts for rock stiffening due to pressure gradients between rock pockets saturated with soft and stiff fluids (Johnson, 2001; Pride et al., 2004). The patchy-saturation mechanism can also be extended to include other so-called "meso-scale" dispersion mechanisms, which account for rock stiffening due to viscous-fluid motion induced by any other source of heterogeneity in compliance, such as: inter-bedding in sandstone, dual porosity, etc. Meso-scale mechanisms occur at a larger spatial scale than the grain-scale effects of squirt-dispersion. We restrict this discussion to situations where no meso-scale heterogeneity in compliance exists; this mechanism will not be discussed further.

Walsh (1965) investigated a different grain-scale dispersion mechanism: "shear-relaxation" or "shear-dispersion", which unlike the mechanism already discussed, is associated with rate-dependent shear tractions induced on the pore boundaries. In the high frequency limit, this mechanism mimics the behavior of a rock with solid-filled pores. In geophysics, the shear-relaxation mechanism has been largely ignored, since shear stresses relax too quickly in rocks saturated with low viscosity fluids. Frequencies at which squirt (f_{squirt}) and shear (f_{shear}) dispersion begin to take effect can be expressed as (O'Connell and Budiansky, 1977, Mavko et al., 2009)

$$f_{squirt} > \frac{K_{dry}\alpha^3}{\eta}, \; f_{shear} > \frac{G_{min}\alpha}{2\pi\eta}. \tag{7.1}$$

In equation 7.1, α is the aspect ratio of soft pores, K_{dry} is the dry rock bulk modulus and G_{min} is the shear modulus of the mineral in rock frame. For rocks saturated with low viscosity fluids (e.g., gas, water, light-oil, etc) effects of shear-dispersion on rock stiffness or seismic velocity can be ignored if measurement frequency is less than ~ 10 MHz. As the fluid viscosity increases, (e.g., cold heavy-oil, kerogen, glycerol, lava, slush ice, etc) both shear and squirt-dispersion mechanisms start to occur at much lower frequencies, while

Biot-dispersion typically occurs at a much higher frequency > 1 GHz. Mavko and Jizba (1991) proposed a quantitative model to estimate the effect of squirt-dispersion on the stiffness of rocks saturated with low viscosity liquids. Assuming a binary pore space divided between stiff and soft pores, which are hydraulically disconnected. This model predicts the *high frequency* or the *unrelaxed* rock frame stiffness: when the stiff pores are drained (empty) and the soft pores are undrained (fluid-saturated); Mavko-Jizba named this the "unrelaxed frame" stiffness. This prediction is entirely based on usually known quantities such as the dry-rock stiffness, porosity, elastic properties of rock constituents, and measurable quantities like soft porosity and high-pressure dry rock stiffness. Thus, the model does not involve any heuristic adjustable parameters such as pore-aspect ratios, which are usually poorly determined and gross idealizations of the pore space. Mukerji and Mavko (1994) extended the Mavko-Jizba relations to the case of anisotropic rocks. In this paper, we restrict our discussion to isotropic rocks.

The Mavko-Jizba relations were derived using reciprocity and superposition, but recently these relations have also been derived independently by Berryman (2007) and Gurevich et al. (2009) using discontinuity formalism of Sayers and Kachanov (1995). Gurevich et al. (2009) also extended the Mavko-Jizba relations to the case of pore-saturating gases, which reduce to Mavko-Jizba relations for liquids. The generalized Mavko-Jizba relations as derived by Gurevich et al. (2009) are

$$\frac{1}{K_{uf}^{(P)}} = \frac{1}{K_{dry}^{(HP)}} + \frac{1}{\dfrac{1}{\dfrac{1}{K_{dry}^{(P)}} - \dfrac{1}{K_{dry}^{(HP)}}} + \dfrac{1}{\left(\dfrac{1}{K_f} - \dfrac{1}{K_{min}}\right)\phi_{soft}}} \tag{7.2}$$

and

$$\frac{1}{\mu_{uf}^{(P)}} = \frac{1}{\mu_{dry}^{(P)}} - \frac{4}{15}\left(\frac{1}{K_{dry}^{(P)}} - \frac{1}{K_{uf}^{(P)}}\right) \tag{7.3}$$

where $K_{uf}^{(P)}$ and $\mu_{uf}^{(P)}$ are the unrelaxed frame bulk and shear moduli at confining pressure P, respectively; $K_{dry}^{(P)}$ and $\mu_{dry}^{(P)}$ are the corresponding dry rock moduli; $K_{dry}^{(HP)}$ is the dry rock bulk modulus at the highest available confining pressure, i.e., $P = HP$, such that all soft pores are closed or filled with the frame mineral; ϕ_{soft} is the soft (crack-like) porosity. K_f and K_{min} are bulk moduli of the pore-fluid and the mineral in the rock frame, respectively. For rocks with low-viscosity fluids, combining the Mavko-Jizba-Gurevich relations (in equations 7.2 and 7.3) with Biot's equations, high-frequency saturated or undrained rock stiffness can be predicted, which is found to be in good agreement with laboratory data (Mavko and Jizba, 1991; Wulff and Burkhardt, 1997; Adam and Otheim, 2013).

For rocks saturated with high viscosity pore fluid, the Mavko-Jizba-Gurevich relations fail to predict the high-frequency limit of the unrelaxed frame, since these do not include the overall rock stiffening due to shear-dispersion. Such effects can be substantial as we will discuss with laboratory data examples in this paper. In this paper, we derive relations for unrelaxed frame moduli which account for the combined effects of squirt and shear-dispersion (solid-squirt). The unrelaxed frame contains soft pores filled with solid or high viscosity fluid. As with the Mavko-Jizba-Gurevich relations, we do not assume any specific pore shape. In the limit of low-viscosity fluids, predictions of the extended unrelaxed frame moduli are identical to those predicted by the Mavko-Jizba-Gurevich method in equations 7.2 and 7.3. The remaining stiff pores are then filled with our solid substitution relations (Mavko and Saxena, 2013; Saxena and Mavko, 2014) to predict the saturated or undrained rock bulk and shear moduli.

7.3. Saturated rock stiffness

Using the viscoelastic correspondence principle (Fung, 1965) the viscoelastic pore fill can be represented as a solid pore fill whose shear modulus is complex. For example, a Newtonian viscous fluid of viscosity η can be modeled with a complex shear modulus $\mu_f \approx 2\pi i f \eta$; where i is the imaginary unit number and f is the frequency. Similarly, a

Maxwell material has a complex shear modulus $\mu_f \approx 2\pi i f\eta/(1+2\pi i f\eta/\mu_\infty)$ where μ_∞ is the shear modulus at infinite frequency $(f \to \infty)$.

Recently we proposed the "embedded bound method" (Mavko and Saxena; 2013; Saxena and Mavko, 2014), to predict the change in effective moduli (bulk and shear) upon change in pore fill material in a two-phase isotropic composite - i.e., fluid and solid-substitution. The only inputs required are pore fill volume fraction (or porosity), elastic properties of constituents, and the initial effective bulk and shear moduli. This approach is *rigorous*, and the estimates are always *realizable*, since the method is based on the recursive use of Hashin-Shtrkiman (HS) bounds (Hashin and Shtrikman, 1963). Each substituted effective modulus prediction is exact and corresponds to a specific load-induced pores stress state (Saxena and Mavko, 2014), thus substitution is inherently non-unique - unless *extra* information on rock microstructure apart from just porosity is available. Therefore, embedded bounds predict a range of substituted effective moduli. The smallest saturated effective bulk modulus predicted by the embedded bound method starting with the measured dry rock bulk modulus (referred here as the lower embedded bound for effective bulk modulus), can be compactly written as

$$K_{sat} = K_{bc} + \frac{\left(1-\frac{K_{bc}}{K_{min}}\right)^2}{\frac{\phi}{K_f}+\frac{1-\phi}{K_{min}}-\frac{K_{bc}}{(K_{min})^2}} \quad , \tag{7.4}$$

where

$$K_{bc} = \frac{(1-\phi)\left(\frac{1}{K_{min}}-\frac{1}{K_{dry}}\right)+\frac{3\phi}{4}\left(\frac{1}{\mu_{min}}-\frac{1}{\mu_f}\right)}{\frac{1}{K_{min}}\left(\frac{1}{K_{min}}-\frac{1}{K_{dry}}\right)+\frac{3\phi}{4}\left(\frac{1}{K_{min}\mu_{min}}-\frac{1}{\mu_f K_{dry}}\right)} \quad . \tag{7.5}$$

In equations 7.4 and 7.5, K_{min} and K_f are the bulk moduli of the mineral in the rock frame and pore fill material, respectively; μ_{min} and μ_f are the shear moduli of the mineral in the

rock frame and pore fill material, respectively; K_{sat} and K_{dry} are the saturated (solid-filled) and dry rock bulk moduli, respectively; ϕ is the porosity.

Saxena and Mavko (2014) have shown that the relation in equation 7.4 can be described as an exact generalization of the original Gassmann's bulk modulus equation (Gassmann, 1951) to the case of solid-filled rocks for which compression-induced mean stress (pressure) in pores is homogeneous. When pores are occupied by an ideal fluid, i.e., $\mu_f = 0$, equation 7.4 reduces to Gassmann's equation. If the induced mean stress in the pore space is heterogeneous, for example due to the presence of soft pores, the true change in effective bulk modulus will be larger than that predicted by equations 7.4 and 7.5, capped by an upper bound. Detailed expressions can be found in Mavko and Saxena (2013). Similarly, the corresponding relation for the smallest change in saturated shear modulus upon substitution can be compactly written as (referred as the lower embedded bound for effective shear modulus):

$$\mu_{sat} = \mu_{bc} + \frac{\left(1 - \dfrac{\mu_{bc}}{\mu_{min}}\right)^2}{\dfrac{\phi}{\mu_f} + \dfrac{1-\phi}{\mu_{min}} - \dfrac{\mu_{bc}}{(\mu_{min})^2}} \quad , \tag{7.6}$$

where

$$\mu_{bc} = \frac{(1-\phi)\left(\dfrac{1}{\mu_{min}} - \dfrac{1}{\mu_{dry}}\right) + \dfrac{3\phi}{4}\left(\dfrac{1}{\chi_{min}} - \dfrac{1}{\chi_f}\right)}{\dfrac{1}{\mu_{min}}\left(\dfrac{1}{\mu_{min}} - \dfrac{1}{\mu_{dry}}\right) + \dfrac{3\phi}{4}\left(\dfrac{1}{\mu_{min}\chi_{min}} - \dfrac{1}{\chi_f \mu_{dry}}\right)} \quad , \tag{7.7}$$

$$\chi = \frac{\mu}{8}\frac{9K + 8\mu}{K + 2\mu} \quad . \tag{7.8}$$

In equations 7.6 and 7.7, μ_{sat} and μ_{dry} are the saturated (solid-filled) and dry rock shear moduli, respectively. When pores are occupied by an ideal fluid, i.e., $\mu_f = 0$, equation 7.6

reduces to Gassmann's shear modulus substitution equation which predicts no change upon fluid substitution.

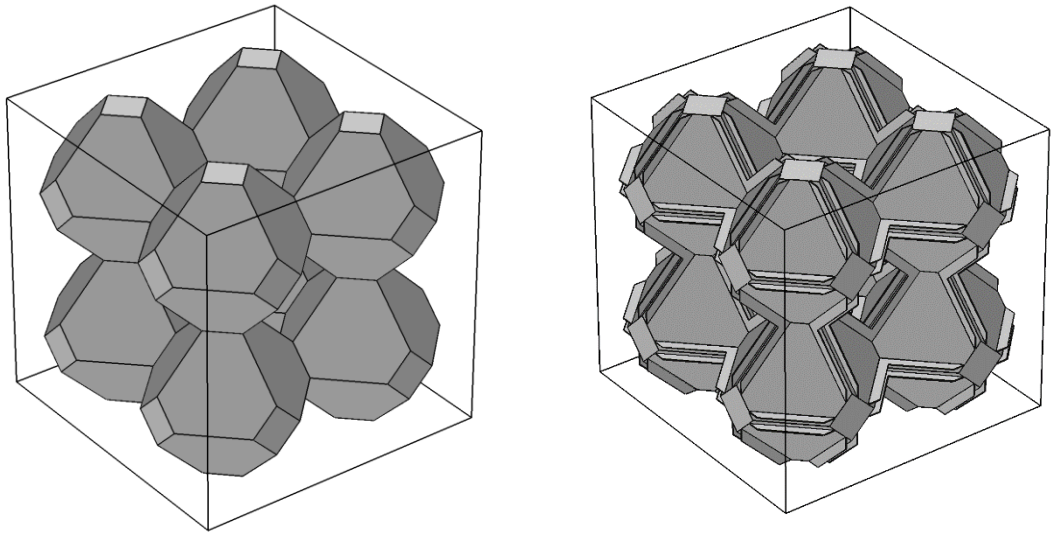

(a) (b)

Figure 7.1: Digital composites (a) only stiff pores and no soft pores (b) stiff and soft pores. Pores are shown in gray and the mineral is transparent.

With the aid of a numerical simulation, we now show that if a rock has identical stiff pores and is devoid of soft pores then our solid substitution relations in equations 7.4-7.8 provide reasonably accurate effective stiffness estimates, this is so since for such a rock induced stresses are relatively homogenous. Consider two digital composites with porosity 0.38 shown in Figure 7.1. Both composites have identical stiff pores, but the composite in Figure 7.1b has some additional flat cracks (soft pores) around the grain contacts (soft porosity of 0.006 and aspect ratio $\approx$ 0.05). For both these composites, we use the finite element method (FEM) to calculate the dry rock effective bulk and shear moduli, assuming quartz ($K_{min} = 36$ GPa; $\mu_{min} = 45$ GPa) as the frame mineral. Next, starting with the FEM calculated dry rock moduli, for a pore fill bulk modulus of 2.25 GPa and a range of pore fill shear moduli varying between 10^{-6} GPa (fluid-case) to 2.5 GPa, we predict the saturated moduli using the embedded bounds. These predictions are compared with the FEM calculated saturated moduli in Figures 7.2a-7.2b for the composite with no soft pores, and in Figures 7.2c-7.2d for the composite with soft pores. We note that the FEM calculated

moduli for the composite without soft pores fall very close to the lower embedded bound predictions. However, the corresponding moduli for the composite with soft pores are much larger when compared to the lower embedded bound prediction, however still capped by the upper embedded bound.

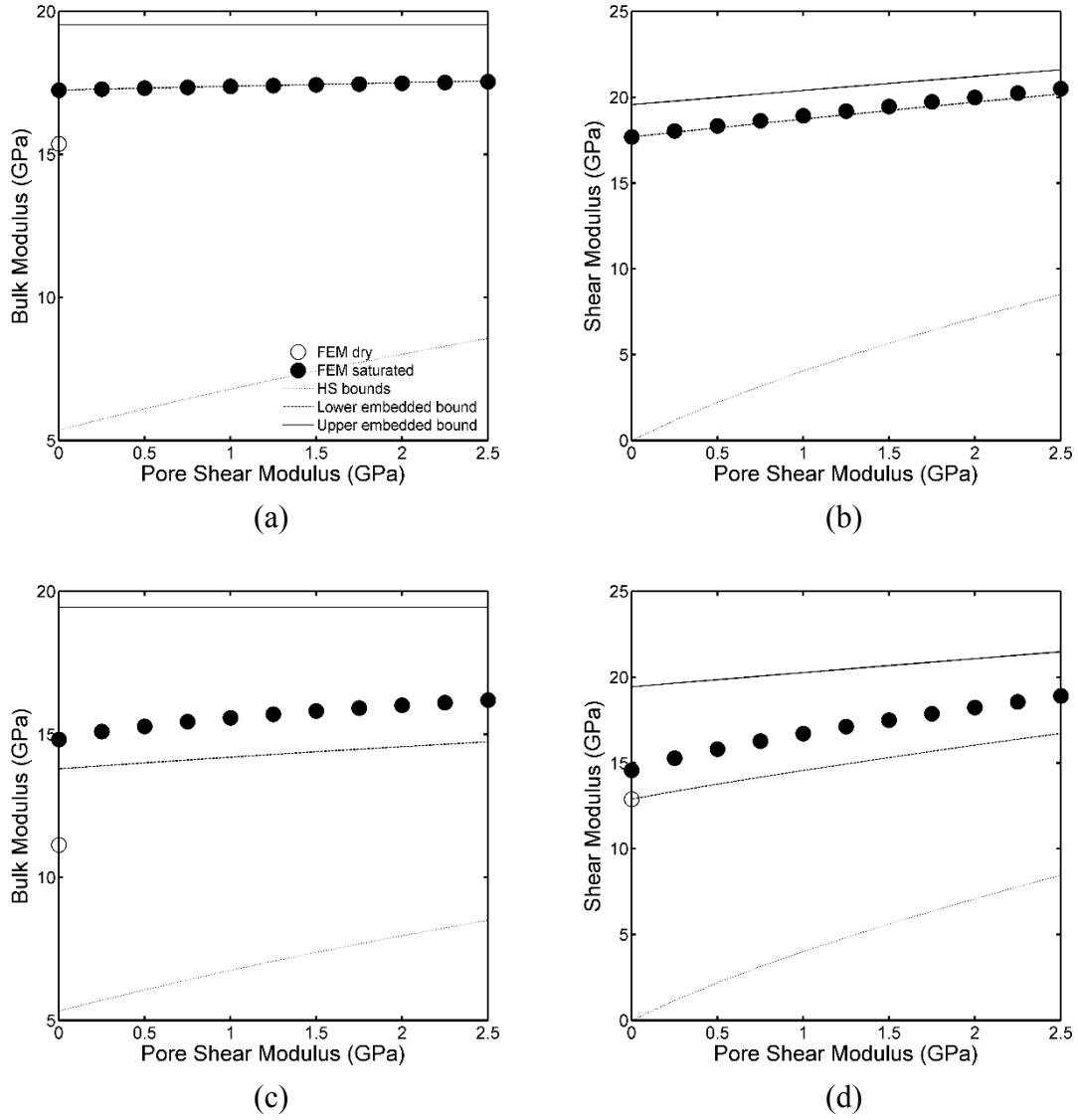

Figure 7.2: Dry and saturated elastic moduli of the composites shown in Figure 7.1, calculated using the FEM for a range of pore fill shear moduli (μ_f) and a fixed pore fill bulk modulus (K_f) of 2.25 GPa. (a) and (b) show bulk and shear moduli of the uncracked composite shown in Figure 7.1a, respectively; whereas (c) and (d) show bulk and shear moduli of the cracked composite shown in Figure 7.1b, respectively. Elastic moduli of the cracked composite deviate from the lower embedded bound predictions shown in dashed curves.

The above example shows that for composites with a mix of stiff and soft pores, the true change in effective moduli will be larger than that predicted by the lower embedded bound relations in equations 7.4-7.8. Even though the largest possible change upon fluid or solid substitution can be contained by the upper embedded bound, the range predicted is quite wide. Also, we must note that if complete details of the pore geometry are available, exact substitution can be achieved for both composites (with or without soft pores) using the solutions obtained by Saxena and Mavko (2014), for instance, with the aid of FEM simulations using digital rock images. However, rock images may not be able to fully capture the presence of thin compliant cracks due to imaging or memory limitations (Andrä et al., 2013).

In the next section, we utilize pressure dependency of rock stiffness and porosity, to obtain the expressions for the unrelaxed frame stiffness to be used in equations 7.4-7.8 in place of the dry rock moduli to obtain better substitution estimates for rocks with a mix of stiff and soft pores.

7.4. Unrelaxed frame stiffness

To estimate the saturated stiffness of rocks with a mix of stiff and soft pores, a plausible approach is to perform substitution in two steps: first, divide the pore-space into soft and stiff pores, and estimate the stiffness of the unrelaxed frame with fluid or solid-filled soft pores and dry stiff pores; and finally saturate the dry stiff pores using the unrelaxed frame stiffness $\left(K_{uf}^{(P)}, \mu_{uf}^{(P)}\right)$ in equations 7.4-7.8 instead of the dry rock stiffness $\left(K_{dry}, \mu_{dry}\right)$. A schematic of the unrelaxed frame is shown in Figure 7.3. In this section, we derive the expressions for the unrelaxed frame stiffness expressed in terms of dry rock stiffness, the high-pressure dry rock stiffness $\left(K_{dry}^{(HP)}, \mu_{dry}^{(HP)}\right)$ and soft porosity $\left(\phi_{soft}\right)$.

Following Gurevich et al. (2009) and using the formalism proposed by Sayers and Kachanov (1991, 1995) we represent the effect of solid-filled soft pores on elastic stiffness by a system of non-interacting displacement discontinuities which are distributed isotropically in the rock frame. We can express the unrelaxed frame stiffnesses as

$$\frac{1}{K_{uf}^{(P)}} = \frac{1}{K_{dry}^{(HP)}} + sB_N \quad , \tag{7.9}$$

and

$$\frac{1}{\mu_{uf}^{(P)}} = \frac{1}{\mu_{dry}^{(HP)}} + \frac{4}{15} sB_N + \frac{2}{5} sB_T \quad , \tag{7.10}$$

where B_N and B_T are the normal and shear compliance of each plane of discontinuity filled with a solid. Symbol *s* represent surface to volume ratio of all discontinuities.

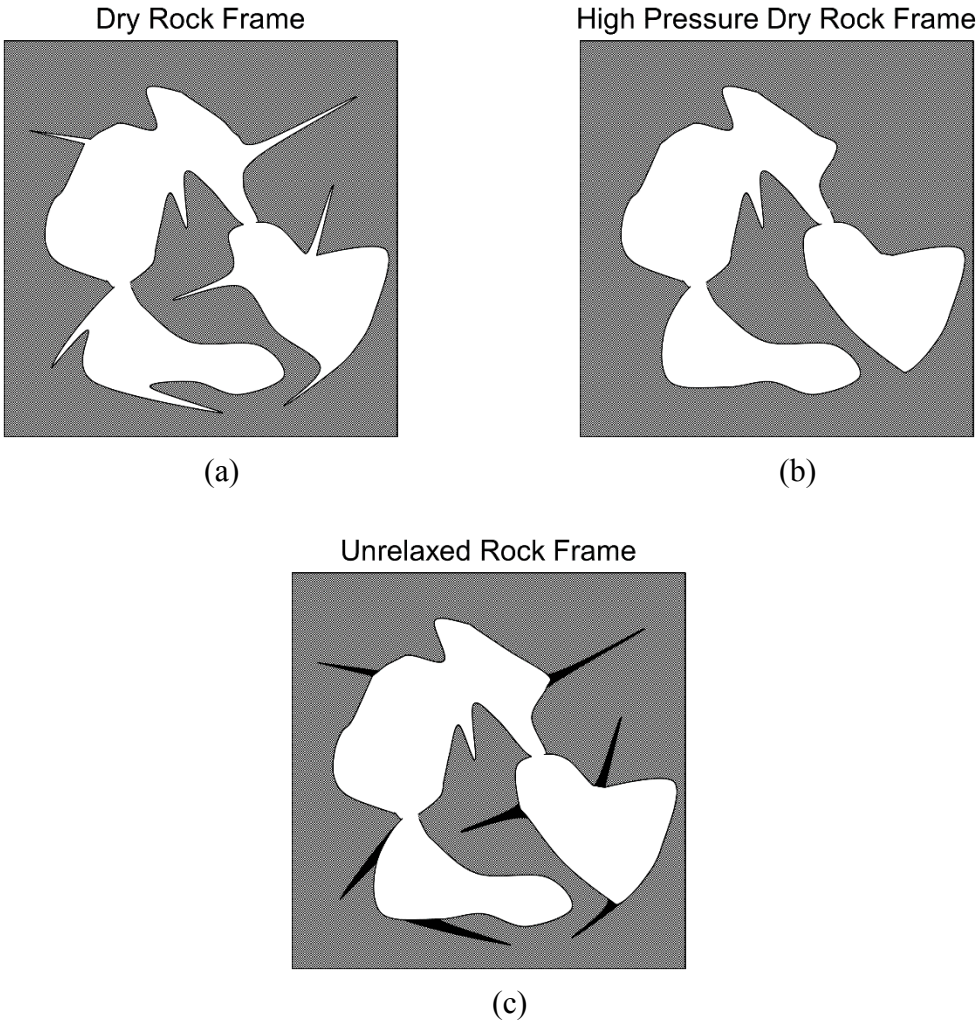

Figure 7.3: A schematic of (a) dry rock with stiff and soft pores (b) high-pressure dry rock with all soft pores closed (c) unrelaxed frame with soft pores filled with a pore fill shown in black. Dry pores and mineral shown in white and gray, respectively.

When soft pores are empty equations 7.9 and 7.10 reduce to

$$\frac{1}{K_{dry}^{(P)}} = \frac{1}{K_{dry}^{(HP)}} + sB_N^{dry} \quad , \tag{7.11}$$

and

$$\frac{1}{\mu_{dry}^{(P)}} = \frac{1}{\mu_{dry}^{(HP)}} + \frac{4}{15} sB_N^{dry} + \frac{2}{5} sB_T^{dry} \quad . \tag{7.12}$$

In equations 7.11 and 7.12, B_N^{dry} and B_T^{dry} are the dry normal and shear compliance of each discontinuity.

7.4.1. **Derivation of unrelaxed frame bulk modulus**

To express the unrelaxed frame bulk modulus $K_{uf}^{(P)}$ in terms of other quantities $\left(K_{dry}^{(P)}, K_{dry}^{(HP)}, \phi_{soft}, \text{etc}\right)$ we need to relate compliances sB_N and sB_N^{dry}. We will now relate these compliances using our generalized Gassmann result in equation 7.4, which is *exact* if compression-induced pressure (negative of the mean stress) in the pores is homogeneous.

Consider a rock composed of only isotropically distributed soft pores (of porosity ϕ_{soft}) that are completely filled with a solid of bulk and shear moduli K_f and μ_f, respectively. The mineral in the rock frame has bulk and shear moduli of K_{min} and μ_{min}, respectively. Assuming that pressure induced in all soft pores is equal or homogeneous we relate the saturated rock bulk modulus K_{sat}^{soft} to the dry rock bulk modulus K_{dry}^{soft} as

$$K_{sat}^{soft} = K_{bc}^{soft} + \frac{\left(1 - \frac{K_{bc}^{soft}}{K_{min}}\right)^2}{\frac{\phi_{soft}}{K_f} + \frac{1-\phi_{soft}}{K_{min}} - \frac{K_{bc}^{soft}}{\left(K_{min}\right)^2}} \quad , \tag{7.13}$$

where

$$K_{bc}^{soft} = \frac{\left(1-\phi_{soft}\right)\left(\frac{1}{K_{min}} - \frac{1}{K_{dry}^{soft}}\right) + \frac{3\phi_{soft}}{4}\left(\frac{1}{\mu_{min}} - \frac{1}{\mu_f}\right)}{\frac{1}{K_{min}}\left(\frac{1}{K_{min}} - \frac{1}{K_{dry}^{soft}}\right) + \frac{3\phi_{soft}}{4}\left(\frac{1}{K_{min}\mu_{min}} - \frac{1}{\mu_f K_{dry}^{soft}}\right)} \quad . \tag{7.14}$$

Since all the pores are crack like, bulk moduli K_{sat}^{soft} and K_{dry}^{soft} can also be related to the mineral modulus as

$$\frac{1}{K_{sat}^{soft}} = \frac{1}{K_{min}} + sB_N \quad , \tag{7.15}$$

and

$$\frac{1}{K_{dry}^{soft}} = \frac{1}{K_{min}} + sB_N^{dry} \quad . \tag{7.16}$$

Using equations 7.13 to 7.16 we obtain

$$sB_N = \frac{sB_N^{dry}\left(1 + \frac{4\mu_f}{3K_{min}}\right)}{1 - \frac{\mu_f}{\mu_{min}} + sB_N^{dry}\left(\frac{K_f + \frac{4}{3}\mu_f}{\phi_{soft}\left(1 - \frac{K_f}{K_{min}}\right)} - \frac{4}{3}\mu_f\right)} \quad . \tag{7.17}$$

Putting equation 7.17 in equations 7.9 and 7.11 we obtain

$$\frac{1}{K_{uf}^{(P)}} = \frac{1}{K_{dry}^{(HP)}} + \frac{1 + \frac{4\mu_f}{3K_{min}}}{\frac{1 - \frac{\mu_f}{\mu_{min}}}{\frac{1}{K_{dry}^{(P)}} - \frac{1}{K_{dry}^{(HP)}}} + \frac{1 + \frac{4\mu_f}{3K_f}}{\left(\frac{1}{K_f} - \frac{1}{K_{min}}\right)\phi_{soft}} - \frac{4}{3}\mu_f} \quad . \tag{7.18}$$

Equation 7.18 is the generalized unrelaxed frame bulk modulus. If $\mu_f = 0$, equation 7.18 reduces to the unrelaxed frame bulk modulus obtained by Gurevich et al. (2009) in equation 7.2. If the pore fill shear modulus is equal to mineral shear modulus $\left(\mu_f = \mu_{min}\right)$, then equation 7.18 becomes independent of the dry rock bulk modulus $K_{dry}^{(P)}$.

7.4.2. **Derivation of unrelaxed frame shear modulus**

For fluid-saturated soft pores (i.e., $\mu_f = 0$) compliances $2sB_T/5$ and $2sB_T^{dry}/5$ in equations 7.10 and 7.12 will be equal, since an ideal pore fluid does not induce any shear tractions at the pore boundary. However, if $\mu_f > 0$ then we expect $2sB_T^{dry}/5 > 2sB_T/5$ which is a consequence of Hill's theorem (Hill, 1963). We need to relate $2sB_T/5$ and $2sB_T^{dry}/5$ in order to express the unrelaxed frame shear modulus $\left(\mu_{uf}^{(P)}\right)$ in terms of other quantities $\left(\mu_{dry}^{(P)}, \mu_{dry}^{(HP)}, \phi_{soft}, \text{etc}\right)$. Similar to our analysis of the bulk modulus problem, we will now use the solid substitution relation in equation 7.6 to relate $2sB_T/5$ and $2sB_T^{dry}/5$. We again consider a rock composed of only soft isotropically distributed pores (of porosity ϕ_{soft}) completely filled with a solid of bulk and shear moduli K_f and μ_f, respectively; the mineral in the rock frame has bulk and shear moduli of K_{min} and μ_{min}, respectively. Assuming that induced stresses in all soft pores are homogenous we can express the saturated rock shear modulus μ_{sat}^{soft} in terms of the dry rock shear modulus μ_{dry}^{soft} as

$$\mu_{sat}^{soft} = \mu_{bc}^{soft} + \frac{\left(1 - \dfrac{\mu_{bc}^{soft}}{\mu_{min}}\right)^2}{\dfrac{\phi_{soft}}{\mu_f} + \dfrac{1-\phi_{soft}}{\mu_{min}} - \dfrac{\mu_{bc}^{soft}}{\left(\mu_{min}\right)^2}}, \tag{7.19}$$

where

$$\mu_{bc}^{soft} = \frac{\left(1-\phi_{soft}\right)\left(\frac{1}{\mu_{min}} - \frac{1}{\mu_{dry}^{soft}}\right) + \frac{3\phi_{soft}}{4}\left(\frac{1}{\chi_{min}} - \frac{1}{\chi_f}\right)}{\frac{1}{\mu_{min}}\left(\frac{1}{\mu_{min}} - \frac{1}{\mu_{dry}^{soft}}\right) + \frac{3\phi_{soft}}{4}\left(\frac{1}{\mu_{min}\chi_{min}} - \frac{1}{\chi_f \mu_{dry}^{soft}}\right)} \quad . \tag{7.20}$$

Since if $\mu_f \geq 0$ we obtain $\mu_{sat}^{soft} \geq \mu_{dry}^{soft}$, equations 7.19 and 7.20 quantify the effect of non-zero shear tractions in a cracked media. Therefore we can write

$$\frac{1}{\mu_{sat}^{soft}} = \frac{1}{\mu_{min}} + \frac{2}{5} sB_T \quad , \tag{7.21}$$

and

$$\frac{1}{\mu_{dry}^{soft}} = \frac{1}{\mu_{min}} + \frac{2}{5} sB_T^{dry} \quad . \tag{7.22}$$

Using equations 7.19 to 7.22 we obtain

$$\frac{2sB_T}{5} = \frac{\frac{2sB_T^{dry}}{5}\left(1 + \frac{4\chi_f}{3\mu_{min}}\right)}{1 - \frac{\chi_f}{\chi_{min}} + \frac{2sB_T^{dry}}{5}\left(\frac{\mu_f + \frac{4}{3}\chi_f}{\phi_{soft}\left(1 - \frac{\mu_f}{\mu_{min}}\right)} - \frac{4}{3}\chi_f\right)} \quad . \tag{7.23}$$

Thus the unrelaxed frame shear modulus is given by

$$\frac{1}{\mu_{uf}^{(P)}} = \frac{1}{\mu_{dry}^{(P)}} + \frac{4}{15}\left(\frac{1}{K_{uf}^{(P)}} - \frac{1}{K_{dry}^{(P)}}\right) + \Lambda^{dry}\left(\frac{1+\frac{4\chi_f}{3\mu_{min}}}{1-\frac{\chi_f}{\chi_{min}}+\Lambda^{dry}\left(\frac{\mu_f+\frac{4}{3}\chi_f}{\phi_{soft}\left(1-\frac{\mu_f}{\mu_{min}}\right)}-\frac{4}{3}\chi_f\right)}-1\right),$$

(7.24)

where

$$\Lambda^{dry} = \frac{2}{5}sB_T^{dry} = \frac{1}{\mu_{dry}^{(P)}} - \frac{1}{\mu_{dry}^{(HP)}} - \frac{4}{15}\left(\frac{1}{K_{dry}^{(P)}} - \frac{1}{K_{dry}^{(HP)}}\right) \quad . \tag{7.25}$$

If $\mu_f = 0$, equation 7.24 reduces to the unrelaxed frame shear modulus obtained by Mavko and Jizba (1991) in equation 7.3. Similar to the bulk modulus solution in equation 7.18, if the pore fill shear modulus is equal to mineral shear modulus $\left(\mu_f = \mu_{min}\right)$, then equation 7.24 becomes independent of the dry rock shear modulus.

Equations 7.18 and 7.24 are the main results of this paper. We note if $K_f \to K_{min}$ and $\mu_f \to \mu_{min}$ then equations 7.18 and 7.24 yield

$$K_{uf}^{(P)} \approx K_{dry}^{(HP)}; \quad \mu_{uf}^{(P)} \approx \mu_{dry}^{(HP)} \quad . \tag{7.26}$$

Hence, if the high-pressure stiffnesses are not directly measured the relations in equation 7.26 can be used to predict the high-pressure stiffnesses if very high-frequency saturated moduli are available.

7.4.3. **Analysis of the result for a weak pore-fill**

For a weak pore-fill material $\left(K_f, \mu_f << K_{min}, \mu_{min}\right)$, the expression for the unrelaxed frame bulk modulus in equation 7.18 can be approximated by retaining only the first order terms, this leads to:

$$\frac{1}{K_{uf}^{(P)}} = \frac{1}{K_{dry}^{(HP)}} + \frac{1}{\left(\frac{1}{K_{dry}^{(P)}} - \frac{1}{K_{dry}^{(HP)}}\right)^{-1} + \frac{K_f + \frac{4}{3}\mu_f}{\phi_{soft}}} \quad . \tag{7.27}$$

From equation 7.27, we note that the unrelaxed frame bulk modulus is affected by pore-fill and soft porosity when the term $\left(K_f + (4/3)\mu_f\right)/\phi_{soft}$ is sufficiently large, this term can also be interpreted as the *apparent pore-fill stiffness* of the solid-fill material saturating the soft pores. Similarly, for a weak pore-fill material the unrelaxed frame shear modulus in equation 7.24 can be approximated as

$$\frac{1}{\mu_{uf}^{(P)}} = \frac{1}{\mu_{dry}^{(P)}} + \frac{4}{15}\left(\frac{1}{K_{uf}^{(P)}} - \frac{1}{K_{dry}^{(P)}}\right) - \frac{\Lambda^{dry}}{\frac{1}{\Lambda^{dry}\frac{\mu_f + \frac{4}{3}\chi_f}{\phi_{soft}}} + 1} \quad , \tag{7.28}$$

thus the unrelaxed frame shear modulus increases with increase in its *apparent pore-fill stiffness* given by $\left(\mu_f + (4/3)\chi_f\right)/\phi_{soft}$. From equations 7.27 and 7.28, we note that when the pore-fill material is weak, the dependence of the unrelaxed frame moduli on pore-fill properties scales by the ratio of pore-fill stiffness and soft porosity.

Similarly, the difference between the new unrelaxed frame moduli and those obtained by Mavko-Jizba-Gurevich (*MJG*; in equations 7.2 and 7.3) for a weak pore-fill can be approximated as

$$\frac{1}{K^{(P)}_{uf-MJG}} - \frac{1}{K^{(P)}_{uf}} = \frac{4}{3}\frac{\mu_f}{\phi_{soft}} \frac{1}{\left(\left(\frac{1}{K^{(P)}_{dry}} - \frac{1}{K^{(HP)}_{dry}}\right)^{-1} + \frac{K_f}{\phi_{soft}}\right)^2} \quad , \tag{7.29}$$

$$\frac{1}{\mu^{(P)}_{uf-MJG}} - \frac{1}{\mu^{(P)}_{uf}} = \frac{4}{15}\left(\frac{1}{K^{(P)}_{uf-MJG}} - \frac{1}{K^{(P)}_{uf}}\right) + \frac{\Lambda^{dry}}{\dfrac{1}{\Lambda^{dry}\dfrac{\mu_f + \frac{4}{3}\chi_f}{\phi_{soft}}} + 1} \quad . \tag{7.30}$$

From equation 7.29 we note that if the term μ_f/ϕ_{soft} is fairly small then the predicted difference in the unrelaxed frame bulk modulus using the present and the Mavko-Jizba-Gurevich relations will be quite small; this difference will increase with increase in μ_f/ϕ_{soft}. The difference in unrelaxed shear modulus using the two methods originates partly due to the difference in unrelaxed frame bulk modulus (first term in the RHS of equation 7.30) but this term is expected to be small when compared to the second term in equation 7.30 which also increases with increase in μ_f/ϕ_{soft}. As an example, consider a hypothetical rock with the following properties: $\mu^{(P)}_{dry} = 20$ GPa, $K^{(P)}_{dry} = 18$ GPa, $\mu^{(HP)}_{dry} = 25$ GPa, $K^{(HP)}_{dry} = 22$ GPa, and $\phi_{soft} = 0.01$, such that the rock is fully saturated with a weak pore-fill of $K_f = 3$ GPa and $\mu_f = 0.1$ GPa. For this rock, the difference between $1/K^{(P)}_{uf-MJG}$ and $1/K^{(P)}_{uf}$ as calculated from equation 7.29 is 10^{-4} GPa^{-1} which is very small in comparison to the term $1/K^{(P)}_{uf-MJG} \approx 0.047$ GPa^{-1} in equation 7.29, hence for this rock we obtain $K^{(P)}_{uf-MJG} \approx K^{(P)}_{uf} \approx 20.9$ GPa. On the contrary, the difference between $1/\mu^{(P)}_{uf-MJG}$ and $1/\mu^{(P)}_{uf}$ is calculated to be 10^{-3} GPa^{-1} which is sufficiently large and cannot be neglected since $1/\mu^{(P)}_{uf-MJG} \approx 0.048$ GPa^{-1}. This difference leads to $\mu^{(P)}_{uf-MJG} \approx 20.8$ GPa and $\mu^{(P)}_{uf-MJG} \approx 21.3$ GPa.

7.4.4. Unrelaxed frame stiffnesses using other methods

Estimates for the unrelaxed frame moduli can also be obtained using other theories (Kuster and Toksöz, 1974; Berryman, 1980; Hudson, 1981) as presented in the Appendix A.

The unrelaxed frame bulk modulus in equation A-19 is derived using the Kuster-Toksöz theory. This result assumes identical penny shape soft pores without considering any specific aspect ratio. Although, this derivation is not as general as the results obtained in equations 7.18 and 7.24 where we assume no specific soft pore shape, it can be argued that our assumption of homogenous stress in using equations 7.13 and 7.14 may require special pore shape. It must be noted however, that in the limit of low viscosity fluids, i.e., $\mu_f = 0$, the Kuster-Toksöz unrelaxed frame bulk modulus in equation A-19 does not agree with the Mavko-Jizba-Gurevich relation in equation 7.2. There are also other previously known limitations of using the Kuster-Toksöz theory for small aspect ratio (or thin) penny shape soft pores. For instance, at any finite concentration if soft pores approach disk shape (zero aspect ratio), then the non-interaction assumption in the Kuster-Toksöz theory will be violated (Berryman, 1980), regardless of the soft porosity. Therefore, for estimating the unrelaxed frame stiffness the Kuster-Toksöz theory *cannot* be used legitimately.

Similarly, analytical solutions to the unrelaxed frame stiffness can also be derived using Hudson's theory for cracked isotropic media (Hudson, 1981). The obtained expression for unrelaxed frame bulk modulus is presented in equation A-21. This solution is limited to a weak solid pore fill (i.e., $\mu_f << \mu_{min}$) and does not agree with our unrelaxed frame bulk modulus result in equation 7.18, due to a small missing term $(1/K_{min})$ - this inconsistency is already known (Gurevich et al., 2009; Hudson et al., 2001).

7.5. High-frequency laboratory examples

7.5.1. Westerly granite

As an example of predicting elastic properties of rocks with soft pores, we predict ultrasonic velocities of a Westerly granite sample (Coyner, 1984) saturated with water

($K_f = 2.25$ GPa). This modeling example was also previously discussed by Mavko and Jizba (1991) and also by Gurevich et al. (2009). For this sample, measurements of soft porosity and dry rock moduli were reported as a function of confining pressure; sample porosity is about 0.8 % and the reported sample grain density is 2.64 g/cm^3. For the mineral bulk and shear moduli we use 56 GPa and 60 GPa, respectively. Once $K_{uf}^{(P)}$ and $\mu_{uf}^{(P)}$ are estimated using equations 7.18 and 7.24, estimates of the unrelaxed fluid-saturated moduli are obtained using generalized Gassmann results in equations 7.4 and 7.6, since for such low porosity rocks Biot-dispersion is negligible. We also predict the velocities corresponding to a more viscous pore-fluid ($K_f = 2.25$ GPa and $\mu_f = 0.1$ GPa).

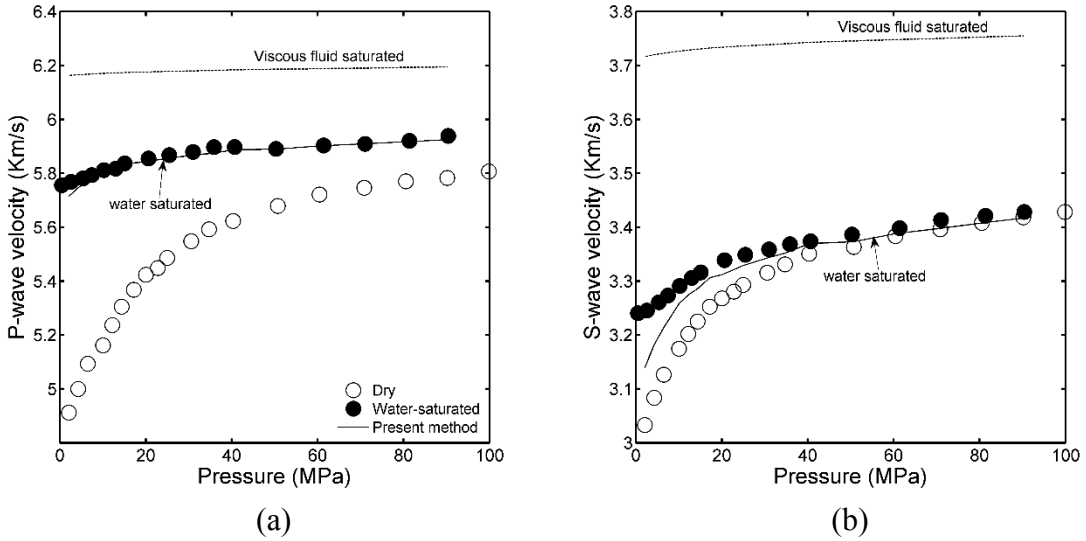

Figure 7.4: P and S-wave velocities for Westerley granite sample as a function of confining pressure. Laboratory measurements of dry and water-saturated rock velocities are shown in open and filled circles, respectively. Predictions for water-saturated velocities using the present method (calculated for $\mu_f = 0$; which are identical to the predictions using the Mavko-Jizba-Gurevich relations along with Gassmann) are shown in full black curves, whereas predictions for the viscous-fluid saturated rock ($\mu_f = 0.1$ GPa) are shown in dashed black curves.

In Figures 7.4a we compare the P-wave velocity predictions using the present method for the water-saturated granite sample; laboratory measured ultrasonic dry and water-saturated velocities are also shown with open and filled circles, respectively. Figure 7.4b shows the same plot but for S-wave velocity. The predicted ultrasonic velocities are within 1-3% of the measured velocities. Figures 7.4a-7.4b also show predictions of hypothetical

viscous fluid-saturated ultra-sonic velocities, which were not measured by Coyner (1984); we note a considerably large change in predicted velocities with increase in fluid shear modulus.

7.5.2. **Glycerol-filled Fontainebleau sandstone**

Glycerol has temperature sensitive viscosity, ranging from 10^8 Pa-s at -80^o C to 10^{-2} Pa-s at 90^o C (Weast, 1967). Dynamic shear moduli of glycerol have also been measured for a range of temperatures at various frequencies by Jeong et al. (1986). The calculated shear moduli from measurements conducted at 2 MHz are shown in Figure 7.5. For this modeling example, we assume that the bulk modulus of glycerol is nearly constant $\approx$ 4.3 GPa.

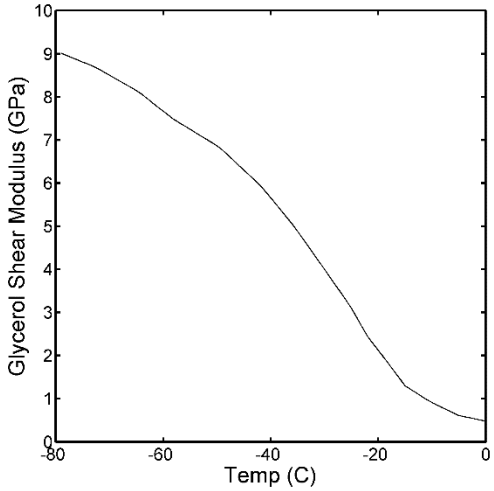

Figure 7.5: Dynamic ultrasonic shear modulus of glycerol for a range of temperatures.

Khalatbari et al. (1991) reported ultra-sonic velocities of a Fontainebleau sandstone sample saturated with glycerol over a wide range of temperatures. The authors also report dry velocities which also vary with temperature. The sample porosity was 5 %, which included of some thin cracks. However, pressure dependency of rock stiffness was not measured. Therefore, we do not have direct measurements of either the soft porosity or the high-pressure moduli, which are needed to predict the glycerol saturated velocities with the

new method. The mineral in the rock frame is quite homogeneous (K_{min} = 36 GPa; μ_{min} = 47 GPa).

Various Fontainebleau sandstone samples have been extensively studied previously (Han, 1986; Carmen, 2009) and it is observed that the high-pressure stiffness (P > 40 MPa) of clean samples (clay < 1%) is very well described by a modified upper HS bound (Hashin and Shtrikman, 1963) shown in Figure 7.6; and soft porosity varies between 0.1 to 1 %. Therefore, to model the measured data we use the predicted high-pressure moduli ($K_{dry}^{(HP)} \approx$ 30 GPa; $\mu_{dry}^{(HP)} \approx$ 37 GPa) from the modified upper HS bound and consider a variable soft porosity between 0.1 and 1 %.

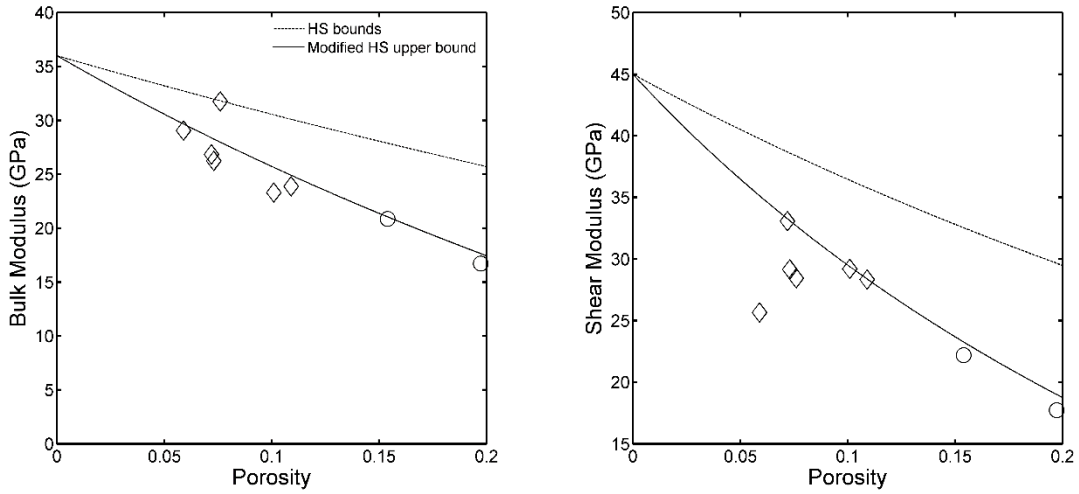

Figure 7.6: Dry Fontainebleau sandstone rock moduli measured at high confining pressures. Data from Han (1986) are shown in circles and data from Carmen (2009) are shown in diamonds. The modified upper HS bound describes the high pressure moduli quite well.

Figures 7.7a-7.7b show the laboratory measured ultrasonic dry and saturated P and S-wave velocities; this Figure 7.7 also shows the model predictions for saturated velocities starting with the measured dry velocities, calculated using the present method (equations 7.4, 7.6, 7.18 and 7.24). To capture the effect of uncertainty in soft porosity, all calculations are made for ϕ_{soft} varying between 0.1 and 1 % such that the shaded region in plots shows

this uncertainty. Note if we use $\mu_f = 0$ (the Mavko-Jizba-Gurevich relations with Gassmann) we estimate the unrelaxed velocities which only include the effects of squirt-dispersion, whereas using $\mu_f > 0$ we predict the unrelaxed velocities which include the combined effects of squirt and shear-dispersion (solid-squirt). We note that varying the crack porosity between 0.1 to 1 % induces little change in the model predictions.

At relatively high temperature ~ 0° C (glycerol viscosity ~ 10 Pa-s), the measured change in P and S wave velocities, from dry to saturated, can be explained by accounting only for squirt-flow, i.e., using $\mu_f \approx 0$ in the present method. For temperatures below 0° C, accounting for only squirt-dispersion using $\mu_f \approx 0$ in the present method is not sufficient to explain the measured dispersion in seismic velocities. Indeed if we use the full solid-squirt model ($\mu_f > 0$, using equations 7.4, 7.6, 7.18 and 7.24), we obtain a good match with the measured velocities. For the temperature range studied, the fluid viscosity is high enough to ignore the effect of Biot dispersion on the measured ultrasonic velocities.

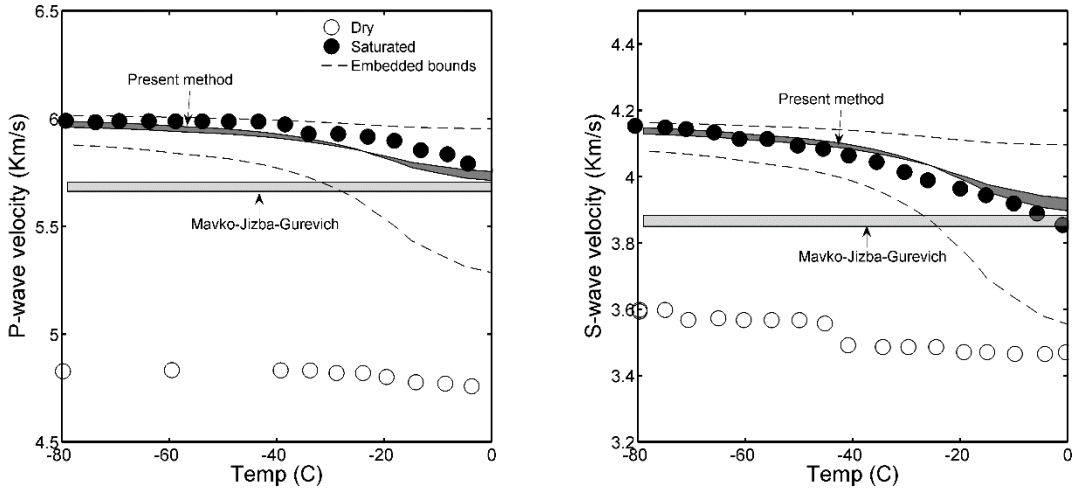

(a) (b)

Figure 7.7: (a) P-wave and (b) S-wave velocities of dry (open circles) and glycerol saturated (filled circles) Fontainebleau sandstone sample as a function of temperature. Predictions of the present method are shown for a range of soft porosities (between 0.1 and 1 %) thus show a range shown in dark gray color, referred in plot as - Present method. Predictions using the Mavko-Jizba-Gurevich relations with Gassmann (identical to the present method with $\mu_f = 0$) are shown in light gray color, referred as - Mavko-Jizba-Gurevich. Embedded bound predictions are also shown in dashed black curves for comparison.

7.5.3. **Uvalde heavy-oil rock**

Behura et al. (2007) measured effective shear moduli of a heavy-oil saturated Uvalde rock sample for various temperatures and frequencies. The authors also reported shear moduli of the saturating heavy oil for various temperature and frequencies, which has API of -5. The sample rock frame is predominantly calcite (K_{min} = 60 GPa; μ_{min} = 30 GPa) and has porosity of 0.25. The dry rock shear modulus of this rock was not measured directly but Makarynska et al. (2010) carefully back calculate it to be 1.45 GPa; thus we assume this value and consider dry rock bulk modulus of 1.5 GPa. In Figure 7.8 we plot the measured effective shear moduli versus the reported heavy-oil shear moduli for various temperatures; we notice that measurements at various temperatures form a tight trend. We take heavy oil bulk modulus to be $K_f = 3$ GPa. No direct measurements of high-pressure stiffness or soft porosity are available. We can back calculate the high-pressure dry rock shear modulus using the measured saturated shear modulus at the highest heavy-oil shear modulus, using equation 7.26, which yields $\mu_{dry}^{(HP)} \approx 16$ GPa; however, since $\mu_f < 1$GPa $<< \mu_{min}$ the predicted $\mu_{dry}^{(HP)}$ is probably much softer than the true value. Thus for this example we use the upper HS bound for the dry rock to calculate $\mu_{dry}^{(HP)} \approx 19$ GPa.

Figure 7.8 shows predictions of the saturated effective shear moduli starting with the dry rock modulus, assuming soft porosity of 0.02. The embedded bounds contain the measured saturated moduli but the range predicted is quite large. Estimating only the squirt-dispersion effects using the Mavko-Jizba-Gurevich relations with Gassmann, severely underestimate the measured saturated moduli; thus if we only account for squirt-flow the measured effective moduli cannot be explained. However, if we account for both squirt and shear-dispersion using the present solid-squirt method, then we note a good match between predictions and measurements.

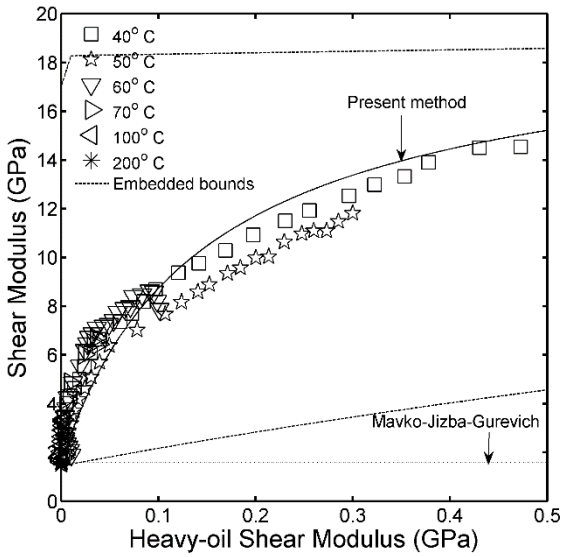

Figure 7.8: Measured shear moduli of Uvalde heavy oil rock sample as a function of heavy-oil shear moduli. Measurements at various temperatures are shown with different symbols. Predictions of the present method are shown in the solid black curve, referred in plot as - Present method. Predictions using the Mavko-Jizba-Gurevich relations along with Gassmann ($\mu_f = 0$) are shown in dashed gray curve. Embedded bound predictions are also shown in dashed black curves for comparison.

7.6. Chapter summary

We present relations for estimating the combined high-frequency effects of squirt and shear-dispersion on effective bulk and shear moduli for rocks saturated with a viscous-fluid. The main results of this paper are presented in equations 7.18 and 7.24. Rock stiffening due to squirt and shear-dispersion (solid-squirt) effects is included by replacing the unrelaxed frame moduli in place of the dry rock moduli in our solid substitution relations in equations 7.4 and 7.6.

The expressions for the unrelaxed frame moduli (in equations 7.18 and 7.24) do not have any adjustable parameters and require information on elastic properties of rock constituents, rock moduli measurements at high-pressure and soft porosity. Thus all required inputs can be directly measured. These relations are extensions of the Mavko-Jizba-Gurevich relations to the case of high viscosity fluid saturated soft pores; and in the

limiting case of low-viscosity fluids (liquids or gasses), the new relations exactly reduce to the Mavko-Jizba-Gurevich relations.

In various data examples of rocks saturated with viscous fluids, we note that accounting for only squirt-dispersion is not sufficient to explain the measured saturated rock stiffness or velocities at high frequencies, measurements can be better explained if effects of both squirt and shear-dispersion are estimated with the new solid-squirt method. The model predicted velocities are in good agreement with laboratory measurements.

7.7. Acknowledgements

We are grateful to Prof. Boris Gurevich for his comments and suggestions. This work was supported by the Stanford Rock Physics and Borehole Geophysics (SRB) Project, and U.S. Department of Energy award DE-FE0001159.

7.8. Appendix A

7.8.1. Unrelaxed frame stiffness using other methods

7.8.1.1. Using Kuster-Toksöz estimates

Consider a monomineralic rock such that the mineral in the rock frame has bulk modulus K_{min} and shear modulus μ_{min}; pores are completely saturated with a material (fluid or solid) of bulk modulus K_f and shear modulus μ_f. The pore space is divided into stiff and soft pores of respective volume fraction (or porosity) ϕ_{stiff} and ϕ_{soft}. For such a rock, the scattering theory based Kuster-Toksöz estimates (Kuster and Toksöz, 1974; Berryman, 1980) for effective saturated bulk (K_{KT}) and shear (μ_{KT}) moduli can be written as

$$X_{KT} = \phi_{stiff}\left(K_f - K_{min}\right)P^{min,f-stiff} + \phi_{soft}\left(K_f - K_{min}\right)P^{min,f-soft} \quad , \tag{A-1}$$

$$Y_{KT} = \phi_{stiff}\left(\mu_f - \mu_{min}\right)Q^{min,f-stiff} + \phi_{soft}\left(\mu_f - \mu_{min}\right)Q^{min,f-soft} \quad , \tag{A-2}$$

where X and Y are related to the effective rock moduli by

$$X_z = \left(K_z - K_{min}\right)\frac{\left(K_{min} + (4/3)\mu_{min}\right)}{\left(K_z + (4/3)\mu_{min}\right)} \quad , \tag{A-3}$$

$$Y_z = \left(\mu_z - \mu_{min}\right)\frac{\left(\mu_{min} + \chi_{min}\right)}{\left(\mu_z^{(P)} + \chi_{min}\right)} \quad . \tag{A-4}$$

In equations A-1 and A-2, $P^{min,f-stiff}$, $Q^{min,f-stiff}$ and $P^{min,f-soft}$, $Q^{min,f-soft}$ are shape coefficients for stiff and soft pores, respectively; these depend on the pore shape, and elastic properties of rock constituents, expressions for various ellipsoidal shapes can be found in Mavko et al. (2009). When all pores are empty, expressions in equations A-1 and A-2 reduce to

$$X_{dry} = \phi_{stiff}\left(-K_{min}\right)P^{min,0-stiff} + \phi_{soft}\left(-K_{min}\right)P^{min,0-soft} \quad , \tag{A-5}$$

$$Y_{dry} = \phi_{stiff}\left(-\mu_{min}\right)Q^{min,0-stiff} + \phi_{soft}\left(-\mu_{min}\right)Q^{min,0-soft} \quad , \tag{A-6}$$

where superscripts 0-*stiff* and 0-*soft* denote dry stiff and soft pores; X_{dry} and Y_{dry} are related to dry rock bulk $\left(K_{dry}\right)$ and shear $\left(\mu_{dry}\right)$ moduli by equations A-3 and A-4.

Similarly, if the soft pores are completely filled with the frame mineral and the stiff pores are empty, we obtain the expressions for the high-pressure dry rock moduli $\left(K_{dry}^{(HP)}, \mu_{dry}^{(HP)}\right)$, and if soft pores are saturated with pore fill material but stiff pores are dry we obtain expressions for the unrelaxed rock frame moduli $\left(K_{uf}, \mu_{uf}\right)$. These expressions are

$$X_{dry}^{(HP)} = \phi_{stiff}\left(-K_{min}\right)P^{min,0-stiff} \quad , \tag{A-7}$$

$$Y_{dry}^{(HP)} = \phi_{stiff}\left(-\mu_{min}\right)Q^{min,0-stiff} \quad , \tag{A-8}$$

$$X_{uf} = \phi_{stiff}\left(-K_{min}\right)P^{min,0-stiff} + \phi_{soft}\left(K_f - K_{min}\right)P^{min,f-soft} \quad , \tag{A-9}$$

$$Y_{uf} = \phi_{stiff}\left(-\mu_{min}\right)Q^{min,0-stiff} + \phi_{soft}\left(\mu_f - \mu_{min}\right)Q^{min,f-soft} \quad . \tag{A-10}$$

Regardless of the shape coefficients or the volume fraction of the stiff pores, from equations A-7 to A-10, we obtain the following relations:

$$X_{dry}^{(HP)} - X_{uf}^{(P)} = \phi_{soft}\left(K_{min} - K_f\right)P^{min,f-soft} \quad , \tag{A-11}$$

$$Y_{dry}^{(HP)} - Y_{uf}^{(P)} = \phi_{soft}\left(\mu_{min} - \mu_f\right)Q^{min,f-soft} \quad , \tag{A-12}$$

$$X_{dry}^{(HP)} - X_{dry}^{(P)} = \phi_{soft}\left(K_{min}\right)P^{min,0-soft} \quad , \tag{A-13}$$

$$Y_{dry}^{(HP)} - Y_{dry}^{(P)} = \phi_{soft}\left(\mu_{min}\right)Q^{min,0-soft} \quad . \tag{A-14}$$

Next, idealizing all soft pores as penny shape cracks of arbitrary but identical aspect ratio α we obtain

$$P^{min,f-soft} = \frac{K_{min} + \frac{4}{3}\mu_f}{K_f + \frac{4}{3}\mu_f + \pi\alpha B_{min}} \quad . \tag{A-15}$$

and

$$P^{min,0-soft} = \frac{K_{min}}{\pi\alpha B_{min}} \quad . \tag{A-16}$$

Replacing aspect ratio in equations A-15 and A-16, we relate shape coefficients $P^{min,f-soft}$ and $P^{min,0-soft}$ as

$$P^{min,f-soft} = \frac{K_{min} + \frac{4}{3}\mu_f}{K_f + \frac{4}{3}\mu_f + \frac{K_{min}}{P^{min,0-soft}}} \quad . \tag{A-17}$$

Note that the relation in equation A-17 does not depend on the aspect ratio of soft pores, but just requires all soft pores to be identical. Using equations A-11, A-13 and A-17, we obtain

$$X_{uf} = X_{dry}^{(HP)} - \frac{\phi_{soft}\left(K_{min} - K_f\right)\left(K_{min} + \frac{4}{3}\mu_f\right)}{K_f + \frac{4}{3}\mu_f + \frac{\phi_{soft} K_{min} K_{min}}{\left(X_{dry}^{(HP)} - X_{dry}\right)}} \quad . \tag{A-18}$$

Equations A-3 and A-18 relate the unrelaxed frame bulk modulus to the dry-rock bulk modulus and the high-pressure dry rock bulk modulus. Similarly, expressing shape coefficients $Q^{min,0-soft}$ as a function of $Q^{min,f-soft}$ we can obtain a relation between the unrelaxed frame shear modulus, dry-rock shear modulus and the high-pressure dry rock shear modulus. The obtained unrelaxed bulk modulus is given by

$$\frac{1}{K_{uf}^{(P)}} = \frac{1}{K_{dry}^{(HP)} + \frac{4\mu_{min}}{3Z}} - \frac{1}{ZK_{dry}^{(HP)} + \frac{4}{3}\mu_{min}} \quad , \tag{A-19}$$

where

$$Z = \frac{\left(K_f + \frac{4}{3}\mu_f\right)}{\left(K_f - K_{min}\right)\left(K_{min} + \frac{4}{3}\mu_f\right)}\left[\frac{\left(K_{min} + \frac{4}{3}\mu_{min}\right)^2}{\phi_{soft}\left(K_{dry}^{(HP)} + \frac{4}{3}\mu_f\right)} + \frac{\left(K_{min}\right)^2\left(K_{dry}^{(P)} + \frac{4}{3}\mu_{min}\right)}{\left(K_f + \frac{4}{3}\mu_f\right)\left(K_{dry}^{(HP)} - K_{dry}^{(P)}\right)}\right] . \tag{A-20}$$

The above expressions assume identical soft pores of penny shape but do not assume any specific aspect ratio.

7.8.1.2. Unrelaxed frame stiffness using Hudson

Following a similar procedure as discussed above but instead using Hudson's theory (Hudson, 1981) we obtain the following solution for the unrelaxed frame bulk modulus

$$\frac{1}{K_{uf}^{(P)}} = \frac{1}{K_{dry}^{(HP)}} + \frac{1}{\dfrac{1}{\dfrac{1}{K_{dry}^{(P)}} - \dfrac{1}{K_{dry}^{(HP)}}} + \dfrac{1}{\left(\dfrac{1}{K_f + \dfrac{4}{3}\mu_f}\right)\phi_{soft}}} \quad . \tag{A-21}$$

Expressions for unrelaxed frame shear modulus can also be obtained, using both Kuster-Toksöz and Hudson, but these are not presented here due to their complicated nature.

7.9. References

Adam, L., and T. Otheim, 2013, Elastic laboratory measurements and modeling of saturated basalts: Journal of Geophysical Research: Solid Earth, 118, 1-12.

Andrä, H., N. Combaret, J. Dvorkin, E. Glatt, J. Han, M. Kabel, Y. Keehm, F. Krzkilla, M. Lee, C. Madonna, M. Marsh, T. Mukerji, E. H. Saenger, R. Sain, N. Saxena, S. Ricker, A. Wiegmann and X. Zhan, 2013, Digital rock physics benchmarks - Part I: Imaging and segmentation: Computers & Geosciences, 50, 25-32.

Behura, J., M. Batzle, R. Hofmann, and J. Dorgan, 2007, Heavy oils: Their shear story: Geophysics, 72, 5, E175–E183.

Berryman, J. G., 1980, Long-wavelength propagation in composite elastic media II. Ellipsoidal inclusions: Journal of the Acoustical Society of America, 68, 1820–1831.

Berryman, J. G., 2007, Seismic waves in rocks with fluids and fractures: Geophysical Journal International, 171, 954–974.

Biot, M.A., 1956, Theory of propagation of elastic waves in a fluid saturated porous solid. I Low frequency range, The Journal of the Acoustical Society of America, 28, 168-178.

Biot, M.A., 1956, Theory of propagation of elastic waves in a fluid saturated porous solid: II Higher frequency range. The Journal of the Acoustical Society of America, 28, 179-191.

Biot, M.A., 1962, Mechanics of deformation and acoustic propagation in porous media, Journal of Applied Physics, 33, 1482-1498.

Carmen, G., 2009, Reservoir Characterization Combining Elastic Velocities and Electrical Resistivity Measurements: Ph.D. thesis, Stanford University.

Chapman, M., S. V. Zatsepin, and S. Crampin, 2002, Derivation of a microstructural poroelastic model: Geophysical Journal International, 151, 427–451.

Coyner, K. B., 1984, Effects of stress, pore pressure, and pore fluids on bulk strain, velocity, and permeability in rocks: Ph.D. thesis, Massachusetts Institute of Technology.

Dvorkin, J., and Nur, A., 1993, Dynamic poroelasticity: A unified model with the squirt and the Biot mechanisms, Geophysics, 58, 524-533.

Dvorkin, J., G. Mavko, and A. Nur, 1995, Squirt flow in fully saturated rocks, Geophysics, 60, 97–107.

Endres, A. L., and R. J. Knight, 1997, Incorporating pore geometry and fluid pressure communication into modeling the elastic behavior of porous rocks: Geophysics, 62, 106–117.

Gassmann, F., 1951, Über die Elastizität poröser Medien: Vierteljahrschrift der Naturforschenden Gessellschaft in Zürich, 96, 1-23.

Gibiansky, L., and S. Torquato, 1998, Rigorous connection between physical properties of porous rock: Journal of Geophysical Research, 103, 23911-23923.

Gurevich, B., D. Makarynska, and M. Pervukhina, 2009, Ultrasonic moduli for fluid-saturated rocks: Mavko-Jizba relations rederived and generalized, 74, 4, N25–N30.

Fung, Y. C., 1965, Foundations of solid mechanics, Prentice-Hall international series in dynamics.

Han, D., 1986, Effects of porosity and clay content on acoustic properties of sandstones and unconsolidated sediment: Ph.D. thesis, Stanford University.

Hashin, Z., and S. Shtrikman, 1963, A variational approach to the elastic behavior of multiphase materials: Journal of the Mechanics and Physics of Solids, 11, 127–140.

Hudson, J. A., E. Liu, and S. Crampin, 1996, The mechanical properties of materials with interconnected cracks and pores: Geophysical Journal International, 124, 105–112.

Hudson, J. A., 1981,Wave speeds and attenuation of elastic waves in material containing cracks.: Geophysical Journal International, 64, 133–150.

Hudson, J. A., T. Pointer, and E. Liu, 2001, Effective-medium theories for fluid-saturated materials with aligned cracks: Geophysical prospecting, 49, 509–522.

Jakobsen, M., and M. Chapman, 2009, Unified theory of global flow and squirt flow in cracked porous media: Geophysics, 74, 2, WA65–WA76.

Jeong, J. H., S. R. Nagel, and S. Bhattacharya, 1986, Ultrasonic investigation of the glass transition in glycerol: Physical Review A, 34, 602–608.

Johnson, D. L., 2001, Theory of frequency dependent acoustics in patchy-saturated porous media: Journal of Acoustical Society of America, 110, 2, 682–694.

Khalatbari, A., D. Vo-Thanh and J. P. Poirier, 1991, Effect of fluid viscosity and saturation on the ultrasonic velocities in a Fontainebleau sandstone: Geophysical Research Letters, 18, 5, 885-888.

Küster, G. T., and M. N. Toksöz, 1974, Velocity and attenuation of seismic waves in two-phase media: Part I. Theoretical formulations: Geophysics, 39, 587–606.

Makarynska, D., B. Gurevich, J. Behura, and M. Batzle, 2010, Fluid substitution in rocks saturated with viscoelastic fluids, Geophysics, 75, E115–E122.

Mavko, G., and D. Jizba, 1991, Estimating grain-scale fluid effects on velocity dispersion in rocks: Geophysics, 56, 1940–1949.

Mavko, G., T. Mukerji, and J. Dvorkin, 2009, The Rock physics handbook: Cambridge University Press.

Mavko, G., and A. Nur, 1975, Melt squirt in the aesthenosphere: Journal of Geophysical Research, 80, 1444–1448.

Mavko, G. and N. Saxena, 2013, Embedded-bound method for estimating the change in bulk modulus under either fluid or solid substitution: Geophysics, 78, 5, L87-L99.

Mukerji, T. and G. Mavko, 1994, Pore fluid effects on seismic velocity in anisotropic rocks: Geophysics, 59, 2, 233-244.

O'Connell, R., and B. Budiansky, 1977, Viscoelastic properties of fluid-saturated cracked solids: Journal of Geophysical Research, 82, 5719–5735.

Pride, S. R., J. G. Berryman, and J. M. Harris, 2004, Seismic attenuation due to wave-induced flow: Journal of Geophysical Research, 109, B01201.

Saxena, N., and G. Mavko, 2014, Exact equations for fluid and solid substitution: Geophysics, in print.

Sayers, C. M., and M. Kachanov, 1991, A simple technique for finding effective elastic constants of cracked solids for arbitrary crack orientation statistics: International Journal of Solids and Structures, 27, 671–680.

Stoll, R. D., and G. M. Bryan, 1970, Wave attenuation in saturated sediments: Journal of Acoustical Society of America, 47, 1440-1447.

Walsh, J., 1965, The effect of cracks on the compressibility of rock: Journal of Geophysical Research, 70, 381-389.

Weast, R. C., 1967, Handboook of chemistry and physics, The Chemical Rubber Company.

Wulff, A.M., and H. Burkhardt, 1997, Mechanisms affecting ultrasonic wave propagation in fluid-containing sandstones under high hydrostatic pressure: Journal of Geophysical Research, 102, 3043–3050.

Chapter 8

Estimating effects of change in rock microstructure on seismic velocities

8.1. Abstract

Naturally occurring rocks are multiphase composites of minerals and fluids with varying elastic properties. Predicting the effects of removal/alteration or substitution of one or more phases on seismic velocities is of practical interest in Geophysics. We present exact relations for replacing *one* or *more* phases (fluid or solid) in a multimineralic isotropic rock, these new solutions are also equivalent to relaxing the assumption of unchanging rock microstructure upon substitution, which is a fundamental assumption in conventional substitution theories such as those proposed by Gassmann, Brown and Korringa, Ciz and Shapiro, Saxena and Mavko, etc. Both pore-filling phase and rock microstructure can change due to digenesis, dissolution, precipitation, partial freezing or

Not published. Digital rocks published in COMPUTERS & GEOSCIENCES: Vol (50)

melting, etc., and these situations can be modeled using the new formulation. Approximate bounds for the change in effective rock stiffness upon change in pore geometry are developed which are in good agreement with laboratory and numerical examples; these bounds depend only on initial effective stiffness, and elastic properties and volume fractions of constituents.

8.2. Introduction

Rock-physics aims to link seismic attributes (Vp/Vs, acoustic impedance, rock stiffness, etc) to properties of the subsurface (pore-fluid, mineralogy, pore geometry, etc). Rock-physics models can also be used to address *what if* scenarios which are of interest in hydrocarbon exploration. One of the most successful rock physics models is Gassmann's fluid substitution theory (Gassmann, 1951), which predicts the change in low-frequency seismic velocities or rock stiffness upon change in pore-fluid. In part, the success of Gassmann's theory is due to the fact that all required inputs are either usually known or directly measured, with no adjustable parameters; these relations can be written as

$$\frac{\left(\frac{1}{K_{dry}}-\frac{1}{K_{ud}}\right)}{\left(\frac{1}{K_{ud}}-\frac{1}{K^{B}}\right)\left(\frac{1}{K_{dry}}-\frac{1}{K^{B}}\right)}=\frac{1}{\phi\left(\frac{1}{K^{f}}-\frac{1}{K^{B}}\right)}\quad , \tag{8.1}$$

and

$$\mu_{ud}=\mu_{dry}\quad , \tag{8.2}$$

where K_{ud} and K_{dry} are un-drained (fluid saturated) and dry rock bulk moduli, respectively; μ_{ud} and μ_{dry} are the corresponding shear moduli; K^{f} and K^{B} are bulk moduli of the pore-fluid and the mineral in rock frame; ϕ is the volume fraction of pores (porosity). Equations 8.1 and 8.2 are exact if

i. rock frame is monomineralic (i.e., single mineral)

ii. initial and final pores are fully saturated with ideal elastic fluids
iii. load-induced pore-pressure under quasi-static deformation is homogeneous
iv. upon substitution there is no change to rock microstructure
v. only the pore phase is substituted.

Brown and Korringa (1975) extended Gassmann's equations to the case of multimineralic rock frame (of mixed mineralogy) thus relaxing assumption (i). Ciz and Shapiro (2007) further generalized Brown and Korringa's results to rocks with solid-filled pores, thus further relaxing assumptions (ii) and (iii). Still, these extensions are fundamentally limited to situations where only *one* phase is substituted and there is *no* change in the pore geometry. There are many problems for which we need to further relax assumptions (iv) and (v). Pore geometry can change due to a variety of geological processes: digenesis, sorting, partial melting/freezing, mineral precipitation, etc. For such problems, inclusion based effective medium models (Wu, 1966; O'Connell and Budiansky, 1974; Kuster and Toksöz, 1974; Berryman, 1980; Cleary et al., 1995), can provide insightful approximate predictions since these loosely relax assumptions (i)-(v), however, these models idealize rock microstructure with ellipsoids and require adjustable parameters such as aspect ratios, which are also poorly determined.

In this chapter, we further relax assumptions (i)-(v) and obtain *exact* solutions for arbitrary pore shape and mixed mineralogy, such that pore geometry can change and more than one phase can be substituted simultaneously.

Digenetic trends are usually modeled (Avseth et al., 2010; Dvorkin and Nur, 1996) by mixing the high-porosity cemented sand-point with the mineral-point using the upper Hashin-Shtrikman (HS) bound (Hashin and Shtrkiman, 1963). Similarly, sorting trends are modeled with the lower HS bound. Although such heuristic approaches have been fairly successful (Avseth et al., 2005) we note that if assumptions (i)-(v) are relaxed, change in rock stiffness due to digenesis, sorting and other geologic processes, can be rigorously modeled and predicted.

Change in pore geometry can also occur due to dissolution/precipitation which typically leads to partial replacement of existing and/or formation of new phases (Hoefiner

and Fogler, 1988; Guen et al., 2007; Vanorio et al., 2011; Vialle and Vanorio, 2011; Bemer et al., 2013). In such situations, since modeling fluid or solid substitution is also accompanied by changes in pore geometry, traditional fluid or solid substitution approaches cannot be employed. For example, assumption (iv) in Gassmann's fluid substitution theory will be violated when modeling time-lapse seismic signatures of subsurface movement of chemically reactive CO_2 due to possible changes in the rock frame (Lumley, 2010).

Additionally, there are also situations where more than one phase in a multimineralic rock needs to be substituted; fundamentally this is equivalent to the problem of predicting rock stiffness change due to changing pore geometry. Examples of such problems include only partially substituting a pore-fill phase in a multimineralic rock - a situation encountered while modeling effects of steam injection in heavy oil reservoirs (Schmitt, 1999; Bianco et al., 2008; Chopra et al., 2010). Similar situations occur when modeling rock stiffness change due to partial melting (Duputel et al., 2009) or due to partial pore-fluid freezing in permafrost (Timur, 1968; Kurfurst, 1976; King, 1977; Zimmerman and King, 1986; King et al., 1988; Jacoby et al., 1996; Sondergeld and Rai, 2007).

The sections of this chapter are organized as follows. In the next section we present our main result and discuss the implication of our exact solutions in the context of past work. Details of derivation are not discussed in the main body and are instead presented in Appendix A. In the subsequent sections, we discuss special cases of our exact solutions.

8.3. Main results

Consider an isotropic composite (rock) with N elastic phases, such that each phase q ($q \in N$) has volume fraction ϕ_q with its bulk and shear moduli given by K^{q1} and μ^{q1}, respectively. Upon substitution, moduli of all but one of these phases change to K^{q2} and μ^{q2}; for convenience, we name the un-changing phase as B ($B \in N$). Then, the exact bulk modulus equation for substitution of N-1 phases in a N phase composite is:

$$\frac{\left(\frac{1}{K_{ud}^{(1)}}-\frac{1}{K_{ud}^{(2)}}\right)}{\left(\frac{1}{K_{ud}^{(1)}}-\frac{1}{K^{B}}\right)\left(\frac{1}{K_{ud}^{(2)}}-\frac{1}{K^{B}}\right)}=\sum_{\substack{q=1\\q\neq B}}^{N}\frac{\left(\frac{1}{K^{q1}}-\frac{1}{K^{q2}}\right)\alpha_1^q+\left(\frac{1}{\mu^{q1}}-\frac{1}{\mu^{q2}}\right)\alpha_2^q}{\phi_q\left(\sum_{\substack{r=1\\r\neq B}}^{N}\left(\frac{1}{K^{r1}}-\frac{1}{K^{B}}\right)\frac{\phi_r}{\phi_q}\frac{\overline{P^{r1}}}{\overline{P^{q1}}}\right)\left(\sum_{\substack{r=1\\r\neq B}}^{N}\left(\frac{1}{K^{r2}}-\frac{1}{K^{B}}\right)\frac{\phi_r}{\phi_q}\frac{\overline{P^{r2}}}{\overline{P^{q2}}}\right)} \quad . \tag{8.3}$$

where $K_{ud}^{(1)}$ and $K_{ud}^{(2)}$ are initial and substituted effective bulk moduli, respectively. In equation 8.3, r is a dummy index which sums over all phases except for phase B. In equation 8.3, P^q is the bulk compression-induced pressure (mean-stress) in any phase q, related to the induced Cauchy stress tensor σ_{ij}^q as

$$\sigma_{ij}^q=-P^q\delta_{ij}+\tau_{ij}^q \ , \tag{8.4}$$

where τ_{ij}^q are the bulk compression-induced deviatoric stresses in any phase q. For each phase stresses are related to strains by Hooke's law

$$P^q=-K^q e^q \ , \tag{8.5}$$

$$\tau_{ij}^q=2\mu^q\gamma_{ij}^q \ . \tag{8.6}$$

In equations 8.5 and 8.6, e^q and γ_{ij}^q are the mean and deviatoric parts of strain induced in any phase q, respectively. Here we use standard summation convention over repeated indices and symbol δ_{ij} is the Kronecker delta function. Symbol $\overline{\Omega^q}$ denotes the volume average of any quantity Ω^q (over the volume of phase q). The parameters α_1^q and α_2^q for each substituted phase q are defined as

$$\alpha_1^q=\frac{\overline{P^{q1}P^{q2}}}{\overline{P^{q1}}\ \overline{P^{q2}}}=\frac{\overline{e^{q1}e^{q2}}}{\overline{e^{q1}}\ \overline{e^{q2}}};\quad \alpha_2^q=\frac{1}{2}\frac{\overline{\tau_{ij}^{q1}\tau_{ij}^{q2}}}{\overline{P^{q1}}\ \overline{P^{q2}}}=2\frac{\mu^{q1}\mu^{q2}}{K^{q1}K^{q2}}\frac{\overline{\gamma_{ij}^{q1}\gamma_{ij}^{q2}}}{\overline{e^{q1}}\ \overline{e^{q2}}} \quad . \tag{8.7}$$

Similarly, the exact substitution equation for shear modulus is

$$\frac{\left(\frac{1}{\mu_{ud}^{(1)}}-\frac{1}{\mu_{ud}^{(2)}}\right)}{\left(\frac{1}{\mu_{ud}^{(1)}}-\frac{1}{\mu^{B}}\right)\left(\frac{1}{\mu_{ud}^{(2)}}-\frac{1}{\mu^{B}}\right)}=\sum_{\substack{q=1\\ q\neq B}}^{N}\frac{\left(\frac{1}{\mu^{q1}}-\frac{1}{\mu^{q2}}\right)\beta_1^q+\left(\frac{1}{K^{q1}}-\frac{1}{K^{q2}}\right)\beta_2^q}{\phi_q\left(\sum_{\substack{r=1\\ r\neq B}}^{N}\left(\frac{1}{\mu^{r1}}-\frac{1}{\mu^{B}}\right)\frac{\phi_r\overline{\tau_{12}^{r1}}}{\phi_q\overline{\tau_{12}^{q1}}}\right)\left(\sum_{\substack{r=1\\ r\neq B}}^{N}\left(\frac{1}{\mu^{r2}}-\frac{1}{\mu^{B}}\right)\frac{\phi_r\overline{\tau_{12}^{r2}}}{\phi_q\overline{\tau_{12}^{q2}}}\right)}\quad, \tag{8.8}$$

where $\mu_{ud}^{(1)}$ and $\mu_{ud}^{(2)}$ are initial and substituted effective shear moduli; P^q and τ_{ij}^q are shear field-induced pressure and deviatoric stresses. The parameters β_1^q and β_2^q for each phase q are defined as

$$\beta_1^q=\frac{1}{2}\frac{\overline{\tau_{ij}^{q1}\tau_{ij}^{q2}}}{\overline{\tau_{12}^{q1}}\;\overline{\tau_{12}^{q2}}}=\frac{1}{2}\frac{\overline{\gamma_{ij}^{q1}\gamma_{ij}^{q2}}}{\overline{\gamma_{12}^{q1}}\;\overline{\gamma_{12}^{q2}}};\quad \beta_2^q=\frac{\overline{P^{q1}P^{q2}}}{\overline{\tau_{12}^{q1}}\;\overline{\tau_{12}^{q2}}}=\frac{1}{4}\frac{K^{q1}K^{q2}}{\mu^{q1}\mu^{q2}}\frac{\overline{e^{q1}e^{q2}}}{\overline{\gamma_{12}^{q1}}\;\overline{\gamma_{12}^{q2}}}\quad. \tag{8.9}$$

Parameter α_1^q describes the heterogeneity of compression-induced pressure in any phase q; whereas parameter α_2^q describes the contribution of compression-induced deviatoric stresses in any phase q. Similarly, parameter β_1^q describes the heterogeneity of shear field-induced deviatoric stresses and the parameter β_2^q describes the contribution of shear field-induced pressure. Derivation of equations 8.3 and 8.8 is presented in Appendix A.

Under the assumptions (i)-(v), equations 8.3 and 8.8 reduce to Gassmann's equations (8.1 and 8.2) which can be easily checked. Relaxing only the first assumption (i) but still assuming (ii)-(v), for shear modulus we recover Gassmann's result in equation 8.2, and for bulk modulus we obtain an algebraically *different* but fundamentally *identical* equation than that previously derived by Brown and Korringa. This new result is

$$\frac{\left(\frac{1}{K_{dry}}-\frac{1}{K_{ud}}\right)}{\left(\frac{1}{K_{ud}}-\frac{1}{K^{B}}\right)\left(\frac{1}{K_{dry}}-\frac{1}{K^{B}}\right)}=\frac{1}{\phi\left(\frac{1}{K^{f}}-\frac{1}{K^{M}}\right)\left(\frac{K^{M-dry}K^{M}}{K^{B}K^{B}}\right)}\quad. \tag{8.10}$$

Equation 8.10 features two additional stiffnesses given by

$$K^M = K^B + \sum_{\substack{r=1 \\ r\neq B,f}}^{N} \frac{\phi_r \overline{e^r}}{\phi e^f}\left(K^B - K^r\right) \quad ; K^{M-dry} = K^B + \sum_{\substack{r=1 \\ r\neq B,f}}^{N} \frac{\phi_r \overline{e^{r-dry}}}{\phi e^{f-dry}}\left(K^B - K^r\right), \tag{8.11}$$

where, e^f and e^{f-dry} are compression induced fluid-saturated and dry pore volumetric strains, respectively; $\overline{e^r}$ and $\overline{e^{r-dry}}$ are the induced volumetric strains (volume averaged) in phase r ($r \in N$), when pores are fluid-saturated and dry, respectively. Note that K^{M-dry} is a "dry" rock property, thus is independent of fluid modulus, whereas K^M depends on the fluid modulus. Further relaxing assumptions (ii) and (iii) we can obtain the solid substitution solutions discussed in chapter 2 (Saxena and Mavko, 2014).

Equations 8.3 and 8.8, also relax assumptions (iv) and (v). This is so since these relations allow for substitution of all but one phase in an isotropic multimineralic rock, which also allows for modeling change in rock microstructure. For example, consider a two-phase monomineralic dry rock; we can divide, albeit virtually, this two-phase composite into a three-phase system: two phases of the (same) mineral in the frame (of identical elastic stiffness) and one phase of dry pores; therefore one of the mineral phases can be substituted thus changing the rock pore geometry.

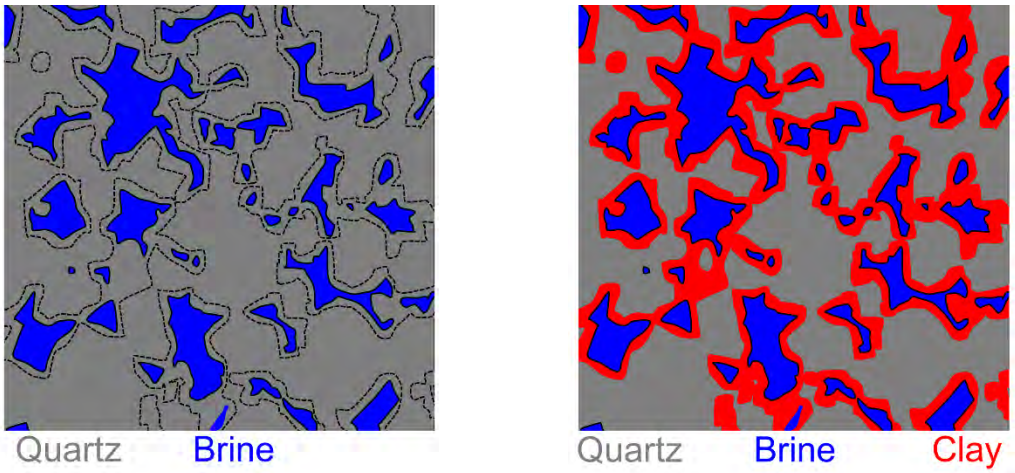

(a) (b)

Figure 8.1: (a) 2D slide of a digital 3D Fontainebleau sandstone sample (Andrä et al., 2013), composed of quartz grains (in gray) and brine saturated pores (in blue), dashed black lines show imaginary cuts. (b) Digitally altered sandstone sample with the region between pore boundaries and imaginary cuts (in Figure 8.1a) replaced with clay (in red).

As an illustration of the exact solution in equations 8.3 and 8.8, we now consider a 3D digital Fontainebleau sandstone sample (porosity 0.15; Andrä et al., 2013). Mineral frame of a Fontainebleau sandstone is typically composed of quartz grains (bulk modulus 36 GPa and shear modulus 45 GPa), but in this exercise we digitally alter a part of quartz grains and replace them with a pore-lining clay phase (bulk modulus 21 GPa and shear modulus 15 GPa). Such that the total volume fraction of clay is 0.27. 2D slices of the original 3D and the digitally altered samples are shown in Figures 8.1a and 8.1b, respectively. We assume that the pores are occupied (for both cases) with brine (bulk modulus 3 GPa and shear modulus 0 GPa). Using the FEM, we calculate the effective bulk moduli of the original and clay sandstone to be 25.6 GPa and 21.7 GPa, respectively. For the FEM calculation we apply bulk strain of magnitude 0.003; Figure 8.2 shows the induced pressure (negative of mean stress) in each phase.

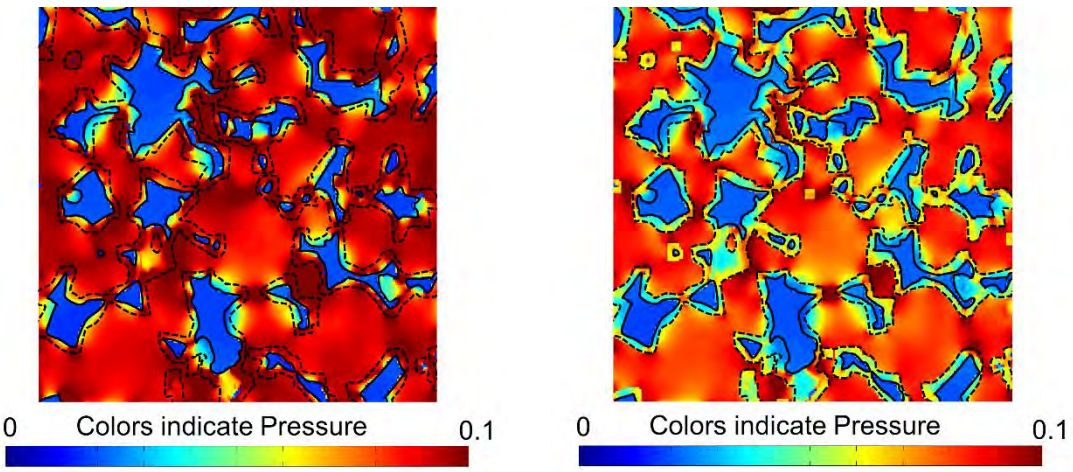

(a) (b)

Figure 8.2: (a) induced pressure upon compression in the original sandstone. (b) Induced pressure in clay sandstone. Color scale is normalized with the same maximum value for both (a) and (b) for direct comparison.

Now we will compare the FEM computed effective bulk modulus of the original rock (with all quartz grains), with that predicted by equation 8.3 starting with the FEM computed bulk modulus of the clay sandstone. The required parameters are: the ratio of volume averaged pressure induced in brine and clay phases in the clay sandstone which is equal to

0.4 (from the FEM), and the ratio of volume averaged pressure induced in brine and quartz (for only the part which has replaced clay) which is equal to 0.22. Also needed are parameters α_1 and α_2 corresponding to the substituted phase (clay to quartz); for these parameters the FEM computed values are $\alpha_1 = 1.13$ and $\alpha_2 = 0.16$. Using these inputs, equation 8.3 predicts the bulk modulus of the original sandstone to be 25.6 GPa, which matches the FEM computed value. In the next sections, we discuss how equations 8.3 and 8.8 can be used in practice.

8.4. Substitution of two phases in a three phase composite

8.4.1. Exact solutions

For the limiting case of substitution of two phases in a three phase multimineralic isotropic rock, such that fluid/solid phases $f1$ and $m1$ (volume fractions ϕ_f and ϕ_m) are to be replaced with new phases $f2$ and $m2$, respectively, our exact results in equations 8.3 and 8.8 reduce to

$$\frac{\left(\frac{1}{K_{ud}^{(1)}}-\frac{1}{K_{ud}^{(2)}}\right)}{\left(\frac{1}{K_{ud}^{(1)}}-\frac{1}{K^B}\right)\left(\frac{1}{K_{ud}^{(2)}}-\frac{1}{K^B}\right)} = \tag{8.12}$$

$$\frac{\left(\frac{1}{K^{f1}}-\frac{1}{K^{f2}}\right)\alpha_1^f+\left(\frac{1}{\mu^{f1}}-\frac{1}{\mu^{f2}}\right)\alpha_2^f+\frac{\phi_m}{\phi_f}\frac{\overline{P^{m1}}}{\overline{P^{f1}}}\frac{\overline{P^{m2}}}{\overline{P^{f2}}}\left(\left(\frac{1}{K^{m1}}-\frac{1}{K^{m2}}\right)\alpha_1^m+\left(\frac{1}{\mu^{m1}}-\frac{1}{\mu^{m2}}\right)\alpha_2^m\right)}{\phi_f\left(\frac{1}{K^{f1}}-\frac{1}{K^B}+\left(\frac{1}{K^{m1}}-\frac{1}{K^B}\right)\frac{\phi_m}{\phi_f}\frac{\overline{P^{m1}}}{\overline{P^{f1}}}\right)\left(\frac{1}{K^{f2}}-\frac{1}{K^B}+\left(\frac{1}{K^{m2}}-\frac{1}{K^B}\right)\frac{\phi_m}{\phi_f}\frac{\overline{P^{m2}}}{\overline{P^{f2}}}\right)}$$

,

and

$$\frac{\left(\frac{1}{\mu_{ud}^{(1)}}-\frac{1}{\mu_{ud}^{(2)}}\right)}{\left(\frac{1}{\mu_{ud}^{(1)}}-\frac{1}{\mu^{B}}\right)\left(\frac{1}{\mu_{ud}^{(2)}}-\frac{1}{\mu^{B}}\right)}= \tag{8.13}$$

$$\frac{\left(\frac{1}{\mu^{f1}}-\frac{1}{\mu^{f2}}\right)\beta_1^f+\left(\frac{1}{K^{f1}}-\frac{1}{K^{f2}}\right)\beta_2^f+\frac{\phi_m\overline{\tau_{12}^{m1}}\,\overline{\tau_{12}^{m2}}}{\phi_f\overline{\tau_{12}^{f1}}\,\overline{\tau_{12}^{f2}}}\left(\left(\frac{1}{\mu^{m1}}-\frac{1}{\mu^{m2}}\right)\beta_1^m+\left(\frac{1}{K^{m1}}-\frac{1}{K^{m2}}\right)\beta_2^m\right)}{\phi_f\left(\frac{1}{\mu^{f1}}-\frac{1}{\mu^{B}}+\left(\frac{1}{\mu^{m1}}-\frac{1}{\mu^{B}}\right)\frac{\phi_m\overline{\tau_{12}^{m1}}}{\phi_f\overline{\tau_{12}^{f1}}}\right)\left(\frac{1}{\mu^{f2}}-\frac{1}{\mu^{B}}+\left(\frac{1}{\mu^{m2}}-\frac{1}{\mu^{B}}\right)\frac{\phi_m\overline{\tau_{12}^{m2}}}{\phi_f\overline{\tau_{12}^{f2}}}\right)}$$

.

8.4.2. **Approximate bounds for weak contrast in substituted phases**

Assuming relatively homogeneous load induced stresses yields: $\alpha_1^{f,m}\approx 1$ and $\beta_1^{f,m}\approx 1$. For composites with homogeneous induced stresses, we (Saxena and Mavko, 2014) have shown that $\alpha_1 >> \alpha_2$ and $\beta_1 >> \beta_2$, thus if $K^{f1}\approx K^{f2}$ and $\mu^{f1}\approx\mu^{f2}$ we can neglect the terms corresponding to parameters $\alpha_2^{f,m}$ and $\beta_2^{f,m}$ in equations 8.12 and 8.13, which is equivalent to assuming $\alpha_2^{f,m}\approx 0$ and $\beta_2^{f,m}\approx 0$. Under these assumptions, both equations 8.12 and 8.13 can be compactly written as

$$\frac{\left(\frac{1}{M_{ud}^{(1)}}-\frac{1}{M_{ud}^{(2)}}\right)}{\left(\frac{1}{M_{ud}^{(1)}}-\frac{1}{M^{B}}\right)\left(\frac{1}{M_{ud}^{(2)}}-\frac{1}{M^{B}}\right)}\approx \tag{8.14}$$

$$\frac{\left(\frac{1}{M^{f1}}-\frac{1}{M^{f2}}\right)+\frac{\phi_f}{\phi_m}\xi^{m1f1}\xi^{m2f2}\left(\frac{1}{M^{m1}}-\frac{1}{M^{m2}}\right)}{\phi_f\left(\frac{1}{M^{f1}}-\frac{1}{M^{B}}+\left(\frac{1}{M^{m1}}-\frac{1}{M^{B}}\right)\xi^{m1f1}\right)\left(\frac{1}{M^{f2}}-\frac{1}{M^{B}}+\left(\frac{1}{M^{m2}}-\frac{1}{M^{B}}\right)\xi^{m2f2}\right)}\ ,$$

In equation 8.14, if we replace M with K and ξ^{mf} with $\left(\phi_m \overline{P^m}\right)/\left(\phi_f \overline{P^f}\right)$ we obtain the equation for bulk modulus, whereas if we replace M with μ and ξ^{mf} and $\left(\phi_m \overline{\tau_{12}^m}\right)/\left(\phi_f \overline{\tau_{12}^f}\right)$ we obtain the equation for shear modulus. Parameters ξ^{mf} describe the averaged stress ratio in phases *f* and *m*. We will now explore the limiting values for parameters ξ^{mf} and put approximate bounds on the problem. Approximating a mix of phases *m* and *f* as a two-phase composite we can write the effective stiffness (Hashin, 1962) as

$$\left(\frac{1}{M^m}-\frac{1}{M_{fm-mix}}\right)\left(1+\xi^{mf}\right)=\left(\frac{1}{M^m}-\frac{1}{M^f}\right) \ , \tag{8.15}$$

where M_{fm-mix} is the effective stiffness of the two-phase composite. More details on the derivation of equation 8.15 can be found in the Appendix A (this equation is a special case of equations A-5 and A-12 for a two phase composite). Using the Hashin-Shtrikman (HS) bounds (Hashin and Shtrikman, 1963) on the effective stiffness M_{fm-mix} we obtain the following inequalities:

$$\frac{M^m\left(M_{fm-mix}^{HS+}-M^f\right)}{M^f\left(M^m-M_{fm-mix}^{HS+}\right)} \geq \xi^{mf} \geq \frac{M^m\left(M_{fm-mix}^{HS-}-M^f\right)}{M^f\left(M^m-M_{fm-mix}^{HS-}\right)} \ , \tag{8.16}$$

where, M_{fm-mix}^{HS+} and M_{fm-mix}^{HS-} are upper and lower HS bounds on effective modulus for a mix of phases *m* and *f*, respectively (expressions for HS bounds are presented in the Appendix B). Equations 8.14 and 8.16 together describe approximate bounds on change in bulk and shear moduli upon substitution. We refer to these as the *HS*- and *HS*+ approximations corresponding to M_{fm-mix}^{HS+} and M_{fm-mix}^{HS-} moduli, respectively. These can be easily extended to model substitution of more than two phases in an *N* phase multimineralic isotropic rock.

8.4.3. **FEM example of a heavy-oil rock**

As an example of substitution of two phases in a three phase multimineralic rock using equations 8.14 and 8.16, we now discuss a numerical example of substitution in a digital bituminous sand sample. This digital sample was imaged, processed and later segmented using a commercially available software. This 3D sample is shown in Figure 8.3.

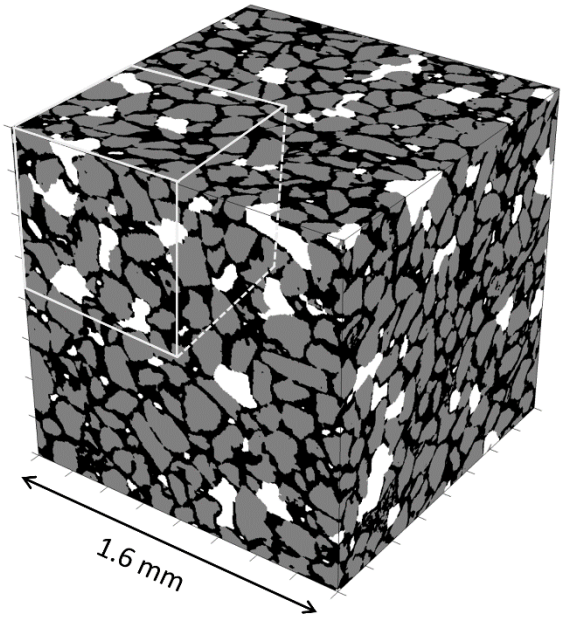

Figure 8.3: Original bituminous sand sample digital cube of size 1.6 mm; sub-cube of size 0.8 mm is also shown.

Imaging revealed grain size roughly between 0.1 mm-0.25 mm (assumed to be quartz; volume fraction 0.56) and some air-saturated pores (volume fraction of about 0.07) in addition to bitumen-filled pores (volume fraction 0.37). The spatial resolution of this segmented digital rock is 0.004 mm (in x, y and z) and the cube length is 1.6 mm. We populate the digital sample with the following elastic properties: quartz grains of 36 GPa bulk modulus and 45 GPa shear modulus, air as an ideal fluid of bulk modulus 0.005 GPa and bitumen as a soft elastic solid of 4 GPa bulk modulus and 0.5 GPa shear modulus. Next, we numerically compute the effective moduli of subsamples of the digital rock using the finite element method (FEM). We also re-calculate the effective moduli after digitally replacing both the air-saturated and bitumen-saturated pores with cold bitumen (bulk

modulus: 4 GPa; shear modulus 1 GPa). Using the *HS*+ and *HS*- approximations (equations 8.14 and 8.16) we predict the change in effective moduli upon substitution of both air-saturated and bitumen-saturated pores with cold bitumen, starting with the initial FEM computed moduli. These predictions are shown in Figures 8.4a and 8.4b for bulk and shear moduli, respectively. Comparing these predictions with the FEM computations, we note that most FEM computations, for both bulk and shear, are closer to predictions of the *HS*+ approximation which, in this example, predicts the least change. The range predicted by the *HS*+ and *HS*- approximations is fairly narrow and contains the FEM computations.

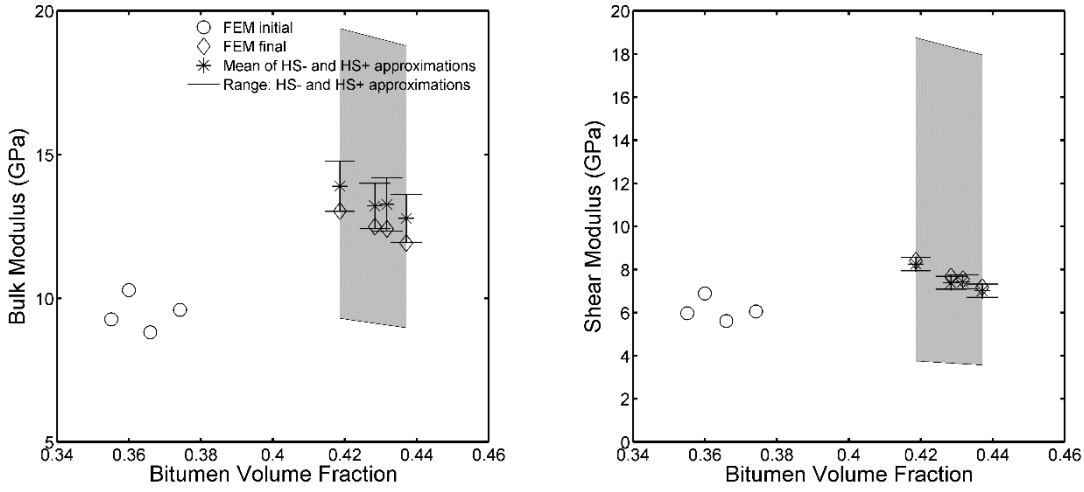

(a) (b)

Figure 8.4: Predicted bulk (a) and shear (b) moduli of bituminous sand with cold bitumen, starting with the FEM computed moduli of bituminous sand with air and bitumen saturated pores. The range predicted by the Hashin-Shtrikman bounds are shown in gray region.

8.4.4. **Laboratory example of permafrost**

Figures 8.5a and 8.5b show laboratory measured ultrasonic velocities of unconsolidated sand (of porosity around 0.4) as reported by Zimmerman and King (1986). The measured velocities are plotted as a function of ice filled porosity (bulk: 8.4 GPa; shear: 3.7 GPa), such that the remaining pores are saturated with water (bulk: 2.2 GPa). Assuming quartz (bulk: 36 GPa; shear: 45 GPa) as the predominant mineral in the rock frame, starting with the fully frozen sand sample velocities (i.e., all pores filled with ice), we predict the

velocities corresponding to the partially frozen sand samples, using the approximate bounds in equations 8.14 and 8.16. We note that the approximate bounds contain these measured velocities. The *HS*+ approximation predicts the least change upon substitution, and the measurements are relatively closer to the *HS*+ approximation when compared to *HS*- approximation. The range predicted by *HS*+ and *HS*- approximations describes the uncertainty of not knowing in which part of the pore space, ice was being replaced with water. Note that for this problem since the contrast between the elastic properties of quartz and ice is quite large our assumption of $\alpha_1^{f,m} \approx 1$, $\beta_1^{f,m} \approx 1$. $\alpha_2^{f,m} \approx 0$ and $\beta_2^{f,m} \approx 0$ may not be justified.

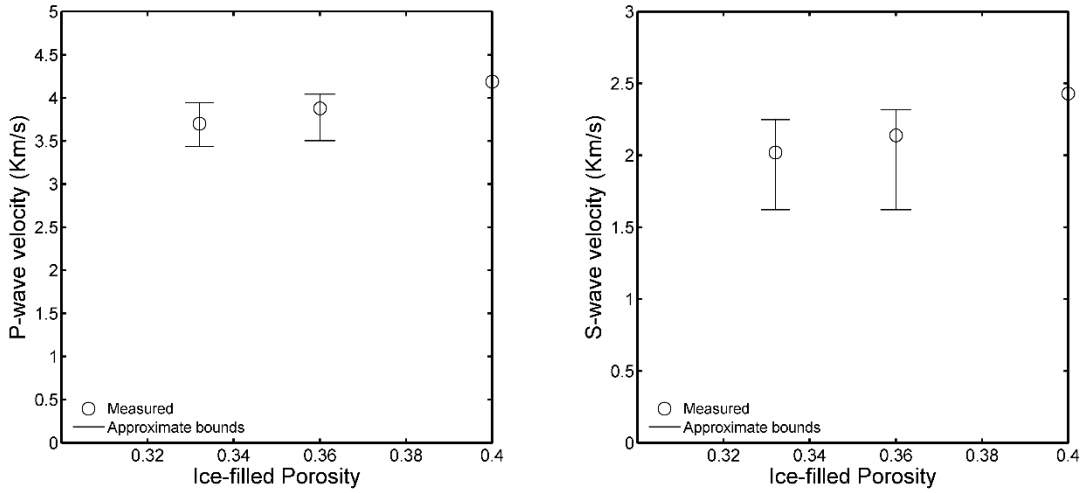

(a) (b)

Figure 8.5: Predicted P-wave (a) and S-wave (b) velocities of sand samples with partially ice-filled pores, starting with the measured velocities of a sand sample fully filled with ice.

8.5. Modeling effects of dissolution or precipitation

8.5.1. Exact solutions

Consider a rock of porosity ϕ_f such that the pores are fully filled with a fluid or solid (denoted by superscript *f*, of bulk modulus K^f and shear modulus μ^f), and the frame is composed of a single mineral/solid (denoted by superscript *B*, of bulk modulus K^B and shear modulus μ^B). For this rock, let's say that the measured/known bulk and shear moduli

are given by $K_{ud}^{(1)}$ and $\mu_{ud}^{(1)}$. Next, suppose we dissolve away a part of the frame mineral such that the newly created pores are also now occupied by the original pore material *f*; the modified porosity is given by $\phi_f + \phi_m$, where ϕ_m is the volume fraction of the rock mineral now replaced by the pore material. Also, let's assume that the modified (and as yet unknown) bulk and shear moduli are given by $K_{ud}^{(2)}$ and $\mu_{ud}^{(2)}$. A conceptual diagram is shown in Figure 8.6.

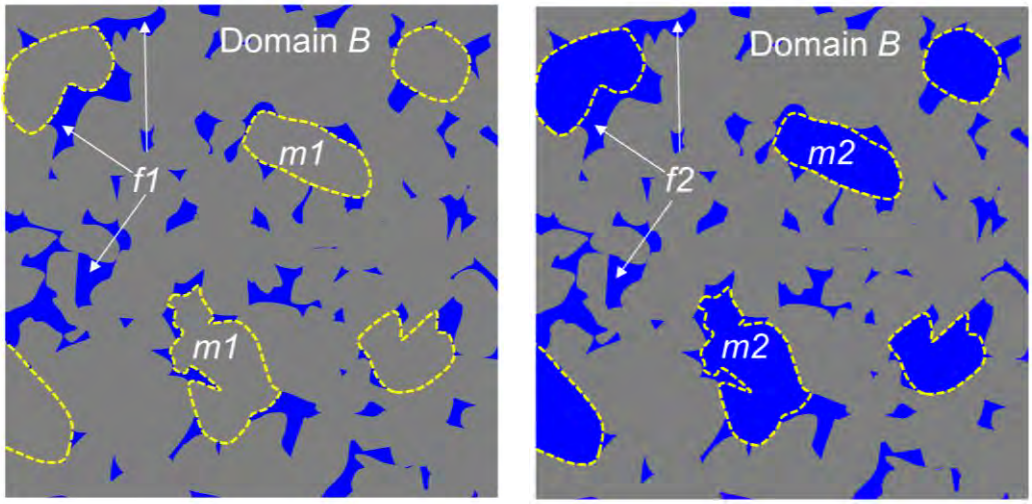

(a) (b)

Figure 8.6: Conceptual diagram of before (a) and after dissolution (b). Frame solid is shown in gray and pore solid is shown in white. Solid curves represent pore boundaries whereas dashed curves represent imaginary cuts.

For this situation, equations 8.3 and 8.8 reduce to the following exact relations

$$\frac{\left(K_{ud}^{(2)} - K_{ud}^{(1)}\right)}{\left(K^B - K_{ud}^{(1)}\right)\left(K^B - K_{ud}^{(2)}\right)} = \frac{\phi_m\left(K^f - K^B\right)\alpha_1^m + \phi_m\left(\mu^f - \mu^B\right)\alpha_2'^m}{\phi_f\left(K^f - K^B\right)^2\left(\dfrac{\overline{e^{f1}}}{\overline{\overline{e^{m1}}}}\right)\left(\phi_f\dfrac{\overline{e^{f2}}}{\overline{\overline{e^{m2}}}} + \phi_m\right)}, \tag{8.17}$$

and

$$\frac{\left(\mu_{ud}^{(2)}-\mu_{ud}^{(1)}\right)}{\left(\mu^{B}-\mu_{ud}^{(1)}\right)\left(\mu^{B}-\mu_{ud}^{(2)}\right)}=\frac{\phi_m\left(K^f-K^B\right)\beta_2'^m+\phi_m\left(\mu^f-\mu^B\right)\beta_1^m}{\phi_f\left(\mu^f-\mu^B\right)^2\left(\dfrac{\overline{\gamma_{12}^{f1}}}{\overline{\gamma_{12}^{m1}}}\right)\left(\phi_f\dfrac{\overline{\gamma_{12}^{f2}}}{\overline{\gamma_{12}^{m2}}}+\phi_m\right)} \quad . \tag{8.18}$$

In equations 8.17 and 8.18, parameters $\alpha_1^m, \alpha_2'^m$, β_1^m and $\beta_2'^m$ are given by

$$\alpha_1^m=\frac{\overline{P^{m1}P^{m2}}}{\overline{P^{m1}}\;\overline{P^{m2}}}=\frac{\overline{e^{m1}e^{m2}}}{\overline{e^{m1}}\;\overline{e^{m2}}};\quad \alpha_2'^m=2\frac{\overline{\gamma_{ij}^{m1}\gamma_{ij}^{m2}}}{\overline{e^{m1}}\;\overline{e^{m2}}} \quad , \tag{8.19}$$

$$\beta_1^m=\frac{1}{2}\frac{\overline{\tau_{ij}^{q1}\tau_{ij}^{q2}}}{\overline{\tau_{12}^{q1}}\;\overline{\tau_{12}^{q2}}}=\frac{1}{2}\frac{\overline{\gamma_{ij}^{m1}\gamma_{ij}^{m2}}}{\overline{\gamma_{12}^{m1}}\;\overline{\gamma_{12}^{m2}}};\quad \beta_2'^m=\frac{1}{4}\frac{\overline{e^{m1}e^{m2}}}{\overline{\gamma_{12}^{m1}}\;\overline{\gamma_{12}^{m2}}} \quad , \tag{8.20}$$

Note that parameters α_2' and β_2' in equations 8.19 and 8.20 are modified versions of parameters α_2 and β_2 (in equations 8.7 and 8.9) expressed in terms of induced strains instead of stresses. In the above equations, the original pores before dissolution are denoted as phase *f*1, whereas phase *m*1 denotes the part of the frame mineral (before dissolution) which is to be replaced by the pore material. Phase *f*2 denotes the original pores but after dissolution and phase *m*2 denotes the newly formed pores post dissolution (initially a part of the frame mineral). Thus, $K^{f1}=K^{f2}=K^f, K^{m1}=K^B, K^{m2}=K^f$, and similarly for the shear modulus, $\mu^{f1}=\mu^{f2}=\mu^f$, $\mu^{m1}=\mu^B$, $\mu^{m2}=\mu^f$.

8.5.2. **Approximate bounds for weak contrast in substituted phases**

To predict the modified effective bulk and shear moduli, we need to know parameters α_1^m, $\alpha_2'^m$, β_1^m, $\beta_2'^m$, and strain ratio parameters $\overline{e^f}/\overline{e^m}$ and $\overline{\gamma_{12}^f}/\overline{\gamma_{12}^m}$. These parameters depend on the detail of initial and final rock microstructure. Parameters $\overline{e^f}/\overline{e^m}$ and $\overline{\gamma_{12}^f}/\overline{\gamma_{12}^m}$ denote the ratio of volume averaged strains in the initial pores and material occupying the newly made pores. Similar to our discussion in the previous section, we explore the limiting values for these parameters and put approximate bounds on the problem.

Approximating a mix of phases *m1* and *f1* as a two-phase composite, using HS bounds we obtain the following *approximate* inequalities:

$$\frac{\left(K^B - K^{HS+}_{fm-mix}\right)}{\left(K^{HS+}_{fm-mix} - K^f\right)} \le \frac{\phi_f K^B \overline{P^{f1}}}{\phi_m K^f \overline{P^{m1}}} = \frac{\phi_f \overline{e^{f1}}}{\phi_m \overline{e^{m1}}} \le \frac{\left(K^B - K^{HS-}_{fm-mix}\right)}{\left(K^{HS-}_{fm-mix} - K^f\right)} \quad , \tag{8.21}$$

$$\frac{\left(\mu^B - \mu^{HS+}_{fm-mix}\right)}{\left(\mu^{HS+}_{fm-mix} - \mu^f\right)} \le \frac{\phi_f \mu^B \overline{\tau^{f1}_{12}}}{\phi_m \mu^f \overline{\tau^{m1}_{12}}} = \frac{\phi_f \overline{\gamma^{f1}_{12}}}{\phi_m \overline{\gamma^{m1}_{12}}} \le \frac{\left(\mu^B - \mu^{HS-}_{fm-mix}\right)}{\left(\mu^{HS-}_{fm-mix} - \mu^f\right)} \quad . \tag{8.22}$$

where, K^{HS+-}_{fm-mix} and μ^{HS+-}_{fm-mix} are upper/lower HS bounds for bulk and shear moduli for a mix of phases *m1* and *f1*, respectively. Approximate inequalities in equations 8.21 and 8.22 are conceptually identical to those discussed in equation 8.16.

Assuming *homogenous* induced stress/strains along with a *weak* elastic contrast between materials *f* and *B*, we can approximate $\alpha_1^m \approx 1$, $\alpha_2'^m \approx 0$, $\beta_1^m \approx 1$ and $\beta_2'^m \approx 0$. For the above case, both phases *f2* and *m2* are occupied by material *f*, thus we can approximate $\overline{e^{f2}} \approx \overline{e^{m2}}$ and $\overline{\gamma_{12}^{f2}} \approx \overline{\gamma_{12}^{m2}}$. Under these assumptions, using the upper HS bound we obtain the *HS+* approximations

$$\frac{\left(K^{(2)}_{ud} - K^{(1)}_{ud}\right)}{\left(K^B - K^{(1)}_{ud}\right)\left(K^B - K^{(2)}_{ud}\right)} = \frac{\phi_m\left(4\mu^B + 3K^f\right)}{\phi_f\left(K^f - K^B\right)\left(4\mu^B + 3K^B\right)\left(\phi_f + \phi_m\right)} \quad , \tag{8.23}$$

and

$$\frac{\left(\mu^{(2)}_{ud} - \mu^{(1)}_{ud}\right)}{\left(\mu^B - \mu^{(1)}_{ud}\right)\left(\mu^B - \mu^{(2)}_{ud}\right)} = \frac{\phi_m\left(9K^B + 8\mu^B\right)}{\phi_f\left(\mu^f - \mu^B\right)\left(15K^B + 20\mu^B\right)\left(\phi_f + \phi_m\right)} \quad . \tag{8.24}$$

Similarly, using the lower HS bound, we obtain the *HS-* approximations

$$\frac{\left(K^{(2)}_{ud} - K^{(1)}_{ud}\right)}{\left(K^B - K^{(1)}_{ud}\right)\left(K^B - K^{(2)}_{ud}\right)} = \frac{\phi_m K^f}{\phi_f\left(K^f - K^B\right)K^B\left(\phi_f + \phi_m\right)} \quad , \tag{8.25}$$

and

$$\mu_{ud}^{(2)} = \mu_{ud}^{(1)} \quad . \tag{8.26}$$

The *HS*+ (equations 8.23 and 8.24) and *HS*- (equations 8.25 and 8.26) approximations are approximate bounds which predict the largest and smallest change in rock stiffness upon dissolution, respectively. After calculating change in rock moduli upon change in rock microstructure, pore-fluid can also be replaced using Gassmann's equations 8.1 and 8.2.

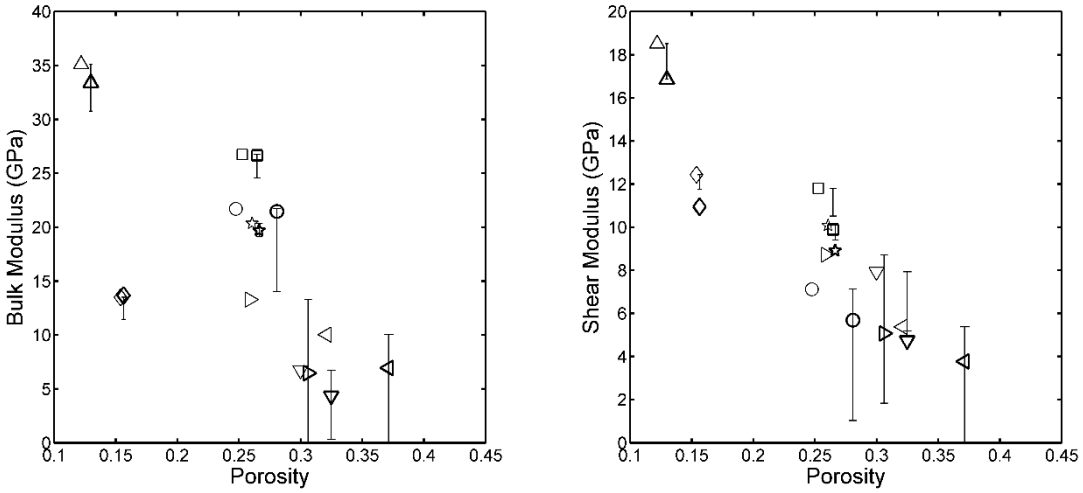

(a) (b)

Figure 8.7: Predictions of change in elastic moduli upon dissolution for dry carbonate samples from Vialle and Vanorio (2011). Open and filled symbols show measurements before and after dissolutions, respectively. Different symbols show different samples.

Figures 8.7a and 8.7b show laboratory measured change in dry rock elastic stiffness of carbonate core samples induced due to dissolution upon injection of carbonated water, reported by Vialle and Vanorio (2011). Since change in volume fraction or porosity was also reported, all inputs needed for the approximate bounds (in equations 8.23-8.26) are available. We compare the range predicted by these approximate bounds with the post-dissolution stiffness measurements. These predictions are also shown in Figures 8.7a and 8.7b. For all samples, we note that approximate bounds in equations 8.23-8.26 fairly contain the laboratory measured change; even though elastic contrast between dry pores

and quartz is quite large for which our assumption of $\alpha_1^m \approx 1$, $\alpha_2'^m \approx 0$, $\beta_1^m \approx 1$ and $\beta_2'^m \approx 0$ may not be justified. Figures 8.8a and 8.8b show the same results as in Figures 8.7a and 8.7b but for water-saturated samples, also for these samples the effect of change in rock microstructure on stiffness is well contained by the approximate bounds.

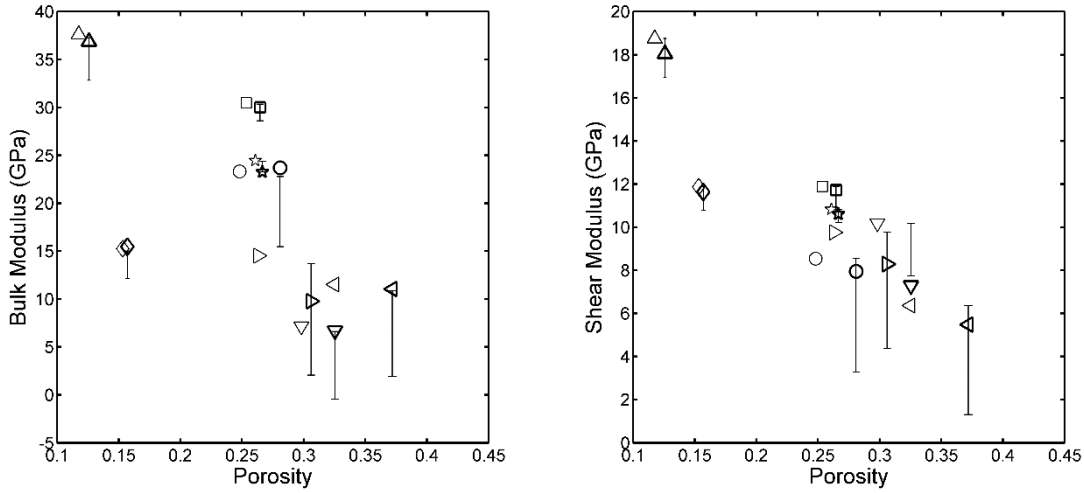

(a) (b)

Figure 8.8: Predictions of change in elastic moduli upon dissolution for water-saturated carbonate samples from Vialle and Vanorio (2011). Open and filled symbols show measurements before and after dissolutions, respectively. Different symbols show different samples.

We note that for most samples, measured change in elastic stiffness is closer to the *HS*- approximation when compared to the *HS*+ approximation. However, to predict the true change more information on the change in pore geometry is needed, in addition to a measure of change in porosity. We also note that the measured stiffness change of these carbonate core samples, give only an average change in stiffness at the core-scale, but the local changes in stiffness in the core plug can be lower or higher, depending on the local pore geometry, the local flow velocities, the reactive surface area and the local chemistry of the circulating fluid.

Also such dissolution experiments are quite poorly constrained since the final pore structure depends on both local pore fluid velocities and chemical kinetics (Guen et al., 2007, Smith et al., 2013 and Vialle et al., 2014). Dissolution can affect all kind of pores

equally or can occur preferentially in the main flow paths; moreover even precipitation can occur in the surrounding "stagnant zones" (Vialle et al., 2013). Therefore, the measured macroscopic change emerges from complex local processes and thus due to heterogeneities between the rock samples, the changes at the pore scale may not be the same from one rock to another. The approximate bounds (in equations 8.23-8.26) only describe a plausible range, and also highlight the uncertainty in estimating the true change in elastic stiffness of a rock upon dissolution.

8.6. Chapter summary

Equations 8.3 and 8.8 are the main results of this chapter; these are the exact fluid/solid substitution relations for substitution of one or more phases in a $N\ (\geq 1)$ phase isotropic multimineralic rocks (but substitution of no more than N - 1 phases). Since these exact equations allow for replacing one or more phases, the rock microstructure does not have to remain invariant upon substitution, as assumed by Brown and Korringa. In addition to the usually known parameters, like volume fractions, properties of rock constituents, etc., these equations depend on parameters which are usually not known unless detailed information on rock microstructure is available; however these parameters have a clear physical interpretation and are directly linked to the ratios of volume averaged stresses/strains induced in rock constituents. Due to a number of required parameters, modeling the change in rock stiffness upon substitution or mineral dissolution is inherently non-unique unless detailed information on pore geometry is available. Therefore, the required parameters must be approximated on the case by case basis.

In equations 8.14 and 8.16, we discuss approximate bounds for substitution of one or more phases simultaneously; these predictions are in good agreement with the examples discussed in this chapter. Similarly, approximate bounds are also developed for predicting change in rock stiffness upon dissolution in equations 8.23-8.26. These predictions fairly contain laboratory measured change in rock stiffness. The range predicted by these

approximate bounds highlights the uncertainty associated with not knowing the details of the rock microstructure.

8.7. Acknowledgements

We are grateful to Stéphanie Vialle for her comments and suggestions. This work was supported by the Stanford Rock Physics and Borehole Geophysics (SRB) Project, and U.S. Department of Energy award DE-FE0001159.

8.8. Appendix A: Derivation of the main results

8.8.1. Bulk Modulus

Let the *outer surface* of an isotropic composite sample with N elastic phases be subjected to compressive surface tractions as

$$T_i = -Pn_i \quad (i = 1, 2, 3) \ , \tag{A-1}$$

where T_i are traction components, n_i are the components of an outward-pointing normal vector to the outer surface, and P is constant. Let the spatially variable stress induced in any phase q ($q = 1$ to N; of volume fraction ϕ_q) be given by σ_{ij}^q, which can be decomposed into isotropic and deviatoric parts as

$$\sigma_{ij}^q = -P^q \delta_{ij} + \tau_{ij}^q \ , \tag{A-2}$$

where P^q is the pressure (negative of mean stress, $-\sigma_{kk}^q / 3$), and τ_{ij}^q are deviatoric stresses. Here we use standard summation convention over repeated indices. Now using Betti-Rayleigh reciprocity theorem (Saxena and Mavko, 2014), we can write the change in elastic energy (ΔE_{12}) upon substitution of N - 1 phases as

$$\Delta E_{12} = \left(\frac{1}{K_{ud}^{(1)}} - \frac{1}{K_{ud}^{(2)}} \right) \langle P \rangle^2 = \sum_{\substack{q=1 \\ q \neq B}}^{N} \phi_q \left(\left(\frac{1}{K^{q1}} - \frac{1}{K^{q2}} \right) \overline{P^{q1} P^{q2}} + \frac{1}{2} \left(\frac{1}{\mu^{q1}} - \frac{1}{\mu^{q2}} \right) \overline{\tau_{ij}^{q1} \tau_{ij}^{q2}} \right) \quad \text{,(A-3)}$$

Now if in equation A-3 we choose $K^{q2} = K^B$ and $\mu^{q2} = \mu^B$, then the composite upon substitution becomes homogeneous, i.e., $K_{ud}^{(2)} = K^B$ and

$$\left(\frac{1}{K_{ud}^{(1)}} - \frac{1}{K^B} \right) \langle P \rangle^2 = \sum_{\substack{q=1 \\ q \neq B}}^{N} \phi_q \left(\left(\frac{1}{K^{q1}} - \frac{1}{K^B} \right) \overline{P^{q1} P^B} + \frac{1}{2} \left(\frac{1}{\mu^{q1}} - \frac{1}{\mu^B} \right) \overline{\tau_{ij}^{q1} \tau_{ij}^B} \right) \quad , \tag{A-4}$$

this also guarantees $P^B = P$ and $\tau_{ij}^B = 0$ everywhere in the composite. Hence, equation A-4 further reduces to

$$\left(\frac{1}{K_{ud}^{(1)}} - \frac{1}{K^B} \right) P = \sum_{\substack{q=1 \\ q \neq B}}^{N} \phi_q \left(\frac{1}{K^{q1}} - \frac{1}{K^B} \right) \overline{P^{q1}} \quad . \tag{A-5}$$

Similarly, if we choose $K^{q1} = K^B$ and $\mu^{q1} = \mu^B$ we get

$$\left(\frac{1}{K_{ud}^{(2)}} - \frac{1}{K^B} \right) P = \sum_{\substack{q=1 \\ q \neq B}}^{N} \phi_q \left(\frac{1}{K^{q2}} - \frac{1}{K^B} \right) \overline{P^{q2}} \quad . \tag{A-6}$$

Next, rearranging terms from equation A-3 we get

$$\langle P \rangle^2 = \sum_{\substack{q=1 \\ q \neq B}}^{N} \phi_q \left(\frac{\left(\frac{1}{K^{q1}} - \frac{1}{K^{q2}} \right)}{\left(\frac{1}{K_{ud}^{(1)}} - \frac{1}{K_{ud}^{(2)}} \right)} \overline{P^{q1} P^{q2}} + \frac{1}{2} \frac{\left(\frac{1}{\mu^{q1}} - \frac{1}{\mu^{q2}} \right)}{\left(\frac{1}{K_{ud}^{(1)}} - \frac{1}{K_{ud}^{(2)}} \right)} \overline{\tau_{ij}^{q1} \tau_{ij}^{q2}} \right) \quad . \tag{A-7}$$

Multiplying equations A-5 and A-6 we get

$$(P)^2 = \left(\sum_{\substack{q=1 \\ q \neq B}}^{N} \phi_q \frac{\left(\frac{1}{K^{q1}} - \frac{1}{K^B}\right)}{\left(\frac{1}{K_{ud}^{(1)}} - \frac{1}{K^B}\right)} \overline{P^{q1}} \right) \left(\sum_{\substack{q=1 \\ q \neq B}}^{N} \phi_q \frac{\left(\frac{1}{K^{q2}} - \frac{1}{K^B}\right)}{\left(\frac{1}{K_{ud}^{(2)}} - \frac{1}{K^B}\right)} \overline{P^{q2}} \right) \quad . \tag{A-8}$$

From equations A-7 and A-8, we obtain bulk modulus substitution equation 8.3.

8.8.2. **Shear Modulus**

Similar to the effective bulk modulus derivation we consider the following surface shear tractions (referred in this chapter as shear field) at the outer surface

$$\begin{pmatrix} T_1 \\ T_2 \\ T_3 \end{pmatrix} = \begin{pmatrix} 0 & \tau & 0 \\ \tau & 0 & 0 \\ 0 & 0 & 0 \end{pmatrix} \begin{pmatrix} n_1 \\ n_2 \\ n_3 \end{pmatrix} \quad . \tag{A-9}$$

For this case, using reciprocity, we can write the change in elastic energy (ΔE_{12}) upon substitution of N - 1 phases (except for phase B) as

$$\left(\frac{1}{\mu_{ud}^{(1)}} - \frac{1}{\mu_{ud}^{(2)}}\right)(\tau)^2 = \sum_{\substack{q=1 \\ q \neq B}}^{N} \phi_q \left(\left(\frac{1}{K^{q1}} - \frac{1}{K^{q2}}\right) \overline{P^{q1} P^{q2}} + \frac{1}{2} \left(\frac{1}{\mu^{q1}} - \frac{1}{\mu^{q2}}\right) \overline{\tau_{ij}^{q1} \tau_{ij}^{q2}} \right) \quad , \tag{A-10}$$

Now if in equation A-10 we choose $K^{q2} = K^B$ and $\mu^{q2} = \mu^B$, then the composite upon substitution becomes homogeneous, i.e., $\mu_{ud}^{(2)} = \mu^B$ and

$$\left(\frac{1}{\mu_{ud}^{(1)}} - \frac{1}{\mu^B}\right)(\tau)^2 = \sum_{\substack{q=1 \\ q \neq B}}^{N} \phi_q \left(\left(\frac{1}{K^{q1}} - \frac{1}{K^B}\right) \overline{P^{q1} P^B} + \frac{1}{2} \left(\frac{1}{\mu^{q1}} - \frac{1}{\mu^B}\right) \overline{\tau_{ij}^{q1} \tau_{ij}^B} \right) \quad . \tag{A-11}$$

Also if all phases are filled with solid B, then $P^B = 0$, $\tau_{11}^B = \tau_{22}^B = \tau_{33}^B = \tau_{23}^B = \tau_{13}^B = 0$ and $\tau_{12}^B = \tau_{21}^B = \tau$ everywhere, this results in

$$\left(\frac{1}{\mu_{ud}^{(1)}}-\frac{1}{\mu^{B}}\right)\tau=\sum_{\substack{q=1\\q\neq B}}^{N}\phi_q\left(\frac{1}{\mu^{q1}}-\frac{1}{\mu^{B}}\right)\overline{\tau_{12}^{q1}} \quad . \tag{A-12}$$

Similarly, if we choose $K^{q1}=K^{B}$ and $\mu^{q1}=\mu^{B}$, then we get

$$\left(\frac{1}{\mu_{ud}^{(2)}}-\frac{1}{\mu^{B}}\right)\tau=\sum_{\substack{q=1\\q\neq B}}^{N}\phi_q\left(\frac{1}{\mu^{q2}}-\frac{1}{\mu^{B}}\right)\overline{\tau_{12}^{q2}} \quad . \tag{A-13}$$

From equations A-10, A-12 and A-13 we get the shear modulus substitution equation 8.6.

8.9. Appendix B: Hashin-Shtrikman bounds

The expressions for HS bounds on elastic bulk and shear moduli of an isotropic two-phase composite are given by

$$K^{HS+/-}=K^{(1)}+\frac{f_2}{\left(K^{(2)}-K^{(1)}\right)^{-1}+f_1\left(K^{(1)}+\frac{4}{3}\mu^{(1)}\right)^{-1}} \quad , \tag{B-1}$$

$$\mu^{HS+/-}=\mu^{(1)}+\frac{f_2}{\left(\mu^{(2)}-\mu^{(1)}\right)^{-1}+f_1\left(\mu^{(1)}+\frac{\mu^{(1)}}{6}\frac{9K^{(1)}+8\mu^{(1)}}{K^{(1)}+2\mu^{(1)}}\right)^{-1}} \quad , \tag{B-2}$$

where the superscripts (1) and (2) refer to the properties of the two phases. Equations B-1 and B-2 yield the upper bound when $K^{(1)}$ and $\mu^{(1)}$ are the *maximum* bulk and shear moduli of the individual phases, and the lower bounds when $K^{(1)}$ and $\mu^{(1)}$ are the *minimum* bulk and shear moduli of the phases. Superscripts *HS+* and *HS-* designate upper and lower HS bounds, respectively.

8.10. References

Andrä, H., N. Combaret, J. Dvorkin, E. Glatt, J. Han, M. Kabel, Y. Keehm, F. Krzkilla, M. Lee, C. Madonna, M. Marsh, T. Mukerji, E. H. Saenger, R. Sain, N. Saxena, S. Ricker, A. Wiegmann and X. Zhan, 2013, Digital rock physics benchmarks - Part I: Imaging and segmentation: Computers & Geosciences, **50**, 25-32.

Avseth, P., T. Mukerji, and G. Mavko, 2005, Quantitative seismic interpretation: Applying rock physics tools to reduce interpretation risk: Cambridge University Press.

Avseth, P., T. Mukerji, G. Mavko, and J. Dvorkin, 2010, Rock physics diagnostics of depositional texture, diagenetic alterations and reservoir heterogeneity in high porosity siliciclastic sediments and rocks — A review of selected models and suggested workflows: Geophysics, **75**, 5, 75A31–75A47.

Bianco, E., S. Kaplan, and D. Schmitt, 2008, Seismic rock physics of steam injection in bituminous oil reservoirs: The Leading Edge, **27**(9), 1132-1137.

Brown, R., and J. Korringa, 1975, On the dependence of the elastic properties of a porous rock on the compressibility of the pore fluid: Geophysics, **40**, 608–616.

Bemer, E., J. Dautriat, M. Fleury and M. Adelinet, 2013, Experimental characterization of chemical alteration effects on carbonate rock dynamic poroelastic properties: Poromechanics V, 1644-1653.

Berryman, J. G., 1980, Long-wavelength propagation in composite elastic media: Journal of the Acoustical Society of America, **68**, 1809–1831.

Berryman, J. G. , 1999, Origin of Gassmann's equations: Geophysics, **64**, 1627–1629.

Chopra, S., L. Lines, D. Schmitt, and M. Batzle, 2010, 1. Heavy-Oil Reservoirs: Their Characterization and Production: Heavy Oils, 1-69.

Ciz, R., and S. A. Shapiro, 2007, Generalization of Gassmann equations for porous media saturated with a solid material: Geophysics, **72**, A75–A79.

Cleary, M. P., I. W. Chen and S. M. Lee, 1980, Self-consistent techniques for heterogeneous media: ASCE Journal of Engineering Mechanics, **106**, 861-887.

Duputel, Z., V. Ferrazzini, F. Brenguier, N. Shapiro, M. Campillo, and A. Nercessian, Real time monitoring of relative velocity changes using ambient seismic noise at the Piton de la Fournaise volcano (La Reunion) from January 2006 to June 2007, Journal of Volcanology and Geothermal Research, **184**, 164-173.

Dvorkin, J., and A. Nur, 1996, Elasticity of high-porosity sandstones: Theory for two North Sea data sets: Geophysics, **61**, 1363–1370.

Gassmann, F., 1951, Über die Elastizität poröser Medien: Vierteljahrschrift der Naturforschenden Gessellschaft in Zürich, **96**, 1-23.

Hashin, Z., 1962, The elastic moduli of heterogeneous materials, Journal of Applied Mechanics, 29, 143-150.

Hashin, Z., and S. Shtrikman, 1963, A variational approach to the elastic behavior of multiphase materials: Journal of the Mechanics and Physics of Solids, **11**, 127–140.

Hoefiner, M. L., and H. S. Fogler, 1988, Pore evolution and channel formation during flow and reaction in porous media: AIChE Journal, **34**, 1, 45–54.

Jacoby, M., J. Dvorkin, and X. Liu, 1996, Elasticity of partially saturated frozen sand, Geophysics, **61**(1), 288-293.

King, M. S., 1977, Acoustic velocities and electrical properties of frozen sandstones and shales: Canadian Journal of Earth Sciences, **14**, 1004–1013.

King, M. S. , R. W. Zimmerman, and R. F. Corwin, 1988, Seismic and electrical properties of unconsolidated permafrost: Geophysical Prospecting, **36**, 349–364.

Kurfurst, P. J., 1976, Ultrasonic wave measurements on frozen soils at permafrost temperatures: Canadian Journal of Earth Sciences, **13**, 1571–1576.

Kuster, G. T., and M. N. Toksöz, 1974, Velocity and attenuation of seismic waves in two phase media: Part I. theoretical formulations: Geophysics, **39**, 587-606.

Le Guen, Y., F. Renard, R. Hellmann, E. Brosse, M. Collombet, D. Tisserand, and J.P. Gratier, 2007, Enhanced deformation of limestone and sandstone in the presence of high PCO2 fluids: Journal of Geophysical Research, 112, B05421.

Lumley, D., 2010, 4D seismic monitoring of CO2 sequestration: The Leading Edge, **29**, 150–155.

O'Connell, R. J., B. Budiansky, 1974, Seismic velocities in dry and saturated cracked solids: Journal of Geophysical Research, **79**, 5412-5426.

Saxena, N., and G. Mavko, 2014, Exact equations for fluid and solid substitution: Geophysics, **79**(3), L21-L32.

Schmitt, D., 1999, Seismic attributes for monitoring of a shallow heated heavy oil reservoir: A case study, Geophysics, **64**(2), 368-377.

Smith, M., Y. Sholokhova, Y. Hao, S. Carroll, 2013, CO_2-induced dissolution of low permeability carbonates. Part I: Characterization and Experiments: Advances in Water Resources, **62**, 370–87.

Sondergeld, C. and C. Rai, 2007, Velocity and resistivity changes during freeze-thaw cycles in Berea sandstone: Geophysics, 72(2), E99-E105.

Timur, A., 1968, Velocity of compressional waves in porous media at permafrost temperatures: Geophysics, **33**, 584-595.

Vanorio, T., A. Nur, Y. Elbert, 2011, Rock physics analysis and time-lapse rock imaging of geochemical effects due to the injection of CO_2 into reservoir rocks: Geophysics, **76** (5), O23-O33.

Vialle, S., and T. Vanorio, 2011, Laboratory measurements of elastic properties of carbonate rocks during injection of reactive CO2-saturated water: Geophysical Research Letters, **38**, L01302.

Vialle S., J. Dvorkin, and G. Mavko, 2013, Implications of pore microgeometry heterogeneity for the movement and chemical reactivity of CO2 in carbonates: Geophysics, 78(5), L69-L86.

Vialle, S., S. , Contraires, B. , Zinzsner, J. B. Clavaud, K. Mahiouz, P. Zuddas and M. Zamora, 2014, Percolation of CO2-rich fluids in a limestone sample: evolution of hydraulic, electrical, chemical and structural properties: Journal of Geophysical Research, Solid Earth, In print.

Wu, T. T., 1966, The effect of inclusion shape on the elastic moduli of a two-phase material: International Journal of Solids and Structures, **2**, 1-8.

Zimmerman, R. W. , and M. S. King, 1986, The effect of the extent of freezing on seismic velocities in unconsolidated permafrost: Geophysics, **51**, 1285-1290.

Chapter 9

Modeling infinitesimal strain creep in organic-rich shale

9.1. Abstract

We present an approach to model effective elastic properties and infinitesimal strain creep functions (or stress relaxation functions) in organic-rich shales. Creeping kerogen is mixed with anisotropic elastic mineral using the anisotropic effective field theory. Elastic properties of isotropic kerogen and elastic mineral are based on laboratory measurements. Two choices exist while mixing kerogen and elastic mineral: aligned inclusions of kerogen in elastic mineral or aligned inclusions of elastic mineral in kerogen. The creep and relaxation functions are calculated using the correspondence principle and the effective field solution. Although mixing inclusions of elastic mineral in kerogen background seem to better match the laboratory measured elastic moduli, there is uncertainty with regards to

which mixing choice describes the laboratory measurements better. However, the calculated corresponding creep and relaxation functions using the two mixing choices are well separated and thus can aid in deciding the mixing scheme. For Haynsville, Bakken, and Barnett shales the model predictions corresponding to kerogen background fit both static and dynamic measurements relatively better when compared to mineral background.

9.2. Introduction

Organic-rich shales represent a vast energy reserve. Organic rich shales are commonly categorized as unconventional reservoirs and display complexity in composition, flow characteristics, distribution of organic matter and pore size, etc. Shales are often found to be strongly anisotropic, due to clay mineral alignment, bedding-parallel distribution of organic matter and possible cracks (Vernik and Nur, 1992; Vernik and Landis, 1996; Sondergeld et al., 2000). Understanding the dependence of mechanical properties of shale on composition is important for various applications such as detection of organic rich shale from seismic, hydraulic fracturing to boost production, designing safe and cost effective drilling approach, etc.

Both dynamic (Vernik and Landis, 1996; Vernik and Liu, 1997) and static properties (Sone, 2012) for various shale rocks have been measured. To model dynamic properties of shales, various approaches have been proposed (Vernik and Nur, 1992; Vernik and Kachanov, 2010); these models are driven by experimental observations and thus have been fairly successful in describing laboratory or well log data (Vernik and Milovac, 2011; Khadeeva and Vernik, 2013). Various other attempts (Bandyopadhyay, 2009; Ruiz and Azizov, 2011) have been made to model the dynamic properties of these complicated rocks using effective medium theories such as the self-consistent (O'Connell and Budiansky, 1974; Berryman, 1980) and differential medium schemes (Cleary et al., 1980; Mukerji et al., 1995). Sayers (2013) used the effective field method of Sevostianov et al. (2005) to model organic-rich shales; this method solves for effective elastic stiffness by placing a representative inclusion in an effective stress field. Sayers (2013) showed that dynamic

measurements of Vernik and Liu (1997) are consistent with mixing elastic mineral inclusions in a kerogen background.

In this chapter, we solve for both effective elastic and creep properties of organic-rich shale rocks, using the effective field theory of Sevostianov et al. (2005). Kerogen is modeled as a power-law viscoelastic material embedded in vertical transversely isotropic elastic mineral. Both dynamic and static properties are calculated for the same microstructure composed using two mixing schemes: inclusions of kerogen in elastic mineral background and inclusions of elastic mineral in a kerogen background. We find that the two schemes show higher separation in static domain when compared to their separation in the dynamic domain. Mixing scheme with kerogen as the background material fits both laboratory measured dynamic and statics measurements relatively better.

9.3. Constitutive relations for VTI media

Transversely isotropic (TI) material with rotational vertical symmetry axis (x_3) are also commonly refereed as vertical transverse isotropic or simply VTI. The elastic stiffness (C) of a VTI material has five independent elastic stiffness coefficients which can be expressed in Voigt matrix notation as

$$\begin{bmatrix} \sigma_{11} \\ \sigma_{22} \\ \sigma_{33} \\ \sigma_{23} \\ \sigma_{13} \\ \sigma_{12} \end{bmatrix} = \begin{bmatrix} C_{11} & C_{12} & C_{13} & 0 & 0 & 0 \\ C_{12} & C_{11} & C_{13} & 0 & 0 & 0 \\ C_{13} & C_{13} & C_{33} & 0 & 0 & 0 \\ 0 & 0 & 0 & C_{44} & 0 & 0 \\ 0 & 0 & 0 & 0 & C_{44} & 0 \\ 0 & 0 & 0 & 0 & 0 & C_{66} \end{bmatrix} \begin{bmatrix} \varepsilon_{11} \\ \varepsilon_{22} \\ \varepsilon_{33} \\ 2\varepsilon_{23} \\ 2\varepsilon_{13} \\ 2\varepsilon_{12} \end{bmatrix} . \tag{9.1}$$

Equation 9.1 is the constitutive relation for a linear elastic VTI material, where σ and ε denote stresses and strains, respectively. For convenience, we now adopt the following notation for stresses and strains:

$$\begin{bmatrix}\sigma_{11}\\ \sigma_{22}\\ \sigma_{33}\\ \sigma_{23}\\ \sigma_{13}\\ \sigma_{12}\end{bmatrix}=\begin{bmatrix}\sigma_{1}\\ \sigma_{2}\\ \sigma_{3}\\ \sigma_{4}\\ \sigma_{5}\\ \sigma_{6}\end{bmatrix} \text{ and } \begin{bmatrix}\varepsilon_{11}\\ \varepsilon_{22}\\ \varepsilon_{33}\\ 2\varepsilon_{23}\\ 2\varepsilon_{13}\\ 2\varepsilon_{12}\end{bmatrix}=\begin{bmatrix}\varepsilon_{1}\\ \varepsilon_{2}\\ \varepsilon_{3}\\ \varepsilon_{4}\\ \varepsilon_{5}\\ \varepsilon_{6}\end{bmatrix}. \tag{9.2}$$

For weakly anisotropic VTI materials, stiffness can also be described in terms of Thomsen's anisotropic parameters ε, γ and δ (Thomsen, 1986), along with stiffness components C_{33} (vertical P-wave modulus) and C_{44} (vertical S-wave modulus). Thomsen's parameters are given by

$$\varepsilon=\frac{C_{11}-C_{33}}{2C_{33}}\ , \tag{9.3}$$

$$\gamma=\frac{C_{66}-C_{44}}{2C_{44}}\ , \tag{9.4}$$

and

$$\delta=\frac{\left(C_{13}+C_{44}\right)^{2}-\left(C_{33}-C_{44}\right)^{2}}{2C_{33}\left(C_{33}-C_{44}\right)}\ . \tag{9.5}$$

Similarly the elastic compliance (S^{eff}) in Voigt matrix notation can be written as

$$\begin{bmatrix}\varepsilon_{1}\\ \varepsilon_{2}\\ \varepsilon_{3}\\ \varepsilon_{4}\\ \varepsilon_{5}\\ \varepsilon_{6}\end{bmatrix}=\begin{bmatrix}S_{11} & S_{12} & S_{13} & 0 & 0 & 0\\ S_{12} & S_{11} & S_{13} & 0 & 0 & 0\\ S_{13} & S_{13} & S_{33} & 0 & 0 & 0\\ 0 & 0 & 0 & S_{44} & 0 & 0\\ 0 & 0 & 0 & 0 & S_{44} & 0\\ 0 & 0 & 0 & 0 & 0 & S_{66}\end{bmatrix}\begin{bmatrix}\sigma_{1}\\ \sigma_{2}\\ \sigma_{3}\\ \sigma_{4}\\ \sigma_{5}\\ \sigma_{6}\end{bmatrix}. \tag{9.6}$$

Compliance coefficients in equation 9.6 are related to the stiffness coefficients in equation 9.1 as

$$S_{11} = \frac{C_{33}}{2C_{33}\left(C_{11}+C_{12}\right)-4C_{13}C_{13}} + \frac{1}{2\left(C_{11}-C_{12}\right)} \quad , \tag{9.7}$$

$$S_{12} = \frac{C_{33}}{2C_{33}\left(C_{11}+C_{12}\right)-4C_{13}C_{13}} - \frac{1}{2\left(C_{11}-C_{12}\right)} \quad ,$$

$$S_{13} = -\frac{C_{13}}{C_{33}\left(C_{11}+C_{12}\right)-2C_{13}C_{13}} \quad ,$$

$$S_{33} = \frac{C_{11}+C_{12}}{C_{33}\left(C_{11}+C_{12}\right)-2C_{13}C_{13}} \quad \text{and} \quad S_{44} = \frac{1}{C_{44}} \quad .$$

Alternatively, constitutive relations in equations 9.1 and 9.6 can also be written as

$$\sigma_k = \sum_{i=1}^{6} C_{ik}\,\varepsilon_i \quad , \tag{9.8}$$

and

$$\varepsilon_k = \sum_{i=1}^{6} S_{ik}\,\sigma_i \quad . \tag{9.9}$$

Similarly, for a linear viscoelastic material the constitutive relations can be written using the convolution operator as

$$\sigma_k(t) = \sum_{i=1}^{6} \int_0^t G_{ik}(t-\tau)\frac{d}{d\tau}\varepsilon_i(\tau)\,d\tau \quad , \tag{9.10}$$

and

$$\varepsilon_k(t) = \sum_{i=1}^{6} \int_0^t J_{ik}(t-\tau)\frac{d}{d\tau}\sigma_i(\tau)\,d\tau \quad . \tag{9.11}$$

In equations 9.10 and 9.11, $G_{ij}(t)$ and $J_{ij}(t)$ are the so-called relaxation and creep functions, respectively. Taking Laplace transform of equations 9.10 and 9.11, with transform variable *s* results in

$$\boldsymbol{\sigma}_k(s) = \sum_{i=1}^{6} s\,\boldsymbol{G}_{ik}(s)\boldsymbol{\varepsilon}_i(s) \quad , \tag{9.12}$$

and

$$\boldsymbol{\varepsilon}_k(s) = \sum_{i=1}^{6} s\,\boldsymbol{J}_{ik}(s)\boldsymbol{\sigma}_i(s) \quad . \tag{9.13}$$

The constitutive linear viscoelasticity relations in equation 9.12 and 9.13 in the Laplace domain resemble the time-independent linear elastic constitutive relations in equations 9.8 and 9.9. These relations show that if the solution to the linear elastic constitutive relation is known then the solution to the corresponding viscoelastic constitutive relation in Laplace domain can be obtained by replacing all elastic stiffness (or compliance) coefficients with transform argument (*s*) times the Laplace transform of the time dependent relaxation (creep) coefficients. The time domain solution is obtained by transforming back to the time domain (Lakes, 2009). This property is also known as the correspondence principle.

9.4. Effective field method for estimation of effective stiffness

To estimate the effective elastic coefficients C_{ij} and S_{ij} for a two phase VTI composite we now use the effective field theory of Sevostianov et al. (2005). This method predicts elastic coefficients by utilizing the one-particle solution for a VTI inclusion in a VTI background. The interaction between inclusions is accounted for by placing a representative inclusion into an average stress/strain field. This approach is distinct from the effective medium theories such as those proposed by O'Connell and Budiansky (1974), Mura (1982), Jakobsen et al. (2000), Nishizawa (2001). Recently, Sayers (2013) discussed applications of the effective field method of Sevostianov et al. (2005) and investigated the effects of kerogen on dynamic and geomechanical properties of organic-rich shales. Sayers

(2013) also provide detailed expressions for calculating the effective elastic coefficients C_{ij} using the effective field method for the special case of symmetry axis x_3 coinciding with the material axis of symmetry for both background and inclusion materials, which themselves can be VTI. The predicted effective elastic coefficients C_{ij}^{eff} can be expressed as a function of the elastic coefficients C_{ij}^{B} of the background (or matrix) material and the elastic coefficients C_{ij}^{I} of the inclusion material, given by

$$C_{ij}^{eff}\left(C_{ij}^{B},C_{ij}^{I},\alpha\right)=C_{ij}^{B}+p\left[\frac{1}{C_{ij}^{B}-C_{ij}^{I}}+(1-p)P_{ij}\right]^{-1}, \tag{9.14}$$

where p and α are the volume fraction and aspect ratio of inclusions, respectively. Coefficient P_{ij} further depends on material properties and inclusion aspect ratio; detailed expressions can be found in Sayers (2013), thus not repeated here. In this study, we model inclusions as horizontally aligned oblate spheroids with aspect ratio α given by

$$\alpha=a_3/a_1 \quad , \tag{9.15}$$

where a_i is length of an spheroidal inclusion along the i^{th} axis.

9.5. Modeling dynamic properties

Following Vernik and Landis (1996) and Sayers (2013), elastic mineral is approximated as a VTI material, whereas kerogen is assumed to be isotropic. Extrapolating experimental results of Vernik and Landis (1996) for organic-rich black shale samples (with moderate clay content) to 100 % elastic mineral and 100 % kerogen, the authors obtain the following stiffness coefficients for kerogen: $C_{11}^{kg}=C_{22}^{kg}=C_{33}^{kg}=9.8$ GPa, $C_{44}^{kg}=C_{55}^{kg}=C_{66}^{kg}=3.2$ GPa; and the following stiffness coefficients for elastic mineral $C_{11}^{sh}=C_{22}^{sh}=85.6$ GPa, $C_{33}^{sh}=65.5$ GPa, $C_{44}^{sh}=24.6$ GPa, $C_{66}^{sh}=29.7$ GPa.

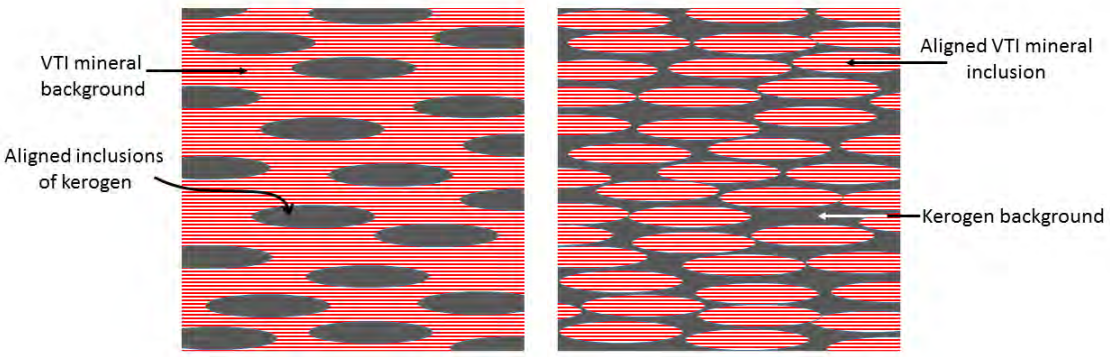

Figure 9.1: Mixing schemes. Left: scheme 1, isotropic kerogen inclusions in elastic mineral background. Right: scheme 2, mineral inclusions in a kerogen background.

Note that since Vernik and Landis did not directly measure C_{13} we approximate $C_{13}^{sh} =$ 21.1 GPa assuming $\delta = 0.5\,\varepsilon$ (Sayers, 2013). Next, we calculate effective stiffness for a mixture of elastic mineral and kerogen using the effective field method of Sevostianov et al. (2005) for two mixing schemes: scheme 1 with kerogen inclusions in an elastic mineral background, and scheme 2 with elastic mineral inclusions in a kerogen background.

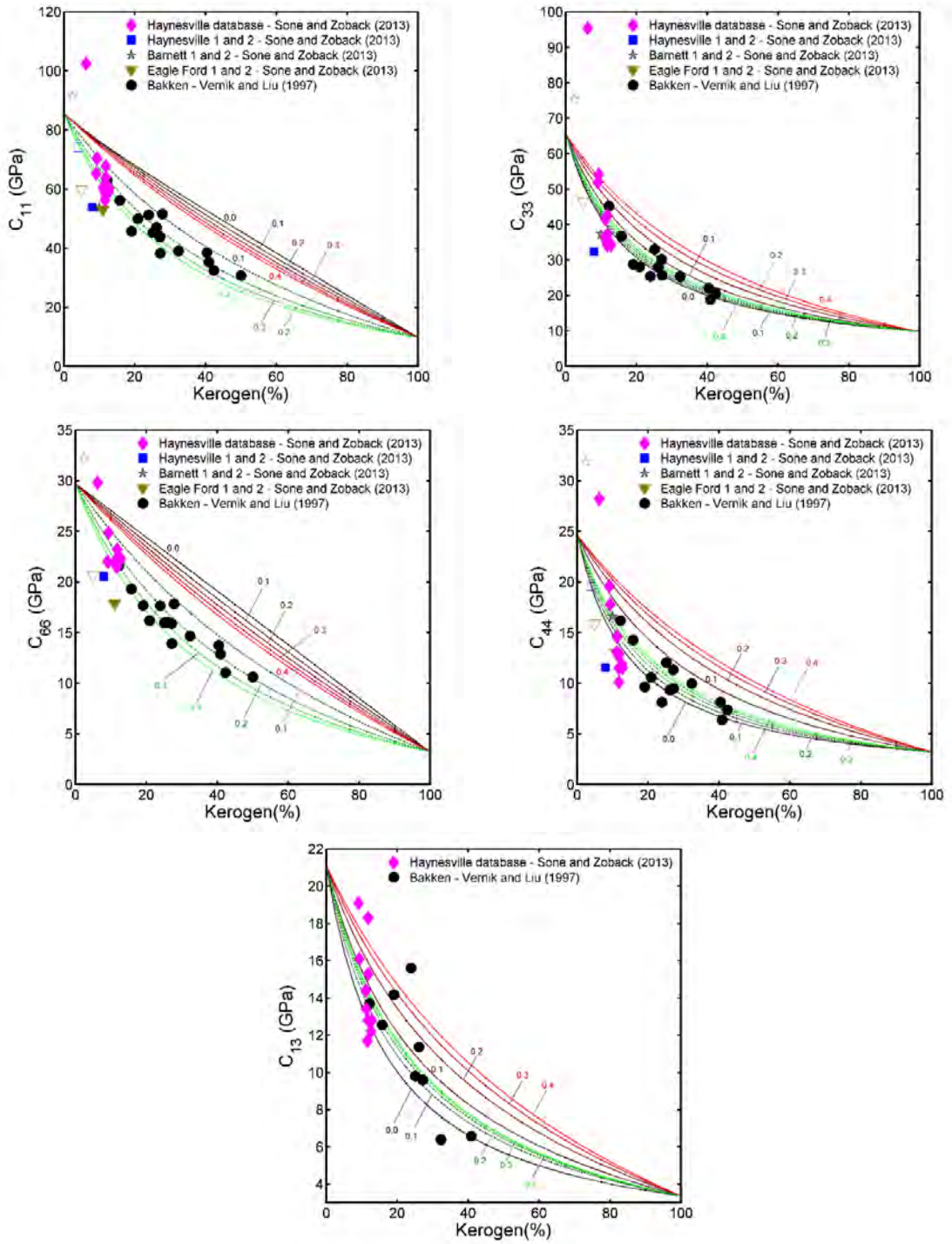

Figure 9.2: Effective stiffness coefficients for a range of kerogen volume fraction. The dashed green curves correspond to inclusions of elastic mineral in kerogen background; aspect ratios are also shown on the plots. The full red curves correspond to inclusions of kerogen in mineral background.

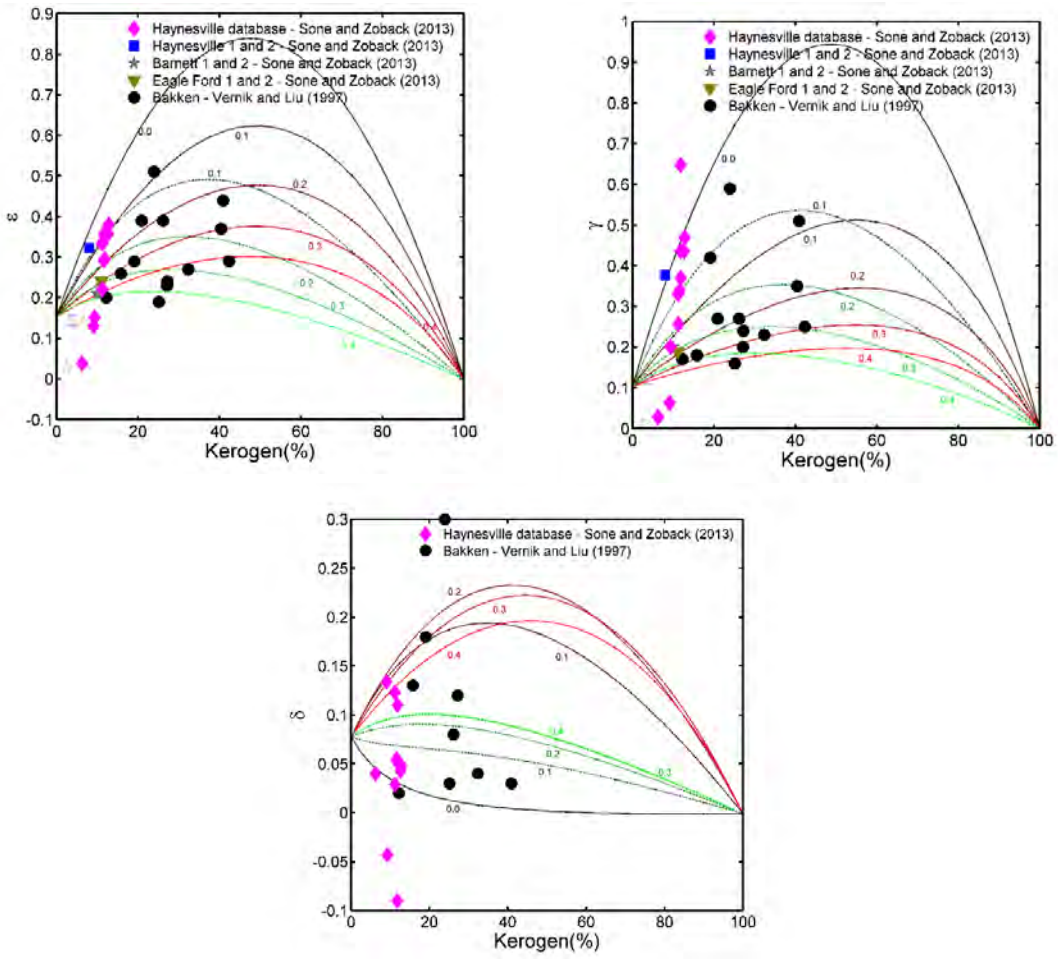

Figure 9.3: Thomsen's parameters for a range of kerogen volume fraction. The dashed green curves correspond to inclusions of elastic mineral in kerogen background; aspect ratios are also shown on the plots. The full red curves correspond to inclusions of kerogen in mineral background.

Figure 9.2 shows the predicted effective stiffness coefficients C_{ij}^{eff} as a function of kerogen volume fraction. Model predictions for kerogen inclusions in an elastic mineral background (scheme 1, Figure 9.1a) are shown with full red lines for aspect ratios varying between 0 (laminated) to 0.4, color darkness also indicates increasing aspect ratio value. Figure 9.2 also show the predictions for the case where inclusions of elastic mineral are floating in a background of kerogen (scheme 2, Figure 9.1b), shown in dashed green curves. Various set of laboratory measured data are compared with these model curves: Bakken shale data from Vernik and Liu (1997), Haynesville and Barnett shale data (two for each) from Sone and Zoback (2013) for which samples 1 has higher clay content than

samples 2. Also compared are some additional data reported by Sone (2012) for Haynseville shale. Figure 9.3 shows the plots for Thomsen's parameters ε, γ and δ, respectively. Figure 9.4 shows the calculated values for the effective compliance coefficients S_{ij}^{eff}.

We note the model curves corresponding to elastic mineral inclusions floating in kerogen background, i.e., scheme 2, better fit the laboratory data, which is consistent with the findings of Sayers (2013). This also supports the hypothesis of Vernik and Liu (1997) that laminated clay floats in kerogen background. However, it must be noted that model predictions of stiffness coefficients for schemes 1 and 2 are not separated enough to make the above statement with confidence. Therefore, although scheme 2 does seem to fit better with the dynamic laboratory measurements, there is still uncertainty with regards to which scheme should be used to address the "what if" scenarios. For example, vertical sonic well logs only yield direct measurements of effective stiffness coefficients C_{33} (vertical P-wave modulus) and C_{44} (vertical S-wave modulus) but to perform further geomechanical analysis estimates of C_{13}, C_{11} and C_{66} are typically required, but these predictions can vary substantially depending on the selected scheme.

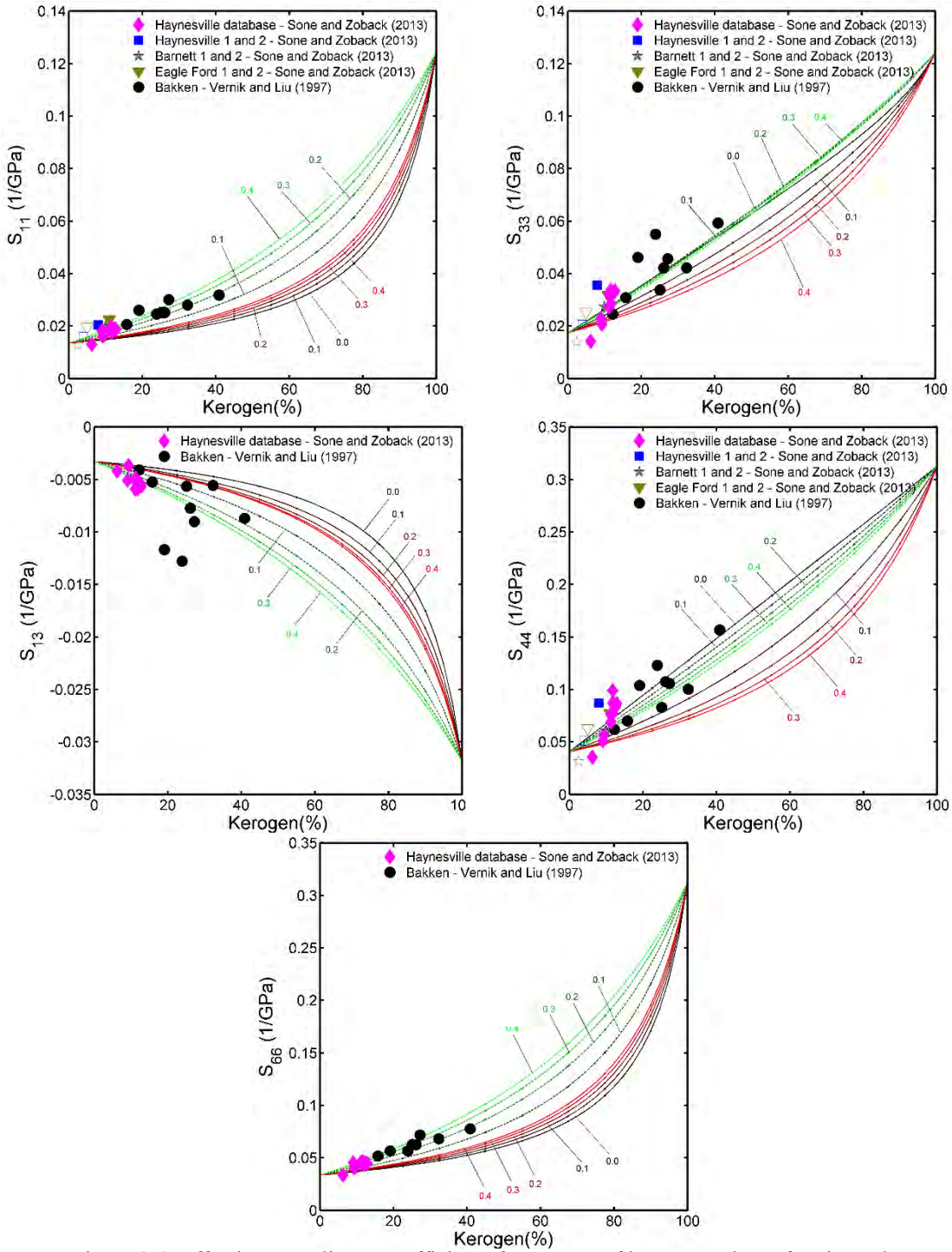

Figure 9.4: Effective compliance coefficients for a range of kerogen volume fraction. The dashed green curves correspond to inclusions of elastic mineral in kerogen background; aspect ratios are also shown on the plots. The full red curves correspond to inclusions of kerogen in mineral background.

9.6. Modeling creep and relaxation functions

We now assume isotropic kerogen to be a power law creeping material obeying the following creep function

$$J_{33}^{kg}(t) = B^{kg} t^{n_{kg}} \quad , \tag{9.16}$$

where B^{kg} is the creep intercept and n_{kg} is the time exponent. Due to assumed isotropy we must have $J_{33}^{kg}(t) = J_{11}^{kg}(t) = J_{11}^{kg}(t)$. Taking Laplace transform of the creep function with respect to transform variable *s*, we obtain

$$\boldsymbol{J}_{33}^{kg}(s) = B^{kg}\Gamma(1+n_{kg})s^{-(n_{kg}+1)} \quad , \tag{9.17}$$

Using the property $\boldsymbol{J}_{33}^{kg}(s) = 1/\left(s^2 \boldsymbol{E}^{kg}(s)\right)$ the corresponding relaxation function in Laplace domain is given by

$$\boldsymbol{E}^{kg}(s) = \frac{1}{B^{kg}\Gamma(1+n_{kg})s^{1-n_{kg}}} \quad . \tag{9.18}$$

Relaxation function $\boldsymbol{E}^{kg}(s)$ has dimensions of Young's modulus. Assuming elastic kerogen bulk modulus K^{kg} we obtain the following relaxation functions in Laplace domain

$$\boldsymbol{G}_{33}^{kg}(s) = \boldsymbol{G}_{22}^{kg}(s) = \boldsymbol{G}_{11}^{kg}(s) = \frac{3K^{kg}\left(3K^{kg} + \boldsymbol{E}^{kg}(s)\right)}{9K - \boldsymbol{E}^{kg}(s)} \quad , \tag{9.18}$$

$$\boldsymbol{G}_{44}^{kg}(s) = \boldsymbol{G}_{55}^{kg}(s) = \boldsymbol{G}_{66}^{kg}(s) = \frac{3K^{kg}\boldsymbol{E}^{kg}(s)}{9K^{kg} - \boldsymbol{E}^{kg}(s)} \quad , \tag{9.19}$$

$$\boldsymbol{G}_{12}^{kg}(s) = \boldsymbol{G}_{21}^{kg}(s) = \boldsymbol{G}_{13}^{kg}(s) = \boldsymbol{G}_{31}^{kg}(s) = \boldsymbol{G}_{23}^{kg}(s) = \boldsymbol{G}_{32}^{kg}(s) = \boldsymbol{G}_{11}^{kg}(s) - 2\boldsymbol{G}_{44}^{kg}(s) \quad . \tag{9.20}$$

Next, using the effective field method (equation 9.14) we calculate the effective relaxation and creep functions in time domain for scheme 1 by solving the following equations

$$G_{ij}^{eff}(t) = L^{-1}\left(C_{ij}^{eff}\left(C_{ij}^{sh}, s\,\boldsymbol{G}_{ij}^{kg}, \alpha\right)/s\right) \ , \tag{9.21}$$

$$J_{ij}^{eff}(t) = L^{-1}\left(\left[C^{eff}\left(C_{ij}^{sh}, s\,\boldsymbol{G}_{ij}^{kg}, \alpha\right)\right]_{ij}^{-1}/s\right) \ , \tag{9.22}$$

where L^{-1} is the inverse Laplace transform operator. In equation 9.22, the term in the square brackets represent inverse of the matrix C^{eff}. Similarly, relaxation and creep functions for scheme 2 can be obtained by solving

$$G_{ij}^{eff}(t) = L^{-1}\left(C_{ij}^{eff}\left(s\,\boldsymbol{G}_{ij}^{kg}, C_{ij}^{sh}, \alpha\right)/s\right) \ , \tag{9.23}$$

$$J_{ij}^{eff}(t) = L^{-1}\left(\left[C^{eff}\left(s\,\boldsymbol{G}_{ij}^{kg}, C_{ij}^{sh}, \alpha\right)\right]_{ij}^{-1}/s\right) \ . \tag{9.24}$$

To solve equations 9.21-9.24 we use the Talbot algorithm (Abate and Whitt, 2006). For simplicity, we assume that all relaxation and creep functions retain power law behavior similar to the input creep function of kerogen but do not necessarily have the same intercept or exponent as of kerogen. Thus the effective relaxation and creep functions can be expressed as

$$G_{ij}^{eff}(t) = A_{ij}\, t^{m_{ij}} \ , \tag{9.25}$$

$$J_{ij}^{eff}(t) = B_{ij}\, t^{n_{ij}} \ . \tag{9.26}$$

At time $t = 1$, we can approximate

$$G_{ij}^{eff}(1) = A_{ij} \approx C_{ij}^{eff} \ , \tag{9.27}$$

$$J_{ij}^{eff}(1) = B_{ij} \approx S_{ij}^{eff} \ , \tag{9.28}$$

where C_{ij}^{eff} and S_{ij}^{eff} are effective stiffness and compliance coefficients calculated for a mix of kerogen and elastic mineral for the choice of mixing scheme (1 or 2), such that Young's modulus and bulk modulus of kerogen is given by $1/B^{kg}$ and K^{kg}, respectively.

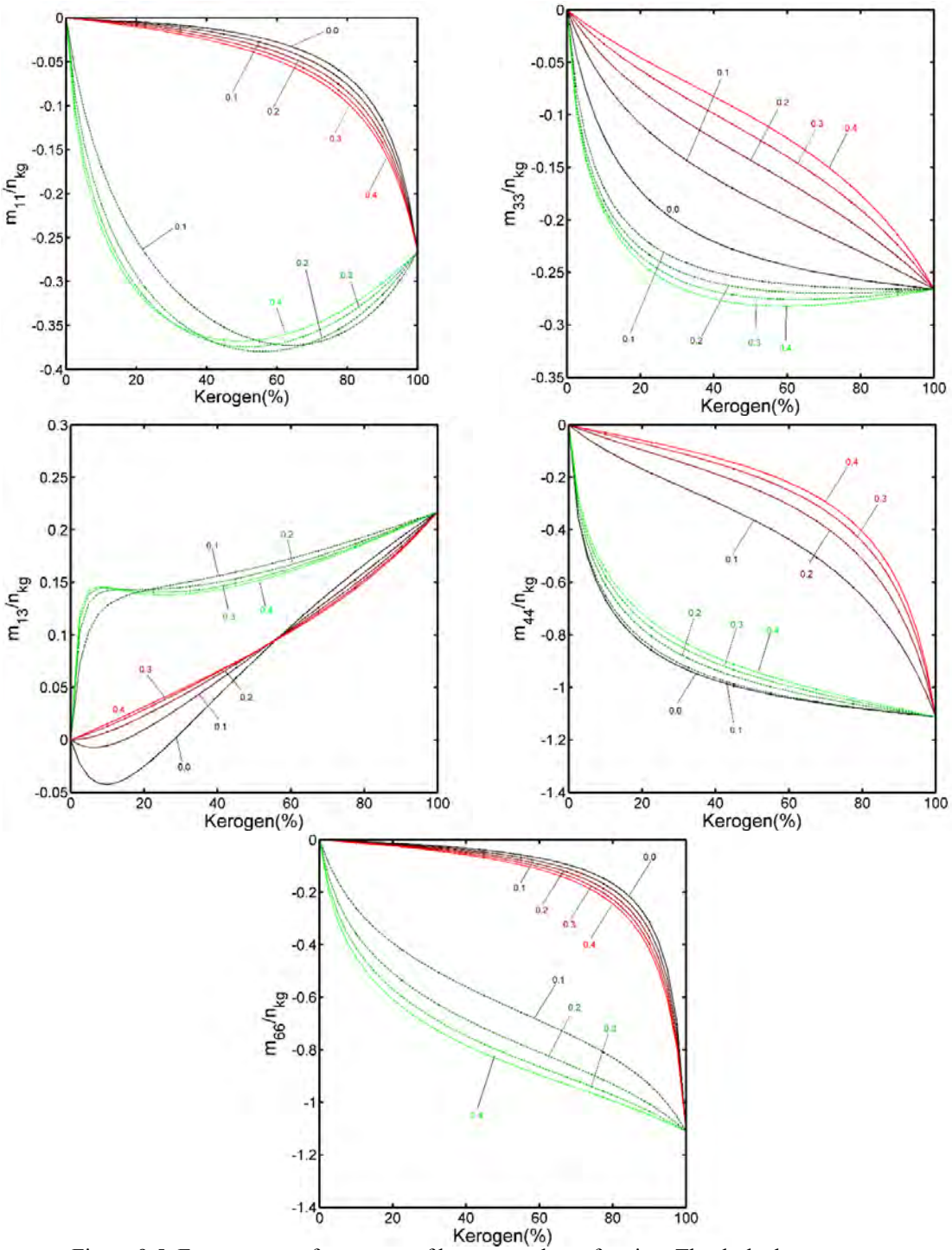

Figure 9.5: Exponents m_{ij} for a range of kerogen volume fraction. The dashed green curves correspond to inclusions of elastic mineral in kerogen background; aspect ratios are also shown on the plots. The full red curves correspond to inclusions of kerogen in mineral background.

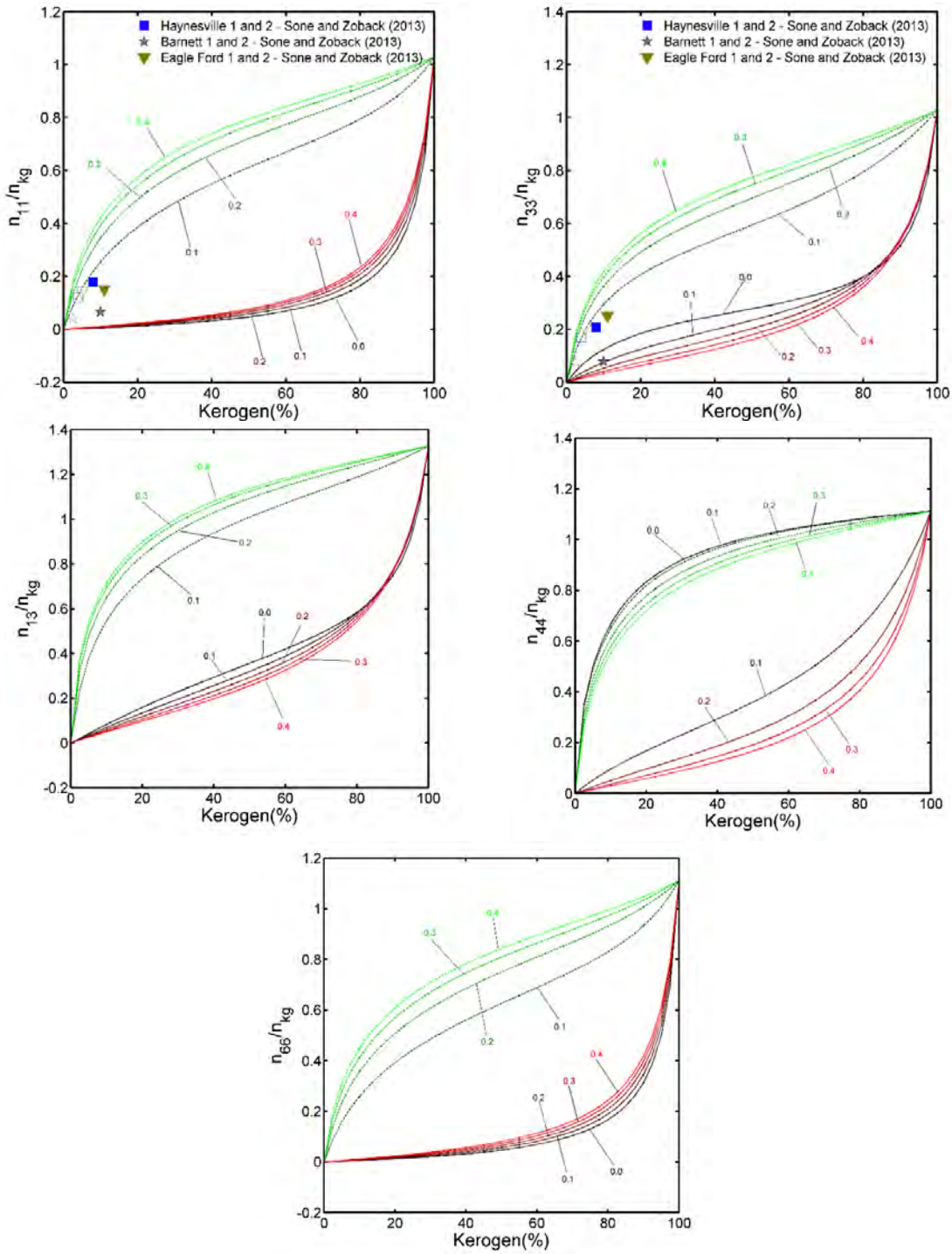

Figure 9.6: Exponents n_{ij} for a range of kerogen volume fraction. The dashed green curves correspond to inclusions of elastic mineral in kerogen background; aspect ratios are also shown on the plots. The full red curves correspond to inclusions of kerogen in mineral background.

Figure 9.5 show the calculated values of exponents m_{ij} normalized by $n_{kg} = 0.25$. Similarly, Figure 9.6 show calculations for n_{ij} normalized by n_{kg}. From Figures 9.5 and 9.6 we note that the model curves corresponding to kerogen background predict relatively larger time exponents (for a range of inclusion aspect ratio: 0 to 0.4) when compared to the model curves corresponding to mineral background. Note that the two sets of curves are relatively better separated for calculation of time exponents when compared to their separation for calculation of elastic coefficients C_{ij}^{eff} and S_{ij}^{eff}. The two sets of model curves contain the laboratory measured time exponents.

We note the laboratory measured time exponents for Haynesville samples (Sone and Zoback, 2013) are difficult to explain with model curves corresponding to mineral background, and can be better explained using model curves of kerogen background. For the laboratory measurements of time exponents for Eagle Ford and Barnett samples, it is not clear which of the two mixing scheme fits the data better. However, model curves corresponding to kerogen background generally seem to better fit the laboratory measurements of both time exponents and stiffness coefficients.

9.7. Discussion

9.7.1. Which mixing scheme to use?

In Figures 9.2-9.4 we note that the predictions of the two mixing schemes (in Figure 9.1) roughly span the range of laboratory measurements. As discussed in the previous section, model curves corresponding to elastic mineral inclusions in kerogen background seem to relatively better fit both static and dynamic laboratory data. Since the model curves corresponding to the two mixing schemes are relatively better separated for calculation of time exponents (n_{ij} or m_{ij}) when compared to effective elastic coefficients (C_{ij}^{eff} or S_{ij}^{eff}), we note that laboratory measurements of creep exponents can aid in deciding which mixing scheme better describes the mechanical properties of organic-rich shale rock.

9.7.2. **Can we predict creep exponents from seismic?**

Figure 9.7a shows cross plot between Vp/Vs (ratio of vertical P and S-wave velocities) and AI (P-wave acoustic impedance), similarly Figure 9.7b shows a cross plot between GI (S-wave acoustic impedance), and AI. We will now analyze these cross plots since it is often possible to invert for AI and GI from seismic data.

From Figure 9.7a we note that predictions of Vp/Vs decrease with increase in inclusion aspect ratio for both mixing schemes. However, some time exponents, for example n_{33}, increase or decrease with increase in aspect ratio depending on the underlying mixing scheme (Figure 9.6), thus it will be difficult to establish any unique relation between Vp/Vs and some of the time exponents. Of course, if we fix restrict this analysis to a mixing scheme, it may be possible to relate Vp/Vs (or GI) to time exponents.

Also, due to the contrast between elastic properties of kerogen and elastic mineral, AI can yield an estimate of volume fraction, which may be further related to time exponents.

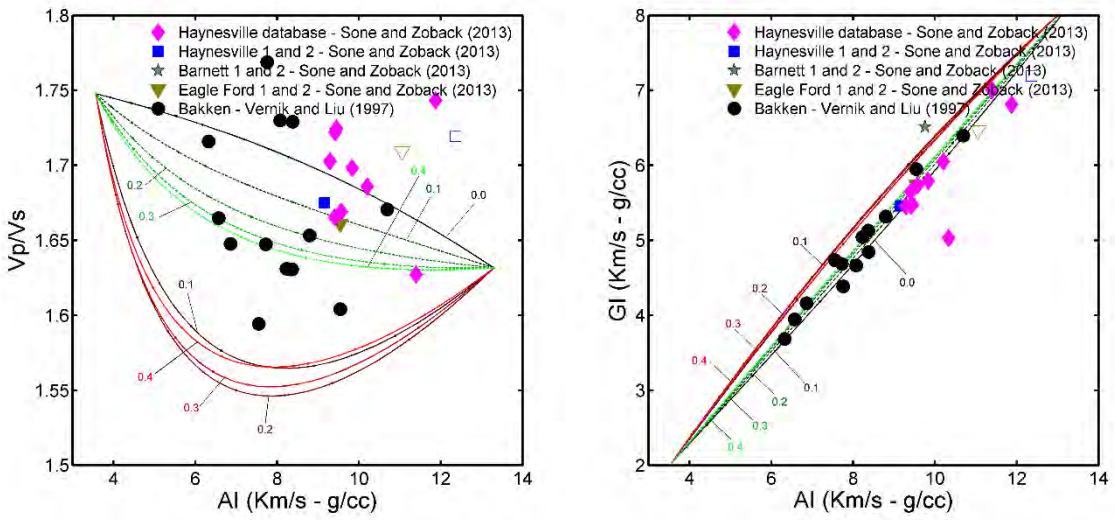

Figure 9.7: Exponents n_{ij} for a range of kerogen volume fraction. The dashed green curves correspond to inclusions of elastic mineral in kerogen background; aspect ratios are also shown on the plots. The full red curves correspond to inclusions of kerogen in mineral background.

9.7.3. **Predicting other creep exponents with n_{33}?**

Figures 8 and 9 show cross-plots between normalized n_{33} and other effective exponents (n_{ij} and m_{ij}). These plots highlight the anisotropic nature of the time exponents, and also suggest that the time exponents strongly depend on the boundary conditions of rock deformation. From these plots we obtain the following first order fits for kerogen inclusions in elastic mineral background

$$m_{11} = -0.26\, n_{33} \quad , \tag{9.29}$$

$$m_{33} = -0.15\sqrt{n_{33}} - 0.05\, n_{33} \quad ,$$

$$m_{13} = 0.1\sqrt{n_{33}} \quad ,$$

$$m_{44} = -1.2\, n_{33} \quad ,$$

$$m_{66} = -4.4\left(n_{33}\right)^2 - 0.1\, n_{33} \quad ,$$

$$n_{11} = -3.2\left(n_{33}\right)^2 + 0.2\, n_{33} \quad , \tag{9.30}$$

$$n_{13} = 1.5\ n_{33} \quad ,$$

$$n_{44} = 1.3\ n_{33} \quad ,$$

$$n_{66} = 3.2\left(n_{33}\right)^2 + 0.25\, n_{33} \quad ,$$

and the following empirical fit for inclusions of elastic mineral in kerogen background

$$m_{11} = 0.8\left(n_{33}\right)^2 - 0.7\, n_{33} \quad , \tag{9.31}$$

$$m_{33} = -0.13\sqrt{n_{33}} - 0.05\, n_{33} \quad ,$$

$$m_{13} = 0.1\sqrt{n_{33}} + 0.05\, n_{33} \quad ,$$

$$m_{44} = -1.6 n_{33} \quad ,$$

$$m_{66} = -1.1 n_{33} \quad ,$$

$$n_{11} = n_{33} \quad , \tag{9.32}$$

$$n_{13} = 1.9\, n_{33} \quad ,$$

$$n_{44} = 2.1\ n_{33} \quad ,$$

$$n_{66} = 1.1 n_{33} \quad .$$

Often it is not possible to directly measure all time exponents due to limitations of the experimental setup. It is however relatively easier to measure the time exponent n_{33}. The time exponent correlations in equations 9.29-9.32 can be used in such situations to obtain a crude estimate of the other time exponents if an estimate of at least of the time exponent is available.

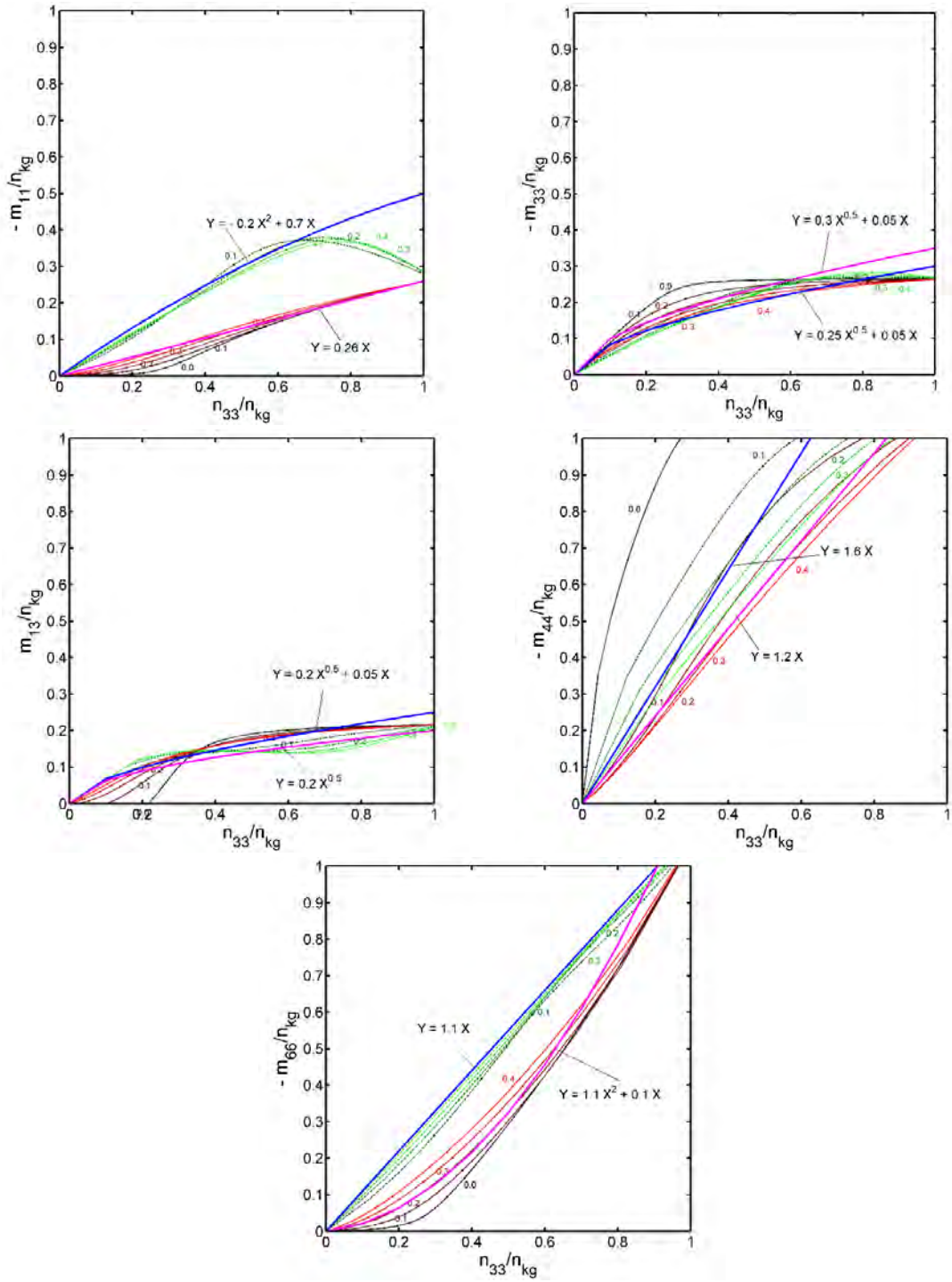

Figure 9.8: Exponents m_{ij} versus n_{33}. The dashed green curves correspond to inclusions of elastic mineral in kerogen background; aspect ratios are also shown on the plots. The full red curves correspond to inclusions of kerogen in mineral background.

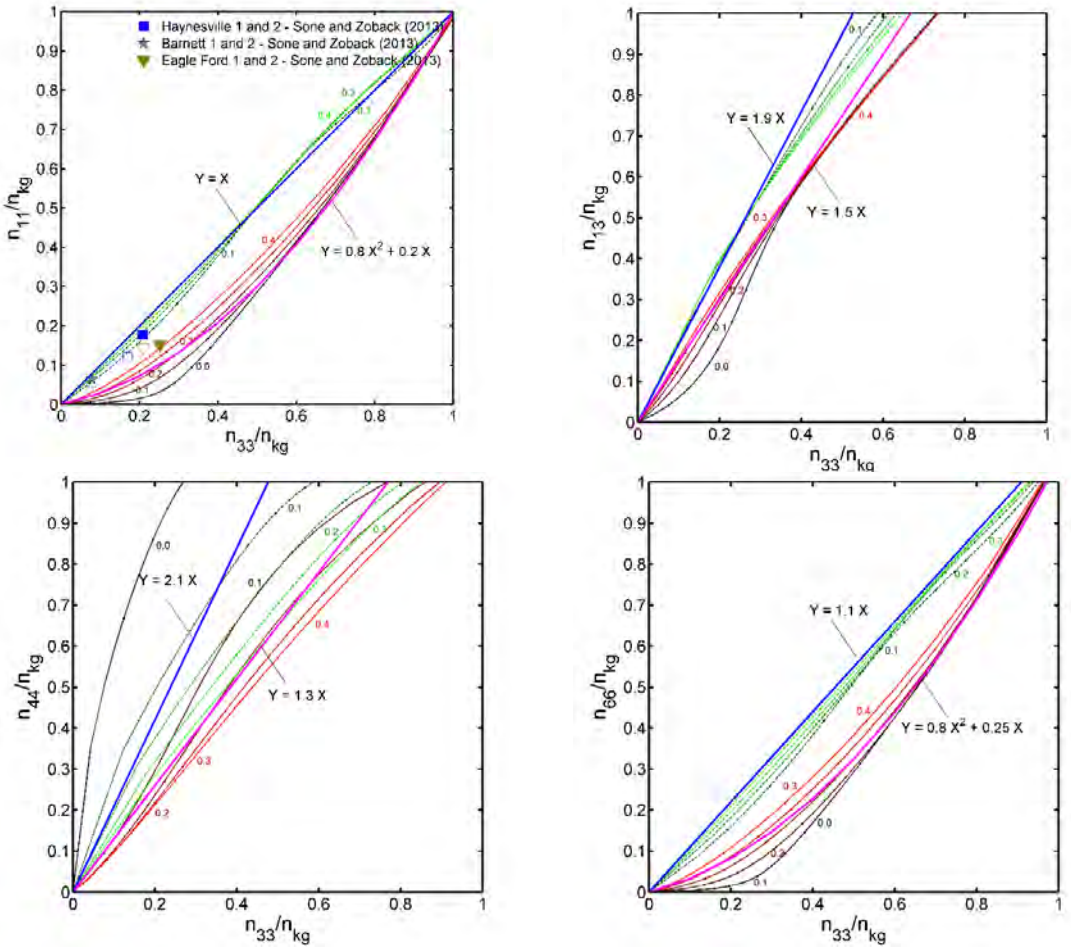

Figure 9.9: Exponents n_{ij} versus n_{33}. The dashed green curves correspond to inclusions of elastic mineral in kerogen background; aspect ratios are also shown on the plots. The full red curves correspond to inclusions of kerogen in mineral background.

9.8. Chapter summary

We present a modeling recipe to compute and analyze effective elastic properties and creep functions in organic rich shale. We note that model curves of elastic mineral inclusions in kerogen background generally fits both dynamic and static data better when compared to model predictions of kerogen inclusions in elastic mineral. This observation is consistent with Vernik and Liu (1997) and Sayers (2013). The two mixing schemes predict very different time exponent coefficients, thus we conclude that static

measurements can be of help in deciding the mixing scheme that better describes dynamic properties for a particular shale rock.

For VTI rocks such as organic rich shales, the creep time exponents will be anisotropic and will also depend on the boundary conditions of rock deformation. Often it is not possible to directly measure all time exponents, thus we present a simple set of empirical relations which can yield crude estimates of unmeasured time exponents starting with those measured directly.

9.9. Acknowledgements

We would like to thank Colin Sayers for his contributions. This work was supported by the Stanford Rock Physics and Borehole Geophysics (SRB) Project, and U.S. Department of Energy award DE-FE0001159.

9.10. References

Albate, J. and W. Whitt, 2006, A unified framework for numerically inverting laplace transforms: INFORMS Journal on Computing, **18**, 4, 408-421.

Bandyopadhyay, K., 2009, Seismic anisotropy: geological causes and its implications to reservoir geophysics: Ph.D. thesis, Stanford University.

Berryman, J. G., 1980, Long-wavelength propagation in composite elastic media: Journal of the Acoustical Society of America, **68**, 1809–1831.

Cleary, M. P., I. W. Chen and S. M. Lee, 1980, Self-consistent techniques for heterogeneous media: ASCE Journal of Engineering Mechanics, **106**, 861-887.

Jakobsen, M., J. A., Hudson, T. A., Minshull, and S. C., Singh, 2000, Elastic properties of hydrate-bearing sediments using effective medium theory: Journal of Geophysical Research, **105**, 561-577.

Khadeeva, Y. and L. Vernik, 2013, Rock-physics model for unconventional shales: The Leading Edge, **33**, 3, 318-322.

Mukerji, T., J., Berryman, G., Mavko, and P., Berge, 1995, Differential Effective Medium Modeling of Rock Elastic Moduli with Critical Porosity Constraints: Geophysical Research Letters, **22**, 555–558.

Lakes, R. S., 2009, Viscoelastic Materials, Cambridge University Press.

Mura, T., 1982, Micromechanics of Defects in Solid: Martinus Nijhoff Pub.

Nishizawa, O., and T., Yoshino, 2001, Seismic velocity anisotropy in mica-rich rocks: An inclusion model: Geophysical Journal International, **145**, 19–32.

O'Connell, R. J., B. Budiansky, 1974, Seismic velocities in dry and saturated cracked solids: Journal of Geophysical Research, **79**, 5412-5426.

Ruiz, F., and I. Azizov, 2011, Tight shale elastic properties using the soft porosity and single aspect ratio models: 81st Annual International Meeting, SEG, Expanded Abstracts, 2241–2245.

Sevostianov, I., N. Yilmaz, V. Kushch, and V. Levin, 2005, Effective elastic properties of matrix composites with transversely-isotropic phases: International Journal of Solids and Structures, **42**, 455–476.

Sayers, C. M., 2013, The effect of kerogen on the elastic anisotropy of organic - rich shales: Geophysics, **78**, 2, D65-D74.

Sondergeld, C. H., C. S. Rai, R. W. Margesson, and K. Whidden, 2000, Ultrasonic measurement of anisotropy in the Kimmeridge Shale: 69th Annual International Meeting, SEG, Expanded Abstracts, 1858–1861.

Sone, H., 2012, Mechanical properties of shale gas reservoir rocks and its relation to the in-situ stress variation observed in shale gas reservoirs: Ph.D. thesis, Stanford University.

Sone, H. and M. Zoback, 2013, Mechanical properties of shale-gas reservoir rocks - Part 1: Static and dynamic elastic properties and anisotropy: Geophysics, **78**, 5, D381-D392.

Thomsen, L., 1986, Weak elastic anisotropy: Geophysics, **51**, 1954–1966

Vernik, L., and C. Landis, 1996, Elastic anisotropy of source rocks: Implications for hydrocarbon generation and primary migration, AAPG Bulletin, **80**, 531–544.

Vernik, L., and X. Liu, 1997, Velocity anisotropy in shales: A petrophysical study: Geophysics, **62**, 521-532.

Vernik, L., and A. Nur, 1992, Ultrasonic velocity and anisotropy of hydrocarbon source rocks: Geophysics, **57**, 727 – 735.

Vernik, L., and M. Kachanov, 2010, Modeling elastic properties of siliciclastic rocks: Geophysics, **75,** no. 6, E171–E182.

Vernik, L., and J. Milovac, 2011, Rock physics of organic shales: The Leading Edge, **30**, no. 3, 318–323.

Chapter 10
Unsolved problems with half-baked solutions

10.1. Simulate physics at grain contacts

10.1.1. Overview

Contact mechanics play a crucial role for determining the elastic stiffness of unconsolidated or poorly consolidated sediments. The deformation in the vicinity of a grain contact and the corresponding repulsive forces are successfully described by the Hertzian contact model and effective-medium theory. Laboratory measurements, however, show significant deviations from the theoretical predictions of effective elastic moduli, in particular for the effective shear modulus. These deviations are due to stress heterogeneity associated with stress chain formation in random grain packs, or due to contact heterogeneity and surface roughness at the scale of the single grain contact. Contact behavior is also altered by the presence of elastic cement at grain contacts. By incorporating

a contact boundary condition into the numerical simulation, we accurately predict the non-linear elastic behavior of a sphere contact and capture well the effects of contact cementation. All our numerical benchmark simulations are in agreement with theoretical predictions, provided that the numerical resolution is fine enough to accurately resolve the stress fields close to the contact surface.

10.1.2. Introduction

The deformation of elastic bodies that are in contact with one another is a classical problem of continuum mechanics and subject of several textbooks (e. g. Johnson, 1985). Stress and deformation of an elastic contact are typically confined within an area that is small with respect to the dimension of the body. The fact that the contact area changes in size as a function of applied forces gives rise to non-linear elastic behavior. An important consequence of contact non-linearity is the pressure-dependence of granular materials such as unconsolidated sediments. Mechanically, those sediments can be described as grain packs, where the interactions of grains with one another are governed by friction and contact laws (e.g. Duffy and Mindlin, 1957; Digby, 1981; Dvorkin et al., 1991; Goddard, 1990; Sain, 2010).

All the above mentioned effective-medium models for granular materials are based on the solution of a single point contact. An analytical solution for the normal forces arising in the contact of curved surfaces was first given by Hertz (1882) under the assumption of small strains and by neglecting surface friction. Hertz found that the contact stiffness k between two elastic bodies is proportional to the radius a of the circular contact area: $k \propto a$. Knowing the contact radius of a sphere $a = \sqrt{R\delta}$, it follows that the contact stiffness grows as $k \propto \sqrt{\delta}$, where R denotes the sphere radius and δ the relative displacement of the center of the sphere with respect to the contact surface. Note that contact radius and displacement should not be confused with the terms virtual overlap $\xi = 2\delta$ and virtual contact radius $b = \sqrt{2}\,a$, both of which are depicted in Figure 10.1.

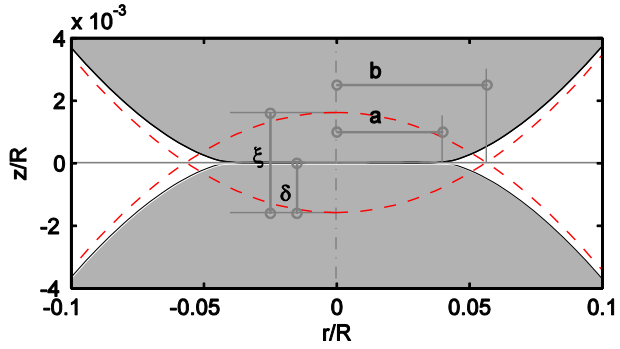

Figure 10.1: Deformed Hertz contact between two equal spheres of radius R with definitions of contact radius a, displacement δ, overlap $\xi = 2\delta$ and virtual contact radius $b = \sqrt{2}a$. Red dashed lines represent two overlapping spheres with the radius R each.

Hertz's solution for the reaction force between two bodies is

$$F = -\int k(\delta)d\delta = -\frac{4}{3}E^*\sqrt{R\delta^3} \tag{10.1}$$

that is, $F \propto \delta^{3/2}$. Here,

$$E^* = \frac{E}{(1-\nu^2)} \tag{10.2}$$

is an effective Young's modulus. Isotropic elastic properties are Young's modulus E and Poisson ratio ν. Many non-Hertzian contact laws are reported in the literature, including cylindrical and conical contact points, as well as rough surfaces (for an overview, see Johnson, 1985). Mindlin (1949) considered tangential forces between two bodies that are transmitted through surface friction. Analytical solutions, however, are based on simplifications and on idealized contact geometries. Effective-medium theories that calculate effective properties based on Hertz-Mindlin theory have quite a few shortcomings. They show significant deviations from laboratory measurements. Sain (2010) showed that these deviations primarily arise since the current effective medium models do not account for heterogeneous strain field and stress relaxation at the grain contacts. This disagreement can also arise due to contact roughness (Goddard, 1990;

Bachrach and Avseth, 2008). In addition to these, contact cements often play a significant role for the behavior of sedimentary rocks (Dvorkin et al., 1991).

The finite-element method offers a possibility to simulate mechanical contact problems with arbitrary geometry efficiently and with high accuracy. The effects of contact cement are easily accounted for by introducing additional material phases to the grain-contact model. Numerical simulations also allow incorporating anisotropic or anelastic material behavior, thus integrating contact mechanics with a more general elastic description. We make use of the commercial software package COMSOL Multiphysics, which offers a potential to couple contact mechanics with other physics problems, such as heat conduction, electrical currents, and magnetic flux in the contact area.

In this section, we compute the stress fields associated with a contact between two spherical grains of equal size. A classical Hertz contact problem is used to benchmark the simulation approach, and we compare the simulation of the Hertz contact with the elastic case of two grains with cement close to the contact point (Figure 10.2).

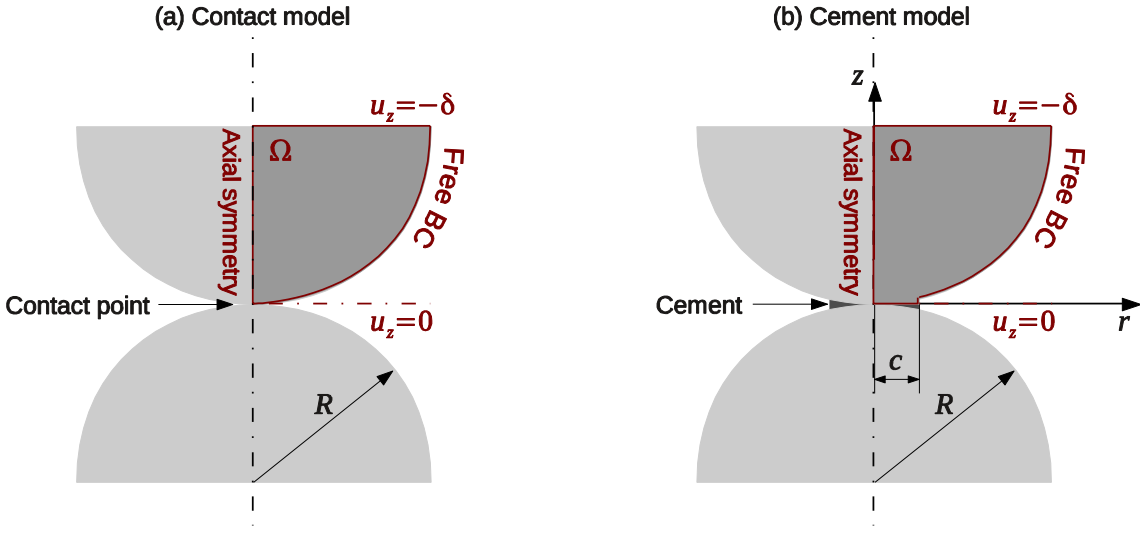

Figure 10.2: Geometries of contact simulations. In the undeformed configuration, two spheres share a contact point (a), while in the case of a cemented contact (b), a cement radius c is defined. We make use of the problem symmetry to minimize the computational domain Ω.

10.1.3. Finite-element simulations of sphere contacts

For our numerical investigations, we assume static loading with no friction at the smooth contact boundary. We solve an elastic sphere contact problem with COMSOL 4.1 Multiphysics. Our numerical model takes advantage of axial symmetry in the geometry as shown in Figure 10.2. Second, we make use of the symmetries at the grain-grain interface and at the sphere equator plane. Strain is imposed on the system by prescribing vertical displacement u_z at the equator plane at $z = R$, while horizontal motion u_x is unconstrained. At the outer sphere surface we apply traction-free boundary conditions. For our simulations, we choose a Young's modulus $E = 70$ GPa and a Poisson ratio $\nu = 0.33$, corresponding to a shear modulus of 26.3 GPa and an effective Young's modulus E^* of 78.6 GPa.

The contact itself is implemented in the COMSOL package by the definition of contact pairs. The elastic solver automatically computes relative distances between the nodes within both pairs and adds an internal repulsive force to the solution in order to ensure that no overlap between the elastic bodies occurs. The solution is obtained using an iterative solver.

An inherent numerical challenge in the field of contact problems is caused by the large difference between the scale of the contact area and the size of the spherical body. The stress and strain fields are very concentrated in the proximity of the contact point, while the stress field is relatively homogeneous within the largest part of the simulation domain. An accurate numerical solution for a point contact requires a fine meshing in the vicinity of the sphere contact, while at a certain distance from the contact point, a coarser mesh is acceptable. We achieve a suitable meshing by using adaptive mesh refinement. This significantly improves the accuracy of solutions for the point-contact case if compared to a homogeneous mesh distribution as depicted in Figure 10.3.

In addition to the sphere contact simulation, we perform an analogous numerical experiment after adding a linearly elastic cement filling at the contact as depicted in Figure 10.2b. Cemented geometries are commonly encountered in rocks which have undergone diagenesis, and it is known that small amounts of cement are able to significantly stiffen

the contacts of poorly consolidated sediments (e.g. Dvorkin and Nur, 1991). This simulation allows us to study the influence of the amount of cement on the elastic stiffness of the contact area. We control the amount of cement by changing the radius of the cemented domain c, thus creating a contact surface with a finite radius, analogous to the Hertz contact radius a under a given stress. The radius c is varied between 0.01R and 0.04R. For the cement material, the same material is used as for the spherical grains ($E = 70$ GPa and $\nu = 0.33$).

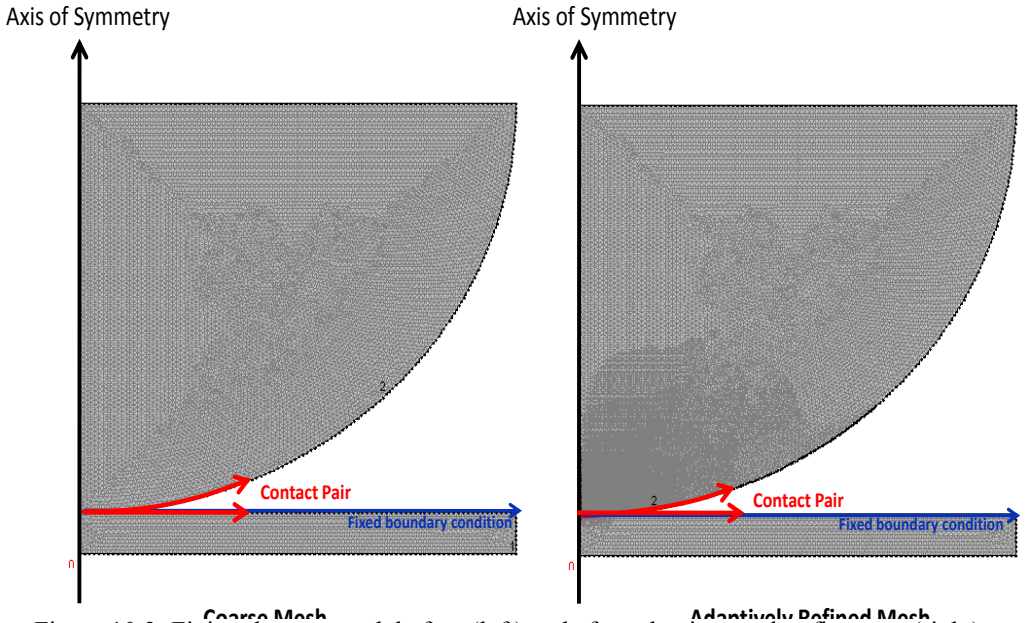

Figure 10.3: Finite-element mesh before (left) and after adaptive mesh refinement (right).

10.1.4. **Numerical results**

10.1.4.1. **Hertz contact**

We numerically explore a contact problem between two spheres of equal size that are in contact with one another. Hertz's theory predicts that the stiffness of the contact grows with the deformation as $\delta^{1/2}$, such that the reaction force is proportional to $\delta^{3/2}$. As the theoretical solution is known, this case serves us as a benchmark test of our finite-element contact mechanics simulations.

We calculate the force for a range of normal displacement δ by integrating the normal component of the traction along the sphere equator plane as follows:

$$F = -\int_{r=0}^{a} \sigma_n(r)\,dr \quad . \tag{10.3}$$

We compare the analytical solution given in equation 10.**Error! Reference source not found.** with the numerically obtained reaction force F, and we find an excellent match with Hertz theory; see Figure 10.4.

The numerical solution allows determining the contact radius in the deformed configuration, by analyzing the surface traction along the sphere grain boundary. According to the imposed free-boundary condition, the traction is zero outside the contact area, while inside the area of contact the normal stress is finite. For a normal displacement of $\delta/R = 16 \times 10^4$, the numerically obtained contact radius $a/R = 0.04$ is in agreement with the theoretical prediction of $a = \sqrt{R\delta}$.

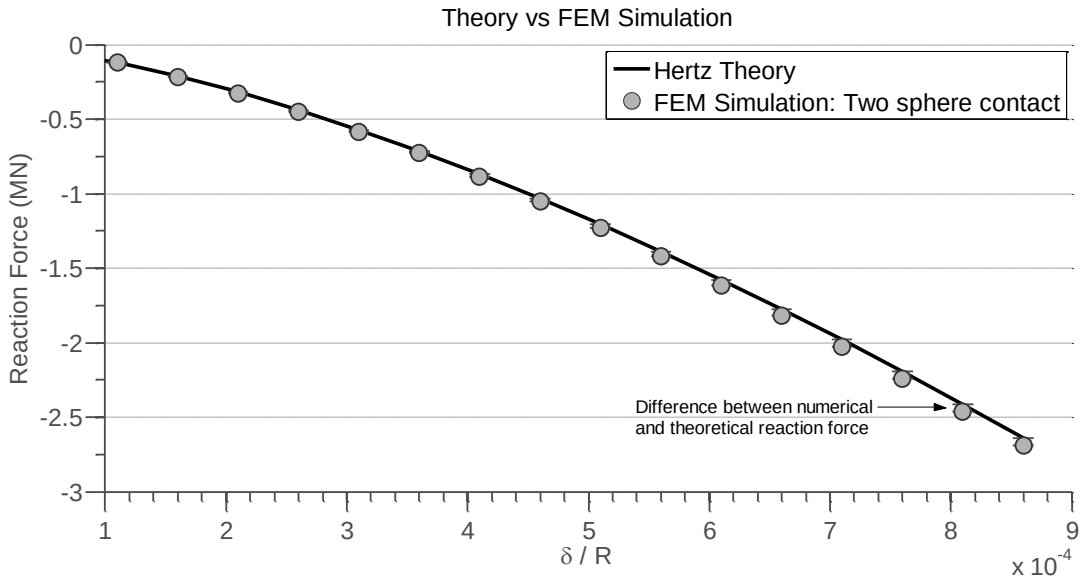

Figure 10.4: Comparison of theoretical prediction and numerical simulation of a Hertz contact.

10.1.4.2. Convergence behavior of the non-linear solver

If the two spheres are not in contact before a confining stress is applied, the solver has difficulty converging. If the compression is imposed by prescribing a displacement of the

sphere quadrant, the solver succeeds in finding a solution for small displacements. The 2-D axial symmetric elasticity solver does not allow applying a point force at the symmetry axis. We find better convergence for the case of displacement-driven boundary conditions if compared to stress-driven boundary conditions. Imposing a displacement is therefore preferred to applying a force in order to deform the model.

10.1.4.3. Stress distributions at sphere contacts

It is a well-known result from contact theory that the stress distribution within a circular contact area depends on the contact interface conditions. Analytical solutions for the traction distribution $p(r)$ are generally available in the form a power law (Johnson, 1985):

$$p(r) = p_0\left(1-\frac{r^2}{a^2}\right)^n \quad . \tag{10.4}$$

where $n = 1/2$ and

$$p_0 = \frac{2E^*}{\pi\sqrt{R}}\sqrt{\delta} \quad . \tag{10.5}$$

for a classical Hertz contact. In our simulations with contact cement, the cement and the grain are in welded contact. The case of the contact cement is therefore approximated by the solution of an elastic cylindrical punch in an elastic half-space, which is represented by $n = -1/2$ and a pressure p_0 at the symmetry axis:

$$p_0 = \frac{E^*}{\pi c}\delta \quad . \tag{10.6}$$

where c is the radius of the cemented area, corresponding to the contact radius a in the Hertz solution.

In Figure 10.5, we show the mean stress field p in the vicinity of the contact for the two cases under consideration, the Hertz model and the cemented model. In both simulations, the contact radius a is $0.04R$ and the displacement δ is 1.6×10^{-3} R. In both models, the

mean stress has a maximum at the contact and shows fast decay further away from it. The cemented model features a clear stress concentration at the outer tip of the cemented area.

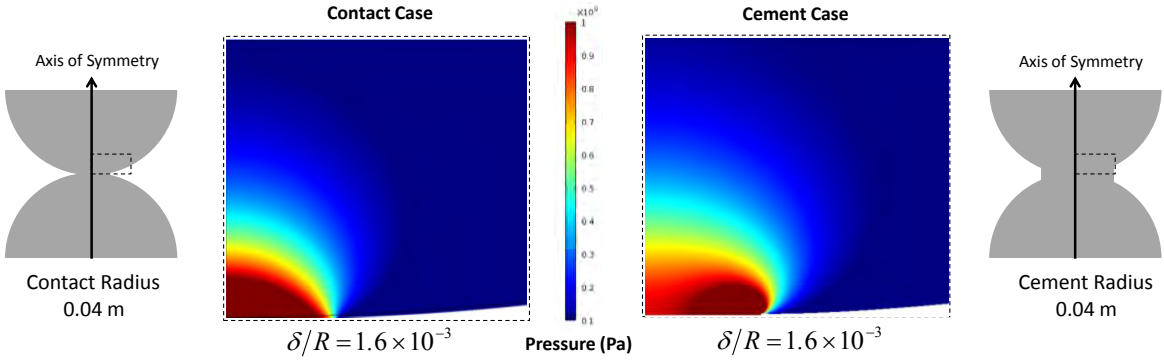

Figure 10.5: Mean stress fields simulated for a sphere contact (left) and a contact with cement (right).

The simulated stress component normal to the contact plane is shown in Figure 10.6 as a function of radial distance r. Our numerical solution shows that the stress distribution is very well described by the contact law given in equation 10.4. The main characteristic of the Hertz contact solution is a maximum at the symmetry axis, while the solution of the cement model shows a dominant stress singularity at the tip of the cemented surface.

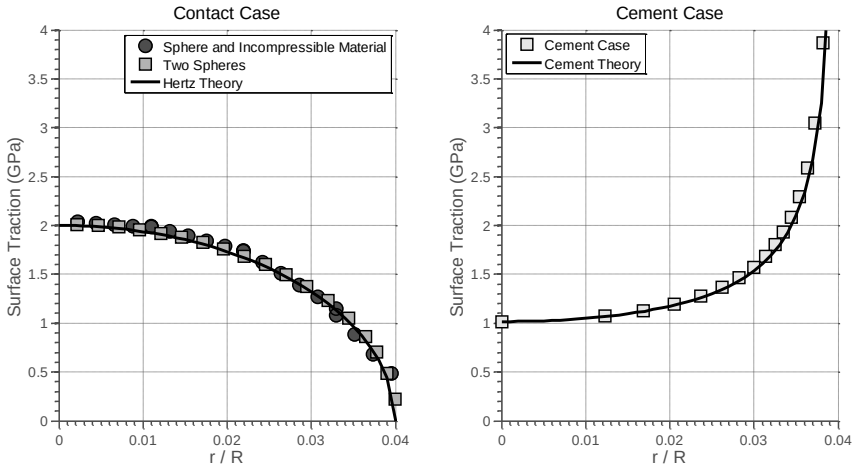

Figure 10.6: Simulated surface traction for the case of a Hertz contact and for a cemented contact. In both simulations, a normal displacement of $\delta/R = 1.6 \times 10^{-3}$ is imposed. The contact radius or the radius of the cemented contact, respectively, is in both cases 0.04R.

If the reaction forces are known, computing the contact stiffness k is straightforward. According the definition of a stiffness constant, $k(\delta) = -dF/d\delta$, it follows that $k = 2E^*a$ for the case of a Hertz contact and $k = 2/3\ E^*c$ for the cemented contact. This shows that in both cases, the contact stiffness is proportional to the contact radius a or c, respectively. Using a series of contact simulations with different strains $0 < \delta/R < 0.0016$, or different radii of cement $0 < c/R < 0.04$, respectively, we confirm that this proportionality holds at small deformations under consideration (results not shown).

10.1.5. **Future outlook**

The classical problem of computing the reaction forces between elastic bodies in contact with one another has theoretical significance for the description of grain packs and unconsolidated granular materials. The contact laws are the basis for both analytical effective medium models and computer simulation of granular dynamics. We show here that finite-element simulations are able to accurately compute the non-linear elastic response associated with contact problems. We confirmed this by carefully benchmarking our numerical results against known analytical solutions of contact mechanics.

We point out that this study is a first step towards addressing more complex grain-contact problems. These may include investigating contact surfaces of non-spherical grains, tangential friction or grain rotation. In general, the assumption of axial symmetry and symmetry with respect to the contact plane is not applicable, but 3-D simulation is necessary. The benchmark tests presented here show that a fine resolution of contact area is crucial for an accurate prediction of contact pressures and reaction forces. The consideration of grain interaction at the scale of a grain ensemble (or grain pack) is currently unfeasible using finite-elements with contact boundary conditions due to high resolution requirements. The solutions obtained on the scale of a single contact may, however be used as an input for theoretical models or granular-dynamics simulations on the scale of a grain pack.

In the future, simulations on the sub-micro scale—i.e. on the scale of the grain contacts—may provide a valuable tool for further investigating the elastic response of grain

contacts, where the flexibility of the finite-element approach in principal allows taking into account complexities that make an analytical treatment unfeasible. Of particular interest are the behavior of irregularly shaped grains, the influence of stiffness and strength of the cement material, and the influence of coupled fluid flow in the pore space on elastic relaxation behavior. This feasibility study may therefore pave the way to addressing a broad range of rock-physics research questions.

10.2. Range for substitution parameters

In chapter 2, we discussed exact solutions to the problem of substitution which depend on parameters $\alpha_{1,2}$ and $\beta_{1,2}$. These non-negative substitution parameters have clear mathematical definitions and thus can be easily calculated for various microstructures using the FEM. The possible range of these parameters is still to be established and requires further investigation.

10.3. Anisotropic solid substitution relations

Anisotropic versions of our exact solutions in chapter 2, 4 and 8 can be easily obtained by defining the energy density function in terms of full stiffness tensor. In this thesis, we only obtain solutions for isotropic case. The practical challenge for such an extension will be to constrain the range of the required substitution parameters.

10.4. Strict bounds on substitution and coupled bounds

In chapter 5, we conjecture that the embedded bounds are strict bounds on solid substitution, this is yet to be proven. Also, our embedded bounds are uncoupled in the sense that initial effective bulk modulus measurement does not affect the effective shear modulus substitution calculation, and vice versa. It is still to be established if bulk and shear calculations can be further restricted.

10.5. Numerically simulate poromechanical behavior of rocks saturated with high-viscosity fluid

10.5.1. Overview

Using the method of volume averaging (Whitaker, 1999; de la Cruz et al., 1985; Sahay et al., 2001; Sahay, 2008) set of macroscopic equations of wave motion for heterogeneous porous media are derived. The porous medium considered consists of an elastic solid frame and interconnected pores filled with a viscous Newtonian fluid. This macroscopic description improves on Biot theory (1956) and is fit for modeling rocks saturated with high viscosity fluids, such as heavy-oil. The description is also consistent from a thermodynamic view point (de la Cruz et al., 1993). The resulting set of equations include dynamic porosity and fluid strain rate - absent in Biot theory.

10.5.2. Introduction

Biot (1956, 1962) published a series of papers discussing an effective medium poromechanics model that allows for spatially varying porosity. This model is well accepted but assumes static porosity, which means the volume fractions of elastic solid and fluid are not changed by a passing acoustic wave. Various authors have pointed out this inconsistency from a thermodynamic viewpoint (de la Cruz et al., 1985; Sahay et al., 2001; Sahay, 2008). Another significant problem with the very starting point of Biot theory is his assumption of the elastic potential function to obtain stress tensors using variational methods (de la Cruz et al., 1993). Such an elastic potential function will not be conserved for viscous fluids because of the strain-rate dependence. Therefore, strictly speaking, Biot theory cannot be used to model rocks saturated with Newtonian or non-Newtonian fluids, examples of such fluids include heavy oil, magma, kerogen, etc.

In this section, we first describe the pore-scale physics equations for a porocontinuum. We then derive macroscopic poromechanics equations for mass balance, momentum balance, stresses and interfacial forces, using the method of volume averaging (discussed

in chapter 3; Whitaker, 1999). Throughout this section, the elastic solid making up the rock frame is denoted by superscript "s" whereas the pore saturating Newtonian fluid is denoted by superscript "f".

10.5.3. Microscopic description

The standard linearized equations of motion at the pore scale for an elastic solid and Newtonian viscous fluid are as follows:

10.5.3.1. Continuity equations

$$\frac{\partial \rho^f}{\partial t} = -\partial_j\left(\rho^f v_j^f\right), \tag{10.7}$$

$$\frac{\rho^s - \rho_0^s}{\rho_0^s} = -\partial_j\left(u_j^s\right). \tag{10.8}$$

Here, u_j^s and v_j^f are the pore-scale solid displacement and fluid velocity components; ρ^s and ρ^f are the solid and fluid densities, respectively. The subscript 0 indicates the unperturbed value.

10.5.3.2. Momentum conservation and stress equations

$$\frac{\partial}{\partial t}\left(\rho^f v_j^f\right) = \partial_k\left(\sigma_{jk}^f\right), \tag{10.9}$$

$$\frac{\partial}{\partial t}\left(\rho^s \frac{\partial}{\partial t} u_j^s\right) = \partial_k\left(\sigma_{jk}^s\right). \tag{10.10}$$

Here, σ_{jk}^s and σ_{jk}^f are the grain-scale stress tensors. We ignore body forces such as gravity.

$$\sigma_{jk}^s = C_{jkln}^s u_{ln}^s, \tag{10.11}$$

and

$$\sigma_{jk}^{f} = -P^{f}\delta_{jk} + C_{jkln}^{f} v_{ln}^{f} \,. \tag{10.12}$$

Here, C_{jkln}^{s} and C_{jkln}^{f} are standard fourth-rank stiffness tensors:

$$C_{jkln}^{s} = K^{s}\delta_{jk}\delta_{ln} + \mu^{s}\left(\delta_{jl}\delta_{kn} + \delta_{jn}\delta_{kl} - \frac{2}{3}\delta_{jk}\delta_{ln}\right), \tag{10.13}$$

and

$$C_{jkln}^{f} = \mu^{f}\left(\delta_{jl}\delta_{kn} + \delta_{jn}\delta_{kl} - \frac{2}{3}\delta_{jk}\delta_{ln}\right). \tag{10.14}$$

K^{s} and μ^{s} are the bulk and shear moduli of the elastic solid, and μ^{f} is the shear viscosity of the Newtonian fluid. In this analysis, we ignore bulk viscosity, which can also be included in equation 10.14. The strain tensors in equations 10.11-10.12 are

$$u_{jk}^{s} = \frac{1}{2}\left(\partial_{k}u_{j}^{s} + \partial_{j}u_{k}^{s}\right), \tag{10.15}$$

and

$$v_{jk}^{f} = \frac{1}{2}\left(\partial_{k}v_{j}^{f} + \partial_{j}v_{k}^{f}\right). \tag{10.16}$$

10.5.3.3. **Pore-scale fluid pressure equation**

$$\frac{\partial P^{f}}{\partial t} = -K^{f}\left(\partial_{k}v_{k}^{f}\right). \tag{10.17}$$

where K^{f} is the bulk modulus of compression of the fluid. Fluid pressure is denoted by P^{f}.

10.5.3.4. **Boundary conditions**

We impose a no-slip condition at pore interfaces and continuity of traction:

$$\frac{\partial u_j^s}{\partial t} = v_j^f \,, \tag{10.18}$$

$$\sigma_{jk}^s n_k = \sigma_{jk}^f n_k \,. \tag{10.19}$$

where n_k is the normal vector to the solid-fluid interface.

10.5.4. **Macroscopic description**

The method of volume averaging links the averages of derivatives to derivatives of averages with the following two averaging theorems:

$$\int_V \partial_i \Psi^A \, dV \;=\; \partial_i \int_V \Psi^A \, dV \;+\; \int_{S^{AB}} \Psi^A \hat{n}_i \, dS \,, \tag{10.20}$$

$$\int_V \partial_t \Psi^A \, dV \;=\; \partial_t \int_V \Psi^A \, dV \;-\; \int_{S^{AB}} \Psi^A v_j^A \hat{n}_j \, dS \,. \tag{10.21}$$

Here Ψ^A is any quantity associated with the species A, and is defined to be zero everywhere outside species A. The symbol S^{AB} refers to the interface between species A and B within the averaging volume V; the unit normal $\hat{n}_j$ points from A to B, and v_j^A is the velocity of the interface between A and B. To denote phasic average, we use an overbar $\left(\overline{\Psi}^A\right)$; we use a hat symbol $\left(\hat{\Psi}^A\right)$ for the average over volume V

$$\overline{\Psi}^A = \frac{1}{V_A} \int_V \Psi^A \, dV \quad , \tag{10.22}$$

$$\hat{\Psi}^A = \frac{1}{V} \int_V \Psi^A \, dV \quad . \tag{10.23}$$

The volume fraction of species A is denoted by η^A. Using equations 10.22 and 10.23, we can write

$$\eta^A = \frac{\hat{\Psi}^A}{\overline{\Psi}^A} = \frac{V_A}{V} \quad . \tag{10.24}$$

Both theorems (equations 10.20 and 10.21) can be applied to all species in a multi-phase system; for convenience we choose two phases A and B. Theorem 1 represents a three-dimensional version of the Leibniz rule for interchanging differentiation and integration. It has been derived by various authors (Marle, 1967; Slattery, 1967; Whitaker, 1967). Theorem 2 is the general transport equation needed to complete the averaging process, because the dependence of volume V on time requires special analysis of time derivatives. The derivation of both theorems is straightforward using first principles of transport equations in the spatial domain. Extensive discussion on this subject can be found in Whitaker (1999).

Using the above volume-averaging theorems (de la Cruz et al., 1985; Sahay et al., 2001; Whitaker, 1999; also see chapter 3) we can volume-average microscopic physics equations to obtain a macroscopic description as follows:

10.5.4.1. Macroscopic continuity equations

Volume-averaging the fluid and solid continuity equations, we get

$$\frac{1}{V}\int_V \left[\frac{\partial \rho^f}{\partial t} + \partial_j \left(\rho^f v_j^f \right) = 0 \right] dV, \tag{10.25}$$

and

$$\frac{1}{V}\int_V \left[\frac{\rho^s - \rho_0^s}{\rho_0^s} + \partial_j \left(u_j^s \right) = 0 \right] dV. \tag{10.26}$$

Applying the averaging theorems, we can simplify equation 10.25 as

$$\frac{\partial \eta \overline{\rho}^f}{\partial t} - \frac{1}{V}\int_{S^{fs}} \rho^f v_j^A \hat{n}_j dS + \partial_j \left(\eta \overline{\rho^f v_j^f} \right) + \frac{1}{V}\int_{S^{fs}} \rho^f v_j^f \hat{n}_j dS = 0 \,, \tag{10.27}$$

or

$$\frac{\partial \eta \overline{\rho}^f}{\partial t} - \frac{1}{V}\int_{S^{fs}} \rho^f \left(v_j^A - v_j^f\right)\hat{n}_j dS + \partial_j\left(\eta \overline{\rho^f v_j^f}\right) = 0\,. \tag{10.28}$$

where η is the porosity. At the interface S^{fs} (surface between fluid and solid) $v^A = v^f$, hence the two area integrals cancel each other. Keeping only the first-order terms, we get

$$\eta_0 \frac{\partial \overline{\rho}^f}{\partial t} + \rho_0^f \frac{\partial \eta}{\partial t} + \rho_0^f \eta_0\, \partial_j \overline{v}_j^f = 0\,. \tag{10.29}$$

Simplifying equation 10.26 for an elastic solid results in

$$\left(1-\eta_0\right)\frac{\overline{\rho}^s - \rho_0^s}{\rho_0^s} + \left(1-\eta_0\right)\partial_j \overline{u}_j^s + \frac{1}{V}\int_{S^{sf}} u_j^s \hat{n}_j dS = 0\,. \tag{10.30}$$

The quantity $u_j^s \hat{n}_j dS$ is the volume swept out by the solid displacement u_j^s at the pore interfaces; hence the area integral in equation 10.30 is actually the change in volume fraction of the solid and is equal to $\eta_0 - \eta$. Therefore, equation 10.30 reduces to

$$\frac{\overline{\rho}^s - \rho_0^s}{\rho_0^s} + \partial_j \overline{u}_j^s - \frac{\eta - \eta_0}{1-\eta_0} = 0\,. \tag{10.31}$$

10.5.4.2. **Macroscopic equations of motion**

Volume-averaging the equations of momentum conservation for the elastic solid and for the Newtonian pore fluid we get

$$\frac{1}{V}\int_V \left[\frac{\partial}{\partial t}\left(\rho^f v_j^f\right) - \partial_k\left(\sigma_{jk}^f\right) = 0\right] dV, \tag{10.32}$$

and

$$\frac{1}{V}\int_V \left[\frac{\partial}{\partial t}\left(\rho^s \frac{\partial}{\partial t} u_j^s \right) - \partial_k \left(\sigma_{jk}^s \right) = 0 \right] dV \,. \tag{10.33}$$

Equations 10.32 and 10.33 reduce to the following

$$\eta_0 \rho_0^f \frac{\partial \overline{v}_j^f}{\partial t} = \eta_0 \, \partial_k \overline{\sigma}_{jk}^f + \frac{1}{V}\int_{S^{fs}} \sigma_{jk}^f \hat{n}_k dS \,, \tag{10.34}$$

and

$$\left(1-\eta_0\right)\rho_0^s \frac{\partial^2 \overline{u}_j^s}{\partial t^2} = \left(1-\eta_0\right)\partial_k \overline{\sigma}_{jk}^s + \frac{1}{V}\int_{S^{sf}} \sigma_{jk}^s \hat{n}_k dS \,. \tag{10.35}$$

Tensors $\eta_0 \overline{\sigma}_{jk}^f$ and $\left(1-\eta_0\right)\overline{\sigma}_{jk}^s$ are the macroscopic stresses for the averaging volume V. The surface integrals in equations 10.34 and 10.35 are related to each other through the boundary condition (equation 10.19) as

$$\frac{1}{V}\int_{S^{sf}} \sigma_{jk}^s \hat{n}_k dS = -\frac{1}{V}\int_{S^{fs}} \sigma_{jk}^f \hat{n}_k dS = I_j \,. \tag{10.36}$$

We will refer to these area integrals as I_j, which is the effective body force per unit averaging volume V exerted by one phase on the other, arising from the interactions across the solid-fluid interfaces.

10.5.4.3. Macroscopic stress equations

Volume averaging the pore-scale stress tensors and using the boundary conditions. we get

$$\eta_0 \overline{\sigma}_{jk}^f = -\eta_0 \overline{P}_f \delta_{jk} + C_{jkln}^f \left[\frac{1}{2}\eta_0 \left\{ \partial_n \overline{v}_l^f + \partial_l \overline{v}_n^f \right\} - \frac{\partial \xi_{ln}}{\partial t} \right], \tag{10.37}$$

and

$$\left(1-\eta_0\right)\overline{\sigma}_{jk}^s = C_{jkln}^s \left[\frac{1}{2}\left(1-\eta_0\right)\left\{ \partial_n \overline{u}_l^f + \partial_l \overline{u}_n^f \right\} - \xi_{ln} \right], \tag{10.38}$$

where

$$\xi_{ln} = \frac{1}{V}\int_{S^{sf}} \frac{1}{2}\left(u_l^s \hat{n}_n + u_n^s \hat{n}_l\right) dS \,. \tag{10.39}$$

We can separate the dilatational part of ξ_{ln} from its deviatoric part in the following way:

$$\xi_{ln} = -\frac{1}{3}\delta_{ln}(\eta - \eta_0) + \frac{1}{V}\int_{S^{sf}} \frac{1}{2}\left(u_l^s \hat{n}_n + u_n^s \hat{n}_l - \frac{2}{3}\delta_{ln} u_p^s \hat{n}_p\right) dS \,. \tag{10.40}$$

It is convenient to refer to the area integral in equation 10.40 as D_{ln}, i.e.

$$D_{ln} = \frac{1}{V}\int_{S^{sf}} \frac{1}{2}\left(u_l^s \hat{n}_n + u_n^s \hat{n}_l - \frac{2}{3}\delta_{ln} u_p^s \hat{n}_p\right) dS \,. \tag{10.41}$$

These macroscopic stress equations for the isotropic and homogeneous case reduce to the following

$$\eta_0 \overline{\sigma}_{jk}^f = -\eta_0 \overline{P}_f \delta_{jk} + \eta_0 \mu^f \left\{\partial_j \overline{u}_k^f + \partial_k \overline{u}_j^f - \frac{2}{3}\delta_{jk}\partial_k \overline{u}_k^f\right\} - 2\mu^f \frac{\partial D_{jk}}{\partial t} \,, \tag{10.42}$$

and

$$\begin{aligned}(1-\eta_0)\overline{\sigma}_{jk}^s = {} & K^s \delta_{jk}\left\{(1-\eta_0)\partial_l \overline{u}_l^s - (\eta - \eta_0)\right\} + \mu^s (1-\eta_0)\left\{\partial_j \overline{u}_k^s + \partial_k \overline{u}_j^s - \frac{2}{3}\delta_{jk}\partial_k \overline{u}_k^s\right\} \\ & + 2\mu^s D_{jk} \,.\end{aligned} \tag{10.43}$$

10.5.4.4. Macroscopic fluid pressure equation

Volume averaging of the fluid pressure equation yields the following equation

$$\frac{1}{V}\int_V \left[\frac{\partial P^f}{\partial t} + K^f\left(\partial_k v_k^f\right) = 0\right] dV \,, \tag{10.44}$$

which reduces to

$$\frac{\partial \overline{\eta P^f}}{\partial t} + \frac{1}{V}\int_{S^{fs}} P^f v \cdot dS = -K^f \left(\eta_0 \bar{v}^f_{k,k} + \frac{\partial \eta}{\partial t} \right) . \tag{10.45}$$

Further simplification leads to

$$\eta_0 \frac{\partial \overline{P}^f}{\partial t} + \overline{P}^f \frac{\partial \eta}{\partial t} + \frac{1}{V}\int_{S^{fs}} P^f v \cdot dS = -K^f \left(\eta_0 \bar{v}^f_{k,k} + \frac{\partial \eta}{\partial t} \right) . \tag{10.46}$$

Assuming equilibrated fluid pore-pressure $\left(P^f = \overline{P}^f\right)$ within the averaging volume V, equation 10.46 reduces to

$$\eta_0 \frac{\partial \overline{P}^f}{\partial t} = -K^f \left(\eta_0 \bar{v}^f_{k,k} + \frac{\partial \eta}{\partial t} \right) . \tag{10.47}$$

Equation 10.47 has been reported by various authors (de la Cruz et al., 1985; Sahay et. al., 2001). We find that for the case of un-equilibrated pore pressure $\left(P^f \neq \overline{P}^f\right)$, equation 10.46 assumes the following form

$$\eta_0 \frac{\partial \overline{P}^f}{\partial t} + \frac{1}{V}\int_{S^{fs}} \left(\overline{P}^f - P^f\right) v \cdot dS = -K^f \left(\eta_0 \bar{v}^f_{k,k} + \frac{\partial \eta}{\partial t} \right) . \tag{10.48}$$

It is not always correct to assume equilibrated fluid pore pressure. For example, naturally occurring porous materials such as rocks usually have compliant pores such as cracks or broken grain boundaries that often form when an in-situ rock is brought to the surface. In fact, such deformations are almost always present in laboratory rock samples (Pride et al., 2003). Local fluid pressure gradients can create oscillatory fluid flow in and out of thin compliant cracks; this mechanism is commonly known as the squirt mechanism (Mavko and Nur, 1975; Mavko and Jizba, 1991). The area integral in equation 10.48 quantifies squirt flow. We simplify equation 10.48 in the effective porosity section.

10.5.4.5. **Interfacial body force equation**

The interfacial interaction force term I_j is just the sum of forces exerted by the solid component on the fluid in a unit volume of the porous medium. In the macroscopic sense, this force results in the relative velocity and the relative acceleration between solid and fluid component. Furthermore, in the presence of gravity there will be an induced buoyancy force acting on the solid from the fluid. Sahay et al., (2001) point out that this force can be simulated by an accelerating porocontinuum. The interfacial interaction force term I_j can be written in the following form

$$I_j = \delta^a_{jk}\left(\frac{\partial \overline{u}^s_k}{\partial t} - \overline{v}^f_k\right) + \rho^a_{jk}\frac{\partial}{\partial t}\left(\frac{\partial \overline{u}^s_k}{\partial t} - \overline{v}^f_k\right) + \delta^b_{jk}\dot{\overline{v}}^m_k \quad , \tag{10.49}$$

where tensorial parameters δ^a_{jk} and ρ^a_{jk} relate interfacial force linearly to the macroscopic motions and are commonly referred to the drag and additional mass parameters, respectively. The coefficient δ^b_{jk} relates interfacial force to $\dot{\overline{v}}^m_j$ which is the poro-continuum acceleration defined as

$$\dot{\overline{v}}^m_j = \frac{1}{\rho^m_0}\left\{(1-\eta_0)\rho^s_0\,\frac{\partial^2 \overline{u}^s_j}{\partial t^2} - \eta_0\rho^f_0\;\dot{\overline{v}}^f_j\right\}, \tag{10.50}$$

where,

$$\rho^m_0 = (1-\eta_0)\rho^s_0 + \eta_0\rho^f_0 \; . \tag{10.51}$$

Additional mass ρ^a_{jk} in equation 10.51 is same as the ρ^{12} coupling parameter discussed by Biot (1956). For pipe-like pores, this coupling coefficient can be assumed to be equal to $-(1/3)\,\eta_0\rho_f$ (Bredford et al., 1984). The drag parameter is related to the Darcy law permeability K_{ij} by

$$\delta_{ij}^{a} = -\frac{\eta_0 \mu_f}{K_{ij}} . \tag{10.52}$$

Due to the dynamic nature of both the drag and additional mass parameters, there are no direct methods of making laboratory measurements of these parameters.

10.5.4.6. **Porosity and deviatoric strain equation**

To complete the set of macroscopic equations, we need to define two macroscopic constitutive relations that bring micro-scale physics to macroscopic description. Taking the case of a homogeneous isotropic medium, we can define these relations as

$$\frac{\partial \eta}{\partial t} = \delta^{s} \frac{\partial \overline{u}_{l,l}^{s}}{\partial t} - \delta^{f} \overline{v}_{l,l}^{f} , \tag{10.53}$$

and

$$2D_{jk} = -\left(1-\eta_0\right)\delta^{\mu}\left\{\partial_j \overline{u}_k^{s} + \partial_k \overline{u}_j^{s} - \frac{2}{3}\delta_{jk}\partial_k \overline{u}_k^{s}\right\} . \tag{10.54}$$

Equation 10.53 relates the change in volume fraction of the fluid to the macroscopic divergence of displacements in the solid and fluid components. Parameters δ^{s} and δ^{f} are functions of pore geometry and mechanical properties of the poro-continuum constituents. Using equation 10.53 we can obtain the fluid pressure equation of the following form

$$\eta_0 \frac{\partial \overline{P}_f}{\partial t} = K^{f}\delta^{s} \frac{\partial \overline{u}_{l,l}^{s}}{\partial t} - K^{f}\left(\eta_0 - \delta^{f}\right)\overline{v}_{l,l}^{f} , \tag{10.55}$$

which is essentially same as the classical Biot fluid pressure equation (Biot, 1962; equation 3.5 in his paper). Similarly, equation 10.54 relates the tensor D_{jk} to the macroscopic deviatoric strain tensor with the parameter δ^{μ}.

10.5.5. Summary of macroscopic equations

Macroscopic continuity equations

$$\eta_0 \frac{\partial \overline{\rho}^f}{\partial t} + \rho_0^f \frac{\partial \eta}{\partial t} + \rho_0^f \eta_0 \, \partial_j \overline{v}_j^f = 0 \,, \tag{10.56}$$

$$\frac{\overline{\rho}^s - \rho_0^s}{\rho_0^s} + \partial_j \overline{u}_j^s - \frac{\eta - \eta_0}{1-\eta_0} = 0 \,. \tag{10.57}$$

Macroscopic equations of motion

$$\eta_0 \rho_0^f \frac{\partial \overline{v}_j^f}{\partial t} = \eta_0 \, \partial_k \overline{\sigma}_{jk}^f - I_j \,, \tag{10.58}$$

$$(1-\eta_0)\rho_0^s \frac{\partial^2 \overline{u}_j^s}{\partial t^2} = (1-\eta_0)\, \partial_k \overline{\sigma}_{jk}^s + I_j \,. \tag{10.59}$$

Macroscopic stress equations

$$\overline{\sigma}_{jk}^f = -\overline{P}_f \delta_{jk} + 2\mu^f \left\{ \overline{u}_{jk}^f - \frac{1}{3}\delta_{jk}\partial_k \overline{u}_k^f \right\} + 2\frac{(1-\eta_0)}{\eta_0}\mu^f \delta^\mu \frac{\partial}{\partial t}\left\{ \overline{u}_{jk}^s - \frac{1}{3}\delta_{jk}\partial_k \overline{u}_k^s \right\}, \tag{10.60}$$

$$\overline{\sigma}_{jk}^s = K^s \delta_{jk} \left\{ \partial_l \overline{u}_l^s - \frac{(\eta - \eta_0)}{(1-\eta_0)} \right\} + 2\mu^s (1-\delta^\mu) \left\{ \overline{u}_{jk}^s - \frac{1}{3}\delta_{jk}\partial_k \overline{u}_k^s \right\}. \tag{10.61}$$

Macroscopic fluid pressure equations

Equilibrated

$$\eta_0 \frac{\partial \overline{P}^f}{\partial t} = -K^f \left(\eta_0 \overline{v}_{k,k}^f + \frac{\partial \eta}{\partial t} \right) \,, \tag{10.62}$$

Squirt

$$\eta_0 \frac{\partial \overline{P}^f}{\partial t} + \frac{1}{V} \int_{S^{fs}} \left(\overline{P}^f - P^f \right) v \cdot dS = -K^f \left(\eta_0 \overline{v}_{k,k}^f + \frac{\partial \eta}{\partial t} \right) \,. \tag{10.63}$$

Interfacial body force equation

$$I_j = \delta^a_{jk}\left(\frac{\partial \overline{u}^s_k}{\partial t} - \overline{v}^f_k\right) + \rho^a_{jk}\frac{\partial}{\partial t}\left(\frac{\partial \overline{u}^s_k}{\partial t} - \overline{v}^f_k\right) + \delta^b_{jk}\dot{\overline{v}}^m_k \quad . \tag{10.64}$$

Porosity equation

$$\frac{\partial \eta}{\partial t} = \delta^s \frac{\partial \overline{u}^s_{l,l}}{\partial t} - \delta^f \overline{v}^f_{l,l} \ , \tag{10.65}$$

Parameters in terms of effective moduli

Parameters δ^f , δ^s and δ^μ can be obtained as discussed in chapter 3

$$\delta^f = \frac{K^f}{\left(K^f - K^s\right)^2}\left[\eta_0 K^f + \left(1-\eta_0\right)K^s - K_{sat-lowf}\right] \quad , \tag{10.66}$$

$$\delta^s = \frac{K^s}{\left(K^f - K^s\right)^2}\left[\eta_0 K^f + \left(1-\eta_0\right)K^s - K_{sat-lowf}\right] \quad , \tag{10.67}$$

$$\delta^\mu = 1 - \frac{\mu_{sat-lowf}}{\mu_s\left(1-\eta_0\right)} \quad , \tag{10.68}$$

where $K_{sat-lowf}$ and $K_{sat-lowf}$ are low-frequency fluid saturated bulk and shear moduli respectively. These can be further related to "dry" rock properties using equations 7.4 and 7.6.

10.5.6. Future outlook

Heavy-oil reservoir compaction can be simulated by solving the macroscopic equations (10.56-10.68). It is still to be established the differences between the predictions of the shear-rate corrected macroscopic equations and Biot theory.

10.6. Acknowledgements

We thank co-author (for section 10.1) Fabian Krzikalla. This research was funded by the Stanford Rock Physics and Borehole Geophysics Project and DOE Award No. DE-FE0002190.

10.7. References

10.7.1. For section 10.1

Bachrach, R., and P. Avseth, 2008, Rock physics modeling of unconsolidated sands: Accounting for nonuniform contacts and heterogeneous stress fields in the effective media approximation with applications to hydrocarbon exploration: Geophysics, 73(6), E197-E209.

Digby, P. J., 1981, The effective elastic moduli of porous granular rocks: Journal of Applied Mechanics, 48, 803–808.

Duffy, J., and R. D. Mindlin, 1957, Stress-strain relations and vibrations of a granular medium: Journal of Applied Mechanics, 24, 585–593.

Dvorkin, J, Mavko, G, and A. Nur, 1991, The Effect of Cementation on the Elastic Properties of Granular Material, Mechanics of Materials, 12, 207–217.

Goddard, J. D., 1990, Nonlinear elasticity and pressure-dependent wave speeds in granular media: Proceedings of the Royal Society of London A, 430, 105–131.

Hertz, H, 1882, Über die Berührung fester elastischer Körper: Journal für Reine und Angewandte Mathematik, 92, 156–171.

Johnson, K. L., 1985, Contact mechanics, Cambridge University Press, Cambridge.

Mindlin, R. D., 1949, Compliance of elastic bodies in contact: Journal of Applied Mechanics, 16, 259–268.

Sain, R., 2010, Numerical simulation of pore-scale heterogeneity and its effects on elastic, electrical and transport properties: PhD thesis, Stanford University.

10.7.2. **For section 10.5**

Biot, M.A., 1941, General theory of three dimensional consolidation, Journal of Applied Physics, 12, 155-164.

Biot, M.A., 1956, Theory of propagation of elastic waves in a fluid saturated porous solid. I Low frequency range, The Journal of the Acoustical Society of America, 28, 168-178.

Biot, M.A., 1956, Theory of propagation of elastic waves in a fluid saturated porous solid. II Higher frequency range. The Journal of the Acoustical Society of America, 28, 179-191.

Biot, M.A., 1957, The elastic coefficients of the theory of consolidation, Journal of Applied Mechanics, Trans. ASME, 24, 594-601.

Biot, M.A., 1962, Mechanics of deformation and acoustic propagation in porous media, Journal of Applied Physics, 33, 1482-1498

Berryman, J. G., 1992, Effective stress for transport properties of inhomogeneous porous rock: Journal of Geophysical Research, 97, 17409–17424.

Bedford, A., Costley, R. D., and Stern, M., 1984, On the drag and virtual mass coefficients in Biot's equations, Journal of Acoustical Society of America, 76, 1804-1810.

Chapman, M., S. V. Zatsepin, and S. Crampin, 2002, Derivation of a microstructural poroelastic model: Geophysical Journal International, 151, 427–451.

de la Cruz, V., Spanos, T., 1985, Seismic wave propagation in a porous medium, Geophysics, 50, 1556-1565.

de la Cruz, V., Sahay, P., Spanos, T., 1993, Thermodynamics of Porous Media, Mathematical and Physical Science, 443, 1917.

Dvorkin, J., and Nur, A., 1993, Dynamic poroelasticity: A unified model with the squirt and the Biot mechanisms, Geophysics, 58, 524-533.

Dvorkin, J., G. Mavko, and A. Nur, 1995, Squirt flow in fully saturated rocks, Geophysics, 60, 97–107.

Fung, Y., C., 1965, Foundations of solid mechanics, Prentice-Hall, Englewood Cliffs, NJ.

Gassmann, F., 1951, Über die Elastizität poröser Medien: Vierteljahrschrift der Naturforschenden Gessellschaft in Zürich, 96, 1-23.

Mavko, G., and D. Jizba, 1991, Estimating grain-scale fluid effects on velocity dispersion in rocks, Geophysics, 56, 1940–1949.

Mavko, G., Mukerji, T., and Dvorkin, J., 1998, The rock physics handbook, Cambridge University Press.

Mavko, G., 1979, Frictional Attenuation: An inherent amplitude depdence, Journal of Geophysical Research, 84, 4769-4775.

Mavko, G., and A. Nur, 1975, Melt squirt in the aesthenosphere: Journal of Geophysical Research, 80, 1444–1448.

Marle, C., 1967, Ecoulements monophasiques en milieu poreux, Revue de l'I.F.P. XXII, No. 10.

Sahay, P., 1996, Elastodynamics of deformable porous media, Proceedings of Royal Society London, 452, 1517-1529.

Sahay, P., Spanos, T., and V. de la Cruz, 2001, Seismic wave propagation in inhomogeneous and anisotropic porous media, Geophys. J. Int., 145, 209-222.

Sahay, P., 2008, On the Biot slow S-wave, Geophysics, 73, N19-N33.

Slaterry, J. C., 1967, Flow of viscoelastic fluids through porous media,AIChEJ 13, 1066-1072.

Whitaker, S, 1967, The method of volume averaging, Kluwer Academic Publishers.